Finite element simulation of heat flow in decomposing polymer composites

Mohammad-Reza Ebrahimi-Looyeh

Finite Element Simulation of Heat Flow in Decomposing Polymer Composites

Mohammad-Reza Ebrahimi-Looyeh

M.Sc., B.Sc., B.A.

A thesis submitted in partial fulfilment

of the requirements for the degree of

Doctor of Philosophy

School of Engineering

The University of Durham

1999

To

my parents and family

Finite Element Simulation Of Heat Flow In Decomposing Polymer Composites

M. R. Ebrahimi-Looyeh

ABSTRACT

Polymer composite materials, particularly glass reinforced plastics (GRP), are increasingly being used in the offshore industry and their behaviour in fire is studied using mathematical and numerical modelling.

A generalised finite element method is developed to analyse the thermally induced response of a widely used GRP, consisting of polyester resin and glass fibre reinforcement. GRP panels, pipes and joins subject to hydrocarbon fires (i.e. high temperatures) are studied.

One- and two-dimensional mathematical models are developed to study the fire performance of: (i) single-skinned GRP panels, (ii) twin-skinned GRP-Vermiculux sandwich panels, and (iii) thin and thick GRP joins (step panels). The models involve thermochemical decomposition of the material (pyrolysis) and include: (i) transient heat conduction, (ii) gas mass movement and internal heat convection of pyrolysis gases, (iii) mass loss and Arrhenius rate decomposition of the resin material into gases and char, and (iv) endothermicity of pyrolysis. The effect of imperfect bonding on heat transfer in sandwich panels and the accumulation of pyrolysis gases and internal pressurisation in thick step panels are also included. The models may be used with any combination of steady or time-dependent boundary conditions including temperature, radiation, chemical reactions, mass diffusion and free and forced convections. Various positions of panels, i.e. vertical, horizontal and inclined are studied. The material is assumed homogeneous and orthotropic with respect to thermal and transport properties which may vary with temperature, pore pressure and moisture.

The finite element models use weighted residual approach with linear elements for one-dimensional and quadrilateral elements for two-dimensional. Non-linear terms and coefficients are evaluated explicitly using an iterative-updating method and nodal temperatures and pore pressures implicitly using Crank-Nicolson solution. The classical finite difference time stepping algorithm is used where an efficient solution is achieved using variable time step.

Numerical results are presented in the form of temperature versus time, temperature versus distance, pore pressure versus distance, mass loss versus distance and moisture versus distance and compared with experimental data where available.

It is shown that the decomposition of the material, endothermicity of pyrolysis and the movement of pyrolysis gases make substantial contributions towards the cooling behaviour and delaying the burn-through. The effect of gas mass movement and surface chemical reactions across the boundary layer adjacent to the fire-exposed surface is very

important in introducing a theoretical boundary condition. An investigation into the effect of inclusion the variable thermal properties reveals considerable improvement in thermal predictions.

Sandwich panels consisting of GRP/Vermiculux/GRP offer good thermal insulation. Thermal contact resistance at an imperfect bonding is important where an average difference of 12% can be found between the thermal responses of sandwich panels with perfect and imperfect bonding.

For thin GRP step panels, a one-dimensional solution is found adequate to predict the fire resistance behaviour of the material. For thick GRP step panels, the effect of internal pressurisation coupled with temperature on the thermal response is considerable.

DECLARATION

ACKNOWLEDGEMENTS

My sincere thanks must go to Professor P. Bettess, my supervisor, for his guidance and considerable encouragement throughout my research at Durham University and for arranging financial support. In this respect, I am very grateful to the Durham University School of Engineering and the Committee of Vice-Chancellors and Principals.

I would like to thank Mr. V. Watts, Master of Grey College, Durham, for his hospitality and for offering me a tutorship.

My special thanks are due to Professor R. W. Girdler of Grey College, Durham, and the University of Newcastle-upon-Tyne for his patience in reading and correcting much of my thesis and for his kindness and understanding.

Special thanks are due to Professor A. G. Gibson, Dr. Y-S. Wu and Dr. N. Dodds of the University of Newcastle-upon-Tyne Centre for Composite Materials Engineering, and to Professor J. M. Davies and Dr. H-B. Wang for valuable discussions and allowing me to use their experimental results.

I am grateful to Dr. P. Boothby, Dr. P. Hill and Mr. D. Vu of British Gas PLC for providing me with useful data for offshore and onshore pipes.

My sincere gratitude goes to Professor B. Fredlund of Lund University, Sweden, for sending a valuable report relevant to my research and to Dr. O. Laghrouche for his advice and useful discussion on the finite element method.

I would like to thank the academic, secretarial, administrative and I.T.S. staff of the School of Engineering at Durham University for providing a friendly environment for my research. My special thanks go to Mrs. J. Barclay, departmental secretary, for her considerable help, patience and kindness.

I would like to thank Mrs. M. Weston for her valuable help in translation from French. I also benefited moral support from friends and colleagues particularly, Miss A. Sadeghzadeh, Miss. M. Jimenez and Mr. S. Jaberzadeh.

Finally, my heartfelt gratitude goes to my parents and family for their loving support, continual encouragement and belief in my abilities.

TABLE OF CONTENTS

LIST OF FIGURES

LIST OF TABLES

LIST OF SYMBOLS

a_i	.....	curve fit coefficient	
A	.....	cross-sectional area	m^2
	.....	pyrolysis constant	s^{-1}
A_g	.....	void area	m^2
A_s	.....	rate constant (surface chemical reactions)	$s^{-1}K^{-1}$
A_w	.....	total surface of pipe swept by fluid flow	m^2
B	.....	nodal shape function derivative	
$\mathbf{B}$	.....	shape function derivative matrix	
c_p	.....	isobar specific heat of GRP	$Jkg^{-1}K^{-1}$
c_{pc}	.....	isobar specific heat of SM	$Jkg^{-1}K^{-1}$
c_{pfr}	.....	isobar specific heat of fibre reinforcement	$Jkg^{-1}K^{-1}$
c_{pg}	.....	isobar specific heat of gas	$Jkg^{-1}K^{-1}$
c_{pr}	.....	isobar specific heat of resin	$Jkg^{-1}K^{-1}$
c_{pv}	.....	isobar specific heat of evaporation (GRP)	$Jkg^{-1}K^{-1}$
c_{pvc}	.....	isobar specific heat of evaporation (SM)	$Jkg^{-1}K^{-1}$
$\mathbf{C}$	.....	capacitance (mass) matrix	
D	.....	internal diameter	m
E	.....	Young's modulus	Pa
	.....	total number of elements	
E_A	.....	activation energy	$kJkmole^{-1}$
E_{As}	.....	activation energy (surface chemical reactions) ..	$kJkmole^{-1}$
f	.....	friction factor	
f_c	.....	correction factor for dehydration	
$f(m_v)$	.....	proportion function for GRP	
$f(m_{vc})$	.....	proportion factor for SM	
F	.....	instantaneous mass fraction	
$\mathbf{f}$	.....	heat load (force) vector	
g	.....	gravitational acceleration	ms^{-2}
h	.....	enthalpy of GRP	Jkg^{-1}
	.....	element width	m
h_b	.....	blowing factor	
h_c	.....	convection heat transfer coefficient	$Wm^{-2}K^{-1}$
h_{fg}	.....	latent heat of evaporation	Jkg^{-1}
h_g	.....	enthalpy of gas	Jkg^{-1}
h_r	.....	radiation heat transfer coefficient	$Wm^{-2}K^{-1}$
h_s	.....	enthalpy of GRP (surface chemical reactions)	Jkg^{-1}
h_{TCR}	.....	thermal contact resistance coefficient	$Wm^{-2}K^{-1}$
H	.....	height/length	m
k	.....	thermal conductivity of GRP	$Wm^{-1}K^{-1}$
k_c	.....	thermal conductivity of sandwich material	$Wm^{-1}K^{-1}$
k_{fr}	.....	thermal conductivity of fibre reinforcement	$Wm^{-1}K^{-1}$
k_g	.....	thermal conductivity of gas	$Wm^{-1}K^{-1}$
	.....	thermal conductivity of gas in void space	$Wm^{-1}K^{-1}$
k_{ij}	.....	element of conductivity tensor	$Wm^{-1}K^{-1}$
k_L	.....	longitudinal thermal conductivity	$Wm^{-1}K^{-1}$

k_r	.....	thermal conductivity of resin	$Wm^{-1}K^{-1}$
k_{rm}	.....	thermal conductivity of moist resin	$Wm^{-1}K^{-1}$
k_T	.....	through-the-thickness thermal conductivity	$Wm^{-1}K^{-1}$
$\mathbf{K}$	.....	conductance matrix	
l	.....	element length	m
l_c	.....	element length in SM domain	m
l_s	.....	element length in GRP domain	m
L	.....	thickness	m
L_c	.....	thickness of SM	m
L_f	.....	overall length of pipe exposed to fire	m
L_g	.....	thickness of void space	m
L_s	.....	thickness of GRP skin	m
m_v	.....	volumetric moisture content (GRP)	
m_{vc}	.....	volumetric moisture content (SM)	
m_w	.....	mass of moisture (GRP)	
m_{wc}	.....	mass of moisture (SM)	
M_g	.....	gas molecular weight	$kgkmole^{-1}$
$\dot{m}_g$	.....	gas mass flux	$kgm^{-2}s^{-1}$
$\dot{m}_{gx}$	.....	gas mass flux in x direction	$kgm^{-2}s^{-1}$
$\dot{m}_{gy}$	.....	gas mass flux in y direction	$kgm^{-2}s^{-1}$
$\dot{\mathbf{m}}_g$	.....	gas mass flux vector	
n_T	.....	total number of spatial nodes	
n_x	.....	normal vector in x direction	
	.....	number of spatial nodes at position x	
n_y	.....	normal vector in y direction	
$\mathbf{n}$	.....	normal vector	
N	.....	nodal shape function	
$\mathbf{N}$	.....	shape function matrix	
$\mathbf{N_x}$	.....	shape function derivative matrix with respect to x	
$\mathbf{N_y}$	.....	shape function derivative matrix with respect to y	
P	.....	pressure	Pa
q	.....	heat flux (heat flow rate per unit area)	Wm^{-2}
q_c	.....	heat flux due to convection	Wm^{-2}
q_{mf}	.....	heat flux due to gas mass movement	Wm^{-2}
q_r	.....	heat flux due to radiation	Wm^{-2}
q_{sr}	.....	heat flux due to surface chemical reactions	Wm^{-2}
q_x	.....	heat flux in x direction	Wm^{-2}
q_y	.....	heat flux in y direction	Wm^{-2}
$\dot{q}$	.....	internally generated heat per unit volume	Wm^{-3}
$\mathbf{q}$	.....	heat flux vector	
	.....	heat load vector	
Q	.....	heat of decomposition	Jkg^{-1}
Q_s	.....	heat of decomposition (surface chemical reactions) ..	Jkg^{-1}
r,θ	.....	Polar co-ordinate system	
$\mathbf{r}$	.....	element nodal vector	
R	.....	gas constant	$8.314\ kJkmole^{-1}K^{-1}$
R_i	.....	internal radius	m
S_{ij}	.....	boundary surface	
S_{ut}	.....	ultimate tensile strength	Pa

t	.....	time	s
T	.....	temperature	^{o}C
T_b	.....	bulk temperature	^{o}C
T_c	.....	surface temperature (SM)	^{o}C
T_f	.....	time-dependent fire temperature	^{o}C
T_F	.....	film temperature	^{o}C
T_g	.....	maximum fire temperature	^{o}C
T_{in}	.....	inlet temperature of fluid flow	^{o}C
T_{out}	.....	outlet temperature of fluid flow	^{o}C
T_r	.....	radiative temperature	^{o}C
T_s	.....	hot surface temperature	^{o}C
T_w	.....	internal surface temperature	^{o}C
$\mathbf{T}$	.....	temperature vector	
u_g	.....	velocity of gas in x direction	ms^{-1}
u,v	.....	velocity in x and y directions	ms^{-1}
V_f	.....	volume fraction	
V_m	.....	mean velocity	ms^{-1}
V_s	.....	rate of modification (surface chemical reactions)	ms^{-1}
W	.....	weighting function	
	.....	width	m
x,y	.....	Cartesian (global) co-ordinate system	
$\mathbf{X}$	.....	unknown vector	
y_i	.....	mole fraction	mole
z	.....	compressibility factor	
	.....	z co-ordinate	
Z	.....	elevation	m
α	.....	thermal diffusivity	m^2s^{-1}
α	.....	cold surface absorptivity	m^2s^{-1}
α_g	.....	gas thermal diffusivity	m^2s^{-1}
α_s	.....	hot surface absorptivity	
β	.....	coefficient of volumetric thermal expansion	K^{-1}
γ	.....	permeability	m^2
γ_g	.....	specific gravity	
γ_x	.....	permeability in x direction	m^2
γ_y	.....	permeability in y direction	m^2
Γ	.....	solution boundary surface	
δ	.....	thickness of hydrodynamic boundary layer	m
δ_t	.....	thickness of thermal boundary layer	m
Ω	.....	solution domain	
ξ,η	.....	local co-ordinate system	
θ	.....	angle	degree
		relative temperature	^{o}C
Θ	.....	time step (weighting) parameter	
ε	.....	cold surface emissivity	
ε_s	.....	hot surface emissivity	
ε_g	.....	gas emissivity	
μ_g	.....	gas dynamic viscosity	Nsm^{-1}
ρ	.....	density of GRP	kgm^{-3}

ρ_c	.....	density of SM	kgm^{-3}
ρ_{fr}	.....	density of fibre reinforcement	kgm^{-3}
ρ_g	.....	density of gas	kgm^{-3}
ρ_r	.....	density of resin	kgm^{-3}
ρ_{rf}	.....	final density of resin	kgm^{-3}
ρ_s	.....	density of composite at the hot surface	kgm^{-3}
	.....	surface reflectivity	
σ	.....	Stefan-Boltzmann constant	5.669×10^{-8} $Wm^{-2}K^{-4}$
ϕ	.....	porosity	
Δh_s	.....	change of enthalpy (surface chemical reactions)	Jkg^{-1}
ΔP	.....	pressure drop	Pa
Δt	.....	time step	s
ΔT	.....	temperature interval	°C

Subscripts

cr	critical
e	environment
j	nodal position in *x* direction
k	nodal position in *y* direction
	Kelvin
M	maximum
o	initial value
R	reference
x	partial derivative with respect to *x*
xx	second partial derivative with respect to *x*
y	partial derivative with respect to *y*
yy	second partial derivative with respect to *y*
∞	ambient

Superscripts

e	element
i	time position
T	transpose
¯	average
.	partial derivative with respect to time

Dimensionless Groups

Gr	Grashof number
Nu	Nusselt number
Pe	Peclet number
Pr	Prandtl number
Ra	Rayleigh number
Re	Reynolds number

Abbreviations

BS	British standard
CMS	chopped strand mat
DC	drop calorimetry
DoE	department of energy
DSC	differential scan calorimetry
DTA	differential thermal analysis
FDM	finite difference method
FEM	finite element method
FRP	fibre reinforced plastics
GRE	glass reinforced epoxy
GRP	glass reinforced plastics
ISO	international organisation for standardisation
IMO	international maritime organisation
NPD	Norwegian petroleum directorate
OD	outer diameter
SM	sandwich material
TGA	thermo gravimetric analysis
TPP	thermo physical property
Uni	unidirectional
WR	woven roving

THESIS STATISTICS

Finite Element Simulation of Heat Flow in Decomposing Polymer Composites

M. R. Ebrahimi-Looyeh
School of Engineering, University of Durham
August 1995-January 1999

KEYWORDS: Arrhenius equation; Finite element method; Glass reinforced plastics; Hydrocarbon fire; Joins; Offshore structures; Panel; Pipe; Polymer composites; Pyrolysis; Sandwich panel; Thermal response, Thermochemical decomposition.

Text	Word ver. 6.0a
Graphs	1. Excel ver. 5.0a 2. Power point ver. 4.0 3. Contour plot program (Bettess, Bettess & Looyeh)
Curve fits	Grapher ver. 1.25
Bibliography	Papyrus ver. 7.0.12
Programming language	FORTRAN 77
Format	Headings: Helvetica Text: Times New Roman Text size: 12 pt. Tables & Figures: 12 pt. Line space: 1.5 pt. Margins (cm): Top (2.5), bottom (2), left (4), right (2)
Sections	23
Chapters	10
Pages (chapters + bibliography)	273
Pages (thesis)	307
Lines (chapters + bibliography)	7748
Lines (thesis)	9102
Words (abstract)	488
Words (chapters + bibliography)	61036
Words (thesis)	70705
Equations	434
Symbols	275
Figures	111
Tables	25
References	113

CHAPTER I

INTRODUCTION

1.1 OBJECTIVE

The objective of this research is to produce a numerical tool, based on the finite element method, to describe and predict the thermally induced response of glass reinforced plastics (GRP) in the form of panels, pipes and joins at high temperatures experienced in offshore hydrocarbon fires. One- and two-dimensional mathematical and numerical models are sought, which include the physical and chemical processes of importance in the material during fire. The research concentrates on the thermochemical decomposition (pyrolysis) of the material and considers all possible boundary conditions. The numerical tool has been tested for polyester-based GRP and can easily be modified for any other GRP once the material properties are defined. Some of the numerical results have been compared with the results of furnace fire tests.

1.2 HISTORICAL BACKGROUND - OFFSHORE TECHNOLOGY

The offshore oil and gas industry has experienced remarkable growth since the late 1940's, when offshore drilling platforms were first used in the Gulf of Mexico [Lee, 1968; McClelland *et al.*, 1986]. A wide variety of offshore structures are now being used, sometimes under severe environmental conditions. Difficulties in design, construction and service are considerable especially such structures are now being located in ever increasing water depths.

Offshore structures have two components, i.e. topsides and a supporting structure (Figure 1.1a). These structures include both mobile and fixed drilling platforms (Figure 1.1) [Sarpkaya & Isaacson, 1981].

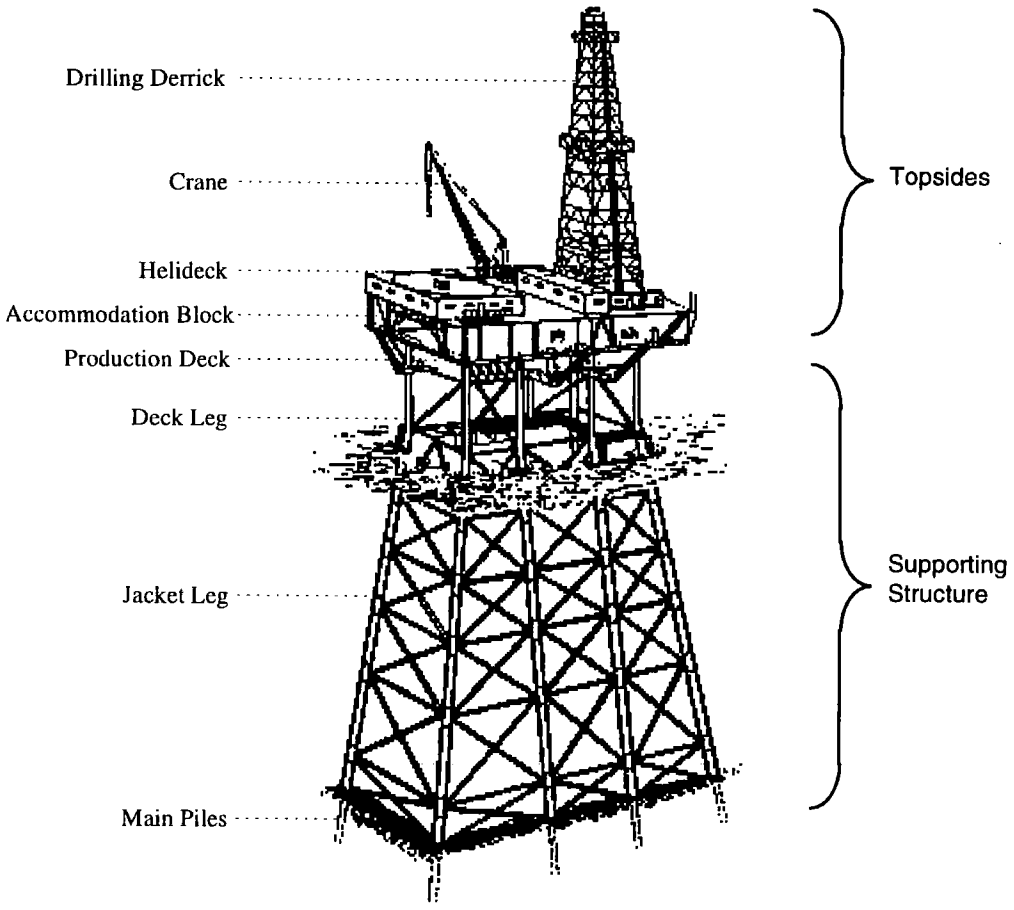

(a)

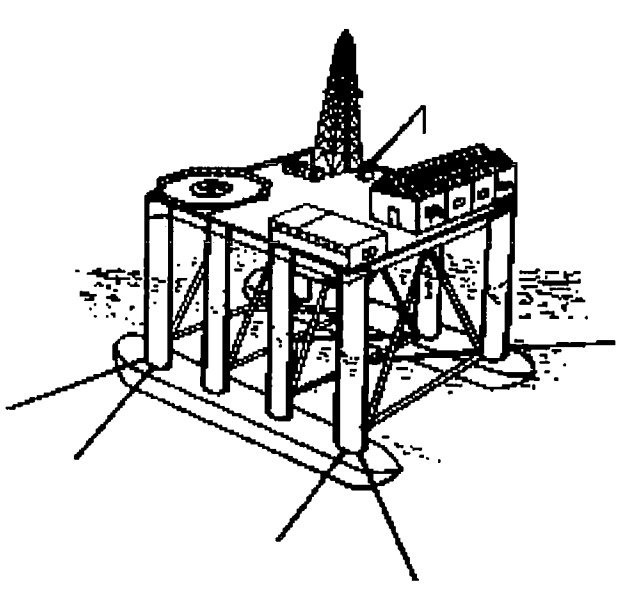

(b)

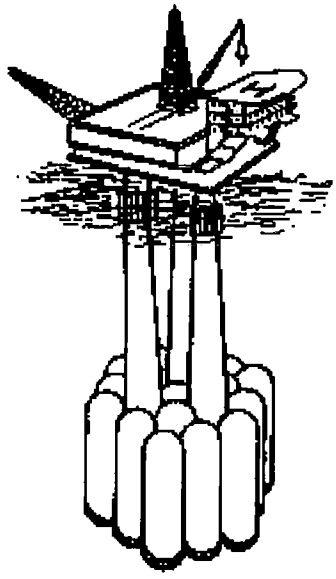

(c)

Figure 1.1 Typical offshore structures which are currently being used for oil and gas development; (a) Jacket type platform; (b) Semi-submersible platform; (c) Concrete gravity platform [from: Sarpkaya & Isaacson, 1981].

The potential for catastrophic failure underlines the critical importance of efficient and reliable design for any environmental conditions. The Piper Alpha disaster was the worst drill-rig accident in Britain for over 50 years; this explosion and fire in July 1988 claimed the lives of 167 men and destroyed the chain platforms worth US$ 1300 millions. This revealed that the dangers on a rig like Piper Alpha were far worse than were allowed in the existing design specifications and a great concern for the potential hazard of fires and explosions. Subsequently, increased demands have been made by national and international health and safety organisations for detailed quantified risk assessment. The potential for a release of hydrocarbons and hence explosions and fires on offshore rigs is relatively high leading to high safety requirements.

1.3 FIRE HAZARDS AND FIRE PROTECTION METHODS

Fire is regarded as an oxidation reaction at the surface of a material releasing reactive gases. Three factors are required for burning to start and once started to continue: (i) a combustible surface, (ii) an oxidising agent and (iii) a source of heat [Shenoi & Wellicome, 1993a].

Fires can result from electrical faults, by spillage and ignition of oil and gas, welding and flame cutting operations [Smith, 1990].

The main fire hazards to human life are [Shenoi & Wellicome, 1993a]: (i) oxygen depletion where a minimum level of 21% in the atmosphere is essential; (ii) direct flames result in burning if skin temperature goes above 65°C; (iii) excess heat; a breathing temperature of 148°C is considered to be the maximum for survival; (iv) fire gas products which can be toxic; (v) smoke which causes suffocation and (vi) structural strength reduction which might result in the collapse of the weakened gratings.

Fires on offshore installations are usually either cellulosic or hydrocarbon. Cellulosic fires are burning timbers and upholstery (as may be found in accommodation areas). Hydrocarbon fires are burning oils and fuels. Hydrocarbons burn far more fiercely than cellulosic materials and consequently require fire protection systems of substantially superior performance.

For fire protection two basic methods are used, i.e. active and passive [Wang, 1995]. Active fire fighting is normally provided by means of automatic detectors, water

sprinklers, deluges and sprays and the use of usual fire extinguishers. When alarms and sprinkler systems respond to fire by some form of actuation, passive fire protection systems are already in situ and absorb the energy of the fire by a variety of means. The passive protection can be achieved either by structure design or by using an external cladding, fire and blast walling and coating which provide fire protection. The protection strategy used depends on the fire type and duration, the equipment and components requiring protection and the time required for evacuation. In practice, an optimised combination of both active and passive methods are used. Here we are concerned with passive fire protection particularly the use of GRP.

1.4 COMPOSITES FOR OFFSHORE USE

Polymer composite materials such as GRP, consisting of resin matrix and glass fibre reinforcement, are increasingly being used on offshore installations. These materials are useful alternatives to steel where corrosion resistance, low weight, low cost, long service life and reduced maintenance are desirable. With organic, flammable matrix resins, attention must be paid to fire risk and hazards from smoke and fumes. The increase use of polymer composites has resulted from the removal of restrictive standards for designs and materials (which was disadvantageous to the use of polymer composites due to their combustibility) [Shenoi & Wellicome, 1993a]. These changes, which resulted partly from the Cullen enquiry into the Piper Alpha disaster [Cullen, 1990], stimulated work on a range of alternative materials. It is now possible to employ these materials offshore, provided their use can be shown to satisfy all the performance-based criteria relating to fire. To execute these criteria, it is necessary to evaluate designs against all possible hazards and to show that both design and material will perform adequately for each case [Gibson, 1997; Spagni & Gibson, 1994]. High temperatures may result loss of strength and stability and subsequent failure of a structure. Also, smoke, toxic gases etc. are other potential problems which may lead to explosion.

The effects of fire varies substantially from one structure to another and the assessment of these effects is complex [Wang, 1995]. Although standard full scale tests [Spagni & Gibson, 1994; Wang, 1995; Wu *et al.*, 1994] give reasonably simple solutions, they can not be generalised. Such evaluations may result in design

modifications. Due to cost, computer modelling has recently been introduced as a cost- and time-effective alternative. With recent advances in computer technology, many research and development centres, involved in fire safety research projects, now use computer simulations as efficient and economic means of supplementing fire testing. Using knowledge of the behaviour of materials at elevated temperatures, computer-generated models for thermal analyses may provide practical and efficient solutions for predicting the thermal response of a structure under a given set of time-varying temperatures. In addition, there have been performance studies of offshore components made of GRP using standard fire tests.

1.4.1 Definitions

At the macroscopic scale a composite may be regarded as consisting of two or more physically distinct materials which have been combined in some controlled manner. The resulting mixture is characterised by properties which are more useful than those possessed by any of the constituents alone [Grove, 1985] (Appendix A).

Here we are interested in polymer-based composites containing fibrous matter. Although, the range of such materials is vast, only a few are used in the offshore industry. These composites comprise a high strength reinforcement in fibrous form, incorporated into and bounded together with a matrix, usually thermosetting polymer [Spagni & Gibson, 1994]. The term fibre reinforced plastic (FRP) is widely used to describe such materials with glass reinforced plastic (GRP) when the reinforcement is glass fibre. Glass reinforced epoxy (GRE) has epoxy resin as the matrix and is mainly used for composite pipework [Marks, 1987; Grim & Twilt, 1991]. In GRP products, most of glass fibres consist of E-glass, a term which once stood for electrical grade glass, as used in insulators and capacitors. There are three different types of E-glass: (i) chopped strand mat (CSM) which contains randomly oriented glass strands of maximum 50mm, held together by the use of a small amount of polymeric binder; (ii) unidirectional rovings (Uni) which can be used directly in GRP and (iii) woven rovings (WR) which are produced by standard textile weaving processes and can have various types of weave, such as plain, satin or twill.

1.4.2 Applications

Fibre reinforced plastics (FRP) on offshore installations have been used since about 1990. FRP are of interest to offshore industry because they are light, cost effective and resistant to corrosion. On the basis of strength and stiffness, FRP do not have a clear advantage particularly when it is noted that their elongation to fracture is much lower than metallic materials with comparable strength. The advantages of FRP appear when the specific modulus (Young's modulus per unit weight) and specific strength (strength per unit weight) are considered.

A feasibility study was made by Bergland and Willners [1988] which considered the possibilities of building the deckhouse of an offshore platform in FRP sandwich panels in order to reduce structural weight. The weight of FRP sandwich panel deckhouse was compared with equivalent structures made of aluminium and steel [Ulfvarson, 1989] (Table 1.1).

Table 1.1 Weights of three equivalent deckhouses [Ulfvarson, 1989].

Material Type	Weight (tonnes)
Fibre reinforced plastic (FRP)	85
Aluminium	108
Steel	155

Some existing offshore applications of FRP are: fire protection panels, water piping systems, walkways and gratings, partition walls, tanks and vessels, cable ladders and trays, boxes, housings and shelters. In particular, FRP find uses in three fire sensitive areas: (i) filament wound pipework; (ii) lightweight walls and partitions for blast and fire protections and (iii) walkways and gratings [Gibson, 1993; Spagni & Gibson, 1994].

1.4.3 Fabrication Methods

The scale of many components in use offshore is larger than in any other engineering applications and unlike the fabrication technology for metallic materials, manufacturing processes for fibre reinforced composites are not yet so adaptable to large scale

constructions [Spagni & Gibson, 1994]. Among many fabrication processes only a few such as contact moulding, resin transfer moulding, pultrusion and filament winding have the potential for efficient use in large structures.

There are many fabrication techniques for FRP. The design of FRP is strongly influenced by the type of fabrication process used. It is interesting to know that all fabrication processes involve the same basic steps [Spagni & Gibson, 1994]. These are: (i) conformation of the reinforcement to the shape of the part; (ii) impregnation of the reinforcement with liquid resin; (iii) consolidation to remove entrapped air and (iv) chemical reaction of the liquid resin to form a solid thermoset (curing).

There are two overall processes for fabrication, i.e. open mould process and closed mould process. Hand lay-up, spray-up, vacuum bag, filament winding and centrifugal casting are classified within the first category and hot press moulding, resin transfer moulding, cold press moulding and pultrusion within the second category [Hull, 1981]. Among these, three major routes to the manufacture of FRP with thermosetting resins are now used in the offshore industry. In these routes, the wet processing method in which low viscosity resin is impregnated into dry fibre is used. These routes are: (i) wet lay-up in which the fibres in the form of a mat are impregnated with resin by rolling and pressing; (ii) wet winding or filament winding in which the fibre tows, i.e. bundles of fibres, are drawn through a bath of resin before winding onto a mandrel or former of the required shape and (iii) resin injection in which the fibres are placed in position in a closed mould and the resin is fed in under gravity or external pressure.

For the purpose of fire experiments, FRP laminates are normally prepared in a lab using the hand lay-up method. In this method, chopped strand mats (CSM), woven rovings (WR) and other fabrics made from the fibres are placed on the mould and impregnated with liquid resin by painting and rolling. Layers are build up until design thickness is achieved. Moulding cures in the atmosphere without extra heat or pressure.

The simplest method for fabricating composite panels and plates is the semi-automated process used for the production of internal structures. In this process, the single- or twin-skinned composite panels are laid up and fabricated into modules of a size which can easily be handled and assembled into large units. The twin-skinned sandwich panels are manufactured by either mechanical fasteners or by using special bonding processes with resin adhesives. For gratings, walkways and decking the pultrusion method is used. The filament winding process is also used for pipe

fabrication. In this method, unidirectional tows are wrapped around a core or mandrel at a constant angle. This process can also be used for tanks and vessels [Gibson, 1993].

1.4.4 Fire Performance

There are no standards which explicitly specifies the suitability of materials for fire hazards. The requirements vary according to the type and duration of fire and the nature of possible hazards such as hydrocarbons. Three aspects of fire behaviour are of great importance for offshore composites [Spagni & Gibson, 1994]. These are: (i) ignitability and heat release; (ii) smoke and toxicity and (iii) fire resistance. Fire resistance is a measurement of the ability to retain structural integrity. Fire resistance is regarded as the most important factor in the use of composites offshore. The current research therefore puts emphasis on this as the major factor in fire performance.

1.4.5 Why Glass Reinforced Plastics?

Figures 1.2 and 1.3 demonstrate some key properties for the selection of structural materials for offshore use [Gibson, 1993]. Materials are compared in terms of specific strength (strength per unit weight, S_{ut}/γ_g) and specific stiffness (stiffness per unit weight, E/γ_g) where S_{ut} is the ultimate tensile strength (MPa), γ_g is the specific gravity and E is the Young's modulus (GPa).

It is seen that nearly all composites are superior to metallics in specific strength (the few exceptions being of few of the glass/polyester composites). In contrast, only the carbon/epoxy and some of aramid/epoxy composites are superior in specific stiffness.

In Figure 1.3 the materials' strength per unit cost (ultimate tensile strength per volume cost) is compared with the stiffness per unit cost (Young's modulus per volume cost). It is evident that none of the composites is competitive with metallics on the basis of stiffness per volume cost and only the glass/polyester composites can compete with metallics on the strength per volume cost. This is why for large structures such as offshore platforms, the glass/polyester composites are preferred to carbon/epoxy or aramid/epoxy composites, which are the most expensive. This is the major reason for the increase use of GRP in the offshore industry. It is worth noting that the comparisons are based upon raw material costs; consideration of installation and through-life costs may result further advantages of GRP over the metallic materials.

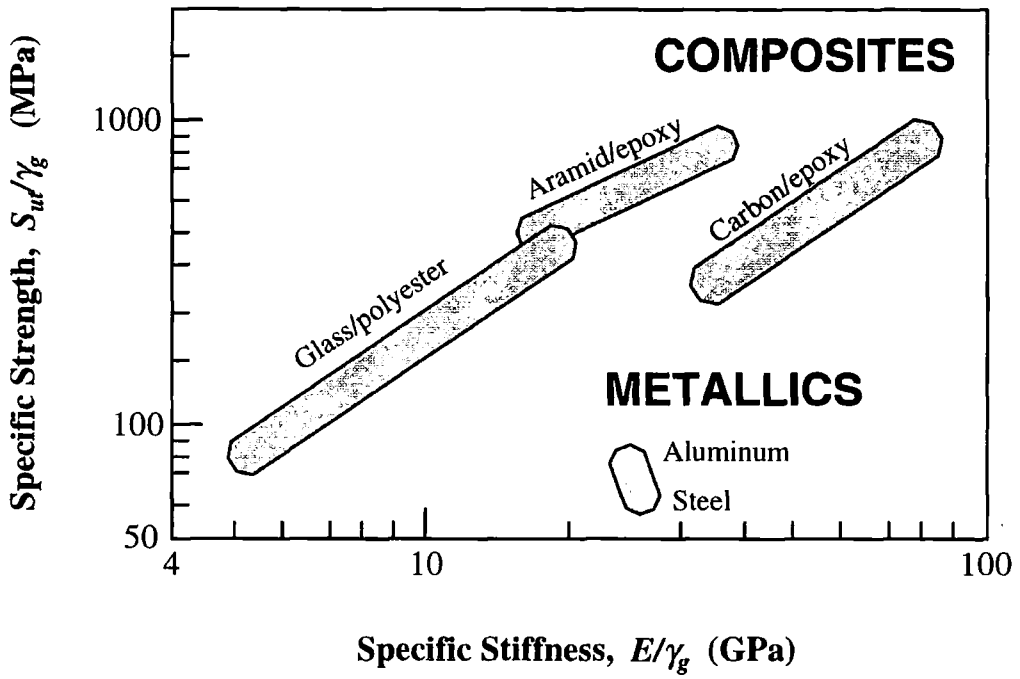

Figure 1.2 Specific strength versus specific stiffness for a range of engineering materials. Specific strength is defined as the ratio of the ultimate tensile strength (S_{ut}) to specific gravity (γ_g) and specific stiffness as the ratio of Young's modulus (E) to specific gravity [from: Gibson, 1993].

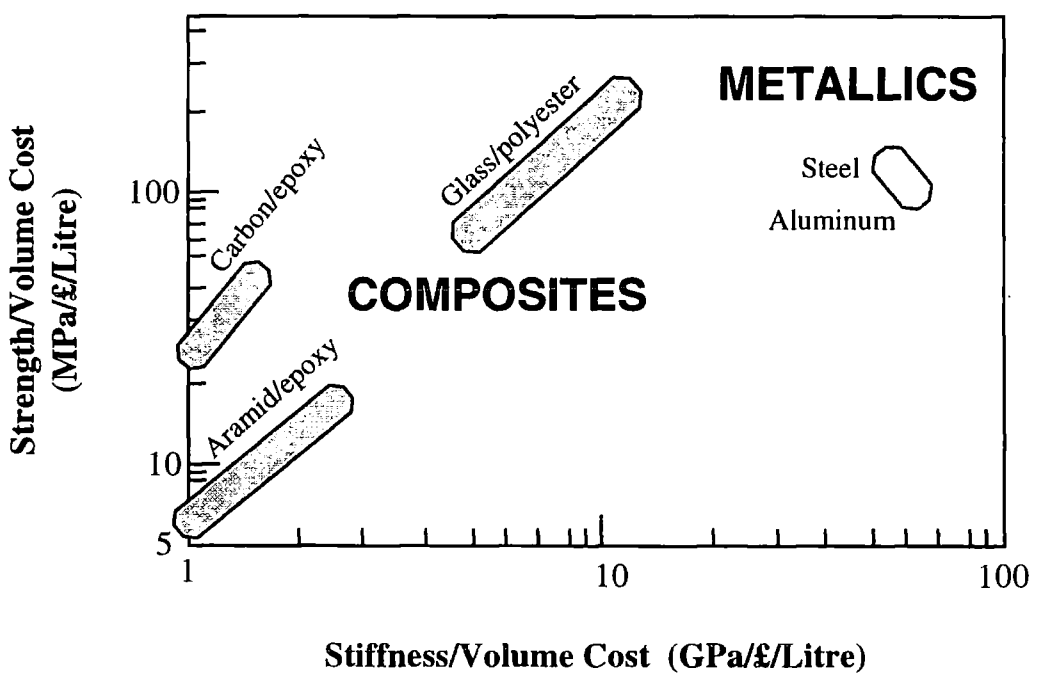

Figure 1.3 Strength per volume cost versus stiffness per volume cost for a range of engineering materials [from: Gibson, 1993].

There remains the choice of the appropriate material from the array of different reinforced resin combinations. The selection of resin matrix is important because it plays a critical role in overall strength, corrosion resistance and more importantly the thermal stability. Table 1.2 shows some of the thermosetting candidates for offshore applications among them unsaturated polyester is most widely used offshore despite the fact that it shows poor performance in fire compared to the others [Gibson, 1993]. For offshore installations the choice of reinforcements is also simplified, since the cost constraints render the more expensive high performance reinforcements, carbon and aramid, unattractive. The emphasis for tonnage use is strongly advised on glass fibre, which can be applied in a variety of forms more preferably woven roving (WR) fabrics for panels and unidirectional (Uni) fabrics for pipes.

Table 1.2 Comparison of thermosetting resins for use in GRP for the offshore industry (based on star rating) [from: Gibson, 1993].

Resin Type	Cost (£/tonne)	Mechanical Strength	Corrosion Resistance	Fire Performance
Polyester	1200-1600	**	**	*
Vinyl ester	2200-2600	***	***	*
Modar	2000-3000	**	**	***
Epoxy	>4000	*****	*****	*
Phenolic	1300-1700	**	**	*****

1.5 STANDARDS FOR FAILURE CRITERIA

The use of composite materials for offshore structures is regulated by the same criteria issued by the International Maritime Organisation (IMO) for all materials in the marine industry. The general requirements specified by IMO [Shenoi & Wellicome, 1993a] are: (i) fire reaction: which is the degree to which a material partakes in the fire process; (ii) fire resistance: which is the ability of a certain structure to resist degradation over a defined time period; (iii) containment: which is the ability of a structure and the material to act as fire, temperature and smoke barrier during a defined time period under specified conditions and (iv) smoke and toxicity: which is the degree to which the material produces smoke and toxic fumes.

To quantify the fire performance of composites particularly GRP in offshore installations, a range of different requirements may apply for different circumstances. There is a similar broad range of standard methods in the internationally accepted ISO 834 [1975]. Among them, the usual criteria for failure in furnace tests are used. These are defined in BS476 [1987] as stability, integrity and insulation requirements for the fire resistance. The fire resistance is therefore defined as the time when some of the following requirements are no longer complied with [Fredlund, 1993]:

1. The insulation requirement; where the rise in temperature over the unexposed surface is not allowed to exceed 160°C on average or 170°C for a hot spot.
2. The integrity requirement; where the structural component is not allowed to be penetrated by flames or hot gases.
3. The load bearing requirement; this requirement is to be excluded for non-load bearing structures.

In this research, it is the first requirement which is used to determine the fire resistance of GRP components. This requirement can also be defined on the basis of the time which is required for the average temperature of the unexposed surface to reach 160°C. There are normally two standard time ratings required for any offshore component to achieve. These are H60 and H120. An H60 rating for a panel means that the rear face temperature remains below the critical temperature 160°C for at least 60 minutes and for an H120 rating for at least 120 minutes [Shenoi & Wellicome, 1993a].

1.6 USE OF EXPERIMENTAL RESULTS

The experimental data presented in this thesis are from the literature by courtesy of other researchers or collected by studies of the literature [Davies & Wang, 1998; Dodds *et al.*, 1998; Holman, 1997; Gibson *et al.*, 1996; Wu & Gibson, Pers. Com., 1996; Wang, 1995; Wu & Gibson, Pers. Com., 1995; Spagni & Gibson, 1994; Wu *et al.*, 1994; Davies *et al.*, 1994a; Lide and Kehiaian, 1994; Looyeh, 1994; API RP 2A-LRFD, 1993; Shenoi & Wellicome, 1993a&b; Sullivan, 1993; Sullivan & Salamon, 1992b; Bradley, 1992; Datoo, 1991; Agarwal, 1990; ISO 5660, 1989; Fredlund, 1988; BS476, 1987; Henderson *et al.*, 1985; Drysdale, 1985; Perry *et al.*, 1984; Sheldon, 1982; Gnielinski,

1976; Churchill & Chu, 1975; ISO 834, 1975; Churchill & Ozoe, 1973; Fujii & Imura, 1972; Hall and Yarborough, 1971; Clifton & Chapman, 1969; Havens, 1969; Friedman, 1965]. A review of the experimental techniques improves understanding of the complex behaviour of composites during fire and enable an assessment of the validity and accuracy of the numerical results.

Several standard experiments are carried out to characterise the thermal response of composite materials during fire. The outputs of such experiments can be the rate of heat release, temperature, pressure, density, mass loss, rate of mass loss, moisture content and surface recession. These are described in brief as follows:

The rate of heat release

Cone calorimetry technique is a method for the measurement of the rate of heat release of composites on the basis of a standard procedure defined in ISO 5660 [1989]. The technique relies upon an empirical law that the ratio of the heat released in a fire to oxygen consumed is almost constant for most materials. Measuring the oxygen concentration enables the heat release rate to be computed indirectly and continuously and more accurately than by the direct calorimetric measurements. This is also possible to measure toxic gases such as carbon monoxide, carbon dioxide and smoke density.

Specific heat

Several methods are used to measure specific heat. The two most widely are drop calorimetry (DC) and differential scanning calorimetry (DSC). DSC is a quick and straightforward method developed in late 60's [Havens, 1969; Brennan *et al.*, 1969] and used for the measurement of specific heat and enthalpy of materials; the specific heat is calculated on the basis of the energy input to the sample, the mass of the sample and the heat rate.

Heat of decomposition

Bamford *et al.* [1946] introduced an in situ measurement for the heat of decomposition in which the heat of decomposition is calculated using the sudden rise of temperature which occurs in the centre of the sample during decomposition due to endothermic or exothermic reactions. Differential thermal analysis (DTA) [Sykes, 1967] and DSC are also used for the measurement of the heat of decomposition.

Mass loss and the rate of mass loss

A dynamic heating method known as thermo gravimetric analysis (TGA) is used for the simultaneous measurement of the mass loss and the rate of mass loss. TGA provides a trace of the mass loss with time as a sample is heated at a constant rate (^{o}C/min) or held at a constant temperature in an oxidising environment. TGA results, based upon mass loss with temperature increases at different heating rates, provide the basis for modelling the decomposition behaviour of composites by fitting an Arrhenius type rate equation [Friedman, 1965; Perry *et al.*, 1984] to the data. Following the method of Friedman [1965] log/log plots are used to determine the values of order of reaction, pre-exponential factor and the activation energy.

Surface spread of flame

This is one of the complementary tests included in the BS476 standard [1987]. The test is normally carried out to compare the flame spread behaviour of different composites. The procedure involves placing a rectangular sample perpendicular to an incandescent matrix burner and recording the progress of any flames observed with time.

Temperature measurements

The fire performance of composite materials is generally assessed by the use of furnace tests [Davies & Wang, 1998; Dodds *et al.*, 1998; Gibson *et al.*, 1996; Wang, 1995; Wu *et al.*, 1994; Spagni & Gibson, 1994; Davies *et al.*, 1994a; Shenoi & Wellicome, 1993b; BS476, 1987; ISO 834, 1975]. Two types of fire tests are normally used: (i) large scale test, requiring a 3m square sample and (ii) indicative test, which uses a smaller sample of 1.2m square [BS476, 1987]. In each case, the furnace temperature is increased in a prescribed manner for two types of fire as shown in Figure 1.4: (i) cellulosic which simulates a conventional fire and is given by a temperature-time curve according to BS476 standard and (ii) hydrocarbon which simulates more severe conditions and much higher initial rate of temperature rise; this fire is given by a temperature-time curve defined by Norwegian Petroleum Directorate (NPD).

Important to note is the simulated NPD fire does not represent the actual characteristics of hydrocarbon fires where very high heating rates, high gas velocity and thermal shock are involved and the existing oxygen is consumed very rapidly.

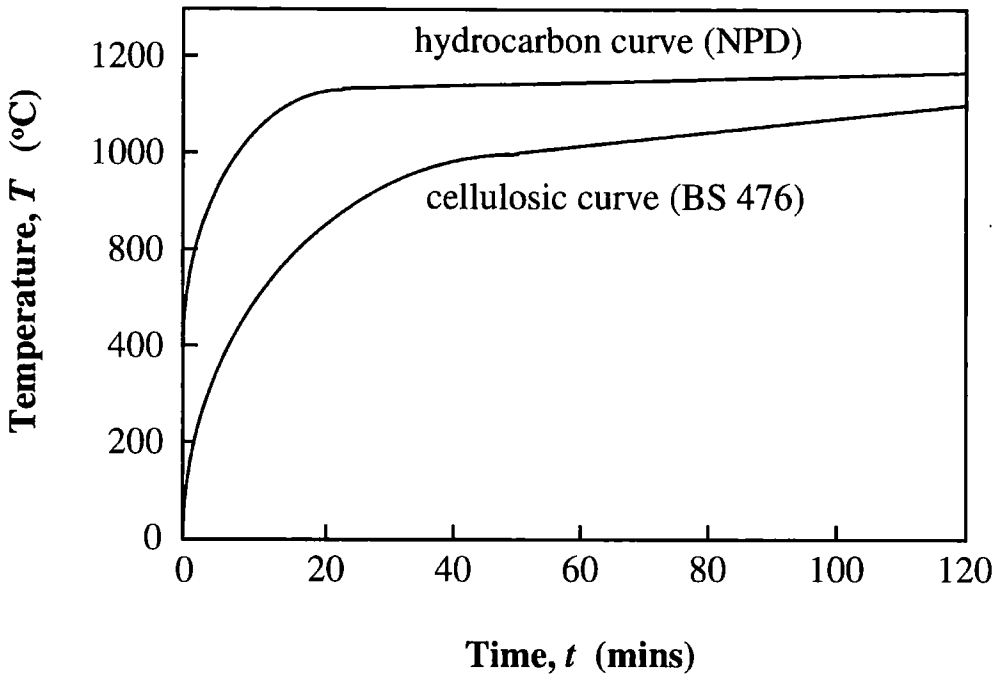

Figure 1.4 Simulated cellulosic (BS476) and hydrocarbon (NPD) fire curves using furnace fire tests [from: Spagni & Gibson, 1994].

For comparison with the numerical results, three sets of experiments were requested from the research groups at the University of Manchester, School of Engineering and the University of Newcastle-upon-Tyne, Centre for Composite Materials Engineering:

1. Laminated single-skinned polyester-based GRP panels;
2. Sandwich panels consisting of polyester-based GRP skins and Vermiculux sandwich material;
3. Polyester-based GRP step panels.

Test samples were manufactured by the hand lay-up method. In each case the laminate was cured at room temperature and then post-cured at 80°C. Temperature sensors were implanted at different layers of the laminates or placed at suitable points through the samples to enable the temperature distribution to be measured. The samples were installed vertically on the furnace door for the fire tests. All samples normally required a period of the order of hours for complete burn-through to occur under the conditions of the cellulosic fire curve. For the NPD hydrocarbon curve the burn-through times were greatly reduced [Dodds *et al.*, 1998; Gibson, *et al.*, 1996; Wu *et al.*, 1994; Davies *et al.*, 1994a]. Throughout this work, the NPD hydrocarbon fire curve is used for the modelling purposes. Due to the experimental limitations, no test was carried out

for large diameter GRP pipes. Figure 1.5 illustrates a schematic view to the fire test room.

Two major limitations of the furnace fire tests are [Spagni & Gibson, 1994]: (i) the procedure was originally intended for non-combustible materials and (ii) the furnace atmosphere is less turbulent than in a real fire. There are also certain circumstances involving hydrocarbon fires where a jet of burning material can run into a structure causing a very severe erosion effect as well as very high heat rates of radiant heat transfer [Spagni & Gibson, 1994]. Experimental works on this type of fires are currently in progress.

Some observations were made by Wu *et al.* [1994] after the furnace fire tests performed for the single- and twin-skinned GRP samples. These observations are outlined in brief in the following:

1. In the experiments the resin matrix was burnt out leaving behind the glass fibres. The glass fibres underwent some degradation in the form of splitting due to the erosive effects of the furnace test.
2. The front face of the sandwich sample was burnt away leaving the exposed core. Little effect was observed in the core materials which remained generally intact after an hour of the fire exposure.

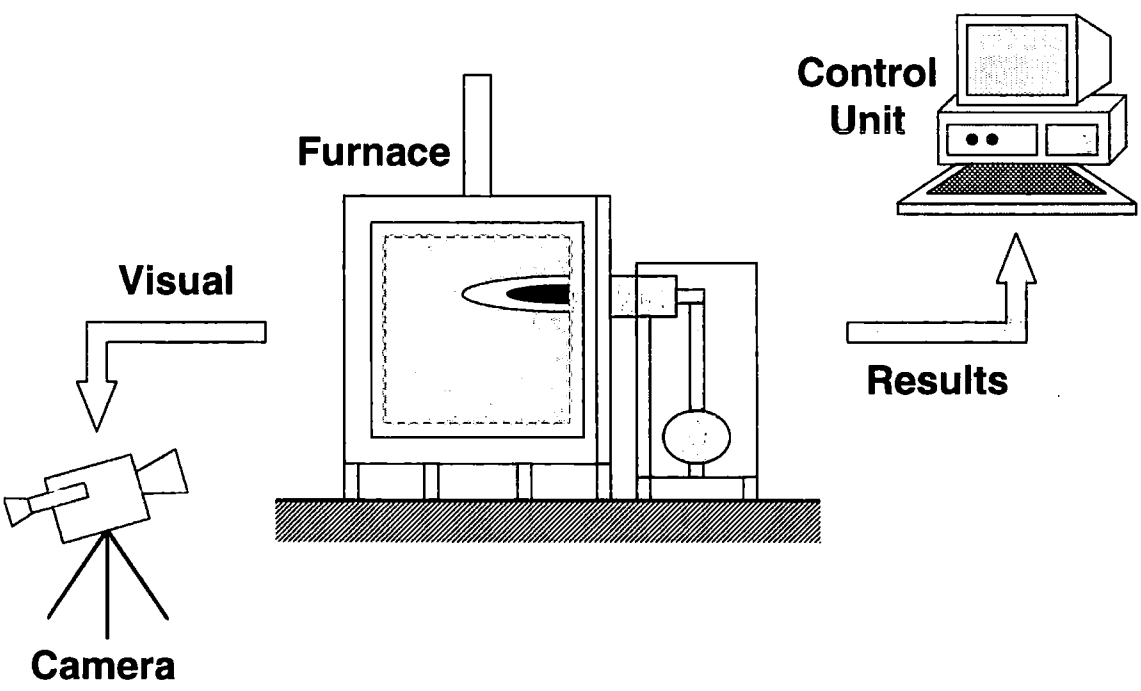

Figure 1.5 A schematic of the arrangement for the furnace fire tests.

1.7 RESEARCH PROBLEM AND HYPOTHESIS

The increasing use of composites offshore requires improvements in technical and safety requirements. Whilst these materials show a range of attractive properties compared to steel and aluminium, making them ideal for a wide range of offshore applications, there are two parameters which limit their use. The first is fire, smoke and toxicity and the second is the service temperature. With such a great concern in the fire performance characteristics of composites used offshore, it is important to be able to predict the thermally induced response of these materials to hydrocarbon fires. Knowledge of the fire performance of these materials is essential for the optimum design of protection and evacuation systems in offshore structures. The thermal response of GRP is also important for integrity, durability and long term performance.

Computer modelling has recently begun to be a cost- and time-effective accessory to full scale fire tests. Along with such a knowledge of the materials behaviour at elevated temperatures obtained from standard fire tests, computer-generated models can provide researchers with practical and efficient solutions. Currently, non-linear heat transfer analysis techniques are increasingly being used by researchers to predict the thermal response of a structure under a given set of time varying temperatures.

Among the various numerical methods suitable for thermal modelling, the finite difference method (FDM) [Gibson *et al.*, 1996; Gibson *et al.*, 1995; Wu *et al.*, 1994; Ozisik, 1993; Henderson *et al.*, 1985; Rohsenow *et al.*, 1985; Anderson *et al.*, 1984; Henderson, 1980; Kung, 1972] has been used to approximate the actual thermochemical decomposition of GRP with little use of finite element method (FEM) [Sullivan, 1993; Wang, 1995]. FEM has the potential to offer some advantages over the FDM. The widespread acceptance of FEM and its versatility for thermal problems involving non-linear governing equations, complex geometries and boundary conditions, suggests it could be an effective tool in thermal design problems.

1.8 JUSTIFICATION FOR THE RESEARCH

Mathematical and numerical modelling of the fire performance of composites for offshore use has two major and long term benefits. First, it speeds up the design process and significantly reduces the cost of using these materials for fire resistance purposes.

Secondly, it improves the knowledge of how these materials behave when exposed to an unwanted fire. A computer simulation can be quickly performed and modified to reach an optimal solution and there will be no need for a lengthy process of designing, fabrication and testing of different designs. Thus, only the final design needs testing in order to satisfy the performance requirements. As the second benefit, the understanding and development of the composite materials may proceed more rapidly. Also the interaction between the material properties and structural configurations can be highly clarified with regard to the fire integrity of the structure. In the meantime, the properties and factors which are found to be of importance can be altered and incorporated for the optimal design.

1.9 BACKGROUND TO THE RESEARCH

1.9.1 Material Behaviour

Figure 1.6 illustrates the general behaviour of a decomposing glass reinforced plastic (GRP) laminate, consisting of resin matrix and glass fibre reinforcement, exposed to fire on one surface.

When a thick GRP laminate (thickness≥1cm) is exposed to high temperature, the initial temperature rise (away from the exposed surface) is primarily due to transient heat conduction; the temperature response for this initial heating period is governed by the thermal properties of the virgin material. During this period, the material experiences no chemical reactions. When the material reaches 200 to 300°C, depending on composition and heating rate, chemical reactions, commonly referred to as pyrolysis, begin to occur. At these temperatures, the resin constituent undergoes thermochemical decomposition and the material breaks down to form gaseous products, solid carbon and glass residue. This results in charring between the pyrolysis zone and the heated surface. Analysis of the pyrolysis gases reveals carbon monoxide, carbon dioxide, hydrogen, nitrogen, methane and lesser products, the amount of each depending upon the specific polymer [Sullivan & Salamon, 1992a]. The pyrolysis zone moves from the heated surface through the material. Meanwhile, the pyrolysis gases diffuse back through the porous charring layer attenuating the conduction of heat to the pyrolysis zone. These gases carry heat energy providing a means for convective cooling.

Simultaneously, the material experiences thermochemical expansion and/or contraction. With time when decomposition is still in its early stages, the pyrolysis gases are trapped due to low porosity and permeability of the material. Such an accumulation of the gases results in the internal pressurisation of the material. For many high density GRP, the porosity and permeability are small enough to cause high internal pressures which in turn causes further expansion of the GRP laminate. As time progresses, the pyrolysis zone widens and advances further into the virgin material. In the mean time, the porosity and permeability of the charring layer increase and the rate of gas flow becomes equal to and then surpasses the rate of gas production. As a result, energy is transferred between the pyrolysis gases and virgin material within the pore network by means of forced convection. This causes peaks in the internal pressure, expansion of the material and the amount of decomposition gases trapped in the material. Given sufficient incident energy, the charring layer penetrates deeper into the virgin material and further chemical reactions occur. These reactions are due to oxidation of the carbon residue and its reaction with the silica filler (present in the glass fibre) at temperatures over 900°C resulting in considerable additional mass loss so that the active material is eventually consumed at the surface of the material leaving a trace of glass fibres and an inert residue containing the pyrolysis gases. At such a time, there is no significant increase in the internal pressure as the permeability is large enough to allow the pyrolysis gases to flow through the pyrolysis and charring zones and eventually escape from the heated surface. Figure 1.7 shows a flow chart involving the thermochemical phenomena of GRP during fire. It should be noted that the pyrolysis and carbon-silica reactions cause large changes in the thermal, kinetic and transport properties of the material. Once the decomposition process begins, the thermal behaviour of the material changes due to the chemical reactions, thermochemical expansion, variable thermal and transport properties and the presence of pyrolysis gases. In addition, the decomposition process is highly dependent upon the heating rate which can be quite different, for example, from a cellulosic fire to a hydrocarbon fire.

In thin laminates (thickness<1cm), a pyrolysis zone does not form but there are some trace of incomplete decomposition. Surface chemical reactions and the eventual consumption of the material occurs before the actual decomposition. These laminates remain entirely isothermal from the hot to the cold surface at any stage of fire exposure and the heat transfer is mainly driven by the thermal conductivity of the material.

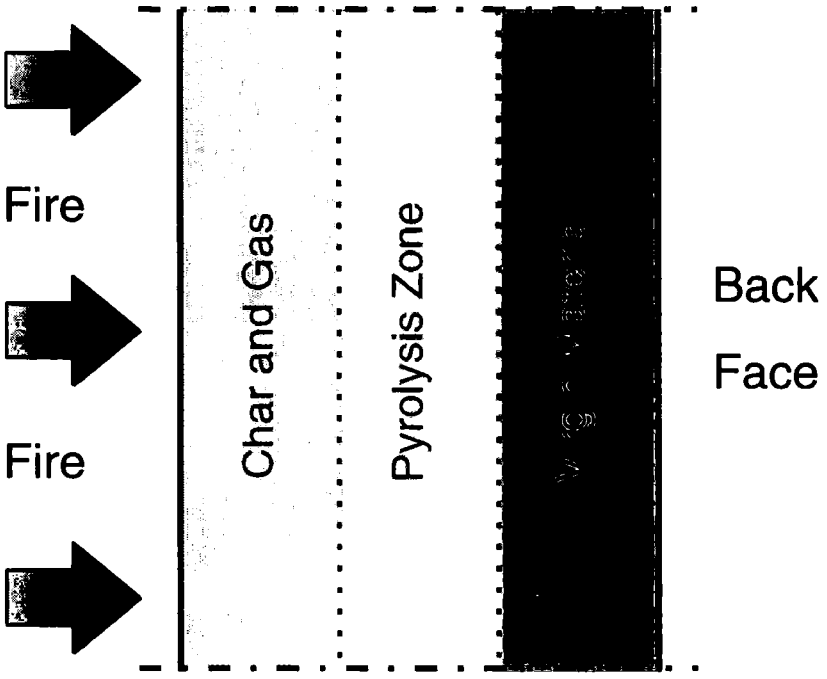

(a)

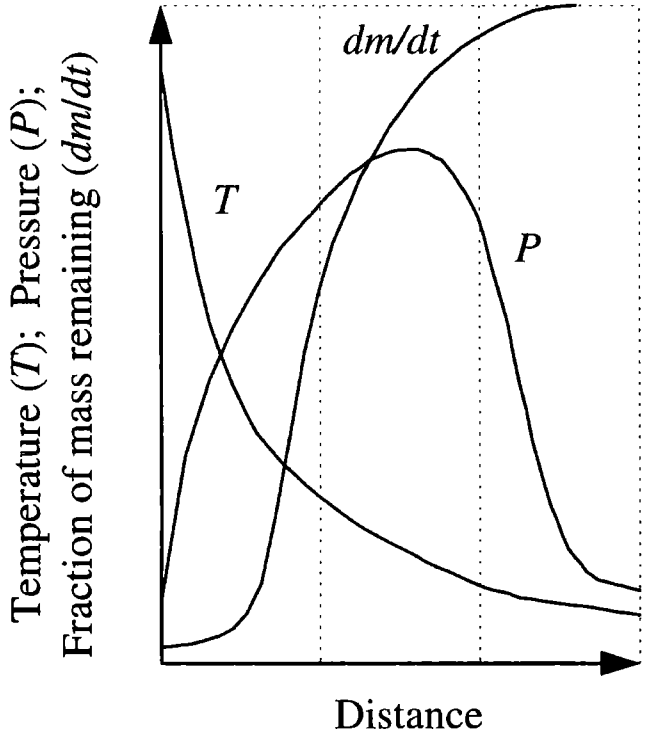

(b)

Figure 1.6 (a) Schematic of pyrolysis phenomenon in a thick GRP laminate subject to fire from one side. The "main zones" during decomposition are: (i) char and gas where most of the resin material has burnt away; (ii) pyrolysis in which there is resin decomposition and (iii) virgin material which represents that part of the material remained unchanged. (b) Qualitative illustration of the variations of temperature, pressure and fraction of mass remaining as functions of distance through the thickness of the laminate.

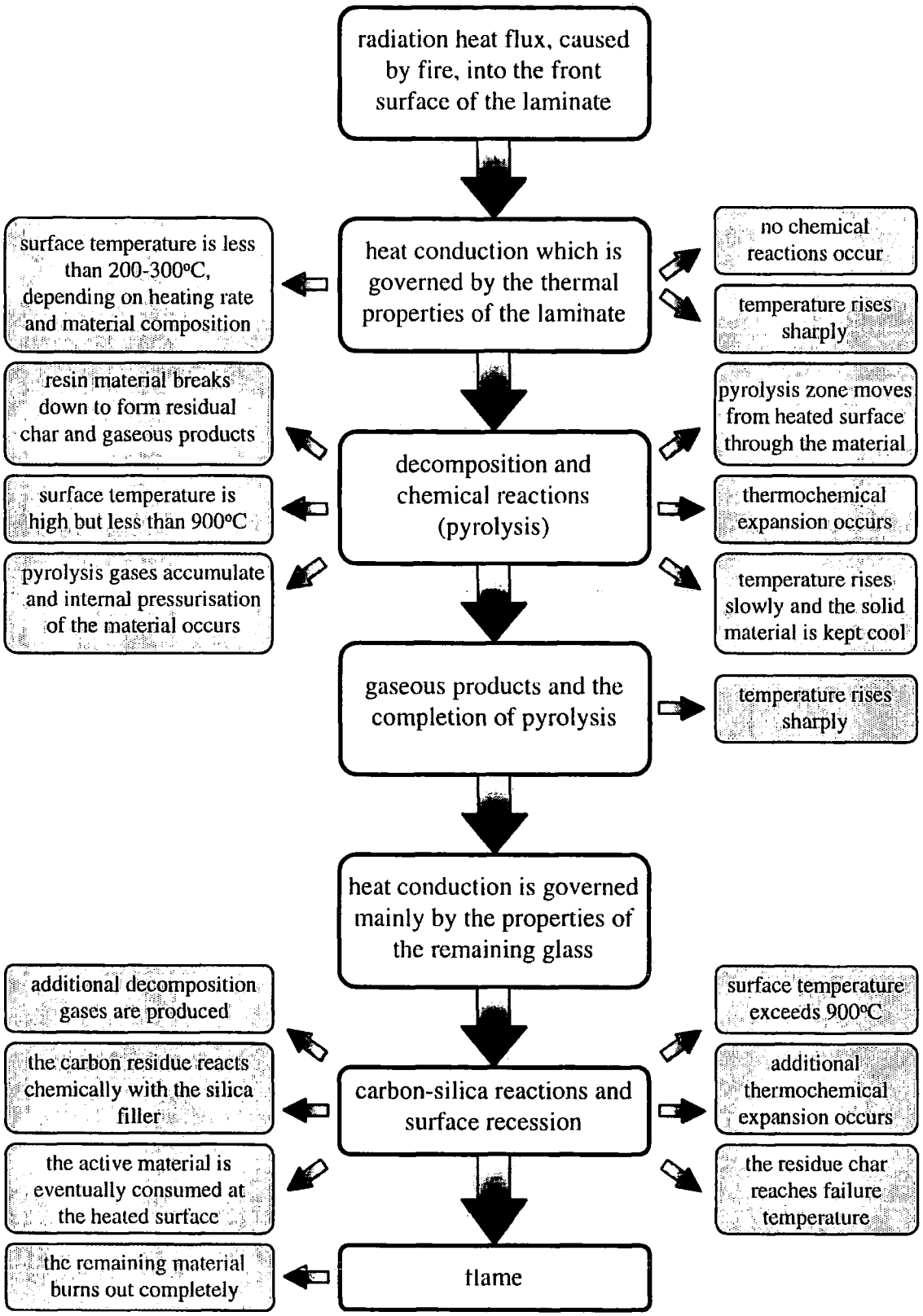

Figure 1.7 Flow chart listing the events in thick polymer composites subject to fire.

The main factors contributing to the overall slow burn-through performance of GRP laminates during fire are [Gibson *et al.*, 1995; Spagni & Gibson, 1994; Gibson, 1993]:

1. Thermal properties of the laminate: The fact that the thermal conductivity, k, and thermal diffusivity, $\alpha=k/\rho c_p$, of GRP are much lower than those of steel and aluminium is clearly an important factor in the initial temperature rise in the virgin material due to the transient heat conduction. As examples, the thermal conductivity of polyester-based GRP, i.e. 0.32 $Wm^{-1}K^{-1}$, is 156 times smaller than the average thermal conductivity of steel, i.e. 50 $Wm^{-1}K^{-1}$, its specific heat, i.e. 1056.8 $Jkg^{-1}K^{-1}$, is 2.3 times larger than that of steel, 450 $Jkg^{-1}K^{-1}$. The larger specific heat means a relatively greater quantity of heat is required to increase the GRP temperature. This property in conjunction with the low thermal conductivity of GRP substantially delays temperature rise due to transient heat conduction.
2. Thermal and transport properties of residual glass: The thermal conductivity of the residual glass, remaining on the surface of the laminate, is smaller than those of the intact glass fibres and resin matrix. Gibson *et al.* [1995] and Wu *et al.* [1994] observed that the residual glass remaining at the heated surface can improve the fire resistance considerably.
3. Decomposition of resin matrix: The process of resin decomposition (pyrolysis) is highly endothermic and therefore temporarily delays the conduction of heat through the laminate, acting as a coolant.
4. Diffusion of pyrolysis gases: The gaseous products (pyrolysis gases and water vapour), which diffuse towards the heated surface, carry a large amount of heat energy. They can therefore be expected to provide a means for convective cooling within the material. In addition when they reach the heated surface, they may form a protective thermal boundary layer.

1.9.2 Review of the Mathematical Models

Several mathematical models have been proposed to predict the thermal response of composite materials undergoing thermochemical decomposition. They range from models which predict the thermal response and rate of decomposition of wood to those which predict the pyrolysis reactions and surface modification of materials for

applications such as atmospheric re-entry. Although, these models are basically similar, they differ in their geometry, material properties, boundary conditions and method of solution. The use of composites offshore is one of the most recent applications and little attempt has been made to obtain mathematical models which can accurately describe the material behaviour and to be used for any configurations and environmental conditions. In this section the mathematical models so far proposed are reviewed.

Bamford *et al.* [1946] proposed the first mathematical model to predict the thermal response of a decomposing material. They used a one-dimensional transient heat conduction equation with an additional term to include the energy associated with the thermal decomposition. Constant thermal properties and a first order decomposition reaction were used. Their work was continued by Munson and Spindler [1961], Friedman [1965], Murty and Blackshear [1967], Panton and Rittmann [1969], Murty [1969] and Kung [1972] to study the pyrolysis of wood in detail. They included variable thermal and physical properties during decomposition, more accurate kinetic properties, the effects of the gas flow through the charring layer and the separation of the decomposing material into its active and residual components. Later, Kansa *et al.* [1977] developed a model which accounted for the porous and permeable structural effects on the gas flow and the overall response of the material. Pittman and Brewer [1966] were the first to develop a mathematical model for the thermal response of a decomposing material other than wood. Their work was extended by Henderson [1980] and Henderson *et al.* [1985] to ablative composite materials taking account of decomposition during both the pyrolysis and carbon-silica reactions, *n*th order kinetic rate equation, temperature and mass dependent thermal and transport properties and the diffusion of the pyrolysis gases through the charring layer. Henderson *et al.* [1985] also carried out several experiments to evaluate the thermal, transport and kinetic properties of the material to be used in their mathematical model. They solved their equations using the finite difference method. Henderson and Wiecek [1987] realised that the ablative material expands considerably during the decomposition process and introduced a model to account for the thermochemical expansion as well as the internal pressurisation of the material due to the storage of the pyrolysis gases. Henderson and Wiecek [1987] used control volume technique to solve their partial differential equations; local thermal equilibrium between gaseous products and solid material was an important assumption in their work. Florio *et al.* [1991] developed a model in which

the local thermal equilibrium did not exist. They found solid to gas temperature differences as high as 200°C which caused an error up to 17% in the prediction of temperature profiles. In recent years there have been a number of attempts to develop mathematical models to analyse the simultaneous thermal and structural response of polymer composites during thermochemical decomposition. Sullivan and Salmon [1992a,b] and Sullivan [1993] introduced coupled solutions for the prediction of the thermostructural response of decomposing, expanding materials exposed to high temperatures. They were among a few researchers who used the finite element technique as the method of solution. Such selection enabled them to formulate a two dimensional geometry and compute temperatures, pore pressures and displacements simultaneously. However, they considered simple geometry and boundary conditions. Finally, Fredlund [1988] introduced a two-dimensional mathematical model for the heat and mass transfer in timbers including more detailed thermochemical decomposition phenomenon and boundary conditions. He realised that the movement of the pyrolysis gases through the material and the heated surface can change the boundary condition at this point substantially. Fredlund also discussed the effect of surface modification on the slow burn-through and the thermal response of the timber in general and included all these in his mathematical model.

Following the Piper Alpha disaster, there has been increasing interest in the use of glass reinforced plastics (GRP) for passive fire protection in the offshore industry [Cullen, 1990]. So far a little attention has been given to the accurate prediction of the response of GRP used in specific structures such as offshore panels, pipes, joins, etc. exposed to hydrocarbon fire [Davies & Wang, 1998; Dodds *et al.*, 1998; Gibson, 1997; Gibson *et al.*, 1996; Wang, 1995; Wu *et al.*, 1994; Spagni & Gibson, 1994; Davies *et al.*, 1994a; Shenoi & Wellicome, 1993a&b]. Experiments in furnace tests and one-dimensional numerical models of offshore panels and plates [Gibson *et al.*, 1995; Wu *et al.*, 1994; Spagni & Gibson, 1994; Davies *et al.*, 1994a] have revealed that GRP have excellent fire resistance properties which have advantages over metallic structures and give protection against fire for considerable periods. These properties are given by the decomposition of the resin material which acts as a coolant. Wu *et al.* [1994] and Gibson *et al.* [1995] developed a mathematical model for GRP panels subject to hydrocarbon fire. Their model was a simplified version of the one introduced by Henderson *et al.* [1985]. They used the model for a single-skinned polyester-based GRP

panel which had already been tested in a furnace fire experiment. They applied the Norwegian petroleum directorate (NPD) hydrocarbon curve at the exposed boundary and considered the back surface to be insulated. They used the finite difference method to solve the partial differential equations. Later, Wang [1995] developed Wu *et al.*'s model to take account of temperature and moisture dependent thermal properties and examined it for several types of GRP and different configurations. He also developed his model to apply it to twin-skinned GRP sandwich panels and GRP pipes but did not include any decomposition terms. Wang solved the governing equations using both finite element and finite difference methods. From 1996 to 1998 more research has been carried out by Gibson *et al.* [1996], Davies *et al.* [1998] and Dodds [1998] in the development of fire experiments but little improvement has been made in the mathematical modelling.

The mathematical models described above for general cases or offshore composites have become more sophisticated with each generation. So far, previous research has not focused on the following important issues in detail:

1. Modelling the single-skinned GRP panels: Attention needs to be given to the accurate definition of the mathematical model; consideration of all possible boundary conditions; incorporation of the temperature and moisture dependent thermal properties; the effect of the remaining resin mass on the overall response; and the use of an efficient solution method such as the finite element technique.
2. Modelling the twin-skinned GRP sandwich panel: Attention should be given to the accurate definition of the mathematical model while imperfect bonds are present between GRP skins and refractory sandwich material. Also studying the most effective approaches to solving the governing equations using the finite element technique.
3. Modelling the single-skinned GRP pipes: Accurate definition of a one dimensional axisymmetric mathematical model including forced convection boundary condition caused by high velocity flowing fluids.
4. Modelling panel/panel, panel/pipe and pipe/pipe joins: The intention is to develop two-dimensional mathematical and numerical models for these types of joins. The consideration of a coupled solution to heat and mass transfer for the accurate prediction of temperatures is essential.

1.10 METHODOLOGY

Development of a predictive and reliable computer modelling resource requires: (i) defining and modelling the physical and chemical processes; (ii) translation into a concise, accurate computer coding and (iii) validating the numerical outputs by comparing with reliable experimental data. The methodology adopted takes account of the experimental foundation aimed at characterising the behaviour and material properties of composites offshore under hydrocarbon fires by Newcastle and Manchester Universities. Regular communications between the author and members of these Universities were maintained [Wu & Gibson, Pers. Com., 1995; Wu & Gibson, Pers. Com., 1996, Dodds & Gibson, Pers. Com., 1997].

The material used is polyester-based GRP which is currently of high interest for applications offshore. The mathematical geometries considered are based on the specimens fabricated for fire test purposes. These specimens are in the form of single-skinned thick GRP panels (thickness≥1cm), twin-skinned GRP sandwich panels and thin (thickness to length ratio less than 1/10) and thick (thickness to length ratio greater than 1/10) GRP step panels (representing specific geometry for GRP joins) prepared at Newcastle and Manchester Universities and tested at the latter.

The key sources of data for the computer modelling are:

1. The material supplier for the primary properties of the resin matrix and fibre reinforcement. The rule of mixtures is used to evaluate the overall material properties of the GRP.
2. Thermo gravimetric analysis (TGA) for quantitative information on the thermal decomposition of the material, understanding of the physical and chemical processes taking place and determination of kinetic properties [Wu & Gibson, Pers. Com., 1996; Dodds & Gibson, Pers. Com., 1997].
3. Furnace fire test and temperature-time data [Courtesy of Manchester University School of Engineering and Newcastle University Centre for Composite Materials Engineering].
4. Thermal, transport and kinetic data are taken from [Davies & Wang, 1998; Dodds *et al.*, 1998; Dodds & Gibson, Pers. Com., 1997; Holman, 1997; Hill, Pers. Com., 1996; Gibson *et al.*, 1996; Wu & Gibson, Pers. Com., 1996; Boothby & Vu, Pers.

Com., 1996; Wang, 1995; Wu & Gibson, Pers. Com., 1995; Spagni & Gibson, 1994; Wu *et al.*, 1994; Davies *et al.*, 1994a; Lide and Kehiaian, 1994; Looyeh, 1994; API RP 2A-LRFD, 1993; Shenoi & Wellicome, 1993a&b; Sullivan, 1993; Sullivan & Salamon, 1992b; Bradley, 1992; Datoo, 1991; Agarwal, 1990; ISO 5660, 1989; Fredlund, 1988; BS476, 1987; Henderson *et al.*, 1985; Drysdale, 1985; Perry *et al.*, 1984; Sheldon, 1982; Gnielinski, 1976; Churchill & Chu, 1975; ISO 834, 1975; Churchill & Ozoe, 1973; Fujii & Imura, 1972; Hall and Yarborough, 1971; Clifon & Chapman, 1969; Havens, 1969; Friedman, 1965].

The mathematical models include: (i) transient heat conduction; (ii) gas mass movement and internal heat convection of the decomposition gases; (iii) mass loss and Arrhenius rate decomposition of active material into decomposition gases and residual char and (iv) endothermicity of the decomposition process.

The main equations used are: (i) Fourier's law of heat conduction; (ii) Darcy's law of diffusion; (iii) the continuity equation; (iv) an Arrhenius type kinetic rate equation and (v) ideal gas equation.

The finite element computer code used is from Bettess and Bettess [1986] for one, two- and three dimensional stress analysis problems. The code has been extended by Looyeh [1994] to include simple one- and two-dimensional steady-state and transient heat conduction analyses.

A Bubnov-Galerkin (weighted residual) finite element approach is adopted. The classical finite difference time stepping algorithm is developed using the methodology of Zienkiewicz and Taylor [1991]. A Crank-Nicolson solution is used to solve the related matrix equation implicitly for the nodal temperatures and pressures. The solution is performed using a non-symmetric profile matrix solver associated with the active column method [Applegarth, 1990]. The non-linear terms and coefficients are quasi-linearised and evaluated at each step of the computations explicitly. Time derivative terms are given by forward difference and the spatial variables by central difference, with the exception of the gas mass flux terms which are represented by backward difference. The time step is updated after each iteration based upon a critical value. The element matrices and heat load vectors are evaluated numerically using Gauss-Legendre quadrature (Appendix C). At each time step a full system of equations needs to be solved.

1.11 OUTLINE OF THESIS

Chapter 2 describes the general mathematical model used in the finite element formulation for the thermal analysis of GRP panels subject to high temperatures (1000°C). The fundamental assumptions are introduced. The mathematical model is developed for single-skinned GRP panels and takes account of: (i) transient heat conduction, (ii) gas mass flux and internal heat convection of pyrolysis gases, (iii) mass loss and Arrhenius decomposition of resin into gaseous products and residual char and glass fibres, and (iv) endothermicity of the pyrolysis reactions. The basic principles of the finite element method are reviewed. A solution is then given by the weighted residual approach. The mathematical and numerical models introduced in this chapter are used and further developed to simulate a variety of GRP structures under hydrocarbon fires.

Chapter 3 addresses various types of environmental conditions that an offshore panel may experience in hydrocarbon fires. This leads to the study of the physical boundary conditions at the fire-exposed and unexposed surfaces. The emphasis is on the conditions used in some full-scale furnace fire tests in order to compare the computed results with the experimental data. At the fire-exposed surface(s) two formulations may be used: (i) an empirical hydrocarbon fire curve, and (ii) theoretical radiation and convection. At the unexposed surface(s) only theoretical approach is used.

The material properties required for the modelling of the thermal response of the GRP panels, pipes and joins are presented in Chapter 4. These include the thermal, transport and kinetic properties of GRP and the thermal and transport properties of the sandwich material. The properties of the gaseous products generated during pyrolysis reactions are also presented. The properties of GRP, sandwich material and pyrolysis gases may change with temperature and moisture gradients. These effects are investigated in this chapter in detail.

In Chapter 5, the general one-dimensional mathematical model introduced in Chapter 2 in conjunction with boundary conditions and material properties defined in Chapters 3 and 4 are used to study the response of a single-skinned polyester-based GRP panel subject to a hydrocarbon fire. The development of the mathematical model is carried out in four stages (referred to as Models 1, 2, 3 and 4). In Model 1, an initial simulation is introduced. The effect of various boundary conditions on the overall response of the

material is investigated in Model 2. In Model 3, additions are made to take account of temperature- and moisture-dependent material properties and the effect of unburnt resin on the thermal response of the material. Taking account of all, Model 4 addresses the effect of gas mass movement and surface chemical reactions on the fire-exposed surface boundary condition. A finite element formulation is then developed for each model. The results of all the models are obtained using the material properties given in Chapter 4 and discussed. These are also compared with some experiments.

Chapter 6 analyses the thermal response of twin-skinned sandwich panels exposed to hydrocarbon fires. A one-dimensional mathematical model is developed for GRP/SM/GRP panels and includes: (i) thermochemical decomposition in the GRP skins, (ii) transient heat conduction in sandwich material (SM), and (iii) the effect of thermal contact resistance occurring at the GRP/SM/GRP interfaces. The finite element method is used for the solution of the mathematical model. To include the effect of imperfect bonding on the temperature variations, two methods are introduced, i.e. explicit and implicit. The results are presented and discussed for both methods and various panels with the object of identifying the best method of solution. Comparisons are also made with some experiments.

Chapter 7 addresses a one-dimensional axi-symmetric mathematical model to simulate the response of GRP pipes subject to hydrocarbon fires. The model is similar to that for GRP panels but with the assumptions that the pipe is thin-walled and has axial symmetry about its centre line. The pipe is assumed to be exposed to a uniform fire on its outer surface, whereas its inner surface is subject to fluid flow. Two types of fluid are investigated: (i) natural gas and (ii) sea water. The forced convection caused by these fluids are discussed in detail and the necessary data are presented. A finite element formulation is developed to solve the governing equations numerically. The results are presented and discussed.

In Chapter 8, a two-dimensional model is developed to simulate the thermal response of GRP joins. The applications of panel-panel, panel-pipe and pipe-pipe joins in the offshore industry are briefly reviewed. A two-dimensional model is then developed to analyse heat transfer in a thin panel-panel GRP join (GRP step panel) which uses the one-dimensional model introduced in Chapter 5. The governing equations are derived using conservation of energy and the continuity equation. The pyrolysis gases are assumed to diffuse in the fire direction only. The weighted residual approach for the

finite element method is used to obtain a solution of the governing equation and discussed in detail. Several finite element meshes are introduced with the object to identify the best for the analysis. The results are presented for the thin GRP step panel and compared with some experiments. They are also compared with those for an equivalent one-dimensional model.

A model is developed in Chapter 9 for heat and mass transfer analysis in thick GRP step panels subject to hydrocarbon fires. The model includes: (i) the conservation of energy equation, (ii) two-dimensional gas diffusion equation, (iii) the kinetic rate Arrhenius equation, (iv) the continuity equation, (v) Darcy's equation and (vi) the ideal gas equation. The accumulation of the pyrolysis gases is also taken into account. The relation of each equation to the others is discussed in detail. A coupled finite element formulation is then introduced for the simultaneous solution of pore pressure and temperature. The results are presented for a thick GRP step panel and compared with those in Chapter 8. Comparisons are also made with some experiments.

A summary of findings, a brief discussion of key results and conclusions to the research are given in Chapter 10. Recommendations for future work are also presented.

CHAPTER II

MATHEMATICAL MODEL AND FINITE ELEMENT METHOD

2.1 INTRODUCTION

A one-dimensional mathematical model is developed to simulate the thermal response of glass reinforced plastic (GRP) panels. The model includes: (i) transient heat conduction; (ii) gas mass movement and internal heat convection of the decomposition gases; (iii) mass loss and Arrhenius rate decomposition of active material into decomposition gases and residual char and (iv) endothermicity of the decomposition process.

The basic principals of the finite element method are reviewed. A solution is then presented for the mathematical model using the finite difference time stepping approach.

Finally, a non-symmetric matrix solver is described. This is used since the system matrices may be non-symmetric due to the terms arising from decomposition process.

2.2 KEY ASSUMPTIONS

For the thermal modelling of GRP the following assumptions for fire exposure are used:

1. Local thermodynamic equilibrium exists between the pyrolysis gases and the virgin material. This implies that the solid and gaseous phases both have the same temperature over a small volume of an arbitrary point within the material.
2. No thermochemical expansion and/or contraction occurs, i.e. the volume of the material remains constant during decomposition, implying mass loss, $\partial m/\partial t$, and density loss, $\partial \rho/\partial t$, are equivalent.

3. No energy is transferred by diffusion, i.e. the energy transferred by diffusion is negligible compared to that by conduction.
4. No water vapour is created during the decomposition, i.e. there is a low percentage of moisture content, implying the internal pressurisation caused by moisture evaporation can be considered negligible.
5. Moving boundaries (during decomposition) and movement of the pyrolysis zone are ignored.
6. Movement of liquid is assumed negligible compared to pyrolysis gases.
7. Pyrolysis gases may be considered "ideal gases".
8. A first-order Arrhenius type kinetic rate equation is used to define mass loss during decomposition.

2.3 MATHEMATICAL MODEL

The one-dimensional mathematical model proposed by Kung [1972] and developed by Henderson *et al.* [1985] is used.

Consider an infinite GRP panel with finite thickness L, exposed to fire on one side (Figure 1.6a). The differential equation describing the one-dimensional transient heat conduction in the plate is generally given by the conservation of energy (Appendix B):

$$\frac{\partial}{\partial t}(\rho h) = -\frac{\partial q}{\partial x} + \dot{q} \tag{2.1}$$

where

t = time (s)

ρ = density of GRP (kgm^{-3})

h = enthalpy of GRP (Jkg^{-1})

q = total heat flux (heat flow rate per unit area) (Wm^{-2})

$\dot{q}$ = internally generated heat per unit volume (Wm^{-3})

The total heat flowing through the material is due to the conduction of heat, which is defined by Fourier's law (Appendix B), and the convection of the pyrolysis gases.

In the original reference [Fourier, 1822], Fourier expressed the heat conduction equation (which became known as Fourier's law) in the following form:

> *"...Let us consider a solid body made of homogeneous material bounded by two infinite and parallel planes A and B with distance 'e'. The lower plane A is maintained at a constant temperature 'a' and the upper plane B at constant temperature 'b' whose value is less than that of 'a'. Let 'F' be the constant heat flow which during unit time would pass through unit area of the solid from A to B. We get:*
>
> $$\frac{F}{\frac{a-b}{e}} = K \quad \text{or} \quad F = K\frac{a-b}{e}$$
>
> *where K is a constant..."*

Kung [1972] introduced the total heat energy flow rate per unit area by the following equation:

$$q = -k\frac{\partial T}{\partial x} + \dot{m}_g h_g \tag{2.2}$$

where

k = thermal conductivity of GRP ($Wm^{-1}K^{-1}$)

T = temperature (^{o}C)

x = spatial co-ordinate starting at the hot surface (m)

$\dot{m}_g$ = gas mass flux ($kgm^{-2}s^{-1}$)

h_g = enthalpy of gas (Jkg^{-1})

Kung [1972] also found that the internally generated heat energy is associated with the heat of decomposition and the rate of mass loss. He expressed $\dot{q}$ by:

$$\dot{q} = -Q\frac{\partial \rho_r}{\partial t} \tag{2.3}$$

where

Q = heat of decomposition (Jkg^{-1})

ρ_r = density of resin (kgm^{-3})

and the negative sign indicates the endothermicity of the decomposition process.

Substituting Equations 2.2 and 2.3 into Equation 2.1 gives:

$$\frac{\partial}{\partial t}(\rho h)=\frac{\partial}{\partial x}\left(k\frac{\partial T}{\partial x}\right)-\frac{\partial}{\partial x}\left(\dot{m}_g h_g\right)-Q\frac{\partial \rho_r}{\partial t} \tag{2.4}$$

The term on left represents the rate of change of internal energy per unit volume. On the right, the first term represents heat conduction; the second, convection of energy resulting from the pyrolysis gases flowing back through the porous charring layer (this term is always negative) and the third term represents the rate of heat generation resulting from the decomposition of the material.

Expanding both left and right sides of Equation 2.4 results in:

$$\frac{\partial \rho}{\partial t}h+\rho\frac{\partial h}{\partial t}=\frac{\partial}{\partial x}\left(k\frac{\partial T}{\partial x}\right)-\frac{\partial \dot{m}_g}{\partial x}h_g-\dot{m}_g\frac{\partial h_g}{\partial x}-Q\frac{\partial \rho_r}{\partial t} \tag{2.5}$$

The enthalpies of the material and the pyrolysis gases are functions of temperature only and given by:

$$h=\int_{T_\infty}^{T} c_p dT \tag{2.6a}$$

$$h_g=\int_{T_\infty}^{T} c_{pg} dT \tag{2.6b}$$

where

c_p = specific heat of GRP ($Jkg^{-1}K^{-1}$)

c_{pg} = specific heat of gas ($Jkg^{-1}K^{-1}$)

Differentiation of Equation 2.6a with respect to t and Equation 2.6b with respect to x result in:

$$\frac{\partial h}{\partial t}=c_p\frac{\partial T}{\partial t} \tag{2.7a}$$

$$\frac{\partial h_g}{\partial x}=c_{pg}\frac{\partial T}{\partial x} \tag{2.7b}$$

Assuming no mass loss from the fibre reinforcement during decomposition leads to:

$$\frac{\partial \rho}{\partial t}=\frac{\partial \rho_r}{\partial t} \tag{2.8}$$

Conservation of mass implies:

$$\frac{\partial \dot{m}_g}{\partial x}=-\frac{\partial \rho_r}{\partial t} \tag{2.9}$$

Substituting Equations 2.7 to 2.9 into Equation 2.5 and rearranging gives:

$$\rho c_p \frac{\partial T}{\partial t} = \frac{\partial}{\partial x}\left(k\frac{\partial T}{\partial x}\right) - \dot{m}_g c_{pg}\frac{\partial T}{\partial x} - \frac{\partial \rho_r}{\partial t}\left(Q + h - h_g\right) \tag{2.10}$$

Equation 2.10 must be solved simultaneously with the equations for the rate of decomposition and the mass flux of the pyrolysis gases. Assuming no expansion of the virgin material, the rate of decomposition can be given by a first-order Arrhenius type kinetic rate equation on the basis of the rate of change of density as follow:

$$\frac{\partial \rho_r}{\partial t} = -A\left(\rho_r - \rho_{rf}\right)\exp\left(\frac{-E_A}{RT_k}\right) \tag{2.11}$$

where

A	=	pyrolysis constant (s^{-1})
ρ_{rf}	=	final density of resin (kgm^{-3})
E_A	=	activation energy ($kJkmole^{-1}$)
R	=	gas constant (8.314 $kJkmole^{-1}K^{-1}$)
T_k	=	temperature (K)

If the accumulation of the generated gas is ignored, the gas mass flux, $\dot{m}_g$, varies with distance as a function of the rate of gas generation at each spatial location. The magnitude of the gas mass flux may be calculated by integrating Equation 2.9 giving:

$$\dot{m}_g = \int_L^{\hat{x}} \frac{\partial \rho_r}{\partial t} dx \qquad \text{for} \qquad 0 \le \hat{x} \le L \tag{2.12}$$

Equations 2.6 and 2.10 to 2.12 form a set of non-linear partial differential equations which may be regarded as the complete one-dimensional mathematical model for a GRP laminate exposed to fire. These equations must be solved simultaneously for T, ρ_r and $\dot{m}_g$ once the initial conditions and appropriate boundary conditions have been defined. The boundary conditions can generally be defined by:

$$-k\frac{\partial T}{\partial x} = f(T) \qquad \text{for} \qquad x = 0,\ t > 0 \tag{2.13a}$$

$$-k\frac{\partial T}{\partial x} = g(T) \qquad \text{for} \qquad x = L,\ t > 0 \tag{2.13b}$$
$$\dot{m}_g = 0$$

A numerical solution to the above equations is given in the following section.

2.4 BASIC THEORY OF THE FINITE ELEMENT METHOD

As a numerical technique, the finite element method is one of the most powerful tools for obtaining approximate solutions to a wide range of engineering problems. The method originated in the early 60's to study the stresses in complex airframe structures [Huebner *et al.*, 1995]. It has been extended and applied to the broad field of continuum mechanics. An important feature of the finite element method is that it is not limited to solid mechanics. In recent years with the development of computer technology, the finite element method has become established as one of the most powerful and versatile tools permitting numerical solutions of intractable problems. The method allows a complex continuum to be subdivided into a series of simple inter-related problems, i.e. it allows consistent techniques for modelling a medium as an assemblage of discrete parts or finite elements [Lewis *et al.*, 1996; Huebner *et al.*, 1995; Zienkiewicz & Taylor, 1994].

2.4.1 Why Finite Elements?

A large number of analytical solutions for heat transfer have been introduced over the past 100 years. In many practical situations the governing equations, boundary conditions and geometries are such that an analytical solution is not possible [Huebner *et al.*, 1995].

Our objective here is to study more practical cases involving complex geometries. Such problems contain non-linear boundary conditions and terms and coefficients rising from non-linear material properties which vary with temperature, moisture, pressure and the mass fraction of the material at different stages. These transient material properties and boundary conditions and complex geometries are such that analytical solutions are almost impossible. For such situations solutions can be obtained using an approximate numerical technique. Several numerical techniques have evolved over the years; among them, the finite difference method is commonly used. This method gives pointwise approximations and can be used for some fairly difficult problems. With irregular geometries and unusual changes of material properties and boundary conditions, the finite difference techniques become hard to use. For such situations, the most effective approach is the finite element technique [Huebner *et al.*, 1995; Zienkiewicz & Taylor, 1994; Lewis *et al.*, 1996]. Unlike the finite difference method, the finite element method

gives a piecewise approximation to the governing equations. In the finite element method, the discrete elements can be put together in a variety of ways and used to represent extremely complex shapes. An important feature of the method is the ability to formulate solutions for individual elements before putting them together to solve the entire problem.

2.4.2 Analysis Procedure

The solution domain is first divided into a number of uniform or non-uniform (the same or different sizes) *finite elements* connected by *nodes*. Within each element the unknown field *dependent variables* are approximated by the use of *interpolation* or *shape functions*. These functions are defined by the field variables at the nodal points. The field variables can then be evaluated by defining their nodal values and the related shape functions. Once the finite element model has been established, the matrix equations expressing the properties of the individual elements can be determined by weighted residual approach. To find the properties of the solution domain all the element properties must be assembled. The resulting equations are then be modified to take account of the boundary conditions. Finally, the equations of system are solved to obtain the unknown nodal values. In some cases, the solution is used to calculate other important variables.

2.4.3 Weighted Residual Approach

This is used to obtain approximate solutions to linear and non-linear partial differential equations [Zienkiewicz & Taylor, 1994; Lewis *et al.*, 1996]. It assumes a general functional behaviour of the dependent variable to satisfy the given differential equation and boundary conditions. An approximation function is substituted into the differential equations and boundary conditions. Any residual error is reduced by averaging over the entire solution domain. This is done by forcing a defined weighted integral to vanish. The weighted integral is the integral of the product of the residual and a weighting function over the entire solution domain. For example, for the following differential equation with the field variable T:

$$A(T) - f = 0 \tag{2.14}$$

giving a solution approximated by $\tilde{T}$ in the solution domain Ω.

When the solution is substituted into Equation 2.14, the residual R is given by:

$$A\left(\tilde{T}\right) - f = R \tag{2.15}$$

The weighted integral of the residual is constructed (for each r node element) with the help of a weighting function W_i given by:

$$\int_{\Omega}\left[A\left(\tilde{T}\right) - f\right]W_i d\Omega = \int_{\Omega} RW_i d\Omega = 0 \qquad i = 1,2,\ldots,r \tag{2.16}$$

with the condition $R \approx 0$.

There are a variety of the weighted residual techniques due to the choice of weighting functions. If the weighting functions are chosen to be the same as shape functions, the method is known as Bubnov-Galerkin approach [Finlayson & Scriven, 1966; Collatz, 1966]. The weighted residual approach of Bubnov-Galerkin type is adopted throughout this work.

2.4.4 Finite Element Formulation

A solution to the set of governing differential equations, Equations 2.6 and 2.10 to 2.12, is given using the Bubnov-Galerkin (weighted residual) approach.

Consider linear one-dimensional elements with two nodes each and assuming the temperature is the only dependent variable, the temperature and temperature gradients are approximated within each element by:

$$T(x,t) = \mathbf{N}(x)\mathbf{T}(t) = \sum_{i=1}^{2} N_i(x)T_i(t) \tag{2.17a}$$

$$\frac{\partial T(x,t)}{\partial x} = \mathbf{B}(x)\mathbf{T}(t) = \sum_{i=1}^{2} B_i(x)T_i(t) \tag{2.17b}$$

where

$\mathbf{N}(x)$ = shape function matrix

$\mathbf{T}(t)$ = temperature vector

$N_i(x)$ = the ith element of the shape function matrix

T_i = the ith element of the temperature vector

$\mathbf{B}(x)$ = shape function derivative matrix

$B_i(x)$ = the ith element of shape function derivative matrix defined by $\partial N_i/\partial x$

The shape function and shape function derivative matrices are defined by:

$$\mathbf{N}(x) = \begin{bmatrix} \frac{l-x}{l} & \frac{x}{l} \end{bmatrix} \tag{2.18a}$$

$$\mathbf{B}(x) = \begin{bmatrix} -\frac{1}{l} & \frac{1}{l} \end{bmatrix} \tag{2.18b}$$

where l is the element length.

Applying the Bubnov-Galerkin approach to Equation 2.10 gives:

$$\int_{\Omega^e} \left[\rho c_p \frac{\partial T}{\partial t} - \frac{\partial}{\partial x}\left(k \frac{\partial T}{\partial x} \right) + \dot{m}_g c_{pg} \frac{\partial T}{\partial x} + \frac{\partial \rho_r}{\partial t}\left(Q + h - h_g \right) \right] N_i d\Omega = 0 \quad i = 1,2$$

or

$$\int_0^l \left[\rho c_p \frac{\partial T}{\partial t} - \frac{\partial}{\partial x}\left(k \frac{\partial T}{\partial x} \right) + \dot{m}_g c_{pg} \frac{\partial T}{\partial x} + \frac{\partial \rho_r}{\partial t}\left(Q + h - h_g \right) \right] N_i dx = 0 \quad i = 1,2 \tag{2.19}$$

where 0 and l denote the co-ordinates of the end nodes of the line element within the global co-ordinate system. Equation 2.19 expresses the desired averaging of the residual at the element boundaries. Integration by parts using (Appendix C):

$$\int_a^b u dv = uv\Big|_a^b - \int_a^b v du \tag{2.20}$$

with $u=N_i$ and separating each term, gives expressions containing lower order derivatives:

$$\int_0^l \rho c_p \frac{\partial T}{\partial t} N_i dx - N_i k \frac{\partial T}{\partial x}\Big|_0^l + \int_0^l k \frac{\partial T}{\partial x} B_i dx + \int_0^l \dot{m}_g c_{pg} \frac{\partial T}{\partial x} N_i dx + \int_0^l \frac{\partial \rho_r}{\partial t}\left(Q + h - h_g \right) N_i dx = 0 \quad i = 1,2 \tag{2.21}$$

If the specific heats of the material and pyrolysis gases are assumed constant, the enthalpies of the material and pyrolysis gases become (from Equations 2.6a and 2.6b):

$$h = c_p\left(T - T_\infty \right) \tag{2.22a}$$

$$h_g = c_{pg}\left(T - T_\infty \right) \tag{2.22b}$$

Equation 2.21 can be rearranged using Equations 2.22a and 2.22b as:

$$\int_0^l \rho c_p \frac{\partial T}{\partial t} N_i dx - N_i k \frac{\partial T}{\partial x}\Big|_0^l + \int_0^l k \frac{\partial T}{\partial x} B_i dx + \int_0^l \dot{m}_g c_{pg} \frac{\partial T}{\partial x} N_i dx + \int_0^l \frac{\partial \rho_r}{\partial t}\left(c_p - c_{pg} \right) T N_i dx + \int_0^l \frac{\partial \rho_r}{\partial t}\left[Q - \left(c_p - c_{pg} \right) T_\infty \right] N_i dx = 0 \quad i = 1,2 \tag{2.23}$$

where the second term in Equation 2.23 represents natural boundary conditions for the element. These are evaluated as:

$$i = 1, \quad N_i k \frac{\partial T}{\partial x}\bigg|_0^l = N_1(l) k \frac{\partial T}{\partial x}(l) - N_1(0) k \frac{\partial T}{\partial x}(0) = -k \frac{\partial T}{\partial x}(0) \tag{2.24a}$$

$$i = 2, \quad N_i k \frac{\partial T}{\partial x}\bigg|_0^l = N_2(l) k \frac{\partial T}{\partial x}(l) - N_2(0) k \frac{\partial T}{\partial x}(0) = k \frac{\partial T}{\partial x}(l) \tag{2.24b}$$

The natural boundary conditions are taken into account when the element matrices are assembled. During assembly, the natural boundary condition terms will cancel at all interior nodes of the solution domain, leaving only the natural boundary conditions to be evaluated at the hot and cold surface boundary points, i.e. $x = 0$ and $x = L$. This implies that Equations 2.24a and 2.24b actually represent the nodal boundary conditions defined by Equations 2.13a and 2.13b for the hot and cold surface boundaries, i.e. the first and last nodes of the solution domain.

Substitute Equations 2.17a and 2.17b into Equation 2.23. The resulting equation becomes:

$$\begin{aligned} &\int_0^l \rho c_p \mathbf{N}^{\mathrm{T}} \dot{\mathbf{T}} \mathbf{N} dx + \int_0^l k \mathbf{B}^{\mathrm{T}} \mathbf{T} \mathbf{B} dx + \int_0^l \dot{m}_g c_{pg} \mathbf{B}^{\mathrm{T}} \mathbf{T} \mathbf{N} dx \\ &+ \int_0^l \frac{\partial \rho_r}{\partial t} \left(c_p - c_{pg}\right) \mathbf{N}^{\mathrm{T}} \mathbf{T} \mathbf{N} dx + \int_0^l \frac{\partial \rho_r}{\partial t} \left[Q - \left(c_p - c_{pg}\right) T_\infty\right] \mathbf{N}^{\mathrm{T}} dx - \begin{bmatrix} f(T) \\ -g(T) \end{bmatrix} = \mathbf{0} \end{aligned} \tag{2.25}$$

where superscript **T** denotes the transpose. Rearranging Equation 2.25 results in:

$$\begin{aligned} &\left(\int_0^l \mathbf{N}^{\mathrm{T}} \rho c_p \mathbf{N} dx\right) \dot{\mathbf{T}} + \left[\int_0^l \mathbf{B}^{\mathrm{T}} k \mathbf{B} dx + \int_0^l \mathbf{B}^{\mathrm{T}} \dot{m}_g c_{pg} \mathbf{N} dx \right. \\ &\left. + \int_0^l \mathbf{N}^{\mathrm{T}} \frac{\partial \rho_r}{\partial t} \left(c_p - c_{pg}\right) \mathbf{N} dx\right] \mathbf{T} + \int_0^l \frac{\partial \rho_r}{\partial t} \left[Q - \left(c_p - c_{pg}\right) T_\infty\right] \mathbf{N}^{\mathrm{T}} dx - \begin{bmatrix} f(T) \\ -g(T) \end{bmatrix} = \mathbf{0} \end{aligned}$$

or $$\mathbf{C}\dot{\mathbf{T}} + \left(\mathbf{K}_o + \mathbf{K}_g + \mathbf{K}_d\right)\mathbf{T} + \left(\mathbf{f}_o + \mathbf{f}_b\right) = \mathbf{0}$$

or $$\mathbf{C}\dot{\mathbf{T}} + \mathbf{K}\mathbf{T} + \mathbf{f} = \mathbf{0} \tag{2.26}$$

where

$\mathbf{C}$	=	element capacitance matrix
$\mathbf{K_o}$	=	element conductance matrix
$\mathbf{K_g}$	=	element gas diffusion matrix
$\mathbf{K_d}$	=	element decomposition matrix
$\mathbf{f_o}$	=	element decomposition vector
$\mathbf{f_b}$	=	element boundary conditions vector

The element matrices and element vectors are given, in global co-ordinate x, by:

$$\mathbf{C} = \int_0^l \mathbf{N}^{\mathrm{T}} \rho c_p \mathbf{N} dx \tag{2.27a}$$

$$\mathbf{K}_{\mathrm{o}} = \int_0^l \mathbf{B}^{\mathrm{T}} k \mathbf{B}\, dx \tag{2.27b}$$

$$\mathbf{K}_{\mathrm{g}} = \int_0^l \mathbf{B}^{\mathrm{T}} \dot{m}_g c_{pg} \mathbf{N} dx \tag{2.27c}$$

$$\mathbf{K}_{\mathrm{d}} = \int_0^l \mathbf{N}^{\mathrm{T}} \frac{\partial \rho_r}{\partial t} \left(c_p - c_{pg}\right) \mathbf{N} dx \tag{2.27d}$$

$$\mathbf{f}_{\mathrm{o}} = \int_0^l \mathbf{N}^{\mathrm{T}} \frac{\partial \rho_r}{\partial t} \left[Q - \left(c_p - c_{pg}\right) T_{\infty}\right] dx \tag{2.27e}$$

$$\mathbf{f}_{\mathrm{b}} = -\begin{bmatrix} f(T) \\ -g(T) \end{bmatrix} \tag{2.27f}$$

The element matrices and element vectors are then transferred from the global to local co-ordinates in order to be integrated numerically. If the local co-ordinate ξ is chosen to be related to the global co-ordinate x by:

$$x = \frac{l}{2}(1+\xi) \tag{2.28}$$

then the shape function and shape function derivative matrices are given, in the local co-ordinate ξ, by:

$$\mathbf{N}(\xi) = \begin{bmatrix} \frac{1}{2}(1-\xi) & \frac{1}{2}(1+\xi) \end{bmatrix} \tag{2.29a}$$

$$\mathbf{B}(\xi) = \begin{bmatrix} -\frac{1}{2} & \frac{1}{2} \end{bmatrix} \tag{2.29b}$$

and the element matrices and element vectors by:

$$\mathbf{C} = \frac{1}{2} \int_{-1}^{1} \mathbf{N}^{\mathrm{T}} \rho c_p \mathbf{N} d\xi \tag{2.30a}$$

$$\mathbf{K}_{\mathrm{o}} = \frac{1}{2} \int_{-1}^{1} \mathbf{B}^{\mathrm{T}} k \mathbf{B}\, d\xi \tag{2.30b}$$

$$\mathbf{K}_{\mathrm{g}} = \frac{1}{2} \int_{-1}^{1} \mathbf{B}^{\mathrm{T}} \dot{m}_g c_{pg} \mathbf{N} d\xi \tag{2.30c}$$

$$\mathbf{K}_{\mathrm{d}} = \frac{1}{2} \int_{-1}^{1} \mathbf{N}^{\mathrm{T}} \frac{\partial \rho_r}{\partial t} \left(c_p - c_{pg}\right) \mathbf{N} d\xi \tag{2.30d}$$

$$\mathbf{f}_a = \frac{1}{2}\int_{-1}^{1} \mathbf{N}^T \frac{\partial \rho_r}{\partial t}\left[Q - \left(c_p - c_{pg}\right)T_\infty\right] d\xi \tag{2.30e}$$

$$\mathbf{f}_b = -\begin{bmatrix} f(T) \\ -g(T) \end{bmatrix} \tag{2.30f}$$

It is evident that $\mathbf{f}_b$ remains unchanged. For numerical integration of the element matrices and vectors, Equations 2.30a to 2.30e, Gauss-Legendre quadrature is used with two Gaussian points (Appendix C). In one-dimensional these integrations can easily be carried out analytically. In two and three dimensions this becomes more difficult, and are almost impossible for distorted elements.

The next step is to form system matrices and vectors for which the element matrices and vectors must be assembled. The assembly procedure is given by the following formulas:

$$\mathbf{C}_{ij} = \sum_{e=1}^{E} \mathbf{C}_{ij}^e \qquad \mathbf{K}_{ij} = \sum_{e=1}^{E} \mathbf{K}_{ij}^e \qquad \mathbf{f}_i = \sum_{e=1}^{E} \mathbf{f}_i^e \tag{2.31}$$

where E is the number of elements in the solution domain.

The numerical solution of the current problem requires solving the set of first order simultaneous ordinary differential equations of the form of Equation 2.26. The finite difference approach adopted in this work and used to obtain the time step algorithms [Zienkiewicz & Taylor, 1991, Lewis *et al.*, 1996].

2.4.5 Time Step Algorithm

The objective is to find an approximation for $\mathbf{T}_{n+1}$ given the value of $\mathbf{T}_n$ with the heat loading vector $\mathbf{f}$ acting in the interval of time Δt [Zienkiewicz & Taylor, 1991; Lewis *et al.*, 1996].

Assume $\mathbf{T}$ can be represented by a polynomial and its linear expansion by:

$$\mathbf{T} \approx \hat{\mathbf{T}}(\tau) = \mathbf{T}_n + \frac{\tau}{\Delta t}\left(\mathbf{T}_{n+1} - \mathbf{T}_n\right) \tag{2.32}$$

where $\tau = t - t_n$.

The equation by which the unknown temperature $\mathbf{T}_{n+1}$ is provided will be the finite difference approximation from 2.26:

$$\int_0^{\Delta t} W\left(\mathbf{C}\dot{\hat{\mathbf{T}}} + \mathbf{K}\hat{\mathbf{T}} + \mathbf{f}\right) d\tau = \mathbf{0} \tag{2.33}$$

Introducing Θ as the weighting (time step) parameter given by:

$$\Theta = \frac{1}{\Delta t}\frac{\int_0^{\Delta t} W\tau\, d\tau}{\int_0^{\Delta t} W d\tau} \tag{2.34}$$

and expanding Equation 2.33 results in:

$$\frac{\mathbf{C}(\mathbf{T}_{n+1} - \mathbf{T}_n)}{\Delta t} + \mathbf{K}\left[\left(\mathbf{T}_n + \Theta(\mathbf{T}_{n+1} - \mathbf{T}_n)\right)\right] + \bar{\mathbf{f}} = 0 \tag{2.35}$$

where $\bar{\mathbf{f}}$ represents an average value of $\mathbf{f}$ given by:

$$\bar{\mathbf{f}} = \frac{\int_0^{\Delta t} \mathbf{f} W d\tau}{\int_0^{\Delta t} W d\tau}$$

or

$$\bar{\mathbf{f}} = \bar{\mathbf{f}}_n + \Theta\left(\bar{\mathbf{f}}_{n+1} - \bar{\mathbf{f}}_n\right) \tag{2.36}$$

if a linear variation of $\mathbf{f}$ is assumed.

Rearranging Equation 2.35 for $\mathbf{T}_{n+1}$ results in [from: Zienkiewicz & Taylor, 1991 as corrected by Looyeh *et al.*, 1997; Zienkiewicz, Pers. Com., 1995]:

$$\mathbf{T}_{n+1} = (\mathbf{C} + \Delta t\Theta\mathbf{K})^{-1}\left\{\left[\mathbf{C} - \Delta t(1-\Theta)\mathbf{K}\right]\mathbf{T}_n - \Delta t\,\bar{\mathbf{f}}\right\} \tag{2.37}$$

At each step of the computation a full set of equations needs to be solved. The non-linear terms and coefficients are quasi-linearised and evaluated explicitly using a simple iterative "updating" procedure. Methods requiring inversion of ($\mathbf{C}+\Delta t\Theta\mathbf{K}$) are known as implicit. There are several types of implicit solution, among them the Crank-Nicolson solution, corresponding to Θ = 1/2, and the backward difference solution, corresponding to Θ = 1, both are used. When Θ = 0 the method is known as explicit where matrix $\mathbf{C}$ is approximated by its lumped equivalent $\mathbf{C}_L$ (Appendix C).

For the convergence of any finite element approximation it is necessary and sufficient to make sure that it is consistent and stable. Finite element solutions with Θ<1/2, e.g. explicit solutions with Θ = 0, are stable conditionally. For such solutions a critical time step is defined below where the solutions are stable. The critical time step, which depends on weighting parameter, element length, density, thermal conductivity and specific heat, is given by [Zienkiewicz & Taylor, 1991]:

$$\Delta t_{cr} = \frac{2}{1-2\Theta}\frac{l^2 \rho\, c_p}{3k} \tag{2.38}$$

It is evident that with any change in the material properties the critical time step will change. It is therefore essential to update the time step after each iteration based upon the new critical time step. By using this method the solution converges with stability and the computing time is minimised. The implicit solutions, i.e. $\Theta \geq 1/2$, are unconditionally stable for any value of the time step Δt whenever the linear governing equations are involved. The stability of the *non-linear* cases which also require iteration at each time interval is different. If the time step is too large, oscillations and instabilities result. To avoid this instability the critical time steps have to be established. In practice, the time step is based on the critical value which is evaluated after each iteration.

2.4.6 Non-Symmetric Matrix Solver

Due to additional terms such as mass loss and gas mass flux in the transient heat conduction equation, the system matrices become non-symmetric. A non-symmetric matrix solver is therefore required. A solver coded by Applegarth [1990] is used. This solver is for a linear system of equations and uses the active column method. The solver has been modified for this work.

For a linear system of equations of the form **AX=B**, the algorithm is given by the following steps:

1. Matrix **A** is decomposed into **LU** and stored into two profile matrices **U** and **L** such that **LUX=B**. The upper part of **A** is stored in **U** and the lower part in **L**. The process includes determination of $\mathbf{U_{ii}}$, $\mathbf{U_{ij}}$ and $\mathbf{L_{ij}}$, respectively.
2. Matrix **B** (right hand side) is modified due to constraints to form $\mathbf{B_c}$. Matrix **LU** is multiplied by the parts of vector **X** which have been constrained.
3. Forward substitution is performed on the lower profile matrix to find **Y** from the matrix equation of the form of $\mathbf{LY=B_c}$.
4. Backward difference is performed to calculate **X** from the matrix equation of the form of **UX=Y**.

CHAPTER III

BOUNDARY CONDITIONS FOR THE HOT AND COLD SURFACES OF PANELS

3.1 INTRODUCTION

Under hydrocarbon fires, offshore panels experience different environmental conditions when they are in use on that portion of the structure which is above water. The aim is to study the physical boundary conditions at the hot and cold surfaces of these panels. This chapter addresses the boundary conditions related to a panel during the full-scale furnace fire tests and then discusses the effects of environmental conditions on the boundaries of a panel used offshore.

Figure 3.1 shows a single-skinned GRP panel, assumed as an infinite plate with finite thickness L, exposed to fire on one side.

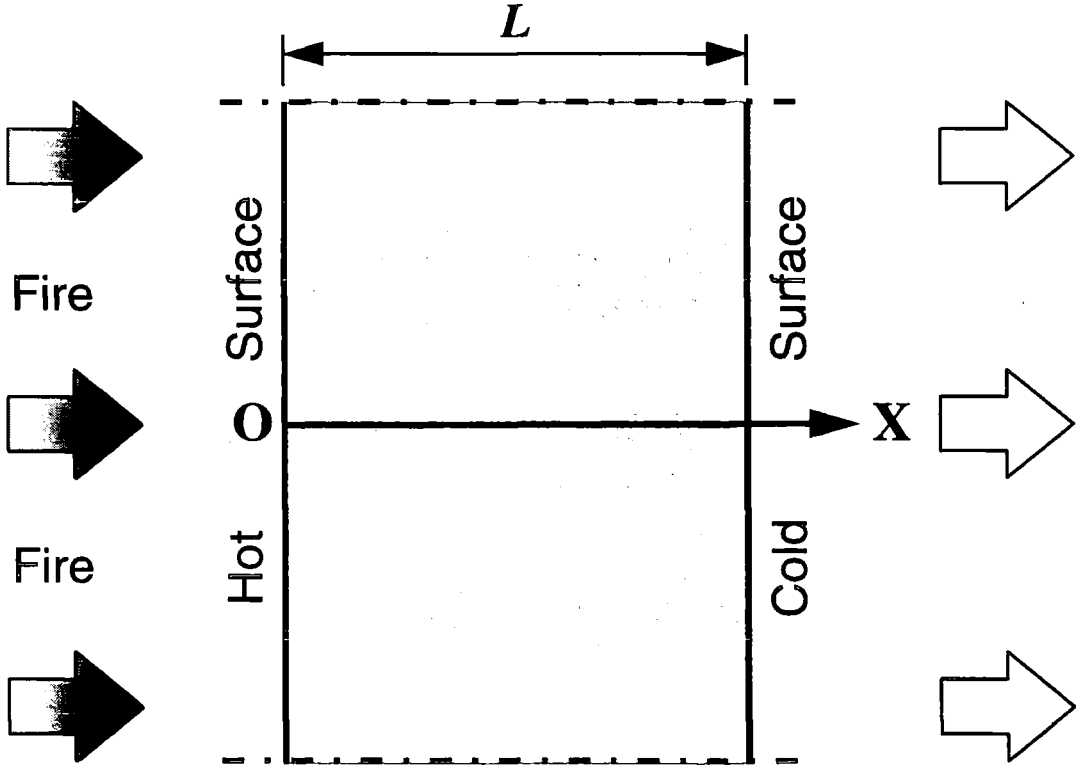

Figure 3.1 The geometry of a single-skinned panel subject to fire on one side. The panel gets heat energy by radiation and convection from the fire at the hot surface (referred to as boundary 1) and looses heat energy by radiation and convection from the cold surface (referred to as boundary 2).

At the fire exposed surface the radiant heat flux can be modelled in two ways by: (i) assuming the temperature-dependent empirical hydrocarbon fire curve introduced by the Norwegian Petroleum Directorate (NPD) [ISO 834, 1975; Spagni & Gibson, 1994; Davies *et al.*, 1994] and (ii) using a theoretical radiation and convection formulation. At the unexposed surface, the possible heat exchanges with the environment are: (i) radiation; (ii) free convection; and (iii) forced convection. The effect of the panel inclination on free convection at both the hot and cold surfaces is also investigated.

3.2 HOT SURFACE BOUNDARY

3.2.1 Empirical Formulation

An empirical formulation [Wu *et al.*, 1994] is used to evaluate the time-dependent temperature of the hot surface of the panel, i.e.

$$T_s(t) = (T_g - 100)\left\{1 - \exp\left\{-\exp\left[0.71\log\left(\frac{t}{124.8}\right)\right]\right\}\right\} + T_\infty \quad \text{for} \quad t > 0 \qquad (3.1)$$

where

$T_s(t)$ = time-dependent hot surface temperature (°C)

T_g = maximum fire temperature (1100°C)

t = time (s)

T_∞ = ambient temperature (20°C)

This includes all heat transfer processes, i.e. radiation and convection.

3.2.2 Theoretical Formulation

The overall boundary condition at the hot surface of the panel (referred to as boundary 1) is due to radiative and convective heat exchange with the fire (Figure 3.1), i.e. the heat gained by radiation and convection from the fire is equal to the heat conducted at the boundary:

$$-k\frac{\partial T}{\partial x} = -(q_{r1} + q_{c1}) \qquad \text{for} \qquad x = 0,\ t > 0 \qquad (3.2)$$

where

k = thermal conductivity ($Wm^{-1}K^{-1}$)

x = spatial co-ordinate starting at the hot surface boundary (m)

q_{r1} = radiative heat flux at the hot surface (Wm^{-2})

q_{c1} = convective heat flux at the hot surface (Wm^{-2})

and the minus sign implies that the heat energy is transferred from the fire to the hot surface.

Radiation at the hot surface

Radiative heat exchange occurs when the rate of heat flow across a boundary is specified in terms of the emitted energy from the surface and the incident radiant thermal energy, emitted and reflected from other solids or fluids. To adopt a suitable formulation for the radiative heat exchange at the hot surface boundary, it is assumed that the panel is diffuse, grey and opaque. A diffuse surface emits and absorbs energy independent of wave length. A medium with such surface is called a grey body, and Kirchoff's law for a grey body states that the monochromatic emissivity ε_s at temperature T is equal to the monochromatic absorptivity α_s, i.e. $\varepsilon_s = \alpha_s$. For an opaque medium $\rho_s+\alpha_s = 1$, where ρ_s is the surface reflectivity [Holman, 1997; Bejan, 1993; Huebner *et al.*, 1995].

Using the Stefan's law of radiation, the radiative heat transfer at the hot surface of the panel can be specified in terms of heat gained by the incident radiation from the fire, $\sigma\varepsilon_{ef}\alpha_s T_{fk}^4$, and heat lost by emitted radiation, which is proportional to the fourth power of the exposed surface temperature, $\sigma\varepsilon_s T_{sk}^4$. Consequently, using Kirchoff's law, the net value of radiative heat transfer per unit time and unit area which gains by the hot surface of the panel is given by:

$$q_{r1} = \sigma\varepsilon_s\left(\varepsilon_{ef} T_{fk}^4 - T_{sk}^4\right) \tag{3.3}$$

where

σ = Stefan-Boltzmann constant (5.669×10^{-8} W $m^{-2}K^{-4}$)

ε_s = hot surface emissivity

ε_{ef} = fire emissivity (0.8)

T_{fk} = time-dependent fire temperature (K)

T_{sk} = hot surface temperature (K)

If $T_{rk} = T_{fk}\sqrt[4]{\varepsilon_{ef}}$ then Equation 3.3 can be written as:

$$q_{r1} = \sigma\varepsilon_s\left(T_{rk}^4 - T_{sk}^4\right) \tag{3.4}$$

where T_{rk} denotes radiative temperature (K).

ISO 834 standard [1975] is used here to obtain the time-dependent fire temperature, i.e.:

$$T_{fk} = T_g\left[1 - 0.345\exp(-0.167t) - 0.204\exp(-1.417t) - 0.471\exp(-15.833t)\right] + 273 \tag{3.5}$$

Radiative heat transfer coefficient

Assuming the hot surface as the only surface receiving heat from the fire, a simplified approach for representing radiative heat transfer can be used. In this approach, an equivalent convective heat transfer, where the non-linearity is considered through a temperature-dependent convection coefficient, is adopted [Holman, 1997; Huebner *et al.*, 1993]. The radiative heat transfer at the hot surface given by Equation 3.4 is replaced by:

$$q_{r1} = h_{r1}\left(T_r - T_s\right) \tag{3.6}$$

where

T_r = radiative temperature (°C)

T_s = hot surface temperature (°C)

and h_{r1} is the equivalent convective coefficient ($Wm^{-2}K^{-1}$) expressed by:

$$h_{r1} = \sigma\varepsilon_s\left(T_{rk}^2 + T_{sk}^2\right)\left(T_{rk} + T_{sk}\right) \tag{3.7}$$

The radiative heat transfer coefficient is critically dependent on the radiative and hot surface temperatures, hence, the linearisation can only be used for special cases of the fire performance of offshore panels.

Free convection at the hot surface

Free convection is a result of the fluid motion due to density changes arising from the heating process.

Assuming no wind, as set out for the furnace fire test [Wu *et al.*, 1994; Davies *et al.*, 1994] a panel experiences free convective heat transfer at the hot surface boundary.

The convective heat transfer at the hot surface of the panel is defined by:

$$q_{c1} = h_{c1}\left(T_f - T_s\right) \tag{3.8}$$

where T_f is the time-dependent fire temperature (°C) and h_{c1} is the average free convective heat transfer coefficient ($Wm^{-2}K^{-1}$) expressed by:

$$h_{c1} = k_{ef} \frac{\overline{Nu}_H}{H} \tag{3.9}$$

where

k_{ef} = thermal conductivity of air at furnace temperature ($Wm^{-1}K^{-1}$)

$\overline{Nu}_H$ = average Nusselt number

and H is the characteristic dimension of the panel dependent on the geometry of the problem. For vertical panels H is the height and for horizontal or inclined panels it is the length of the panels.

3.3 COLD SURFACE BOUNDARY

A theoretical formulation is developed for the boundary condition at the cold surface. This surface (referred to as boundary 2) exchanges radiative and convective heat energy with the environment (Figure 3.1), i.e. heat conducted at this boundary is equal to the heat lost by radiation and convection:

$$-k\frac{\partial T}{\partial x} = q_{r2} + q_{c2} \qquad \text{for} \qquad x = L,\ t > 0 \tag{3.10}$$

where

q_{r2} = radiative heat flux at the cold surface (Wm^{-2})

q_{c2} = convective heat flux at the cold surface (Wm^{-2})

Radiation from the cold surface

It is assumed that the panel is a wall or floor or ceiling within a closed compartment on an offshore topside structure whose elements have uniform surface temperature. It is also assumed that the thermal radiation passing between the panels within the compartment is substantially unaffected by the intervening air. The radiant energy emitted from the body per unit time and unit area is $\sigma\varepsilon T_k^4$ and the corresponding absorbed radiant energy from the other elements within the compartment is $\sigma\alpha T_{\infty k}^4$.

Consequently, the net value of heat flow per unit area from the cold surface boundary is $\sigma\varepsilon T_k^4$-$\sigma\alpha T_{\infty k}^4$. Using Kirchoff's law gives:

$$q_{r2} = \sigma\varepsilon\left(T_k^4 - T_{\infty k}^4\right) \tag{3.11}$$

where

ε = cold surface emissivity

α = cold surface absorptivity

T_k = cold surface temperature (K)

$T_{\infty k}$ = ambient temperature (293K)

Radiative heat transfer coefficient

Using the same assumption made in Section 3.2 for the linearisation of the radiative heat transfer at the hot surface boundary, the radiative heat transfer at the cold surface given by Equation 3.11 can be replaced by:

$$q_{r2} = h_{r2}\left(T - T_\infty\right) \tag{3.12}$$

where

T = cold surface temperature (°C)

and h_{r2} is the equivalent convective coefficient expressed by:

$$h_{r2} = \sigma\varepsilon\left(T_k^2 + T_{\infty k}^2\right)\left(T_k + T_{\infty k}\right) \tag{3.13}$$

Free convection at the cold surface

The convective heat transfer at the cold surface of the panel is defined, in the same manner as for the hot surface boundary, by:

$$q_{c2} = h_{c2}\left(T - T_\infty\right) \tag{3.14}$$

and h_{c2} is the average free convective heat transfer coefficient ($Wm^{-2}K^{-1}$) expressed by:

$$h_{c2} = k_{e\infty}\frac{\overline{Nu}_H}{H} \tag{3.15}$$

where

$k_{e\infty}$ = thermal conductivity of air at ambient temperature ($Wm^{-1}K^{-1}$)

Forced convection at the cold surface

Convection flow is forced subject to pressure gradients, e.g. when a velocity field is imposed on the fluid. Forced convection at the cold surface boundary occurs when wind forces are exerted on the topside of the offshore structure where the panel is used. Forced convective heat transfer can be defined similarly by Equation 3.14. The average forced convective heat transfer coefficient can be evaluated using Equation 3.15 in which the average Nusselt number for forced convection is different from that of free convection.

3.4 EVALUATION OF NUSSELT NUMBER

3.4.1 Free Convection

Three overall positions of a panel experiencing free convective heat transfer are studied. These are: (i) vertical; (ii) horizontal and (iii) inclined.

For vertical and horizontal panels all the properties are evaluated at film temperature, $T_F = (T+T_{ef})/2$ or $T_F = (T+T_{e\infty})/2$. For inclined panels, however, all the properties should be evaluated at a reference temperature T_R defined by $T_R = (T+T_F)/2$.

(i) Free convection from a vertical panel

An empirical relation that is valid for all Rayleigh and Prandtl numbers has been introduced by Churchill and Chu [1975]:

$$\overline{Nu}_H = \left\{ 0.825 + \frac{0.387 Ra_H^{1/6}}{\left[1+(0.492/Pr)^{9/16}\right]^{8/27}} \right\}^2 \qquad \begin{matrix} 10^{-1} < Ra_H < 10^{12} \\ \text{for all Pr} \end{matrix} \qquad (3.16)$$

where Ra_H denotes Rayleigh number and Pr denotes Prandtl number (Appendix B). The Nusselt, the dimensionless heat transfer coefficient, and Rayleigh numbers are formulated for the height H of the vertical panel.

The Rayleigh number is defined by:

$$Ra_H = Gr_H \, Pr \qquad (3.17)$$

where

$$\mathrm{Gr_H} = \frac{g\beta(T - T_e)H^3\rho_e^2}{\mu_e^2} \tag{3.18}$$

$$\mathrm{Pr} = \frac{\mu_e c_{pe}}{k_e} \tag{3.19}$$

and

$\mathrm{Gr_H}$ = Grashof number (Appendix B)

g = gravitational acceleration ($\mathrm{ms^{-2}}$)

β = coefficient of volumetric thermal expansion evaluated at film temperature, $\beta = 1/T$ ($\mathrm{K^{-1}}$)

T_e = temperature of environment, $T_{e\infty}$ or T_{ef} (°C)

ρ_e = density of environment, $\rho_{e\infty}$ or ρ_{ef} ($\mathrm{kgm^{-3}}$)

μ_e = dynamic viscosity of environment, $\mu_{e\infty}$ or μ_{ef} ($\mathrm{Nsm^{-1}}$)

c_{pe} = specific heat of environment, $c_{pe\infty}$ or c_{pef} ($\mathrm{Jkg^{-1}K^{-1}}$)

k_e = thermal conductivity of environment, $k_{e\infty}$ or k_{ef} ($\mathrm{Wm^{-1}K^{-1}}$)

(ii) Free convection from a horizontal panel

In the case of a horizontal panel, two flow types are encountered: (a) when the surface is hot and faces upward, or when it is cold and faces downward, and (b) when the surface is hot and faces downward or when it is cold and faces upward. A two-sided panel will have flow of one type on the top side and flow of the other type at the bottom side.

For hot surfaces facing upward, or cold surfaces facing downward Fujii and Imura [1972] and Llyod and Moran [1974] introduced the following empirical relations for the average Nusselt number at various Rayleigh numbers:

$$\overline{\mathrm{Nu}}_\mathrm{H} = 0.54\ \mathrm{Ra}_\mathrm{H}^{1/4} \qquad 2\times10^4 \le \mathrm{Ra_H} < 8\times10^6 \tag{3.20a}$$

$$\overline{\mathrm{Nu}}_\mathrm{H} = 0.15\ \mathrm{Ra}_\mathrm{H}^{1/3} \qquad 8\times10^6 \le \mathrm{Ra_H} < 8\times10^{11} \tag{3.20b}$$

The corresponding empirical relation for hot surfaces facing downward or cold surfaces facing upward is evaluated by [Hatfield & Edwards, 1981; Fujii & Imura, 1972; Clifton & Chapman, 1969]:

$$\overline{\mathrm{Nu}}_\mathrm{H} = 0.27\ \mathrm{Ra}_\mathrm{H}^{1/4} \qquad 10^5 \le \mathrm{Ra_H} < 10^{11} \tag{3.21}$$

The characteristic dimension for use with these relations is taken as the length of the side of a square panel or the mean of length and width of a rectangular panel.

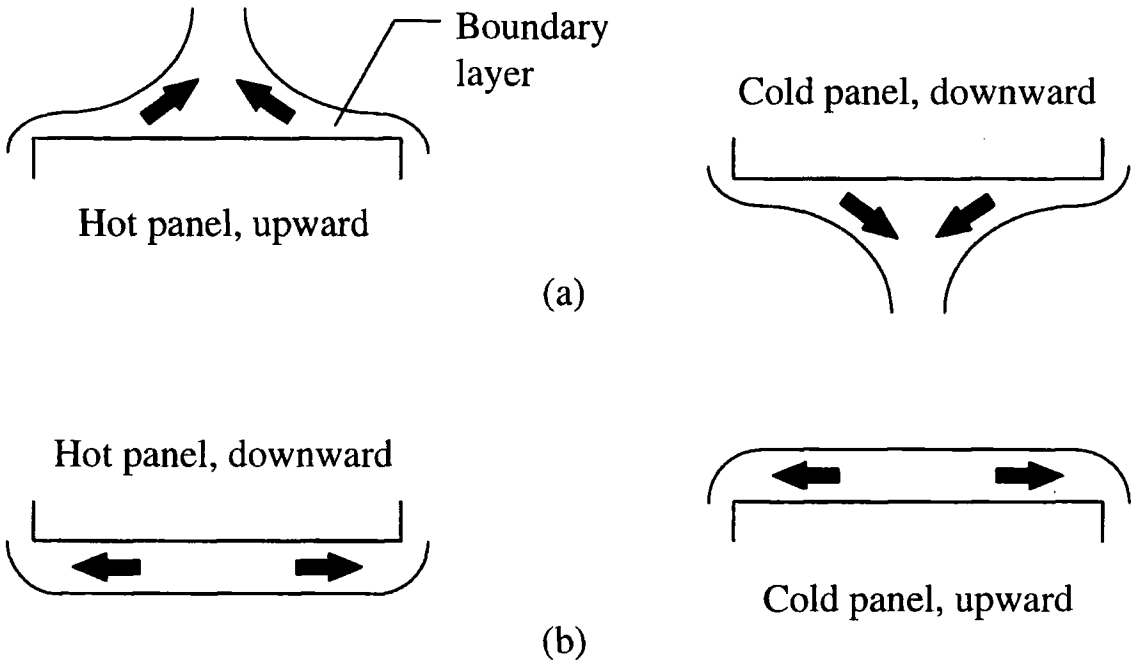

Figure 3.2 Horizontal panels with two types of convective heat flow (shown by arrows) in the boundary layer: (a) hot panel, facing upward or cold panel, facing downward (b) hot panel, facing downward and cold panel, facing upward [from: Bejan, 1993].

(iii) Free convection from an inclined panel

There are four possible configurations in which a panel is inclined relative to the vertical direction (Figure 3.3). The angle which the panel makes with the vertical is designated θ and restricted to the ranges $-75^{\circ}<\theta<-15^{\circ}$ and $0<\theta<90^{\circ}$ [Holman, 1997]. The positive angles indicate that the hot surface faces downward or the cold surface faces upward, cases (a) and (d), where the effect of the angle θ is to thicken the tail end of the boundary layer and to give it a tendency to separate from the panel. In the cases labelled (b) and (c) an opposite effect occurs where the boundary layer is squeezed against the panel until it flows over the trailing edge.

Theoretically, the average Nusselt number given for the vertical panels can be used for the inclined panels by replacing g with $g\cos\theta$. Fujii and Imura [1972] conducted some experiments for hot plates in water at various angles. They introduced the following empirical relations for an inclined panel with positive angle which can be used for any environment:

$$\overline{Nu}_H = 0.56\left(Ra_H \cos\theta\right)^{1/4} \qquad \theta \le 88^{\circ},\ 10^5 < Ra_H \cos\theta < 10^{11} \tag{3.22a}$$

$$\overline{Nu}_H = 0.58\left(Ra_H\right)^{1/5} \qquad 88^{\circ} < \theta < 90^{\circ},\ 10^6 < Ra_H < 10^{11} \tag{3.22b}$$

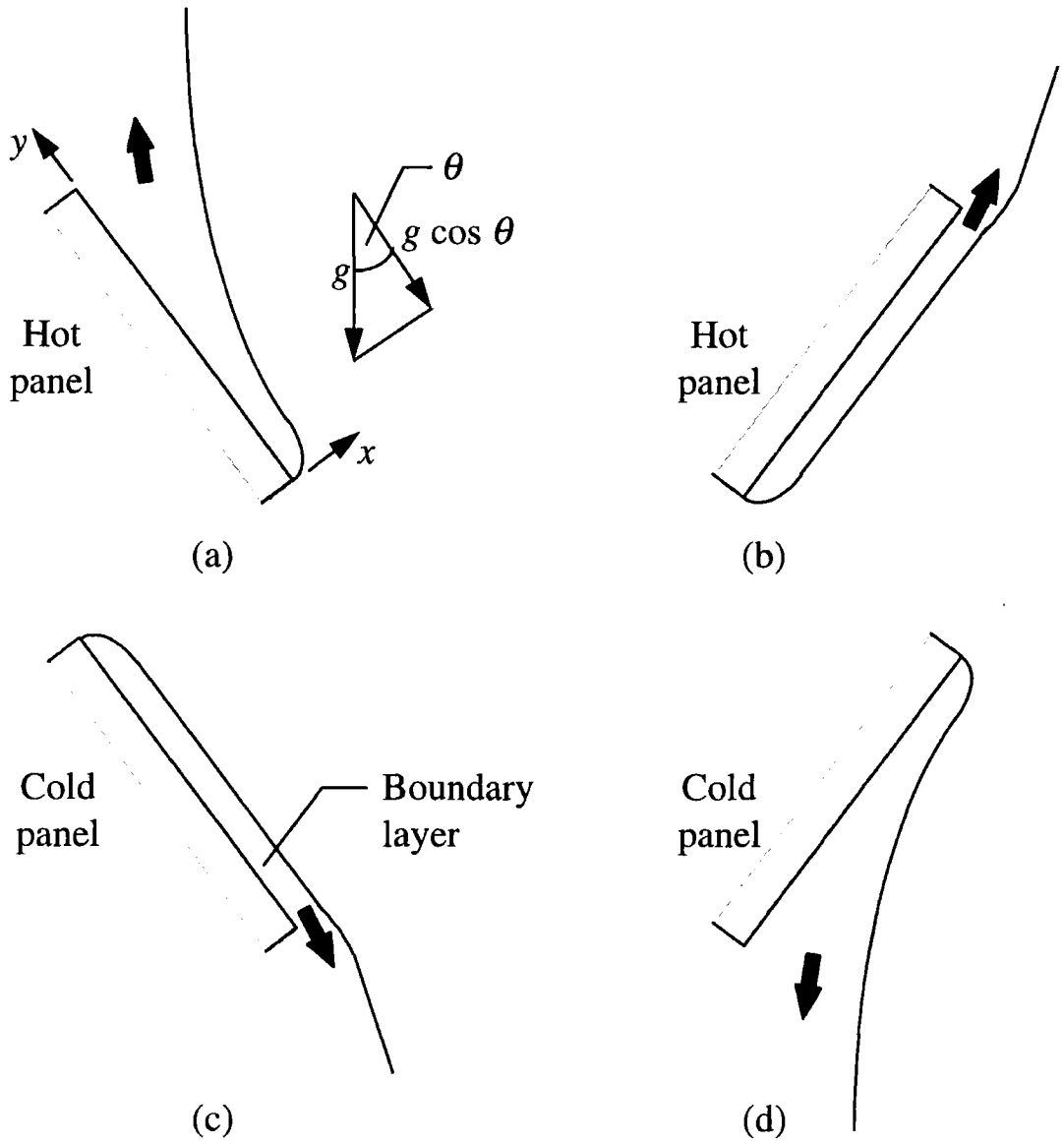

Figure 3.3 Panels inclined relative to the vertical direction. (a) hot panel, facing downward with positive angle; (b) Hot panel, facing upward with negative angle; (c) Cold panel, facing downward with negative angle and (d) cold panel, facing upward with positive angle. Arrows represent the convective heat flows in the boundary layers [from: Bejan, 1993].

For an inclined panel with negative angle the following empirical relation was obtained [Fujii & Imura, 1972]:

$$\overline{Nu}_H = 0.14\left[Ra_H^{1/3} - (Gr_{cr}Pr)^{1/3}\right] + 0.56(Ra_H \cos\theta)^{1/4} \quad 10^5 < Ra_H \cos\theta < 10^{11} \quad (3.23)$$

where Gr_{cr} is the critical Grashof number and is given for different angles in Table 3.1 [Fujii & Imura, 1972; Holman, 1997].

Table 3.1 Critical values for Grashof number at different angles [from: Holman, 1997].

θ, degrees	Gr_{cr}
-15	5×10^9
-30	2×10^9
-60	10^8
-75	10^6

3.4.2 Forced Convection

Empirical relations were introduced by Churchill and Ozoe [1973] for the average Nusselt number with laminar and turbulent flows by:

$$\overline{Nu}_H = \frac{0.928 Pr^{1/3} Re_H^{1/2}}{\left[1+(0.0207/Pr)^{2/3}\right]^{1/4}} \qquad Re_H \le 5\times10^5,\ Pe_H \ge 100 \qquad (3.24a)$$

and $$\overline{Nu}_H = 0.037 Pr^{1/3}\left(Re_H^{4/5} - 23{,}550\right) \qquad 5\times10^5 < Re_H \le 10^8,\ Pr \ge 0.5 \qquad (3.24b)$$

respectively. Re_H and Pe_H denote Reynolds and Peclet numbers and are represented by (Appendix B):

$$Re_H = \frac{\rho_e V_m H}{\mu_e} \qquad (3.25)$$

$$Pe_H = Re_H Pr \qquad (3.26)$$

where

V_m = mean wind velocity (ms^{-1})

Wind mean velocity

Winds are generated in response to atmospheric pressure gradients, Coriolis force and friction. The wind velocity at elevation Z is empirically related to the velocity V_R at the reference elevation Z_R by a power law [API RP 2A-LRFD, 1993] of the following form:

$$V_m = V_R\left(\frac{Z}{Z_R}\right)^n \qquad (3.27)$$

where the exponent n varies from 1/6 to 1/8.5 for sustained winds, and up to 1/13 for gusts winds.

In order to define wind mean velocity, API RP 2A-LRFD [1993] recommends n=1/8 for one hour of the wind duration. Besides, to establish an environmental condition, it is assumed that the structure is located in the Gulf of Mexico North of 27°N Latitude and West of 86°W Longitude. The reference velocity is recommended by API RP 2A-LRFD [1993] for this location. The value of elevation for a typical offshore structure can also be approximated based on the supplied data for the defined location by simple summation of maximum wave height, deck clearance and the half value of the structure topside height. Thus, a set of offshore panel, wind and location data are summarised in Table 3.2.

Table 3.2 Offshore panel and wind data for the Golf of Mexico with Latitude 27°N and Longitude 86°W [from: API RP 2A-LRFD, 1993; Wu *et al.*, 1994].

Property	Value
Nominal panel size, $L \times W \times H$ (cm)	1.09×90×90
Gravitational acceleration, g (ms^{-2})	9.80665
Ambient temperature, T_∞ (°C)	20
Reference velocity, V_R (ms^{-1})	41
Reference elevation, Z_R (m)	10
Elevation evaluated, Z (m)	30.5
Wind mean velocity, V_m (ms^{-1})	47.1

3.5 THERMO PHYSICAL PROPERTIES OF AIR

Thermo physical properties (TPP) of air, i.e. thermal conductivity, specific heat and dynamic viscosity, at atmospheric pressure and the temperature range 200 to 1500K are given by Holman [1997] and Bejan [1993]. For computer coding purposes, a general formula has been constructed by fitting each set of data to a polynomial curve. The general formula is:

$$\text{TPP} = a_1 + a_2 T_k + a_3 T_k^2 + a_4 T_k^3 + a_5 T_k^4 \tag{3.28}$$

where a_i (i=1,2,...,5) are polynomial coefficients listed in Table 3.3. A formula has also been fitted to density of air as function of temperature for the range 200 to 1500K. The formula is:

$$\rho_e = \frac{352.989}{T_k} \tag{3.29}$$

Table 3.3 a_i coefficients for thermal conductivity, specific heat and dynamic viscosity of air.

Coefficient	Thermal Conductivity, k_e, ($Wm^{-1}K^{-1}$)	Specific Heat, c_{pe}, ($Jkg^{-1}K^{-1}$)		Dynamic Viscosity, μ_e, (Nsm^{-1})
	200-1500 K	260-610 K	610-1500 K	200-1500 K
a_1	1.3003×10^{-3}	1.0454	1.0027	2.2880×10^{-6}
a_2	9.3676×10^{-5}	-3.1618×10^{-4}	-1.6309×10^{-4}	6.2598×10^{-8}
a_3	-4.4425×10^{-8}	7.0838×10^{-7}	5.6991×10^{-7}	-3.1320×10^{-11}
a_4	2.3172×10^{-11}	-2.7052×10^{-10}	-2.6826×10^{-10}	8.1504×10^{-15}
a_5	-6.5998×10^{-15}	0	0	0

3.6 SUMMARY

In this chapter the physical boundary conditions at the hot and cold surfaces appropriate for panels in offshore fire conditions were studied. In addition, use was made for some panels in laboratory furnace fire tests.

Two formulations, i.e. (i) empirical and (ii) theoretical, were introduced to simulate radiative and convective heat transfer at the hot surface boundary. The cold surface boundary was considered to exchange heat energy with the environment in the form of: (i) radiation; (ii) free convection and (iii) forced convection. The effect of the panel inclination on free convection at both the hot and cold surfaces was also studied.

The formulations for the hot and cold surface boundary conditions can be used in Chapters 5, 6, 8 and 9 for modelling the single-skinned GRP panels, twin-skinned GRP sandwich panels and any type of GRP joins.

CHAPTER IV

MATERIAL PROPERTIES

4.1 INTRODUCTION

The accurate modelling of the thermal response of the components made of polymer composites requires the provision of accurate material properties and modelling parameters.

In this chapter, the material properties required for the modelling of single-skinned glass reinforced plastic (GRP) panels and pipes, twin-skinned GRP sandwich panels and GRP joins are assembled. These include thermal, transport and kinetic properties of the selected GRP, i.e. polyester-based GRP, and thermal and transport properties of the selected sandwich material, i.e. Vermiculux.

The key sources of the material properties are: (i) Suppliers' data; (ii) Thermo gravimetric analysis; (iii) Furnace fire tests and temperature-time data and (iv) Literature studies. These are discussed in this chapter in detail.

4.2 DESCRIPTION OF MATERIALS

4.2.1 Polyester-Based Glass Reinforced Plastic

Composition

The composite material studied in this work is the polyester-based glass reinforced plastic (GRP) which has already been used in the Marinetech research fire test programme [Dodds *et al.*, 1998; Davies & Wang, 1998; Gibson *et al.*, 1996; Wang, 1995; Spagni & Gibson, 1994; Wu *et al.*, 1994; Davies *et al.*, 1994]. This composite consists of isophthalic polyester resin as the matrix and woven roving glass fibre of E-glass type as the reinforcement. The polyester resin is of the thermosetting type, i.e. it

undergoes chemical cross linking during fabrication. For fire test purposes, the GRP laminates were manufactured using the contact moulding or hand-lay up method. These composites were cured at room temperature for at least 24 hours. They were then post-cured at 80°C for 4 hours in order to fully maximise the cross linking reaction and remove any trace of residual styrene [Gibson *et al.*, 1996; Wu *et al.*, 1994]. As a result, the GRP laminates exhibit homogeneous and orthotropic behaviour. Table 4.1 lists the constituents in this composite and their physical properties. The mass of moisture content of the GRP is about 1%.

Table 4.1 Basic properties of the components of polyester-based GRP consisting of 53.5% polyester resin and 46.5% glass fibre [Gibson *et al.*, 1996; Wu *et al.*, 1994].

Property	Resin (Isophthalic Polyester)	Reinforcement (Woven Roving Glass Fibre)
Density, kgm^{-3}	1200	2560
Thermal cond., $Wm^{-1}K^{-1}$	0.2	1.09
Specific heat, $Jkg^{-1}K^{-1}$	1600	760

Rule of mixtures

The initial density, specific heat and thermal conductivity of polyester-based GRP can be calculated using the "rule of mixtures" [Agrawal & Broutman, 1990; Taya & Arsenault, 1989; Sheldon, 1982; Hashin, 1983; Hull, 1981; Hale, 1976].

Two configurations of polyester-based GRP are used: (i) single-skinned panels in which the material is homogeneous and isotropic and (ii) step panels in which the material is homogeneous and orthotropic.

The density, specific heat and thermal conductivity of the single-skinned polyester-based GRP panels are evaluated by:

$$\rho = V_f \rho_{fr} + (1 - V_f)\rho_r \tag{4.1}$$

$$\frac{1}{c_p} = \frac{V_f}{c_{pfr}} + \frac{1 - V_f}{c_{pr}} \tag{4.2}$$

$$\frac{1}{k} = \frac{V_f}{k_{fr}} + \frac{1 - V_f}{k_r} \tag{4.3}$$

where

ρ = density of GRP (kgm^{-3})

V_f = volume fraction

ρ_{fr} = density of glass fibre (kgm^{-3})

ρ_r = density of polyester (kgm^{-3})

c_p = specific heat of GRP ($Jkg^{-1}K^{-1}$)

c_{pfr} = specific of glass fibre ($Jkg^{-1}K^{-1}$)

c_{pr} = specific heat of polyester ($Jkg^{-1}K^{-1}$)

k = thermal conductivity of GRP ($Wm^{-1}K^{-1}$)

k_{fr} = thermal conductivity of glass fibre ($Wm^{-1}K^{-1}$)

k_r = thermal conductivity of polyester ($Wm^{-1}K^{-1}$)

The density and specific heat of polyester-based GRP step panels are evaluated in the same manner as the single-skinned type because of homogeneity. The thermal conductivities in through-the-thickness and longitudinal directions are different and evaluated by:

$$\frac{1}{k_T} = \frac{V_f}{k_{fr}} + \frac{1 - V_f}{k_r} \tag{4.4}$$

$$k_L = V_f k_{fr} + (1 - V_f)k_r \tag{4.5}$$

where

k_T = through-the-thickness thermal conductivity of GRP ($Wm^{-1}K^{-1}$)

k_L = longitudinal thermal conductivity of GRP ($Wm^{-1}K^{-1}$)

4.2.2 Vermiculux (Calcium Silicate)

For the twin-skinned polyester-based GRP sandwich panels, i.e. two GRP skins and a refractory sandwich board, isophthalic polyester resin is used as the structural adhesive and Vermiculux board as the refractory sandwich material. Vermiculux is a well-established calcium silicate with dry density approximately 460 kgm^{-3}. This material has excellent fire properties and good mechanical strength. Vermiculux readily absorbs water and this can significantly extend the fire resistance properties of the sandwich constructions. Table 4.2 lists the physical properties of Vermiculux.

Table 4.2 Basic properties of Vermiculux (Calcium Silicate, $CaSiO_3$) [Gibson *et al.*, 1996; Wang, 1995; Davies *et al.*, 1994].

Property	Value
Mass of moisture content, %	11.5
Density, kgm^{-3}	460 / 475
Thermal conductivity, $Wm^{-1}K^{-1}$	0.13
Specific heat, $Jkg^{-1}K^{-1}$	840

4.3 PROPERTIES OF POLYESTER-BASED GRP

A complete list of thermal, transport and kinetic properties for polyester-based GRP is presented in Table 4.3, where:

θ = relative temperature, i.e. $\theta = T_k - T_{\infty k}$ (°C)

T_k = temperature (K)

$T_{\infty k}$ = ambient temperature (293K)

c_{pv} = specific heat of moisture evaporation ($Jkg^{-1}K^{-1}$)

$f(m_v)$ = proportion function

F = instantaneous mass fraction

and $f(m_v)$ [Wang, 1995; Jacob, 1949] and F are given by:

$$f(m_v) = 1.0819 + 1.7675 \times 10^{-1} m_v - 8.7812 \times 10^{-3} m_v^2 + 1.7617 \times 10^{-5} m_v^3 \quad (4.6)$$

$$F = \frac{\rho_r - \rho_{rf}}{\rho_{ro} - \rho_{rf}} \quad (4.7)$$

Table 4.3 Properties for polyester-based GRP.

Pyrolysis constant, A (s^{-1})	7.525×10^{3}	
Rate constant (surface reactions), A_s (s^{-1})	0.975×10^{-3}	
Initial specific heat of GRP, c_{po} ($Jkg^{-1}K^{-1}$)	1056.84	
Specific heat (glass fibre), c_{pfr} ($Jkg^{-1}K^{-1}$)	$760+3.88\times10^{-2}\theta$	$20\leq\theta\leq1100$
Specific heat (polyester resin), c_{pr} ($Jkg^{-1}K^{-1}$)	$1600+0.8\theta$	$20\leq\theta<90$
Specific heat (polyester resin), c_{pr} ($Jkg^{-1}K^{-1}$)	$1600+c_{pv}+0.8\theta$	$90\leq\theta\leq120$
Specific heat (polyester resin), c_{pr} ($Jkg^{-1}K^{-1}$)	$1600+0.8\theta$	$120<\theta\leq1100$
Activation energy, E_A ($kJkmole^{-1}$)	6.115×10^{4}	
Surface activation energy, E_{As} ($kJkmole^{-1}$)	5.9918×10^{4}	
Initial thermal cond. of GRP, k_o ($Wm^{-1}K^{-1}$)	0.322	
Thermal cond. (glass fibre), k_{fr} ($Wm^{-1}K^{-1}$)	$1.09+2.05\times10^{-4}\theta$	$20\leq\theta<1100$
Thermal cond. (polyester), k_r ($Wm^{-1}K^{-1}$)	$0.2f(m_{vo})-1.356\times10^{-4}\theta$	$20\leq\theta<90$
Thermal cond. (polyester), k_r ($Wm^{-1}K^{-1}$)	$0.2f(m_v)-1.356\times10^{-4}\theta$	$90\leq\theta\leq120$
Thermal cond. (polyester), k_r ($Wm^{-1}K^{-1}$)	$0.2-1.356\times10^{-4}\theta$	$120<\theta\leq200$
Thermal cond. (polyester), k_r ($Wm^{-1}K^{-1}$)	$0.2+2.0\times10^{-4}\theta$	$200<\theta\leq1100$
Thermal cond. (polyester), k_r ($Wm^{-1}K^{-1}$)	$0.2+3.88\times10^{-2}\theta$	$20\leq\theta\leq1100$
Initial moisture content, m_{vo}	1.8%	$20\leq\theta<90$
Moisture content, m_v	$0.06-0.6\times10^{-3}\theta$	$90\leq\theta\leq120$
Heat of decomposition, Q (Jkg^{-1})	2.3446×10^{6}	
Surface heat of decomposition, Q_s (Jkg^{-1})	2.0971×10^{7}	
Volume fraction, V_f	0.465	
Surface emissivity, ε_s	$0.755+2.5\times10^{-4}\theta$	$20\leq\theta\leq600$
Permeability, $\gamma(m^2)$	$8.8\times10^{-21}e^{11(1-F)}$	$20\leq\theta\leq1100$
Initial density of GRP, ρ_o (kgm^{-3})	1832.4	
Density of glass fibre, ρ_{fr} (kgm^{-3})	2560	
Initial density of polyester, ρ_{ro} (kgm^{-3})	1200	
Fraction resin mass remaining, ρ_r/ρ_{ro}	0.02	
Porosity, ϕ	$0.15F+0.325(1-F)$	$20\leq\theta\leq1100$

In Chapter 1 we described how the pyrolysis gases are generated during the decomposition process. Analysis of the pyrolysis gases reveals carbon monoxide, carbon dioxide, hydrogen, nitrogen, methane and lesser products, the amount of each depending on the composition of the original resin [Sullivan & Salamon, 1992a; Henderson, 1980]. For polyester resin a list of properties of the pyrolysis gases [Wang, 1995; Wu *et al.*, 1994, Sullivan, 1993; Sullivan & Salamon, 1992a, Henderson *et al.*, 1985; Henderson, 1980] are given in Table 4.4.

Table 4.4 Properties for pyrolysis gases.

Gas specific heat, c_{pg} ($Jkg^{-1}K^{-1}$)	$2386.5+1.05\theta$	$20 \le \theta \le 1100$
Gas thermal conductivity, k_g ($Wm^{-1}K^{-1}$)	$3.28\times10^{-2}+1.4\times10^{-4}\theta$	$20 \le \theta \le 1100$
Gas molecular weight, M_g ($kgkmole^{-1}$)	18.35	
Gas dynamic viscosity, μ_g (Nsm^{-2})	$1.53\times10^{-5}+2.5\times10^{-8}\theta$	$20 \le \theta \le 1100$

The thermal, transport and kinetic properties of polyester-based GRP are discussed in details in the following sections.

4.3.1 Thermal Properties

For most materials, thermal properties are temperature- and moisture-dependent.

Variations of thermal properties with temperature are obtained experimentally [Wang, 1995; Davies *et al.*, 1994a; Sullivan, 1993; Sullivan & Salamon, 1992b; Datoo, 1991; Fredlund, 1988; Henderson *et al.*, 1985; Drysdale, 1985]. These are normally given as linear functions of temperature.

During the manufacturing process, the resin component of GRP absorbs moisture from the surrounding environment. This hygroscopic process is reversible. For example, exposure to high temperature will eventually cause the moisture to evaporate making it difficult to take into account a combination of heat and moisture transfer. The hygroscopic process involves moisture redistribution, temperature, chemical reactions, multiphase mass transfer, permeability and non-linear thermal properties [Wang, 1995; Datoo, 1991; Harmathy, 1965].

To take account of moisture evaporation, both simple and sophisticated models have been proposed [Wang, 1995; Jacob, 1949]. Simple models concentrate on heat transfer and disregard mass diffusion and pressure build-up so that the effect of moisture is simulated by considering the energy of evaporation. Sophisticated models consider the convective and diffusive heat and mass transfer based on an evaporation-condensation mechanism driven by pore pressure and moisture concentration.

The moisture content in GRP can be in the form of chemically or physically trapped water. The energy necessary to vaporise this moisture comprises: (i) the heat absorbed in dehydration process for chemical bonded water and (ii) the energy needed to drive off the water (including physically absorbed free water) from the material [Drysdale, 1985]. To quantify these processes we need to consider the effect of moisture on specific heat and thermal conductivity.

In this section the thermal properties of polyester-based GRP and pyrolysis gases listed in Tables 4.3 and 4.4 are discussed in detail.

Specific heat

The effect of moisture evaporation on specific heat is simulated by assuming a simple evaporation-condensation mechanism driven only by the moisture concentration gradients [Wang, 1995; Drysdale, 1985]. The evaporation is assumed to take place during a temperature interval ΔT=30°C (between 90°C and 120°C) with a specific heat given by:

$$c_{pv} = \frac{f_c h_{fg} m_w}{\Delta T} \tag{4.8}$$

where

c_{pv} = specific heat of moisture evaporation ($Jkg^{-1}K^{-1}$)

f_c = correction factor for dehydration (1.33)

h_{fg} = latent heat of evaporation (2.257×10^6 Jkg^{-1})

m_w = mass of moisture content

The correction factor f_c has been determined experimentally [Mehaffy, 1994]. The latent heat of evaporation is known for a given pressure and temperature [Wang, 1995]. For this work a triangular function of temperature is considered (Figure 4.1). This neglects the extra energy required for the moisture evaporation-condensation migration under high pressure.

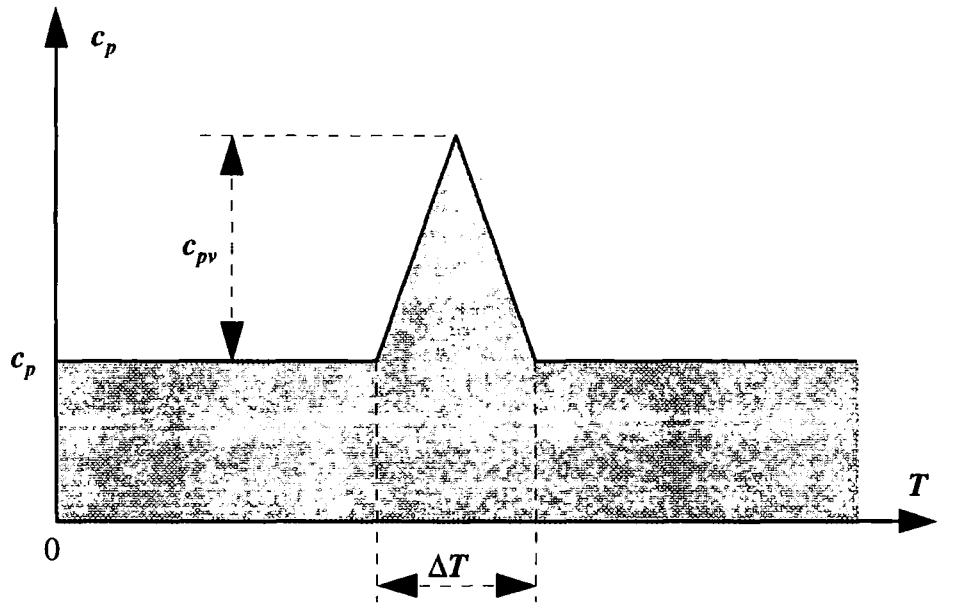

Figure 4.1 The triangular variation of specific heat during moisture evaporation and before the beginning of pyrolysis.

The specific heat increases with temperature and moisture evaporation. The simple relationship between specific heat and temperature is given by a linear function [Wang, 1995] as:

$$c_p(T) = c_{p_0} + c_{p_1}\left(T_k - T_{\infty k}\right) \tag{4.9}$$

where

$c_p(T)$ = temperature-dependent specific heat ($Jkg^{-1}K^{-1}$)

c_{po} = initial specific heat ($Jkg^{-1}K^{-1}$)

c_{p1} = curve fit coefficient ($Jkg^{-1}K^{-1}\,{}^{o}C^{-1}$)

and Equation 4.9 is valid for both polyester resin and glass fibre.

The specific heat of polyester resin over temperature interval ΔT is given by:

$$c_p(T) = c_{p_0} + c_{pv} + c_{p_1}\left(T_k - T_{\infty k}\right) \quad \text{for} \quad 90 \le T_k - T_{\infty k} \le 120^{\circ}\mathrm{C} \tag{4.10}$$

Thermal conductivity

The effective thermal conductivity depends on temperature, density variations, moisture gradient, porosity and permeability [Wang, 1995].

In porous solids the thermal conductivity must be evaluated experimentally [Henderson, 1980; Henderson *et al.*, 1985; Wang, 1995].

During the fire exposure and at the time of moisture evaporation, the thermal conductivity rises considerably. This is due to the pores containing water, which is a better conductor of heat than air, plus the heat transferred by the migration of the moisture. For polyester-based GRP, the effect of moisture evaporation on the thermal conductivity of the glass fibre is negligible; whereas the thermal conductivity of the moist polyester resin is given by:

$$k_{rm} = k_r f(m_v) \tag{4.11}$$

where

k_{rm} = thermal conductivity of moist polyester resin ($Wm^{-1}K^{-1}$)

k_r = thermal conductivity of dry polyester resin ($Wm^{-1}K^{-1}$)

$f(m_v)$ is given by Equation 4.6 and the moisture gradients by the linear expression:

$$m_v(x,t) = m_{v0} + m_{v1}(T_k - T_{\infty k}) \tag{4.12}$$

where

m_v = volumetric moisture content

m_{v0} = initial moisture content

m_{v1} = curve fit coefficient ($^oC^{-1}$)

This implies the thermal conductivity increases with increasing temperature for a given moisture content [Parrott & Audrey, 1975]. The total moisture content is gradually reduced as heating proceeds giving a limiting value of thermal conductivity resulting from both effects.

Thermal conductivity changes with temperature and the stage of decomposition. For polyester-based GRP, it also depends on the ratio of polyester resin to glass fibre. A general expression for the thermal conductivity assuming a linear function of temperature [Wang, 1995; Hollaway, 1978] is given by:

$$k(T) = k_0 + k_1(T_k - T_{\infty k}) \tag{4.13}$$

where

$k(T)$ = temperature-dependent thermal conductivity ($Wm^{-1}K^{-1}$)

k_0 = initial dry/moist thermal conductivity ($Wm^{-1}K^{-1}$)

k_1 = curve fit coefficient ($Wm^{-1}K^{-1}\ ^oC^{-1}$)

Surface emissivity

The surface emissivity determines how much heat is gained or lost from the surrounding environment. It varies with temperature and material physical state. Some composite materials can reflect fire radiation. The surface emissivity of polyester-based GRP can be expressed by:

$$\varepsilon_s(T) = \varepsilon_{so} + \varepsilon_{s1}\left(T_k - T_{\infty k}\right) \tag{4.14}$$

where

$\varepsilon_s(T)$ = temperature-dependent surface emissivity

ε_{so} = initial surface emissivity

ε_{s1} = curve fit coefficient ($^oC^{-1}$)

Specific heat, thermal conductivity and dynamic viscosity of pyrolysis gases

The specific heat, thermal conductivity and dynamic viscosity of the pyrolysis gases are linear functions of temperature [Sullivan, 1993; Sullivan & Salamon, 1992a] given by:

$$c_{pg}(T) = c_{pg_0} + c_{pg_1}\left(T_k - T_{\infty k}\right) \tag{4.15}$$

$$k_g(T) = k_{g_0} + k_{g_1}\left(T_k - T_{\infty k}\right) \tag{4.16}$$

$$\mu_g(T) = \mu_{g_0} + \mu_{g_1}\left(T_k - T_{\infty k}\right) \tag{4.17}$$

where

$c_{pg}(T)$= temperature-dependent gas specific heat($Jkg^{-1}K^{-1}$)

c_{pgo} = initial gas specific heat ($Jkg^{-1}K^{-1}$)

c_{pg1} = curve fit coefficient ($Jkg^{-1}K^{-1}\ ^oC^{-1}$)

$k_g(T)$ = temperature-dependent gas thermal conductivity ($Wm^{-1}K^{-1}$)

k_{go} = initial gas thermal conductivity ($Wm^{-1}K^{-1}$)

k_{g1} = curve fit coefficient ($Wm^{-1}K^{-1}\ ^oC^{-1}$)

$\mu_g(T)$ = temperature-dependent gas dynamic viscosity (Nsm^{-2})

μ_{go} = initial gas dynamic viscosity (Nsm^{-2})

μ_{g1} = curve fit coefficient ($Nsm^{-2}\ ^oC^{-1}$)

4.3.2 Transport Properties

The density of polyester-based GRP is evaluated by Equation 4.1 and its variation by Equation 2.11.

Porosity is defined as the ratio of void volume to total volume of the solid and calculated as a weighted function of the instantaneous mass fraction:

$$\phi = \phi_0 F + \phi_1 (1 - F) \tag{4.18}$$

where

ϕ_0 = initial porosity

ϕ_1 = curve fit coefficient

and F is defined by Equation 4.7.

Permeability is a function of pore system, porosity and the properties of the gas mixture. Since there is no theoretical formulation to give the permeability, it is determined experimentally. This is normally carried out in a pyrolysis experiment by evaluating the pressure gradients at certain points in the material. In the literature there are several models which can be used to relate permeability to the structure of the porous solid [Sullivan, 1993; Sullivan & Salamon, 1992a, Fredlund, 1988]. The permeability used here is obtained from a best fit empirical formula:

$$\gamma = \gamma_0 \exp[\gamma_1 (1 - F)] \tag{4.19}$$

where

γ_0 = initial permeability (m^2)

γ_1 = curve fit coefficient

This was proposed by Fredlund [1988] for wood and is considered as a temporary solution to evaluate the permeability of polyester-based GRP.

4.3.3 Kinetic Properties

The evaluation of the thermal response of GRP requires a description of its kinetic properties at different stages of decomposition process. The resin decomposition is accompanied by cooling and this is a large factor in the fire-resistance properties of laminated GRP. The kinetic properties of GRP are evaluated using thermo gravimetric analysis (TGA). TGA provides a trace of the mass loss as the material is heated at a

constant rate or kept at a constant temperature in an oxidising environment. There are several factors which introduce uncertainty into the results of TGA such as specimen particle size and surface area [Gibson *et al.*, 1996; Friedman, 1965; Perry *et al.*, 1984]. For fire performance, the atmosphere of interest is usually air or nitrogen and the heating rates very rapid. TGA measurements under ideal conditions provide data to fit an Arrhenius type kinetic rate equation which can be used in the finite element modelling.

In contrast to polyester resin, glass fibre does not show any appreciable change in the fire tests apart from a minimal amount of melting and erosion, the structural integrity of GRP being maintained.

The TGA data are normally presented as a plot of mass loss versus temperature for different heating rates and environmental conditions (Figure 4.2). The plot is often presented as a log-log plot [Friedman, 1965]. For a particular rate of heating and environmental conditions, the mass loss versus temperature can then be used to evaluate the final fraction of resin mass, order of reaction, pyrolysis constant and activation energy. According to a recent TGA carried out by Gibson *et al.* [1996] polyester-based GRP shows a very simple thermal behaviour so that the mass loss with temperature can be modelled successfully using a first-order Arrhenius equation (Figure 4.2). It is seen that at above approximately 500°C less than 5% of the polyester mass remains intact.

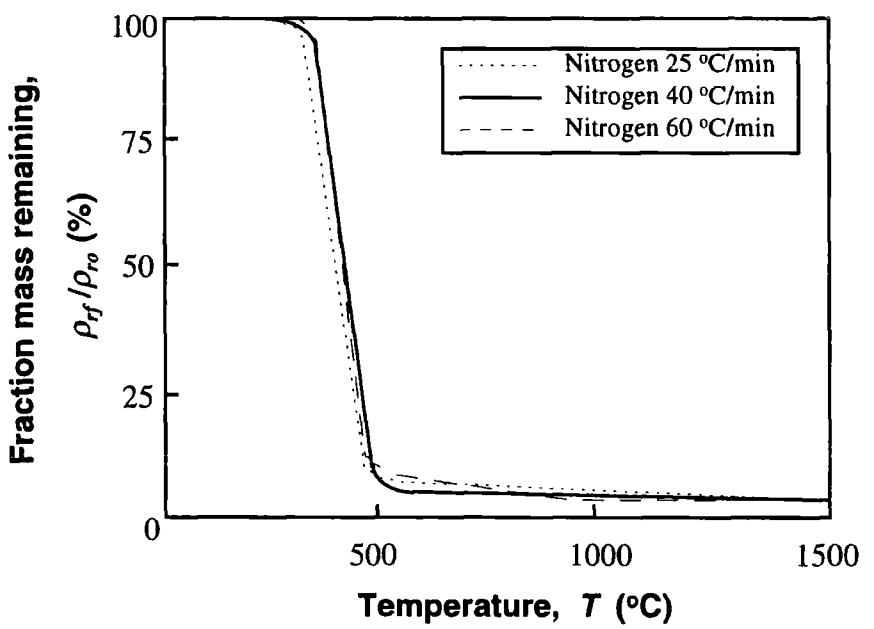

Figure 4.2 TGA results for polyester resin at different heating rates and nitrogen atmosphere [from: Gibson *et al.*, 1996].

4.4 PROPERTIES OF VERMICULUX

A list of thermal and transport properties for Vermiculux is presented in Table 4.5.

Table 4.5 Properties for Vermiculux (calcium silicate).

Initial specific heat, c_{pco} ($Jkg^{-1}K^{-1}$)	840	
Specific heat, c_{pc} ($Jkg^{-1}K^{-1}$)	$840+0.8\theta$	$20\leq\theta<90$
Specific heat, c_{pc} ($Jkg^{-1}K^{-1}$)	$840+c_{pcv}+0.8\theta$	$90\leq\theta<120$
Specific heat, c_{pc} ($Jkg^{-1}K^{-1}$)	$840+0.8\theta$	$120\leq\theta\leq1100$
Initial thermal conductivity, k_{co} ($Wm^{-1}K^{-1}$)	0.13	
Thermal conductivity, k_c ($Wm^{-1}K^{-1}$)	$0.13f(m_{vco})+1.4\times10^{-4}\theta$	$20\leq\theta<90$
Thermal conductivity, k_c ($Wm^{-1}K^{-1}$)	$0.13f(m_{vc})+1.4\times10^{-4}\theta$	$90\leq\theta<120$
Thermal conductivity, k_c ($Wm^{-1}K^{-1}$)	$0.13+1.4\times10^{-4}\theta$	$120\leq\theta\leq1100$
Initial moisture content, m_{vco}	5.5%	$20\leq\theta<90$
Moisture content, m_{vc}	$0.183-1.83\times10^{-3}\theta$	$90\leq\theta\leq120$
Density, ρ_c (kgm^{-3})	460-475	

In Table 4.5, c_{pvc} represents specific heat of moisture evaporation in Vermiculux ($Jkg^{-1}K^{-1}$); $f(m_{vc})$ is the proportion function [Wang, 1995; Jacob, 1949] given by:

$$f(m_{vc}) = 1.0819 + 1.7675\times10^{-1} m_{vc} - 8.7812\times10^{-3} m_{vc}^2 + 1.7617\times10^{-5} m_{vc}^3 \quad (4.20)$$

and m_{vc} denotes temperature-dependent volume of the moisture in Vermiculux given by:

$$m_{vc}(x,t) = m_{vco} + m_{vc1}(T_k - T_{\infty k}) \quad (4.21)$$

where

m_{vc} = volumetric moisture content of Vermiculux

m_{vco} = initial moisture content of Vermiculux

m_{vc1} = curve fit coefficient ($^oC^{-1}$)

Most sandwich constructions contain substantial amount of water, a large percentage into sandwich materials (SM). Conventional sandwich materials are found to absorb more water than GRP laminates under the same environmental conditions making the mechanism of the heat and moisture transfer in sandwich constructions very complicated. Predicting the influence of moisture on the heat flow through the twin-skinned GRP sandwich panels with different percentages of water in the two materials demands a detailed study particularly at the GRP/SM/GRP interfaces.

The specific heat and thermal conductivity of Vermiculux are influenced by moisture evaporation and the variations of temperature.

Specific heat

The effect of moisture evaporation on the specific heat of Vermiculux is simulated by assuming a simple evaporation-condensation mechanism similar to the method used for GRP laminates [Drysdale, 1985]. This approach concentrates on heat transfer and disregards mass transfer and the build-up of internal pressure. The moisture evaporation takes place during a temperature interval ΔT = 30°C (between 90°C and 120°C) with a specific heat given by:

$$c_{pvc} = \frac{f_c h_{fg} m_{wc}}{\Delta T} \tag{4.22}$$

where

c_{pvc} = specific heat of moisture evaporation in Vermiculux ($Jkg^{-1}K^{-1}$)

f_c = correction factor for dehydration (1.33)

h_{fg} = latent heat of evaporation (2.257×10^6 Jkg^{-1})

m_{wc} = mass of moisture content in Vermiculux

and a triangular function of temperature is considered (Figure 4.1).

A simple relationship between specific heat of Vermiculux and temperature is given by a linear function [Wang, 1995] as:

$$c_{pc}(T) = c_{pco} + c_{pc_1}\left(T_k - T_{\infty k}\right) \tag{4.23}$$

where

$c_{pc}(T)$= temperature-dependent specific heat of Vermiculux ($Jkg^{-1}K^{-1}$)

c_{pco} = initial specific heat of Vermiculux ($Jkg^{-1}K^{-1}$)

c_{pc1} = curve fit coefficient ($Jkg^{-1}K^{-1}\,{}^{o}C^{-1}$)

The specific heat of Vermiculux over temperature interval ΔT is given by:

$$c_{pc}(T) = c_{pco} + c_{pvc} + c_{pc1}\left(T_k - T_{\infty k}\right) \quad \text{for} \quad 90 \le T_k - T_{\infty k} \le 120^\circ\text{C} \qquad (4.24)$$

Thermal conductivity

The thermal conductivity of Vermiculux varies with moisture evaporation and temperature variations [Wang, 1995].

The effect of moisture evaporation on the thermal conductivity of Vermiculux is given by:

$$k_{rcm} = k_{rc} f\left(m_{vc}\right) \qquad (4.25)$$

where

k_{rcm} = thermal conductivity of the moist Vermiculux ($Wm^{-1}K^{-1}$)

k_{rc} = thermal conductivity of the dry Vermiculux ($Wm^{-1}K^{-1}$)

and $f(m_{vc})$ is given by Equation 4.20:

The thermal conductivity varies linearly with temperature [Wang, 1995; Hollaway, 1978] given by:

$$k_c(T) = k_{co} + k_{c1}\left(T_k - T_{\infty k}\right) \qquad (4.26)$$

where

$k_c(T)$ = temperature-dependent thermal conductivity of Vermiculux ($Wm^{-1}K^{-1}$)

k_{co} = initial dry/moist thermal conductivity of Vermiculux ($Wm^{-1}K^{-1}$)

k_{c1} = curve fit coefficient ($Wm^{-1}K^{-1}\,{}^{o}C^{-1}$)

4.5 SUMMARY

For the study of GRP panels, pipes and joins, polyester-based GRP, consisting of polyester resin and woven roving glass fibres, and Vermiculux (calcium silicate) sandwich material were selected. A complete set of material properties obtained from a number of sources was presented with some information on pyrolysis gases. The effect of temperature and moisture gradients on the material properties was also investigated in detail. These materials will be used for any analysis throughout this thesis.

CHAPTER V

A ONE-DIMENSIONAL FINITE ELEMENT MODEL FOR THE THERMAL RESPONSE OF GLASS REINFORCED PLASTIC PANELS

5.1 INTRODUCTION

This chapter involves modelling the thermal response of a thick single-skinned polyester-based glass reinforced plastic (GRP) panel subject to fire from one side. A one-dimensional mathematical model and the appropriate finite element solution were developed in Chapter 2. Various boundary conditions were introduced in Chapter 3 and the material properties of polyester-based GRP presented in Chapter 4. The information in these chapters are now used to further develop the one-dimensional mathematical and numerical models and to study how different terms and boundary conditions may affect on the temperature distributions within the material.

In the development of the mathematical model, we consider four stages (referred to as Models 1, 2, 3 and 4):

1. An infinite vertical panel with finite thickness L exposed to fire on one side is considered (Figure 1.6a). The progressive heating results in three main zones: (i) Char and gas, (ii) Pyrolysis and (iii) Virgin material. The resin material is assumed to burn away completely at the end of pyrolysis. The fire exposed (hot) surface boundary condition is simulated by an empirical formula and the unexposed (cold) surface is assumed to be insulated. The thermal properties are assumed constant throughout fire exposure except for thermal conductivity which is assumed to have a step change at the end of pyrolysis.

2. This model extends Model 1 by including: (i) Heat energy (radiation and convection) exchange with the environment at the cold surface and (ii) Different inclinations of the panel, i.e. vertical, horizontal and inclined.
3. Like Model 1, this model assumes a vertical panel but includes: (i) Variable thermal properties, i.e. they vary with temperature and moisture gradients and (ii) A fraction of the resin remaining at the end of pyrolysis affecting the mass loss.
4. This model extends Model 3 by applying a theoretical formulation for the simulation of boundary conditions at the hot surface. This includes heat fluxes due to: (i) Radiation, (ii) Convection, (iii) Outward movement of pyrolysis gases and (iv) Surface chemical reactions.

At each stage, new terms are introduced and added to the mathematical and numerical models. A 1.09cm single-skinned polyester-based GRP panel is studied. The results of each successive stage are compared and discussed. The numerical results are also compared with some experimental data where available.

5.2 MATHEMATICAL MODEL

MODEL 1

This is a simplified version [Looyeh *et al.*, 1997] of the mathematical model introduced in Chapter 2 and is considered as the initial simulation. Further simplifying assumptions are:

1. The specific heats of GRP and pyrolysis gases are constant throughout the fire exposure; whereas the thermal conductivity experiences a step change at the end of pyrolysis.
2. Resin material burns away completely at the end of pyrolysis.
3. The temperature of the hot surface boundary is evaluated using a time-dependent empirical formula.
4. The cold surface boundary is insulated, i.e. an adiabatic boundary condition is adopted.

Figure 5.1 shows the geometry of the one-dimensional mathematical model for the single-skinned polyester-based GRP panel subject to fire from one side.

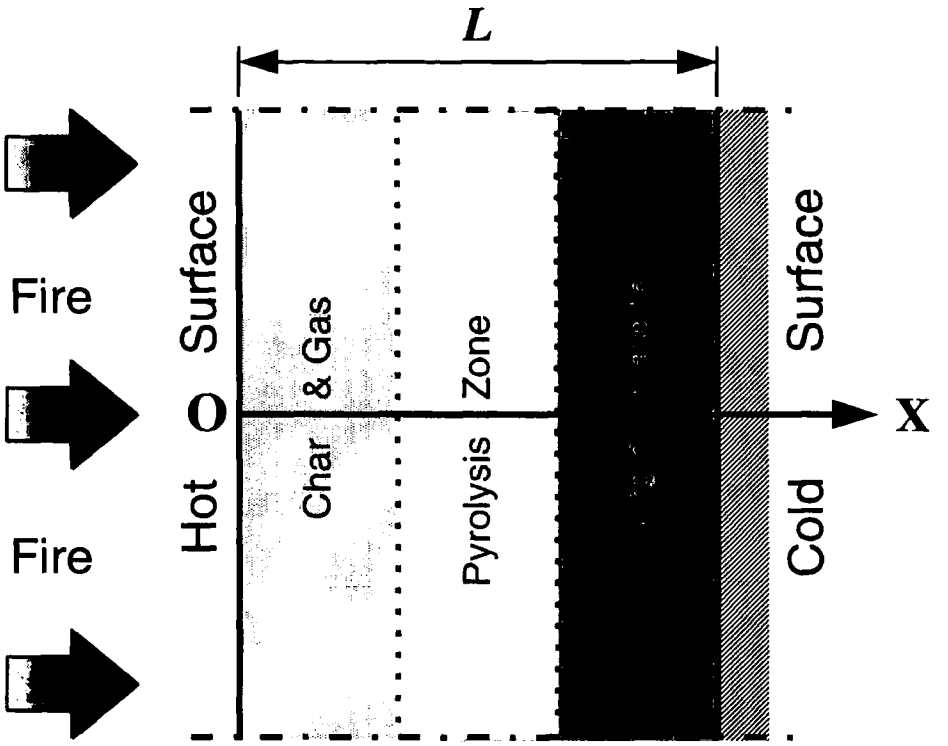

Figure 5.1 The geometry of the one-dimensional mathematical model defined in Model 1. The thick GRP panel is subject to fire on one side and insulated on the other. The "main zones" during decomposition are: (i) char and gas where most of the resin material has burnt away; (ii) pyrolysis in which there is resin decomposition and (iii) virgin material which represents that part of the material remained unchanged.

Use the first and second assumption into Equations 2.10 and 2.11, these equations become:

$$\rho c_p \frac{\partial T}{\partial t} = k\frac{\partial^2 T}{\partial x^2} - \dot{m}_g c_{pg}\frac{\partial T}{\partial x} - \frac{\partial \rho_r}{\partial t}\left(Q + h - h_g\right) \tag{5.1}$$

$$\frac{\partial \rho_r}{\partial t} = -A\rho_r \exp\left(\frac{-E_A}{RT_k}\right) \tag{5.2}$$

where

$$\dot{m}_g = \int_L^{\hat{x}} \frac{\partial \rho_r}{\partial t} dx \qquad \text{for} \qquad 0 \le \hat{x} \le L \tag{5.3}$$

$$h = c_p\left(T - T_\infty\right) \tag{5.4}$$

$$h_g = c_{pg}\left(T - T_\infty\right) \tag{5.5}$$

and ρ = density of GRP(kgm^{-3})

c_p = specific heat of GRP ($Jkg^{-1}K^{-1}$)

T = temperature (°C)

t = time (s)

k = thermal conductivity of GRP ($Wm^{-1}K^{-1}$)

x = spatial co-ordinate starting at the hot surface (m)

$\dot{m}_g$ = gas mass flux ($kgm^{-2}s^{-1}$)

c_{pg} = gas specific heat ($Jkg^{-1}K^{-1}$)

ρ_r = density of resin (active) material (kgm^{-3})

Q = heat of decomposition (Jkg^{-1})

h = enthalpy of GRP (Jkg^{-1})

h_g = enthalpy of gas (Jkg^{-1})

A = pyrolysis constant (s^{-1})

E_A = activation energy ($kJkmole^{-1}$)

R = gas constant (8.314 $kJkmole^{-1}K^{-1}$)

T_k = temperature (K)

L = thickness (m)

T_∞ = ambient temperature (20°C)

Equations 5.1 to 5.5 must be solved simultaneously for T, ρ_r and $\dot{m}_g$ once the initial conditions and appropriate boundary conditions have been defined.

The initial conditions are given by:

$$\begin{matrix} T(x,t) = T_\infty & \rho = \rho_o \\ \dot{m}_g = 0 & k = k_o \end{matrix} \quad \text{for} \quad \begin{matrix} 0 \le x \le L \\ t = 0 \end{matrix} \tag{5.6}$$

and the hot and cold surface boundary conditions by:

$$T(x,t) = T_s(t) \qquad \text{for} \qquad x = 0,\ t > 0 \tag{5.7}$$

$$\frac{\partial T}{\partial x} = 0\ ,\ \dot{m}_g = 0 \qquad \text{for} \qquad x = L,\ t > 0 \tag{5.8}$$

where subscript o denotes initial and $T_s(t)$ is the time-dependent hot surface temperature introduced in Chapter 3 by an empirical relation [Wu *et al.*, 1994], i.e.:

$$T_s(t) = (T_g - 100)\left\{1 - \exp\left\{-\exp\left[0.71\log\left(\frac{t}{124.8}\right)\right]\right\}\right\} + T_\infty \quad \text{for} \quad t > 0 \tag{5.9}$$

where T_g is the maximum fire temperature (1100°C).

It should be noted that the density, specific heat and thermal conductivity of polyester-based GRP are evaluated using the "rule of mixtures" as explained in Chapter 4.

MODEL 2

The mathematical model defined in Model 1, i.e. Equations 5.1 to 5.6, are used together with various boundary conditions introduced in Chapter 3 to study the effect different boundary conditions on the thermal response of the single-skinned polyester-based GRP panel of thickness 1.09cm.

MODEL 3

Polymer composites are sensitive to variations of material properties as well as decomposition due to the rate of energy consumption and the rate of thermal, transport and kinetic properties being functions of the constituent materials and the rate of decomposition. To predict the thermal response of polymer composites accurately it is important to have knowledge of variations in the material properties which are temperature dependent and affected by moisture gradients [Looyeh & Bettess, 1998a]. The differences in the thermal response of different polymer composites are mainly due to surface properties and low conductivities. For GRP, the rate of decomposition is the major factor which determines their fire resistance capabilities. This is true when accurate values of thermal, transport and kinetic properties are used.

Some of the simplifying assumptions made in Models 1 and 2 are no longer applied here. We assume:

1. The thermal properties of polyester-based GRP and pyrolysis gases are functions of temperature and moisture content.
2. The resin does not burn away completely. A fraction of resin remains intact at the end pyrolysis.
3. The temperature of the hot surface is evaluated using a time-dependent empirical formula.
4. The cold surface boundary is in radiative and convective heat exchange with the surrounding environment.

In the development of the mathematical model, Equations 5.1 and 5.3 to 5.5 are valid for the current case with the exception that the thermal properties vary with temperature and moisture gradients and must be evaluated explicitly using Equations 3.6, 3.8 to 3.15.

A recent thermo gravimetric analysis (TGA) revealed that a fraction of resin, i.e. ρ_{rf}/ρ_r, remains intact at the end of pyrolysis. The rate of decomposition is therefore given by Equation 2.11 to take account of the final fraction of the resin mass, i.e.:

$$\frac{\partial \rho_r}{\partial t} = -A\left(\rho_r - \rho_{rf}\right)\exp\left(\frac{-E_A}{RT_k}\right) \tag{5.10}$$

where ρ_{rf} is the final density of resin (kgm^{-3}).

The initial conditions are given by:

$$\begin{array}{lll} T(x,t) = T_\infty & m_v(x,t) = m_{vo} & \\ \dot{m}_g = 0 & \rho = \rho_o & \text{for} \quad 0 \le x \le L \\ c_p = c_{po} & k = k_o & \text{for} \quad t = 0 \\ c_{pg} = c_{pgo} & \varepsilon = \varepsilon_o & \end{array} \tag{5.11}$$

where ε is surface emissivity.

The boundary condition at the hot surface (referred to as boundary 1) is given by:

$$T(x,t) = T_s(t) \qquad \text{for} \qquad x = 0,\ t > 0 \tag{5.12}$$

and at the cold surface (referred to as boundary 2) by:

$$-k\frac{\partial T}{\partial x} = q_{r2} + q_{c2}\ ,\ \dot{m}_g = 0 \qquad \text{for} \qquad x = L,\ t > 0 \tag{5.13}$$

where $T_s(t)$ is given by Equation 5.9 and q_{r2} and q_{c2} by Equations 3.12 and 3.14, i.e.:

$$q_{r2} = h_{r2}\left(T - T_\infty\right) \tag{5.14}$$

$$q_{c2} = h_{c2}\left(T - T_\infty\right) \tag{5.15}$$

h_{r2} and h_{c2} are the equivalent convection coefficient ($Wm^{-2}K^{-1}$) and the convection coefficient ($Wm^{-2}K^{-1}$) expressed by Equations 3.13 and 3.15, i.e.:

$$h_{r2} = \sigma\varepsilon\left(T_k^2 + T_{\infty k}^2\right)\left(T_k + T_{\infty k}\right) \tag{5.16}$$

$$h_{c2} = k_{e\infty}\frac{\overline{\mathrm{Nu}}_H}{H} \tag{5.17}$$

where

σ = Stefan-Boltzmann constant ($5.669\times10^{-8}\ Wm^{-2}K^{-4}$)

T_k = cold surface temperature (K)

$T_{\infty k}$ = ambient temperature (293K)

$k_{e\infty}$ = thermal conductivity of air at ambient temperature ($Wm^{-1}K^{-1}$)

$\overline{Nu}_H$ = average Nusselt number (given by Equation 3.16 for vertical panels)

H = height of panel (m)

MODEL 4

The behaviour of GRP subject to fire was described in detail in Chapter 1. At the intermediate stages when the material has been exposed to fire for some time, the accumulated pyrolysis gases tend to flow back through the porous charring layer, adjacent to hot surface boundary, and escape from the hot surface where further chemical reactions may occur (Figure 5.2).

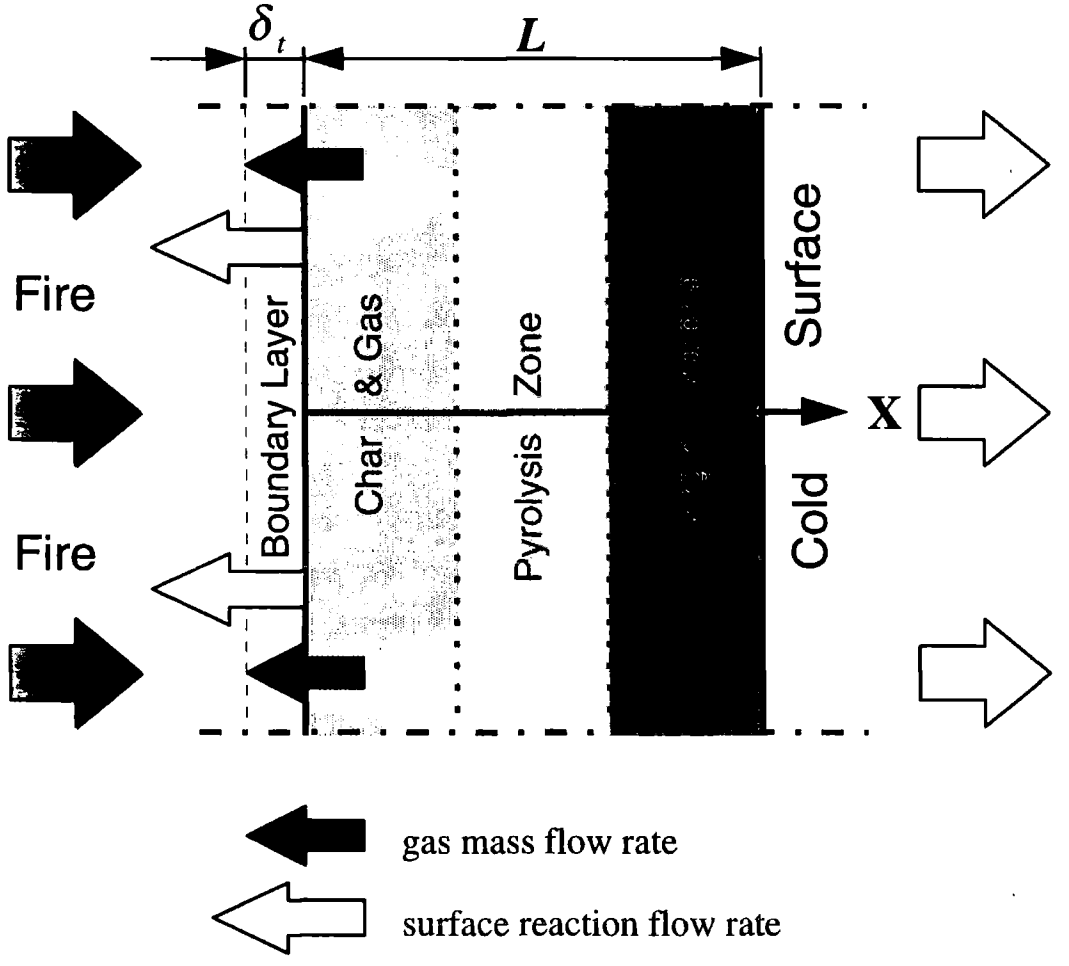

Figure 5.2. The geometry of the one-dimensional mathematical model defined in Model 4. The panel is subject to fire on one side. The heat exchanges at the hot surface (boundary 1) are due to (i) radiation; (ii) convection, (iii) outward movement of the pyrolysis gases at the thermal boundary layer and (iv) surface chemical reactions. At the cold surface (boundary 2) radiative and convective heat energy are exchanged with the surrounding environment.

The definition of the hot surface boundary condition is not limited to radiative and convective heat exchange with fire and further terms are evidently involved due to surface phenomena [Looyeh & Bettess, 1998b]. The effects of surface chemical reactions and gas mass movement on the boundary condition of the hot surface are investigated here for the first time.

For Model 4, the time-dependent empirical relation, i.e. Equation 5.9, is no longer used. Instead, a theoretical formulation is introduced based for the phenomena of heat and mass transfer at the hot surface boundary of the material. This includes the effects of: (i) radiation; (ii) convection; (iii) outward movement of the pyrolysis gases and (iv) surface chemical reactions. This results in two additional terms. In Chapter 3 we developed the first two terms, i.e. heat fluxes due to radiation and convection, for the hot surface boundary. The two new terms, i.e. heat fluxes due to gas mass movement and surface chemical reactions are derived in this Model.

The mathematical model is similar to that for Model 3 except for the definition of the hot surface boundary condition. This includes Equations 5.1, 5.3 to 5.5 and 5.10 along with the new definition of the initial and boundary conditions. The thermal properties are assumed to vary with temperature and moisture gradients as explained in Model 3.

The initial conditions are given by:

$$\begin{array}{ll} T(x,t) = T_\infty & m_v(x,t) = m_{vo} \\ \dot{m}_g = 0 & \rho = \rho_o \\ c_p = c_{po} & k = k_o \\ c_{pg} = c_{pgo} & \varepsilon_s = \varepsilon_{so} \\ \rho_g = 0 & \varepsilon_e = \varepsilon_{eo} \\ k_g = k_{go} & \phi = \phi_o \end{array} \quad \text{for} \quad \begin{array}{c} 0 \le x \le L \\ t = 0 \end{array} \tag{5.18}$$

where

ρ_g = density of pyrolysis gases (kgm^{-3})

ε_{ef} = fire emissivity (0.8)

k_g = thermal conductivity of pyrolysis gases ($Wm^{-1}K^{-1}$)

ϕ = porosity

The boundary condition at the hot surface (referred to as boundary 1) is given by:

$$\begin{array}{l} -k\dfrac{\partial T}{\partial x} = -q_{r1} - q_{c1} + q_{mf1} + q_{sr1} \\ P(x,t) = P_\infty \end{array} \quad \text{for} \quad x = 0,\ t > 0 \tag{5.19}$$

where

q_{r1} = radiation heat flux from fire (Wm^{-2})

q_{c1} = convection heat flux at hot surface boundary (Wm^{-2})

q_{mf1} = heat flux due to gas mass movement at hot surface boundary (Wm^{-2})

q_{sr1} = heat flux due to surface chemical reactions (Wm^{-2})

P = pressure (Pa)

P_∞ = ambient pressure (0.1 MPa)

and the boundary condition at the cold surface (referred to as boundary 2) is defined in the same manner as given by Equation 5.13.

The heat flux terms of the hot surface boundary condition, i.e. q_{r1}, q_{c1}, q_{mf1} and q_{sr1}, are derived below.

(i) Heat flux due to radiation

q_{r1} is given by Equation 3.6, i.e.:

$$q_{r1} = h_{r1}\left(T_r - T_s\right) \tag{5.20}$$

where

T_r = radiative temperature (°C)

T_s = hot surface temperature (°C)

h_{r1} is the equivalent convection coefficient ($Wm^{-2}K^{-1}$) expressed by Equations 3.7, i.e.:

$$h_{r1} = \sigma\varepsilon_s\left(T_{rk}^2 + T_{sk}^2\right)\left(T_{rk} + T_{sk}\right) \tag{5.21}$$

where T_{rk} is the radiative temperature (K) calculated by:

$$T_{rk} = T_{fk}\sqrt[4]{\varepsilon_{ef}} \tag{5.22}$$

T_{sk} = hot surface temperature (K)

and T_{fk} is the time-dependent fire temperature (K) [ISO 834, 1975] given by Equation 3.5, i.e.:

$$T_{fk} = T_g\left[1 - 0.345\exp(-0.167t) - 0.204\exp(-1.417t) - 0.471\exp(-15.833t)\right] + 273 \tag{5.23}$$

(ii) Heat flux due to convection

q_{c1} is given by Equation 3.8, i.e.:

$$q_{c1} = h_{c1}\left(T_f - T_s\right) \tag{5.24}$$

where T_f is the time-dependent fire temperature (°C).

h_{c1} is the convection coefficient ($Wm^{-2}K^{-1}$) expressed by Equation 3.9, i.e.:

$$h_{c1} = k_{ef} \frac{\overline{Nu}_H}{H} \tag{5.25}$$

and k_{ef} is the thermal conductivity of air at furnace temperature ($Wm^{-1}K^{-1}$).

(iii) Heat flux due to outward movement of the pyrolysis gases

The pyrolysis gases given off at the thermal boundary layer adjacent to the hot surface boundary influence the convective boundary condition. Owing to this effect, the temperature gradients across this boundary will no longer be linear [Fredlund, 1988].

In forced convection configurations, the mass conservation and momentum equations are sufficient for determining the variation of the fluid velocity at the thermal boundary layer. In such cases the variation of fluid temperature can be determined using the principle of energy conservation. In free convection, the variations of fluid velocity and temperature must be determined simultaneously using the mass conservation principle, the momentum equations and the equation for energy conservation.

For a panel subject to fire, the free convection around the hot surface boundary is influenced by a forced convection caused by the gas mass movement adjacent to the surface. Thus, there is a combination of free and forced convection. The derivation of the differential equation for mixed free and forced convection at every point in the fluid and thermal boundary layer is given for simple cases by Bejan [1993], Holman [1997] and Fredlund [1988]. To obtain the variation of fluid temperature in the thermal boundary layer, the problem may be simplified to the study of the effect of the gas mass movement on the convective coefficient of the free convection heat transfer.

The general expression for the energy equation [Holman, 1997; Bejan, 1993] is given, in (x,y) co-ordinate system, by:

$$\alpha \frac{\partial^2 T}{\partial x^2} = u \frac{\partial T}{\partial x} + v \frac{\partial T}{\partial y} \tag{5.26}$$

where

α = thermal diffusivity (m^2s^{-1})

u = velocity in x direction (ms^{-1})

v = velocity in y direction (ms^{-1})

Referring to Figure 5.3, we now make the following simplifying assumptions:

1. The fluid is incompressible with laminar flow.
2. Heat flow is negligible in y direction.
3. The velocity of the pyrolysis gases is small, i.e. the energy equation for the free convection is the same as that for forced convection.
4. The thermal conductivity, specific heat and viscosity of the pyrolysis gases are constant.

By assuming the heat flow is one-dimensional (assumption 2), i.e. pyrolysis gases flow only along the direction of fire, Equation 5.26, in $(-x,y)$ co-ordinate system, simplifies to:

$$\alpha_g \frac{\partial^2 T}{\partial x^2} = -u_g \frac{\partial T}{\partial x} \tag{5.27}$$

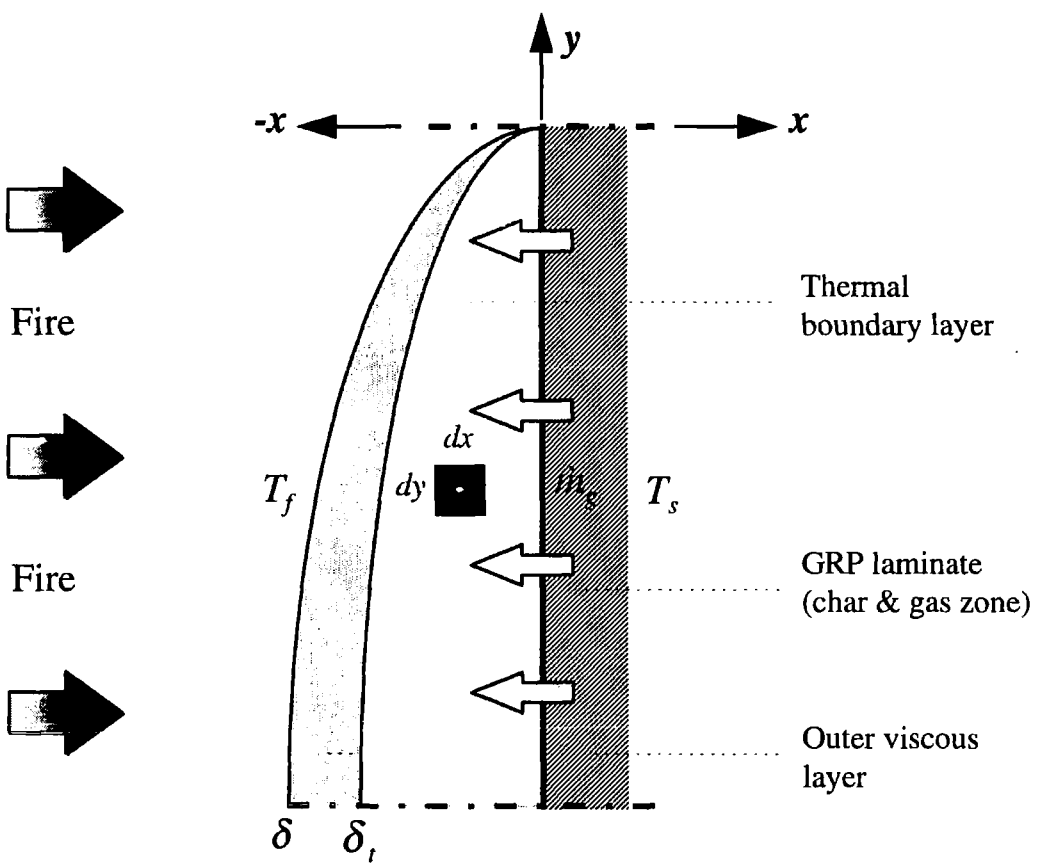

Figure 5.3 The structure of the thermal and velocity boundary layers adjacent to the hot surface boundary of a vertical GRP panel subject to fire.

or, in (x,y) co-ordinate system, becomes:

$$\alpha_g \frac{\partial^2 T}{\partial x^2} + u_g \frac{\partial T}{\partial x} = 0 \tag{5.28}$$

where

α_g = thermal diffusivity of the pyrolysis gases (m^2s^{-1})

u_g = velocity of the pyrolysis gases in x direction (ms^{-1})

The thermal diffusivity and velocity of the pyrolysis gases are given by:

$$\alpha_g = \frac{k_g}{\rho_g c_{pg}} \tag{5.29}$$

$$u_g = \frac{\dot{m}_g}{\rho_g} \tag{5.30}$$

where

k_g = thermal conductivity of the pyrolysis gases ($Wm^{-1}K^{-1}$)

ρ_g = density of pyrolysis gases (kgm^{-3})

c_{pg} = specific heat of pyrolysis gases ($Jkg^{-1}K^{-1}$)

$\dot{m}_g$ = mass flux of pyrolysis gases ($kgm^{-2}s^{-1}$)

Applying Equations 5.29 and 5.30 into Equation 5.28, the energy equation can be written as:

$$k_g \frac{\partial^2 T}{\partial x^2} + \dot{m}_g c_{pg} \frac{\partial T}{\partial x} = o \tag{5.31}$$

For the thermal boundary layer of thickness δ_t (Figure 5.4), a solution to this second-order partial differential equation is given by:

$$T(x,t) = T_s + \frac{T_f - T_s}{\left[\exp\left(\frac{\dot{m}_g c_{pg} \delta_t}{k_g}\right) - 1\right]}\left[\exp\left(\frac{\dot{m}_g c_{pg}}{k_g} x\right) - 1\right] \tag{5.32}$$

where

T_s = hot surface temperature (°C)

T_f = time-dependent fire temperature (°C)

If the thickness of the thermal boundary layer is approximated by $\delta_t = k_g/h_{c1}$ [Fredlund, 1988], the temperature gradients across the thermal boundary layer can be calculated by differentiating Equation 5.32 with respect to x and replacing $x = 0$, i.e.:

$$\left.\frac{\partial T}{\partial x}\right|_{x=0} = \frac{\dot{m}_g c_{pg}}{h_{c1}}\left[\frac{1}{\exp\left(\dot{m}_g c_{pg}/h_{c1}\right)-1}\right]\frac{\left(T_f - T_s\right)}{\delta_t} \tag{5.33}$$

The last term of the right hand side, i.e. $(T_f - T_s)/\delta_t$, represents the linear variation of temperature at the hot surface boundary due to convection only (Curve 1 of Figure 5.4), i.e. when:

$$\left.\frac{\partial T}{\partial x}\right|_{x=0} = \frac{\left(T_f - T_s\right)}{\delta_t} \tag{5.34}$$

To include the convective effect of the gas mass movement, the following non-linear coefficient, known as blowing factor, is required:

$$h_b = \frac{\dot{m}_g c_{pg}}{h_{c1}}\left[\frac{1}{\exp\left(\dot{m}_g c_{pg}/h_{c1}\right)-1}\right] \tag{5.35}$$

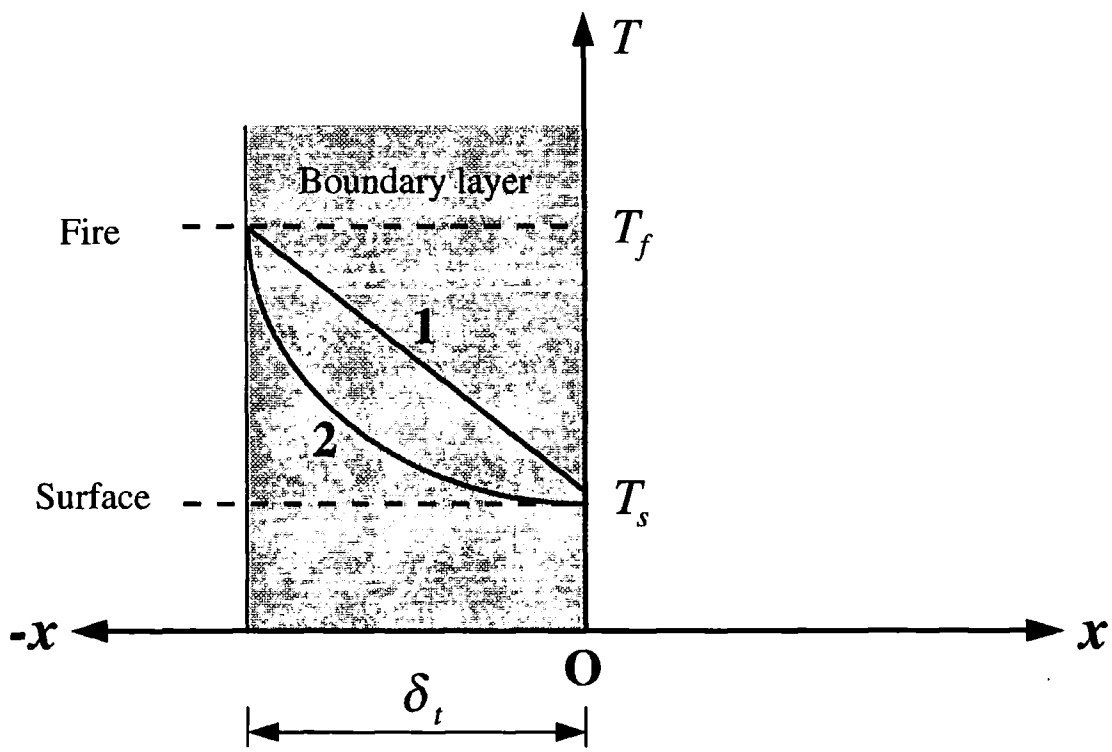

Figure 5.4 Variation of temperature across the thermal boundary layer adjacent to the hot surface. Curve 1 indicates linear variation of temperature due to convection and Curve 2 shows non-linear variation of temperature due to additional heat flux from the outward movement of pyrolysis gases.

Substitute Equation 5.35 into Equation 5.33 and replace δ_t with k_g/h_{c1}, Equation 5.33 becomes (Curve 2 of Figure 5.4):

$$-k_g \left.\frac{\partial T}{\partial x}\right|_{x=0} = -h_b h_{c1}\left(T_f - T_s\right) \tag{5.36}$$

where the left hand term equals to the summation of the heat fluxes due to convection and gas mass movement at the hot surface. The total convective heat transfer results in:

$$-q_{c1} + q_{mf1} = -h_b h_{c1}\left(T_f - T_s\right) \tag{5.37}$$

Using Equation 5.24 into Equation 5.37, the heat flux due to the outward movement of the pyrolysis gases is then given by:

$$q_{mf1} = h_{c1}\left(1 - h_b\right)\left(T_f - T_s\right) \tag{5.38}$$

(iv) Heat flux due to surface chemical reactions

During the charring process which occurs when the fire exposed surface reaches a sufficiently high temperature, the resin matrix chain breaks down and decomposes into water vapour, pyrolysis gases, solid carbon and glass residues. At the beginning of decomposition, when the reaction is relatively slow, pyrolysis gases can diffuse into the interior of the porous material faster than they can be consumed by the chemical reactions at the surface. As the temperature rises, the rate of decomposition exceeds the rate of diffusion and a part of the pyrolysis gases begin to flow in the opposite direction reacting with oxygen at the fire exposed surface. At higher temperatures, the reaction retreats to the surface of the material with no significant penetration of pyrolysis gases into the interior of the material. At this stage the carbon residue reacts with silica (presents in the residual glass fibres) [Henderson *et al.*, 1985; Fredlund, 1988; Sullivan, 1993; Sullivan & Salamon, 1992a; Florio *et al.*, 1991].

The heat flux due to the chemical reactions at the hot surface boundary of the material, i.e. q_{sr1}, affects the total radiation gained by the surface. This effect is introduced by Fredlund [1988] and represented as:

$$q_{sr1} = \rho_s V_s \Delta h_s \tag{5.39}$$

where

ρ_s = density of the material at the hot surface (kgm^{-3})

V_s = rate of modification due to chemical reactions (ms^{-1})

Δh_s = change of enthalpy at the hot surface (Jkg^{-1})

The actual processes involved in the surface chemical reactions are complicated and depend on the temperature and the concentration of oxygen at the surface. Although a complete model must deal with both diffusion and kinetic rate equations [Fredlund, 1988; Munson & Spindler, 1961], a simplified model can be considered to conform to an kinetic rate Arrhenius relationship only at both low and high temperatures and any level of oxygen concentrations. According to this simplified model, ρ_s, V_s and Δh_s can be evaluated by:

$$\rho_s = \rho_g \phi + \rho(1-\phi) \tag{5.40}$$

$$V_s = T_{sk} A_s \exp\left(-\frac{E_{As}}{RT_{sk}}\right) \tag{5.41}$$

$$\Delta h_s = Q_s + h_s - h_g \tag{5.42}$$

where

ρ_g = density of pyrolysis gases (kgm^{-3})

ϕ = porosity

ρ = density of GRP (kgm^{-3})

T_{sk} = hot surface temperature (K)

A_s = rate constant ($s^{-1}K^{-1}$)

E_{As} = activation energy due to surface chemical reactions ($kJkmole^{-1}$)

R = gas constant (8.314 $kJkmole^{-1}K^{-1}$)

Q_s = heat of decomposition due to surface chemical reactions (Jkg^{-1})

h_s = enthalpy of the material at the hot surface (Jkg^{-1})

h_g = enthalpy of the pyrolysis gases (Jkg^{-1})

h_s and h_g are evaluated using Equation 5.4 and 5.5, the gas density by the ideal gas equation:

$$\rho_g = \frac{PM_g \phi}{RT_{sk}} \tag{5.43}$$

and the porosity of the material by Equation 4.18, i.e.:

$$\phi = \phi_0 F + \phi_1 (1-F) \tag{5.44}$$

where

P = pressure (Pa)

M_g = gas molecular weight ($kgkmole^{-1}$)

ϕ_0 = initial porosity

ϕ_1 = curve fit coefficient

and F is the instantaneous mass fraction given by Equation 4.7, i.e.:

$$F = \frac{\rho_r - \rho_{rf}}{\rho_{ro} - \rho_{rf}} \tag{5.45}$$

The kinetic constants for the surface chemical reactions are evaluated experimentally as explained in Chapter 4.

5.3 FINITE ELEMENT FORMULATION

In this section we develop finite element solutions to the sets of governing differential equations defined for the Models 1 to 4 using the Bubnov-Galerkin (weighted residual) approach. The complete description of the finite element formulation was given in Chapter 2. All terms and coefficients are evaluated explicitly using an iterative-updating procedure at each step of computations. Nodal temperatures are computed implicitly using the Crank-Nicolson solution.

5.3.1 Explicit Evaluations of Terms and Coefficients

For all cases, the terms and coefficients are evaluated explicitly using an iterative-updating procedure at each step of computations. A general notation $(\,)_j^i$ is used where i represents the time interval and j the spatial position. Time derivative terms are given by forward difference and the spatial variables by central difference, with exception of the gas mass flux term which is represented by backward difference.

MODELS 1 & 2

From Equations 5.2 and 5.3, the mass loss rate $\partial\rho_r/\partial t$ and gas mass flux $\dot{m}_g$ are represented by:

$$\left(\frac{\partial \rho_r}{\partial t}\right)_j^{i+1} = \frac{(\rho_r)_j^{i+1} - (\rho_r)_j^i}{\Delta t} \tag{5.46}$$

$$\left(\dot{m}_g\right)_j^{i+1} = \sum_{j=n_x}^{n_T}\left[\frac{(\rho_r)_j^{i+1} - (\rho_r)_j^i}{\Delta t}\right] l_j \tag{5.47}$$

where
$$\frac{(\rho_r)_j^{i+1} - (\rho_r)_j^i}{\Delta t} = -A(\rho_r)_j^i \exp\left[\frac{-E_A}{R(T_k)_j^i}\right] \tag{5.48}$$

and Δt = time step size (s)

l = element length (m)

n_x = number of mesh seeds at location x

n_T = total number of mesh seeds in x direction

Rearrange 5.48 for ρ_r at time interval i+1 and position j and use the rule of mixtures for density, i.e. Equation 4.1, the density of GRP becomes:

$$\rho_j^{i+1} = (\rho_r)_j^i \left\{1 - A\Delta t \exp\left[\frac{-E_A}{R(T_k)_j^i}\right]\right\}\left(1 - V_f\right) + \rho_{fr} V_f \tag{5.49}$$

Using Equation 5.4, 5.5, 5.46, 5.47 and 5.49, Equation 5.1 at each time interval and nodal position can be given by:

$$\rho_j^{i+1} c_p \frac{\partial T}{\partial t} = k\frac{\partial^2 T}{\partial x^2} - \left(\dot{m}_g\right)_j^{i+1} c_{pg} \frac{\partial T}{\partial x} - \left(\frac{\partial \rho_r}{\partial t}\right)_j^{i+1}\left[Q + \left(c_p - c_{pg}\right)(T - T_\infty)\right] \tag{5.50}$$

where T_∞ is the ambient temperature (20°C).

MODELS 3 & 4

Equations 5.46 and 5.47 are valid for Models 3 and 4 when:

$$\frac{(\rho_r)_j^{i+1} - (\rho_r)_j^i}{\Delta t} = -A\left[(\rho_r)_j^i - \rho_{rf}\right]\exp\left[\frac{-E_A}{R(T_k)_j^i}\right] \tag{5.51}$$

where ρ_{rf} is the final density of resin (kgm^{-3}).

Rearranging 5.48 for ρ_r at time interval i+1 and position j and using the rule of mixtures for density gives:

$$\rho_j^{i+1} = \left\{(\rho_r)_j^i - A\Delta t\left[(\rho_r)_j^i - \rho_{rf}\right]\exp\left(\frac{-E_A}{R(T_k)_j^i}\right)\right\}\left(1 - V_f\right) + \rho_{fr} V_f \tag{5.52}$$

For the present cases, the thermal properties vary with temperature and moisture gradients and must be evaluated at each step of computations. Equation 5.1 at each time interval and nodal position becomes:

$$\rho_j^{i+1}\left(c_p\right)_j^{i+1}\frac{\partial T}{\partial t}=(k)_j^{i+1}\frac{\partial^2 T}{\partial x^2}-\left(\dot{m}_g\right)_j^{i+1}\left(c_{pg}\right)_j^{i+1}\frac{\partial T}{\partial x}$$

$$-\left(\frac{\partial \rho_r}{\partial t}\right)_j^{i+1}\left\{Q+\left[\left(c_p\right)_j^{i+1}-\left(c_{pg}\right)_j^{i+1}\right]\left(T-T_\infty\right)\right\} \qquad (5.53)$$

Expressions for the thermal conductivity and specific heat of GRP and specific heat of pyrolysis gases at each time and spatial position are given in Tables 4.3 and 4.4.

5.3.2 Finite Element Equations

Using the Bubnov-Galerkin (weighted residual) approach described in Chapter 2, the finite element equations can be given in the form:

$$\mathbf{C}\dot{\mathbf{T}}+\mathbf{K}\mathbf{T}+\mathbf{f}=\mathbf{0} \qquad (5.54)$$

where

$\mathbf{C}$	=	element capacitance matrix
$\dot{\mathbf{T}}$	=	vector of temperature derivatives with respect to time
$\mathbf{K}$	=	element conductance matrix
$\mathbf{T}$	=	temperature vector
$\mathbf{f}$	=	element heat load vector

The element equation for each model is evaluated in a similar way to that explained in Chapter 2.

MODEL 1

$$\left(\int_0^l \mathbf{N}^{\mathrm{T}}\rho_j^{i+1}c_p\mathbf{N}dx\right)\dot{\mathbf{T}}+\left[\int_0^l \mathbf{B}^{\mathrm{T}}k\mathbf{B}dx+\int_0^l \mathbf{B}^{\mathrm{T}}\left(\dot{m}_g\right)_j^{i+1}c_{pg}\mathbf{N}dx\right.$$

$$\left.+\int_0^l \mathbf{N}^{\mathrm{T}}\left(\frac{\partial \rho_r}{\partial t}\right)_j^{i+1}\left(c_p-c_{pg}\right)\mathbf{N}dx\right]\mathbf{T}+\int_0^l\left(\frac{\partial \rho_r}{\partial t}\right)_j^{i+1}\left[Q-\left(c_p-c_{pg}\right)T_\infty\right]\mathbf{N}^{\mathrm{T}}dx-\begin{bmatrix}-k\dfrac{\partial T}{\partial x}(0)\\ 0\end{bmatrix}=\mathbf{0}$$

or

$$\mathbf{C}\dot{\mathbf{T}}+\left(\mathbf{K}_o+\mathbf{K}_g+\mathbf{K}_d\right)\mathbf{T}+\left(\mathbf{f}_o+\mathbf{f}_b\right)=\mathbf{0} \qquad (5.55)$$

where superscript **T** denotes the transpose quantity and

$\mathbf{N}$ = shape function matrix

$\mathbf{B}$ = shape function derivative matrix

$\mathbf{K_o}$ = element conductance matrix

$\mathbf{K_g}$ = element gas diffusion matrix

$\mathbf{K_d}$ = element decomposition matrix

$\mathbf{f_o}$ = element decomposition vector

$\mathbf{f_b}$ = element boundary conditions vector

N and **B** are given by Equations 2.18a and 2.18b. The vector $\mathbf{f_b}$ contains the natural boundary conditions in which the prescribed temperature at the hot surface boundary, i.e. Equation 5.9, is introduced to the matrix equation after assembling the element matrices (Appendix C) and the second term is zero due to adiabatic boundary condition at the cold surface.

MODEL 2

$$\left(\int_0^l \mathbf{N}^{\mathrm{T}}\rho_j^{i+1}c_p\mathbf{N}dx\right)\dot{\mathbf{T}}+\left[\int_0^l \mathbf{B}^{\mathrm{T}}k\mathbf{B}dx+\int_0^l \mathbf{B}^{\mathrm{T}}\left(\dot{m}_g\right)_j^{i+1}c_{pg}\mathbf{N}dx+\int_0^l \mathbf{N}^{\mathrm{T}}\left(\frac{\partial\rho_r}{\partial t}\right)_j^{i+1}\left(c_p-c_{pg}\right)\mathbf{N}dx\right]\mathbf{T}$$

$$+\int_0^l\left(\frac{\partial\rho_r}{\partial t}\right)_j^{i+1}\left[Q-\left(c_p-c_{pg}\right)T_\infty\right]\mathbf{N}^{\mathrm{T}}dx-\begin{bmatrix}\left(h_{r1}+h_{c1}\right)T-h_{r1}T_r-h_{c1}T_f\\-\left(h_{r2}+h_{c2}\right)\left(T-T_\infty\right)\end{bmatrix}=\mathbf{0} \quad (5.56)$$

where the last vector contains the radiation and convection boundary conditions at the hot and cold surfaces.

MODEL 3

$$\left[\int_0^l \mathbf{N}^{\mathrm{T}}\rho_j^{i+1}\left(c_p\right)_j^{i+1}\mathbf{N}dx\right]\dot{\mathbf{T}}+\left\{\int_0^l \mathbf{B}^{\mathrm{T}}k_j^{i+1}\mathbf{B}dx\right.$$

$$\left.+\int_0^l \mathbf{B}^{\mathrm{T}}\left(\dot{m}_g\right)_j^{i+1}\left(c_{pg}\right)_j^{i+1}\mathbf{N}dx+\int_0^l \mathbf{N}^{\mathrm{T}}\left(\frac{\partial\rho_r}{\partial t}\right)_j^{i+1}\left[\left(c_p\right)_j^{i+1}-\left(c_{pg}\right)_j^{i+1}\right]\mathbf{N}dx\right\}\mathbf{T}$$

$$+\int_0^l\left(\frac{\partial\rho_r}{\partial t}\right)_j^{i+1}\left\{Q-\left[\left(c_p\right)_j^{i+1}-\left(c_{pg}\right)_j^{i+1}\right]T_\infty\right\}\mathbf{N}^{\mathrm{T}}dx-\begin{bmatrix}-k_j^{i+1}\dfrac{\partial T}{\partial x}(0)\\-\left(h_{r2}+h_{c2}\right)\left(T-T_\infty\right)\end{bmatrix}=\mathbf{0} \quad (5.57)$$

where the prescribed temperature at the hot surface boundary, i.e. Equation 5.9, is introduced to the matrix equation after assembling the element matrices (Appendix C) and the radiation and convection boundary condition at the cold surface is introduced directly in the equation as can be seen in the last vector.

MODEL 4

$$\left[\int_0^l \mathbf{N}^{\mathrm{T}}\rho_j^{i+1}\left(c_p\right)_j^{i+1}\mathbf{N}dx\right]\dot{\mathbf{T}}+\left\{\int_0^l \mathbf{B}^{\mathrm{T}}k_j^{i+1}\mathbf{B}dx+\int_0^l \mathbf{B}^{\mathrm{T}}\left(\dot{m}_g\right)_j^{i+1}\left(c_{pg}\right)_j^{i+1}\mathbf{N}dx\right.$$

$$\left.+\int_0^l \mathbf{N}^{\mathrm{T}}\left(\frac{\partial\rho_r}{\partial t}\right)_j^{i+1}\left[\left(c_p\right)_j^{i+1}-\left(c_{pg}\right)_j^{i+1}\right]\mathbf{N}dx\right\}\mathbf{T}+\int_0^l\left(\frac{\partial\rho_r}{\partial t}\right)_j^{i+1}\left\{Q-\left[\left(c_p\right)_j^{i+1}-\left(c_{pg}\right)_j^{i+1}\right]T_\infty\right\}\mathbf{N}^{\mathrm{T}}dx$$

$$-\begin{bmatrix}h_{r1}\left(T-T_r\right)+h_{c1}h_b\left(T-T_f\right)+\rho_s V_s\left\{Q_s+\left[\left(c_p\right)_j^{i+1}-\left(c_{pg}\right)_j^{i+1}\right]\left(T-T_\infty\right)\right\}\\ -\left(h_{r2}+h_{c2}\right)\left(T-T_\infty\right)\end{bmatrix}=\mathbf{0} \quad (5.58)$$

where the last vector contains the radiation, convection, gas mass movement and surface chemical reactions terms as the boundary condition for the hot surface and radiation and convection terms as the boundary condition for the cold surface.

5.3.3 Time Step Algorithm

A solution to the matrix equation of the form Equation 5.54 is given by [from: Zienkiewicz & Taylor, 1991 as corrected by Looyeh *et al.*, 1997; Zienkiewicz, Pers. Com., 1995]:

$$\mathbf{T}_{n+1}=\left(\mathbf{C}+\Delta t\Theta\mathbf{K}\right)^{-1}\left\{\left[\mathbf{C}-\Delta t(1-\Theta)\mathbf{K}\right]\mathbf{T}_n-\Delta t\,\bar{\mathbf{f}}\right\} \quad (5.59)$$

where

Δt = time step size (s)

Θ = weighting (time step) parameter

$\bar{\mathbf{f}}$ is the average value of **f** defined by Equation 2.36 and subscripts **n** and **n+1** represent known and unknown quantities.

The time step is based on the critical time step Δt_{cr} which depends on the weighting parameter Θ, the element length l, density ρ, thermal conductivity k and specific heat c_p as given by Zienkiewicz & Taylor [1991]:

$$\Delta t_{cr}=\frac{2}{1-2\Theta}\frac{l^2\rho\,c_p}{3k} \quad (5.60)$$

For Models 1 and 2 a constant time step is used. For Models 3 and 4 the time step is evaluated and updated at each step of computations, i.e.:

$$\Delta t_{cr} = \frac{2}{1-2\Theta} \frac{l_j^2 \rho_j^{i+1} \left(c_p\right)_j^{i+1}}{3k_j^{i+1}} \tag{5.61}$$

The Crank-Nicolson solution, corresponding to $\Theta=1/2$ is used.

5.3.4 The Computer Code Algorithm

The operations flow charts of the finite element computer code developed in Models 1 to 4 are given in Figures 5.5 to 5.8, respectively.

MODEL 1 - Main Finite Element Program

1. initialize the system matrices, vectors and principle variables.
2. read finite element mesh data, thermal, kinetic and transport properties and also control ID value to perform different solutions.
3. start time-dependent calculation and determine furnace temperature.
4. set the initial values for thermal and transport properties, Eqs. 4.1 to 4.3.
5. calculate the mass loss rate, instantaneous density and gas mass flux regarding the control ID value for the required solution.
6. choose a suitable option according to the input element type and create element matrices, **K** and **C**, and element force vector, **f**, Eq. 5.55.
7. assemble the system matrices and force vector, if any.
8. calculate and apply the constant time step.
9. form system equations according to Eq. 5.54.
10. calculate the hot surface temperature and apply it to the matrix equation.
11. solve the matrix equation using Eq. 5.59 and find temperature and mass loss profiles.
12. add the time step, determined in step 8, then go to step 5, otherwise stop.

Figure 5.5 Flow chart listing the key steps for the main program of the finite element computer code to perform one-dimensional heat transfer analysis developed in Model 1.

To assess the effect of different boundary conditions on heat transfer, two set of control ID values are added to the finite element program (Figure 5.6).

MODEL 2 - Main Finite Element Program

1. initialize the system matrices, vectors and principle variables.
2. read finite element mesh data, thermal, kinetic and transport properties, and also control ID values for the appropriate boundary conditions and performing different solutions.
3. start time-dependent calculation and determine furnace temperature.
4. set the initial values for thermal and transport properties, Eqs. 4.1 to 4.3.
5. determine the hot and cold surface boundary conditions, Eqs. 3.1 to 3.15.
6. calculate the mass loss rate, instantaneous density and gas mass flux regarding the control ID value for the required solution.
7. choose a suitable option according to the input element type and create element matrices, **K** and **C**, and element force vector, **f**, Eq. 5.56.
8. assemble the system matrices and force vector, if any.
9. calculate and apply the constant time step.
10. form system equations according to Eq. 5.54.
11. apply hot surface and cold surface boundary conditions.
12. solve the matrix equation using Eq. 5.59 and find temperature and mass loss profiles.
13. add the time step, determined in step 9, then go to step 5, otherwise stop.

Figure 5.6 Flow chart listing the key steps for the main program of the finite element computer code to perform one-dimensional heat transfer analysis developed in Model 2.

To take account of the temperature- and moisture-dependent thermal properties, two key steps are added to the main finite element program. The equation for the rate of decomposition is modified to take account of the final mass of resin remained at the end of pyrolysis reactions (Figure 5.7).

MODEL 3 - Main Finite Element Program

1. initialize the system matrices, vectors and principle variables.
2. read finite element mesh data, thermal, kinetic and transport properties, boundary condition parameters and also control ID value to perform different solutions.
3. start time-dependent calculation and determine furnace temperature.
4. set the initial values and calculate additional specific heat and the proportion function of the moisture content, Eqs. 4.1 to 4.3, 4.6, 4.8 and 4.12.
5. determine the hot and cold surface boundary conditions, Eqs. 5.9 and 5.12 to 5.17.
6. calculate the temperature-dependent thermal properties, Eqs. 4.9 and 4.13 to 4.17.
7. calculate the effect of moisture content on thermal properties using additional specific heat obtained in step 4, Eqs. 4.10 and 4.11.
8. calculate the mass loss rate, instantaneous density and gas mass flux regarding the control ID value for the required solution.
9. choose a suitable option according to the input element type and create element matrices, **K** and **C**, and element force vector, **f**, Eq. 5.57.
10. assemble the system matrices and force vector, if any.
11. calculate and update the time step using Eq. 5.61 or consider the chosen value for the implicit solutions.
12. form system equations according to Eq. 5.54.
13. apply hot surface and cold surface boundary conditions.
14. solve the matrix equation using Eq. 5.59 and find temperature, mass loss and moisture profiles.
15. add the time step, determined in step 11, then go to step 4, otherwise stop.

Figure 5.7 Flow chart listing the key steps for the main program of the finite element computer code to perform one-dimensional heat transfer analysis developed in Model 3.

For Model 4 the hot surface boundary condition is modified due to additional terms, i.e. gas mass movement and surface chemical reactions (Figure 5.8).

MODEL 4 - Main Finite Element Program

1. initialize the system matrices, vectors and principle variables.
2. read finite element mesh data, thermal, kinetic and transport properties, boundary condition parameters and also control ID value to perform different solutions.
3. start time-dependent calculation.
4. set the initial values and calculate additional specific heat, the proportion function of the moisture content and gas density, Eqs. 4.1 to 4.3, 4.6, 4.8, 4.12 and 5.43.
5. determine the hot and cold surface boundary conditions, Eqs. 5.19 to 5.25, 5.35, 5.38 and 5.39 to 5.45.
6. calculate the temperature-dependent thermal properties, Eqs. 4.9 and 4.13 to 4.17.
7. calculate the effect of moisture content on thermal properties using additional specific heat obtained in step 4, Eqs. 4.10 and 4.11.
8. calculate the mass loss rate, instantaneous density and gas mass flux regarding the control ID value for the required solution.
9. calculate instantaneous mass fraction and porosity and update gas density, Eqs. 5.43 to 5.45.
10. determine gas blowing factor and rate of modification due to surface chemical reactions, Eqs. 5.35 and 5.41.
11. choose a suitable option according to the input element type and create element matrices, **K** and **C**, and element force vector, **f**, Eq. 5.58.
12. assemble the system matrices and force vector, if any.
13. calculate and update the time step using Eq. 5.61 or consider the chosen value for the implicit solutions.
14. form system equations according to Eq. 5.54.
15. apply hot surface and cold surface boundary conditions.
16. solve the matrix equation using Eq. 5.59 and find hot surface temperature, temperature distributions, mass loss and moisture profiles.
17. add the time step, determined in step 13, then go to step 4, otherwise stop.

Figure 5.8 Flow chart listing the key steps for the main program of the finite element computer code to perform one-dimensional heat transfer analysis developed in Model 4.

There are two main subroutines: (i) Element matrices and vectors and (ii) non-symmetric matrix solver (Chapter 2). Flow charts listing the key steps for these subroutines are given in Figures 5.9 and 5.10.

Element Matrices and Vectors Subroutine

1. get element shape functions and their derivatives.
2. calculate the element matrices and element force vector contributions regarding the input control ID value.
3. integrate the element matrices and element force vector and add the results to the pervious values, then go to step 1.
4. choose a suitable solution of the finite element method, i.e. explicit or implicit (backward difference; Crank-Nicolson).

Figure 5.9 Flow chart listing the key steps for the element matrices and vectors subroutine of the finite element computer code (valid for all models).

Non-Symmetric Matrix Solver Subroutine

1. decompose matrix A into lower and upper profile matrices, where AX=B.
2. modify right hand side, i.e. matrix B, due to constraints.
3. perform forward substitution on the lower profile matrix.
4. perform backward substitution to find the unknown values.

Figure 5.10 Flow chart listing the key steps for the non-symmetric matrix solver subroutine of the finite element computer code (valid for all models).

5.4 FIRE EXPERIMENTS

For comparison with the numerical results, a furnace fire experiment was requested from the research groups at the University of Manchester, School of Engineering and the University of Newcastle-upon-Tyne, Centre for Composite Materials Engineering. The experiment was carried out for a typical 1.09×90×90cm single-skinned polyester-based GRP panel (Figure 5.11). The panel was manufactured in Newcastle University by the hand lay-up method. Nine temperature sensors were implanted at different layers of the panel and two were placed at the hot and cold surfaces to enable the temperature distribution to be measured (Figure 5.11). The panel was installed vertically on the door of a ceramic furnace with an active volume of 3.375m^3 and maximum fire temperature 1100°C [Davies *et al.*, 1994a; Wu *et al.*, 1994]. The panel was fire tested in furnace conditions controlled by the standard hydrocarbon fire [Spagni & Gibson, 1994; ISO 834, 1975; BS476, 1987].

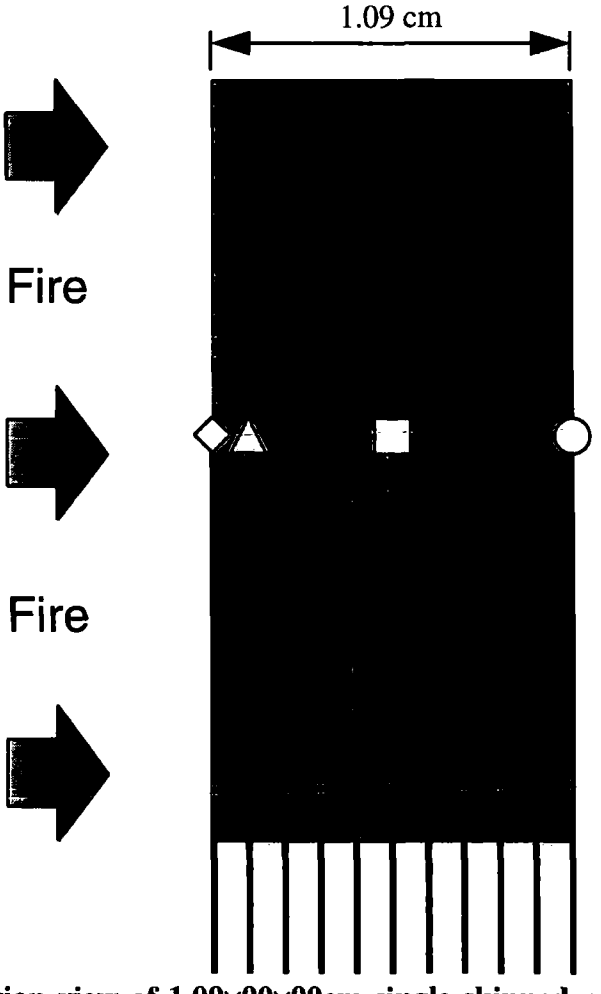

Figure 5.11 Elevation view of 1.09×90×90cm single-skinned polyester-based GRP panel with 11 embedded temperature sensors; the locations of key sensors are shown (◇△□○).

5.5 COMPARISON OF THE FINITE ELEMENT COMPUTATIONS WITH EXPERIMENTAL RESULTS AND DISCUSSION

MODEL 1

The properties for polyester-based GRP were discussed in Chapter 4 and listed in Table 4.3. The initial density of polyester-based GRP is 1832.4 kgm^{-3}. The density varies with temperature based on a first-order Arrhenius rate equation and the final density is 1190.4 kgm^{-3} when the polyester resin has burnt away completely. The thermal conductivity is assumed constant throughout the pyrolysis (0.322 $Wm^{-1}K^{-1}$). From the end of pyrolysis and then the transient heat conduction is followed by the thermal conductivity of glass fibre (1.09 $Wm^{-1}K^{-1}$). The specific heat of GRP is assumed constant throughout the fire exposure (1056.84 $Jkg^{-1}K^{-1}$). The preliminary estimations for pyrolysis constant, activation energy and heat of decomposition are $1000s^{-1}$, 500 $MJkmole^{-1}$ and 2.3446 $MJkg^{-1}$, respectively. The time step is chosen 5 seconds.

In Figure 5.12, the predicted temperatures are plotted versus time at the four spatial locations shown in Figure 5.11, i.e. x/L= 0, 1/10, 5/10 and 1, and compared to the experimental data. Assuming the experimental results to be correct, it is seen that:

(i) The hot surface temperatures are under-predicted compared to experimentally measured temperatures for the range 1 to 7 minutes. After 7 minutes there is very close agreement between the empirical curve and the measured temperatures.

(ii) At the inter-laminar position close to the hot surface, i.e. x/L=1/10, (referred to as inter-laminar 1), the numerical model over-predicts temperatures by up to 100°C for the first 5 minutes. The temperature sensor showed somewhat erratic behaviour especially for t>7 minutes making it difficult to compare the computed and experimental results. At this stage the sensor being no longer in touch with the material as a sharp drop of the temperature is so unlikely. Sensor disassociation occurs after 8 minutes where the material temperature is about 750°C. This is highly likely to be due to material delamination as observed by Wu *et al.* [1994].

(iii) At the middle inter-laminar position, i.e. x/L=5/10, (referred to as inter-laminar 2), the trends for the predicted and measured temperatures are similar for t<8

minutes but temperatures are over-predicted by an average of 30°C for t>8 minutes.

(iv) The cold surface temperatures are in good agreement with the measured values except the numerical model appears to over-predict temperatures between 1.5 and 6 minutes and after 11 minutes.

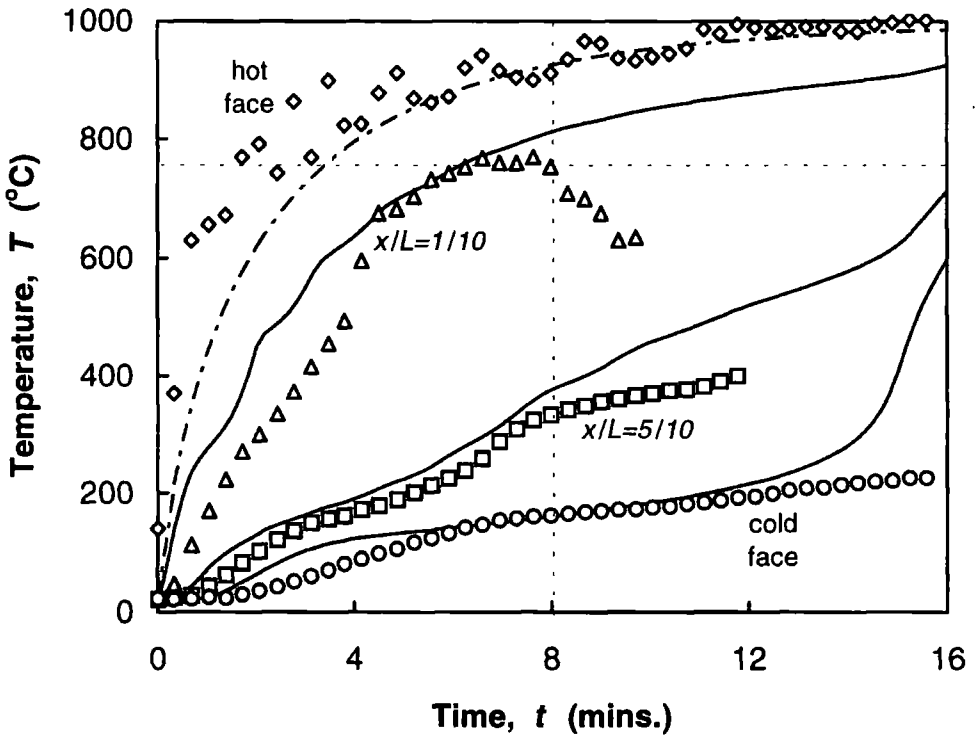

Figure 5.12 Comparisons of the computed and experimental temperatures at four spatial locations. The temperatures, computed by Model 1, are shown as solid lines and the experimental results for four sensors as ◇ △ □ ○, the position of which are shown in Figure 5.11. The temperature sensor at x/L=1/10 losses contact with the material after 8 minutes at about 750°C due to delamination.

For t>12 minutes the heat conduction is governed by the residual glass fibres as the polyester resin has burnt away completely. At this stage the thermal conductivity of GRP, i.e. 0.322 $Wm^{-1}K^{-1}$, is replaced by that for glass fibre, i.e. 1.09 $Wm^{-1}K^{-1}$. The sharp increase of the temperature is expected due to the sudden increase of thermal conductivity by a factor of three.

The few inconsistencies which do exist between the computed and experimental temperatures are thought to be due to the following factors: (i) The thermal properties were assumed constant; (ii) Thermal conductivity was assumed to experience a sudden change at the end of pyrolysis; (iii) The kinetic properties were approximated; (iv) The

volume of material was assumed constant; (v) Accumulation of the pyrolysis gases was not considered; (vi) radiation and convection heat transfer was ignored at the cold surface; (vii) The empirical hydrocarbon fire cure did not represent real hydrocarbon fire conditions; and, finally, (viii) The complete physical and chemical phenomena including heat and mass transfer and surface chemical reactions were not considered. Although the influence of these factors are significant in many cases, the overall effect of each factor on the final response is not clear. Some of these factors are studied in the next models.

The average temperature difference for all data points is 29.6°C, except for inter-laminar 1 for t>8 minutes.

To show how each term of the governing equation, i.e. Equation 5.1, contributes to the temperature rise through the GRP panel, four equations are computed and shown in Figure 5.13 (next page). These are:

(1) Transient heat conduction;

$$\rho c_p \frac{\partial T}{\partial t} = k \frac{\partial^2 T}{\partial x^2}$$

(2) Transient heat conduction and gas mass flux;

$$\rho c_p \frac{\partial T}{\partial t} = k \frac{\partial^2 T}{\partial x^2} - \dot{m}_g c_{pg} \frac{\partial T}{\partial x}$$

(3) Transient heat conduction and mass loss;

$$\rho c_p \frac{\partial T}{\partial t} = k \frac{\partial^2 T}{\partial x^2} - \frac{\partial \rho_r}{\partial t}\left(Q + h - h_g\right)$$

(4) transient heat conduction plus full decomposition;

$$\rho c_p \frac{\partial T}{\partial t} = k \frac{\partial^2 T}{\partial x^2} - \dot{m}_g c_{pg} \frac{\partial T}{\partial x} - \frac{\partial \rho_r}{\partial t}\left(Q + h - h_g\right) \qquad (5.1)$$

From the cold surface temperature profile (Figure 5.13) it is possible to evaluate the fire resistance or insulation failure of the panel exposed to fire. Fire resistance is defined as the time required for the average temperature of the unexposed (cold) surface to reach 160°C. The numerical results suggests fire resistance occurs around 7.9 minutes which differs from the experimental prediction (7.5 minutes) by 0.4 minutes. This indicates a small difference of 5.6 percent between the predicted and experimental fire resistance results.

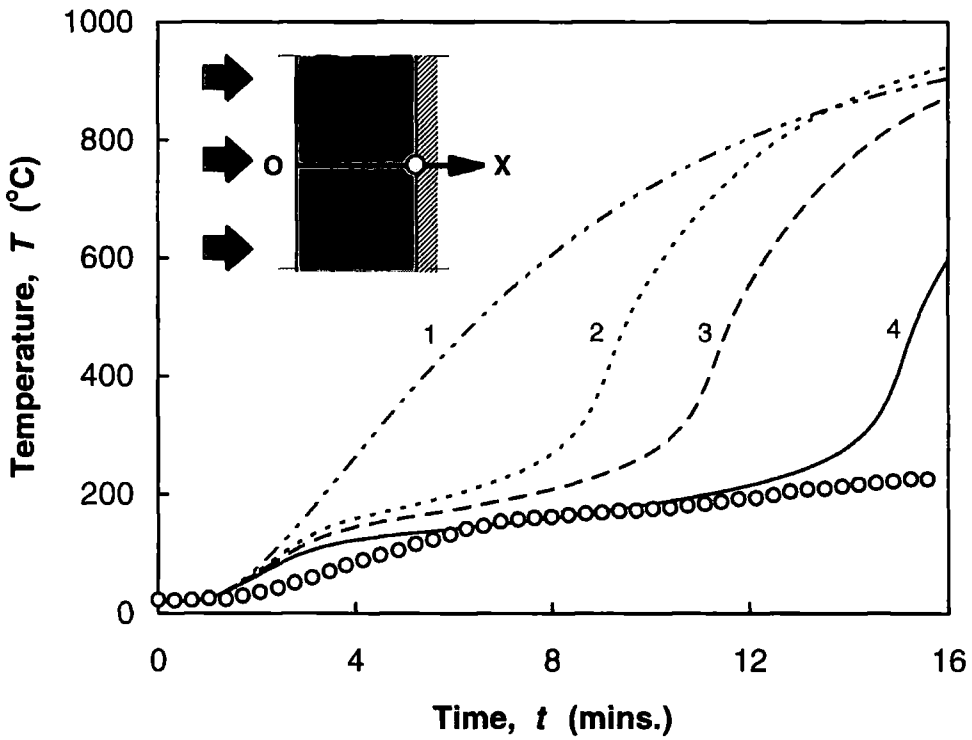

Figure 5.13 Comparison of the effects of different terms in the governing equation on the cold surface temperatures predicted by Model 1. Curves (1) to (4) show the computed cold surface temperature profiles due to: (1) transient heat conduction only; (2) transient heat conduction plus gas mass flux term; (3) transient heat conduction plus mass loss term and (4) transient heat conduction plus full decomposition. The experimental data are given by O as shown in the inset.

In Figure 5.14 the predicted temperatures are plotted versus distance from the hot surface to the cold surface of the panel at 1, 2, 4, 8 and 16 minutes. The steep variations of temperature profiles are evident from this figure. This is thought to be due to the low thermal conductivity, i.e. 0.322 $Wm^{-1}K^{-1}$, which is assumed constant during pyrolysis. Observation of this figure also reveals that the average temperature difference between two adjacent profiles remains almost unchanged except from 1 to 2 minutes. This temperature difference is expected to decrease with time when constant time intervals are used. This implies that the rate of heat transfer is reduced as the pyrolysis reactions zone progresses through the material.

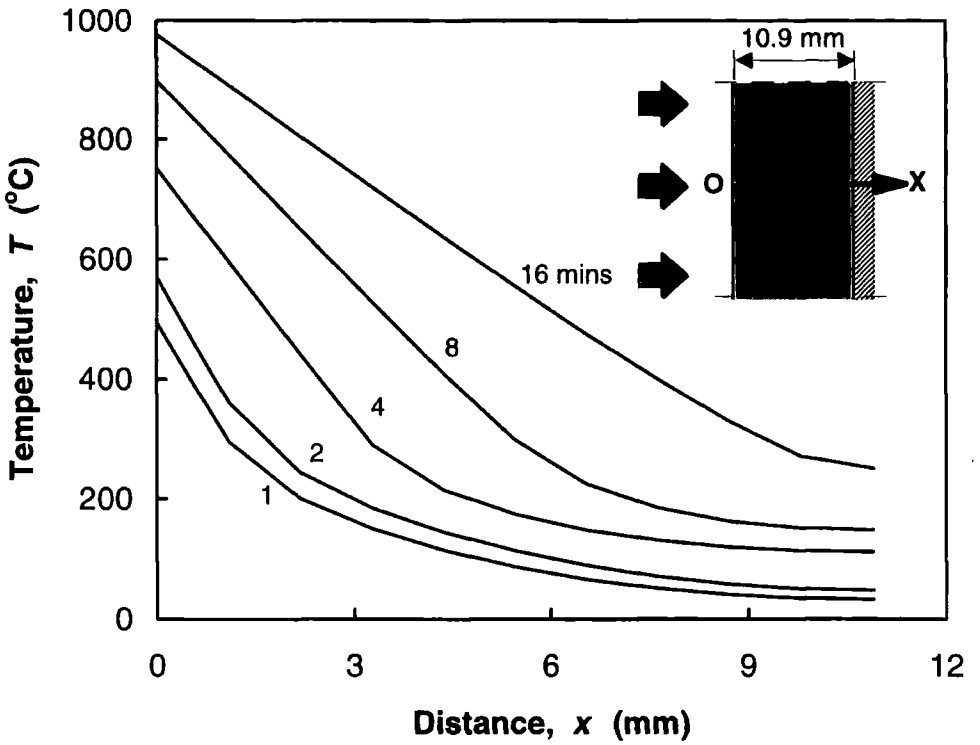

Figure 5.14 Temperature, predicted by Model 1, versus distance x for various times (minutes).

In Figure 5.15 the predicted variations of the mass of polyester resin are plotted versus time from the hot surface to the cold surface at four spatial locations, i.e. x/L=0, 1/10, 5/10 and 1. It is evident that pyrolysis has reached completion at the hot surface of the GRP panel for times grater than 1.9 minutes. Observation also reveals that by 15 minutes the pyrolysis reactions zone has progressed to the unexposed (cold) surface.

Figure 5.16 shows the predicted variations of the GRP mass versus time for the same spatial locations. It can be seen that 63.6% of GRP remains unchanged at the pyrolysis reaction, i.e. the pyrolysis results in a mass loss of 36.4%. The remained mass is that for the residual glass fibres which undergoes no thermochemical decomposition. A comparison of Figures 5.14 and 5.16 shows that pyrolysis is initiated in the temperature range of approximately 200 to 300°C and reach completion in the temperature range of approximately 600 to 700°C.

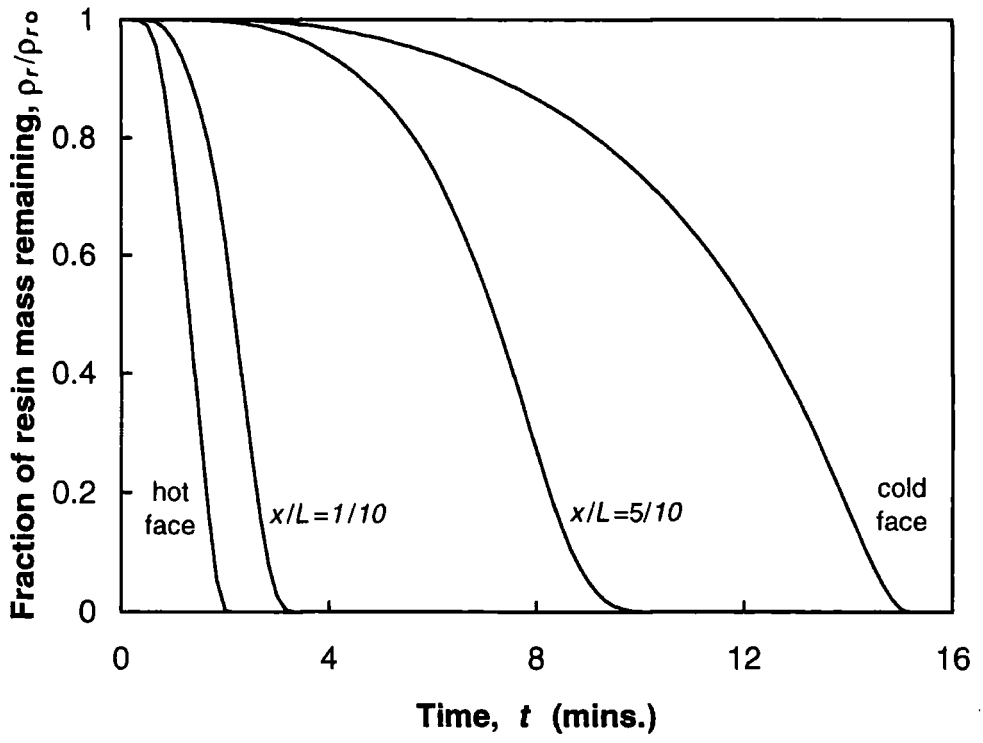

Figure 5.15 Fraction of polyester resin mass versus time for various distances, i.e. x/L = 0, 1/10, 5/10 and 1. Model 1 is used. It is seen that after 15 minute of fire exposure polyester resin has burnt away completely.

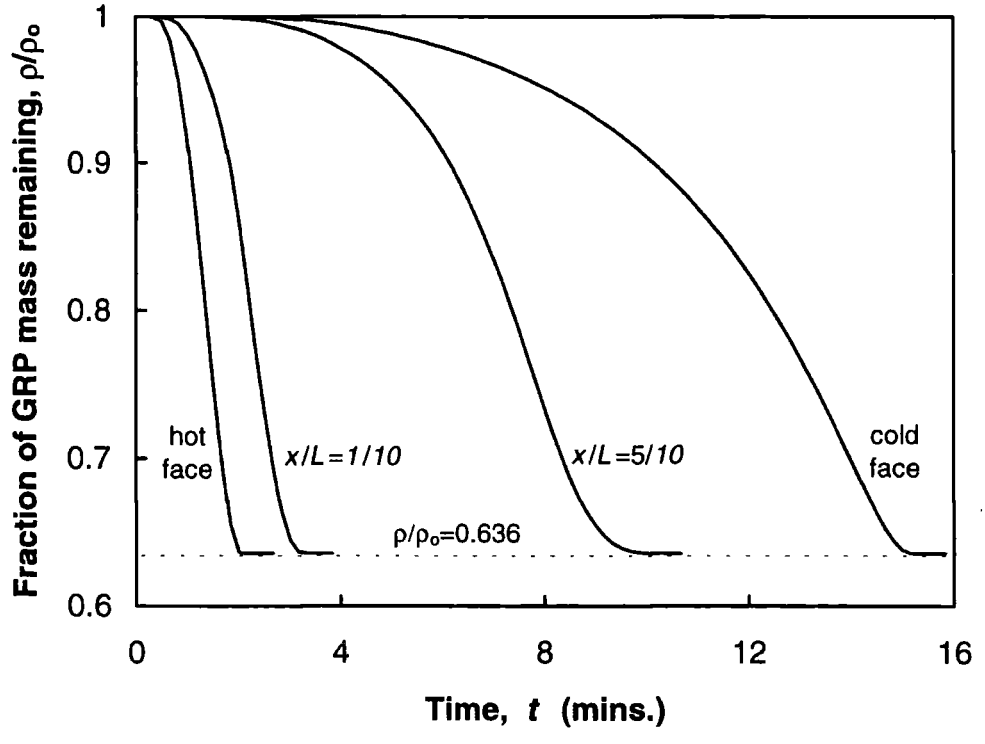

Figure 5.16 Fraction of the mass of polyester-based GRP versus time for various distances, i.e. x/L = 0, 1/10, 5/10 and 1. Model 1 is used. It is seen that 63.6% of GRP remains intact at the end of pyrolysis. This relates to the mass of residual glass fibres.

Figure 5.17 illustrates the predicted rate of resin mass loss versus time at four spatial locations. The rate of resin mass loss is formulated using a first-order kinetic rate Arrhenius equation. This figure clearly demonstrates the time derivatives of the mass profiles presented in Figure 5.15. It is seen that the maximum peak occurs at or near the hot surface boundary. With time, this peak moves back towards the cold surface where less gradients and smoother curves can be observed.

The feature presented by the resin mass loss rate profiles, i.e. Figure 5.17, in conjunction with the corresponding temperature and resin mass fraction profiles, i.e. Figures 5.14 and 5.15, provide some useful patterns illustrating the pyrolysis reactions. The panel layers progressively lying deeper from the hot surface, illustrate a progressively lower maximum pyrolysis rate and a progressively wider range of temperature at which pyrolysis occurs. In fact, the ratio of the maximum pyrolysis rate to the temperature at which it occurs is roughly constant. While the rate of resin mass loss curves near the hot surface are sharp, those at the inter-laminar spatial locations and near the cold surface show rather smooth and regular changes with a constant rate for a certain duration.

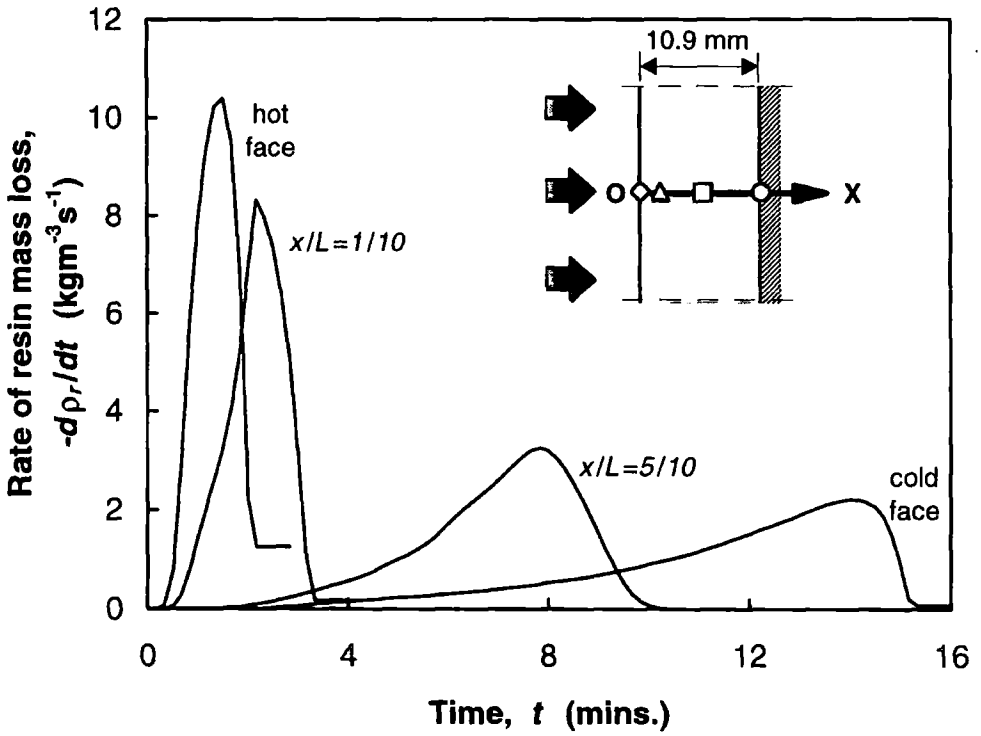

Figure 5.17 Rate of resin mass loss versus time for four spatial locations as shown in the inset. Model 1 is used. It is seen that the maximum peak occurs at or near the hot surface boundary meaning that the resin mass decomposes much faster in this region compared to the rest of material.

MODEL 2

In Model 1 the cold surface was assumed insulated. In the present model various boundary conditions are applied to the cold surface. The effect of these boundary conditions on the cold surface temperature is studied.

Tables 5.1 lists the final computed temperatures of the cold surface boundary after 16 minutes. These results are compared with the experimental results where available.

It is seen that by applying the radiation and convection boundary condition to the cold surface boundary a closer agreement is achieved between the computed and experimental results. The cold surface temperature resulted from Model 1 with insulated cold surface is 257.6°C which differs from the experimental value by 10.5%. For a vertical panel, the temperature value for the cold surface boundary exchanging radiative and convective heat energy with environment is 241.7°C which is different from that of experimental by 3.7%.

Table 5.1 Temperature results, predicted by Model 2, for the cold surface boundary subject to different boundary conditions after 16 minutes.

Type of boundary condition	Cold surface temperature (°C)	Difference with Insulated (%)	Difference with Experimental (%)
Insulated	257.6	0.0	10.5
V.Fr.C.	243.9	5.3	4.4
V.Fo.C.	207.5	19.5	-
H.Fr.C. (U.H.S.)	243.5	5.5	-
H.Fr.C. (L.H.S.)	245.0	4.9	-
I.Fr.C. (N.A.)	244.1	5.2	-
I.Fr.C. (P.A.)	244.4	5.1	-
V.Fr.C. + R.B.C.	241.7	6.1	3.7
V.Fo.C. + R.B.C.	205.4	25.4	-
H.Fr.C. (U.) + R.B.C.	241.2	6.4	-
H.Fr.C. (L.) + R.B.C.	242.7	5.8	-
I.Fr.C. (N.) + R.B.C.	242.3	5.9	-
I.Fr.C. (P.) + R.B.C.	242.1	6.0	-

V.Fr.C. = vertical free convection
V.Fo.C. = vertical forced convection
H.Fr.C. = horizontal free convection
U.H.S. = upper heated surface
L.H.S. = lower heated surface
I.Fr.C. = inclined free convection
N.A. = negative angle
P.A. = positive angle
R.B.C. = radiation boundary condition

Evident from Table 5.1 is that the combination of forced convection and radiation boundary condition at the cold surface boundary, which represents the working condition for offshore panels, results in the lowest cold surface temperature for the same period of fire exposure, i.e. 16 minutes.

The average temperature difference for all data points with experimental data, predicted using Model 1, was 29.6°C. This is reduced to 24.5°C when radiation and convection boundary condition is maintained at the cold surface.

For the case of vertical panel exchanging radiation and free convection heat energy with environment, the fire resistance, which is the time for the cold surface to reach 160°C, is predicted 7.7 minutes. This is different from the experimental fire resistance, i.e. 7.5 minutes, by 2.5%. It is worth noting that the fire resistance predicted by Model 1, i.e. 7.9 minutes, is different from the experimental by 5.6%.

MODEL 3

The initial density, specific heat and thermal conductivity of the GRP are 1832.4 kgm^{-3}, 1056.84 $Jkg^{-1}K^{-1}$ and 0.322 $Wm^{-1}K^{-1}$, respectively.

Density decreases with temperature and reaches 1203.24 kgm^{-3} at the end of pyrolysis. Specific heat increases with temperature linearly. It increases by 4.6% at the beginning of the pyrolysis (200 to 300°C) and by 11.7% when the pyrolysis reaches completion (600 to 700°C). The variation of thermal conductivity with temperature is more complex. By 200°C a reduction of 9.9% occurs in the thermal conductivity causing less heat flow through the material at the beginning of fire exposure. From this point to the beginning of pyrolysis (200 to 300°C), thermal conductivity experiences a rapid rise by 20.2%. The linear rise of thermal conductivity with temperature continues until it reaches 0.494 $Wm^{-1}K^{-1}$ at the end of pyrolysis (600 to 700°C) which indicates an increase of 53.4%.

Pyrolysis constant, activation energy and heat of decomposition are 7525 s^{-1}, 611.5 $MJkmole^{-1}$ and 2.3446 $MJkg^{-1}$, respectively. These are evaluated by fitting a first order Arrhenius rate equation to the results of a recent thermo gravimetric analysis (TGA). TGA results also revealed that about 2 to 3% of polyester resin remains intact at the end of pyrolysis.

The initial time step is chosen 5 seconds based on the critical time step. At the end of each iteration the time step is updated and then applied to the next iteration.

The hot surface boundary condition is given by an empirical time-dependent temperature which is the same as that for Model 1. The cold surface exchanges radiation and convection heat energy with environment which was discussed in Model 2.

Figure 5.18 shows the predicted temperatures plotted versus time for various locations in the panel with the experimental data. A closer agreement between predicted temperatures and experimental data is apparent when account is taken for the variations of thermal properties with temperature and moisture. However, the model under-predicts temperatures at the locations with high fire exposure time. This may be due to inaccuracies in the thermal properties at higher temperatures. The inter-laminar sensor closer to the hot surface losses contact with the material during the experiment. The point of sensor failure is marked on Figure 5.18.

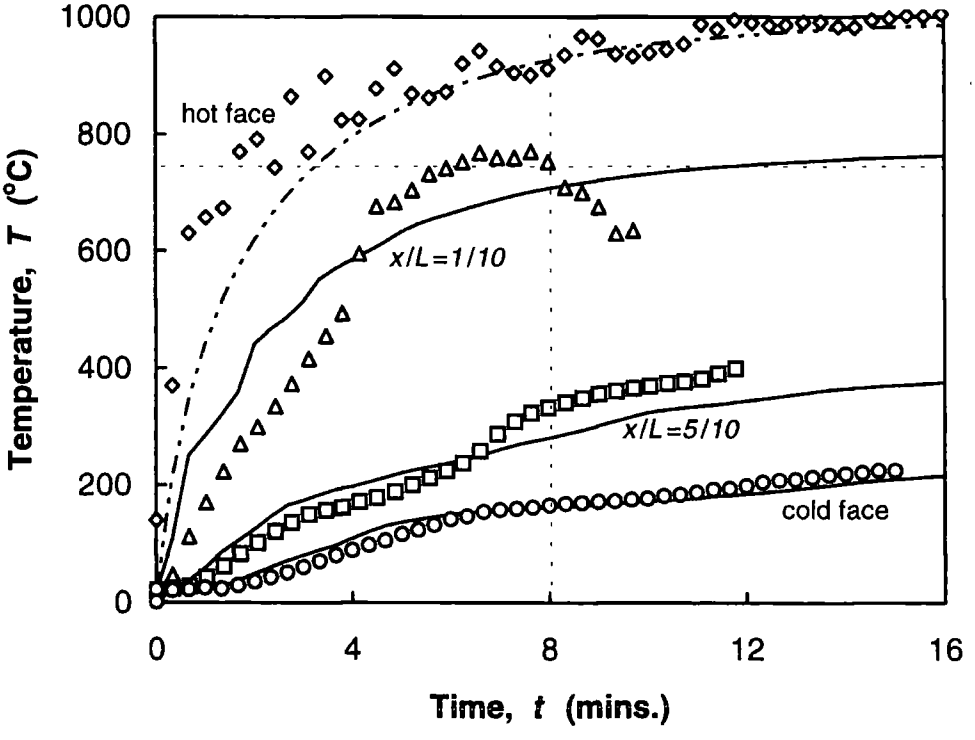

Figure 5.18 Comparisons of the computed and experimental temperatures at four spatial locations. The computed results are from Model 3. The one-dimensional computed temperatures are shown as solid lines and the experimental results for four sensors as ◇ △ □ ○, the position of which are shown in Figure 5.11. The failure of the inter-laminar sensor △ occurs after 8 minutes.

For easier comparison, the predicted temperatures of the present model and those for Model 1 (Figure 5.12) including the experimental data are plotted versus time (Figure 5.19). The solid lines represent the temperature profiles resulting from Model 3 and the dot lines from Model 1. It is seen that the results of the present model show closer agreement with the experimental at both low and high fire exposure times. The temperatures predicted by Model 1 exhibit relatively poor agreement at high fire exposure times. For times less than 5 minutes, the improvement is more prominent (up to 45%). The better predictions from Model 3 is thought to be mainly due to the thermal conductivity which decreases with temperatures under 200°C. Also, the temperature results for times greater than 12 minutes are noticeable. For Model 1 we assumed that the heat transfer at the end of pyrolysis is governed by the thermal properties of the residual glass fibre. This causes a sudden change in the thermal properties. For Model 3, it is assumed that the thermal properties vary with temperature and moisture steadily. This implies that at the end of pyrolysis, where 2 to 3% of polyester resin has remained intact, the heat transfer is followed by the thermal properties of both polyester resin and glass fibre.

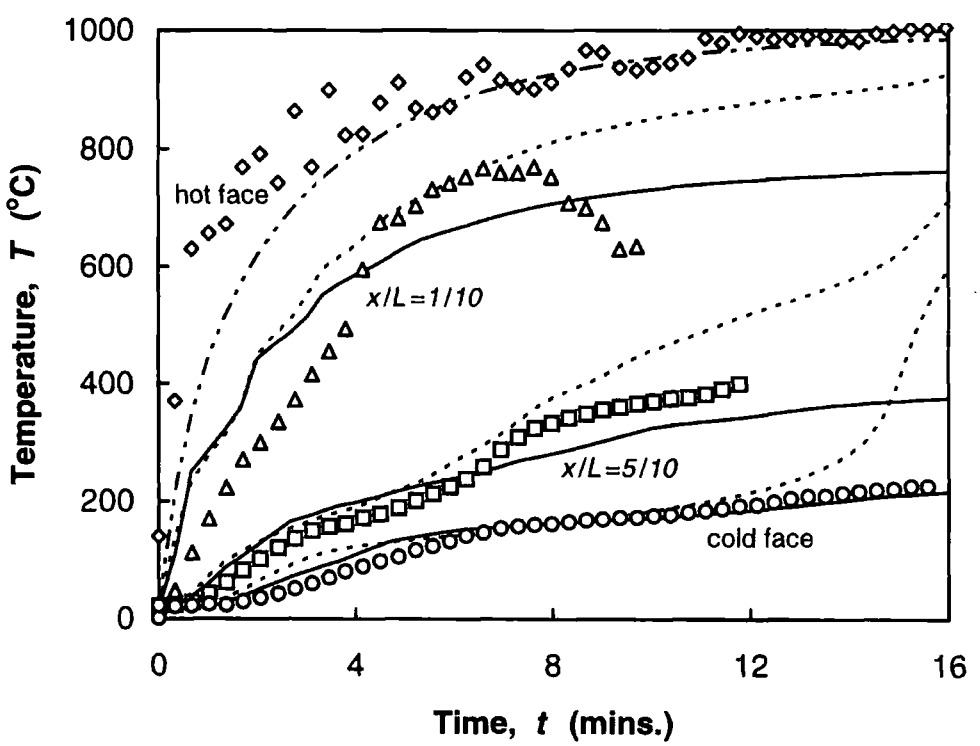

Figure 5.19 Comparisons of the computed and experimental temperatures at four spatial locations. The solid lines represent the results of Model 3 with variable thermal properties and the dot lines the results of Model 1 with constant thermal properties. The experimental results for four sensors are shown by ◇ △ □ ○, the position of which are indicated in Figure 5.11.

The average temperature difference for all data points between the present model and experimental data is 21.4°C. Comparisons of this value with those for Models 1 and 2, i.e. 29.6°C and 24.5°C, indicate improvements in the fire prediction by 27.7% and 12.6%, respectively. Earlier, we discussed that the improvement gained from 29.6°C to 24.5°C was due to the application of radiation and convection boundary condition at the cold surface boundary. It is evident that the present improvement, i.e. from 24.5°C to 21.4°C, is due to two factors: (i) variable thermal properties and (ii) 2 to 3% polyester resin remaining at the end of pyrolysis.

To show how this model improves the fire resistance behaviour of the material, the cold surface temperatures are plotted versus time with the results of Model 1 and the experimental temperatures (Figure 5.20). The fire resistance, i.e. the time in which the cold surface reaches 160°C, predicted by this model is 7.6 minutes which differs from the experimental , i.e. 7.5 minutes, by 1.3%. The fire resistance values obtained from Models 1 and 2 were 7.9 and 7.7 minutes. These indicated differences of 5.6% and 2.5% with the experimental.

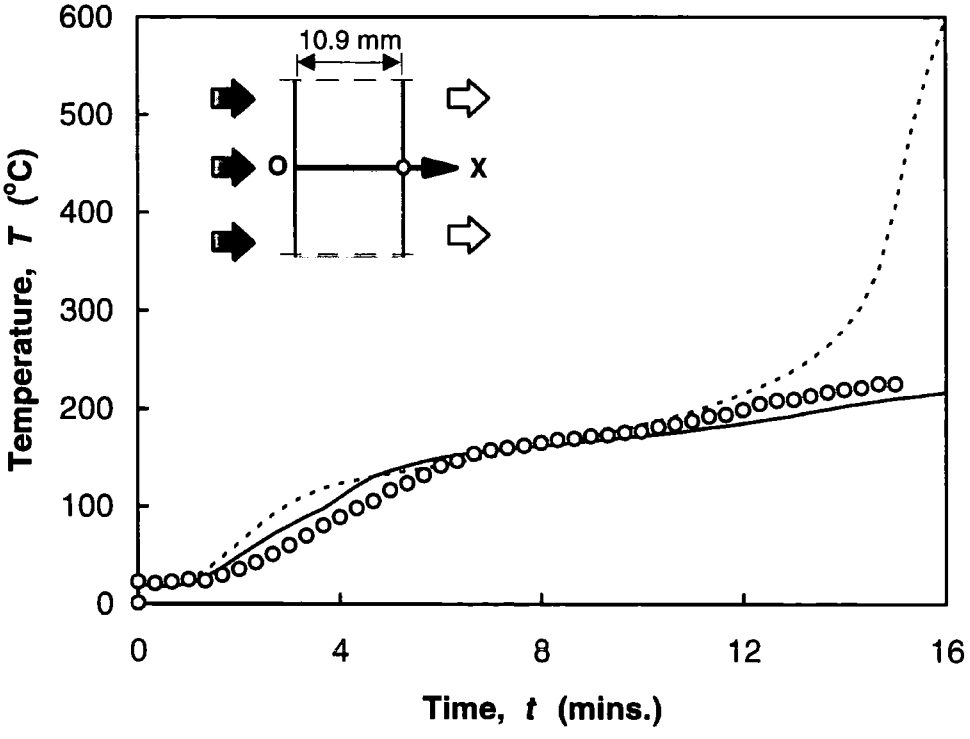

Figure 5.20 Comparisons of the computed and experimental cold surface temperatures at various times. The solid line represents the results of Model 3 with variable thermal properties and the dot line that for Model 1 with constant thermal properties. The experimental data are shown by O.

In Figure 5.21 the predicted temperatures are plotted versus distance from the hot surface to the cold surface of the GRP panel for various times. More regular distributions of the temperature profiles are evident compared to Figure 5.14.

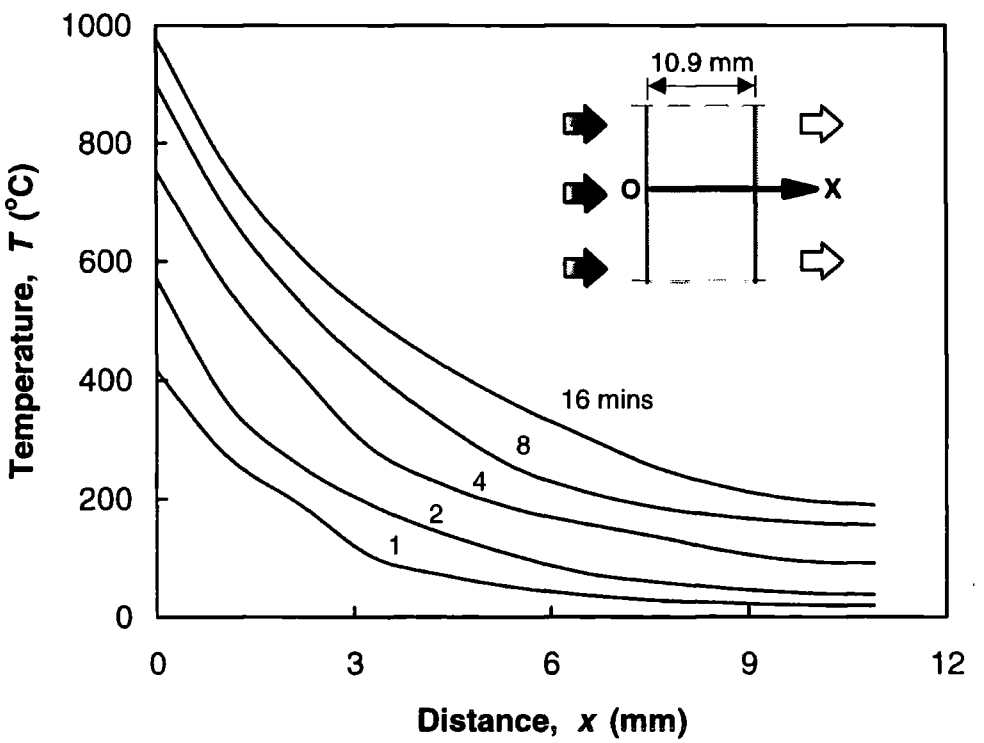

Figure 5.21 Temperature, computed by Model 3, versus distance x for various times (minutes).

Figure 5.22 shows the fraction of the resin mass with distance for various time intervals. For times greater than 2 minutes the pyrolysis reaches completion at the hot surface of the GRP panel. This value is almost the same as that for Model 1, i.e. 1.9 minutes. It is seen that after about 12 minutes half of the resin material has burnt away.

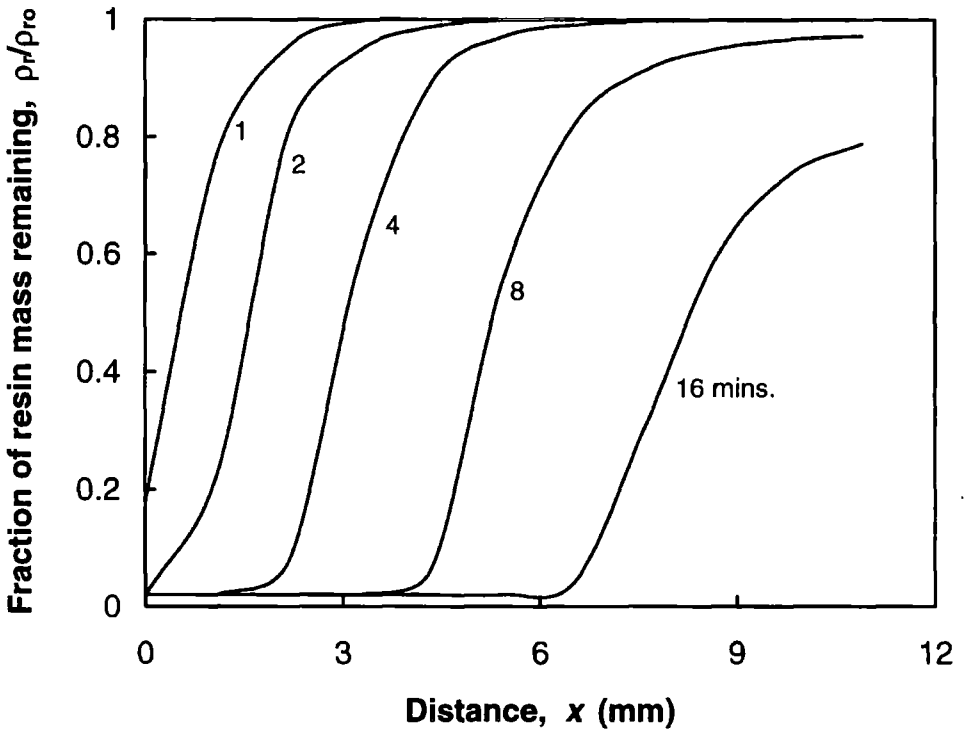

Figure 5.22 Mass fraction of the resin constituent as a function of distance x for various times (minutes).

To make a comparison between Model 1 and Model 3, the resin mass fractions of both models are plotted versus time for various locations in Figure 5.23. The solid lines represent the mass fraction results for Model 3 and the dot lines those for Model 1. At the hot surface and the first inter-laminar position, the results are very close by less than 6% average difference. At the second inter-laminar position and the cold surface, the average differences are 23.3% and 31.4%, respectively. There are two factors which are thought to cause these discrepancies:

1. The behaviour of the material described in these models is somewhat different. For Model 1, polyester resin is assumed to have burnt out completely at the end of pyrolysis; whereas, for Model 3, 2 to 3% of polyester resin remains intact. These considerations were based on two different TGA tests. Thus in Model 3, a continuous contribution of the resin to the thermal response of the material is assumed even though the resin percentage falls below 5%; whereas in Model 1 this contribution is ignored and it is assumed that, at this stage, the heat conduction is followed by the thermal properties of the glass fibre only.

2. Different kinetic properties were used for Models 1 and 3. For both models, the kinetic properties were evaluated by fitting first-order kinetic rate Arrhenius equations to the results of the TGA tests. For Model 1, the rate constant and activation energy were given by 1000 s^{-1} and 500 $MJkmole^{-1}$ and for Model 3 by 7525 s^{-1} and 611.5 $MJkmole^{-1}$, respectively. Both TGA test revealed the same heat of decomposition, i.e. 2.3446 $MJkg^{-1}$. Different samples and heating rate were used for TGA tests. These are thought to be the major factors causing huge differences in the TGA test results.

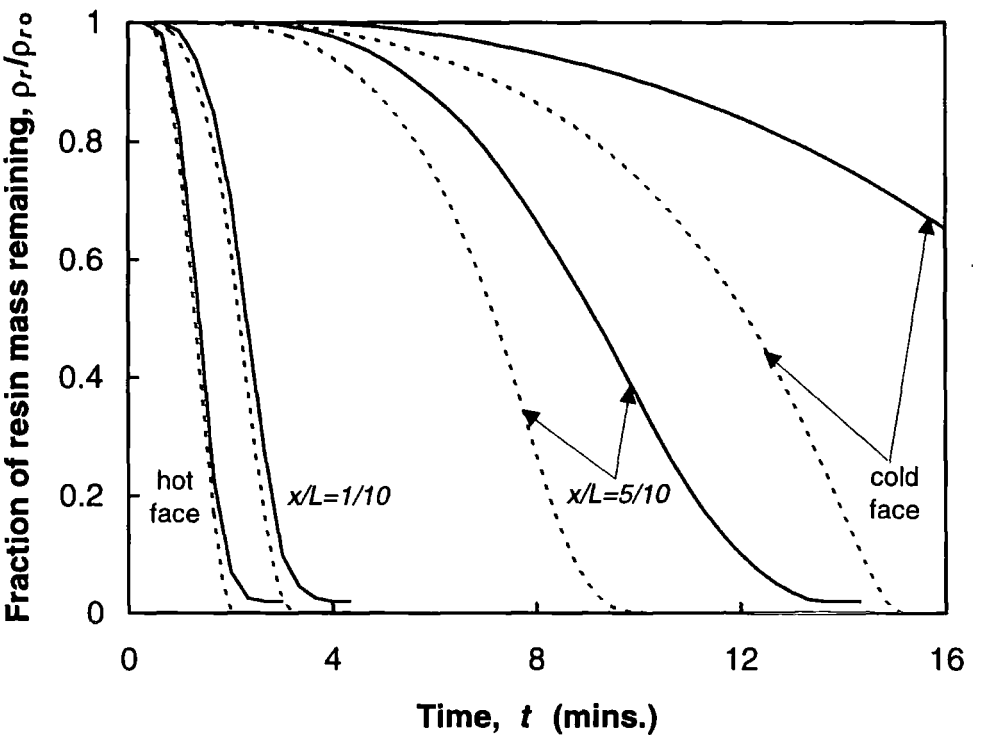

Figure 5.23 Comparison of the computed resin mass fractions between Model 3 (solid lines) and Model 1 (dot lines).

Finally, Figure 5.24 shows moisture content variations versus distance for various time intervals from the hot surface to the cold surface of the panel. It is seen that the moisture content at the hot surface evaporates in less than 0.5 minute. The line of 4 minutes indicates that the moisture content is about to disappear from the material but the actual completion of the moisture evaporation occurs at 4.5 minutes.

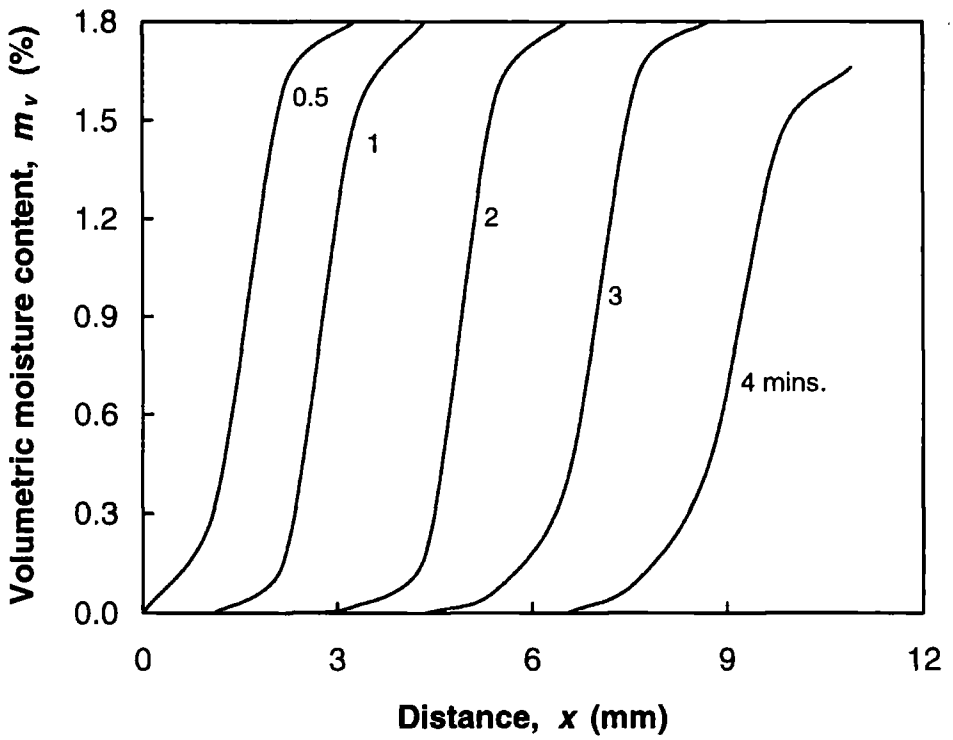

Figure 5.24 Volumetric moisture content of GRP as a function of distance x for various times (minutes).

MODEL 4

The initial properties of polyester-based GRP used for this model are the same as those given for Model 3. The atmospheric temperature and pressure are taken as 20°C and 0.1MPa. Maximum fire temperature and fire emissivity are 1100°C and 0.8. Rate constant, activation energy and heat of decomposition of the surface chemical reactions are 0.975×10^{-3} $s^{-1}K^{-1}$, 59.918 $MJkmole^{-1}$ and 20.971 $MJkg^{-1}$, respectively. The molecular weight of the pyrolysis gases is 18.35 $kgkmole^{-1}$. The initial time step is chosen 5 seconds and updated based on the critical time step after each iteration.

In Figure 5.25 the predicted hot surface temperatures are plotted versus time along with the empirical curve and experimental results. The temperature sensor showed somewhat erratic behaviour especially for $t<10$ minutes making it difficult to compare the computed and experimental results. There is no sign of sensor failure but the oscillation of the temperatures is evident. However, it is seen that the hot surface temperatures are under-predicted compared to experimentally measured temperatures

and the empirical curve for the range 1 to 7 minutes. After 7 minutes, there is a close agreement with both the measured and empirical hot surface temperatures. Three possible reasons for the lack of agreement in the early heating rates are:

1. The non-linear radiation heat transfer is defined as an equivalent linear convection heat transfer. This linearisation method reduces accuracy in the final results.
2. The surface emissivity at low temperatures and the fire emissivity may not be accurate. They were taken from literature for similar materials and environments.
3. TGA tests are normally carried out for temperatures up to 1500°C but less accuracy is achieved for T>1000°C specially at the stage of surface chemical reactions. The kinetic properties of the material due to surface chemical reactions were obtained by studying literature and may not be accurate.

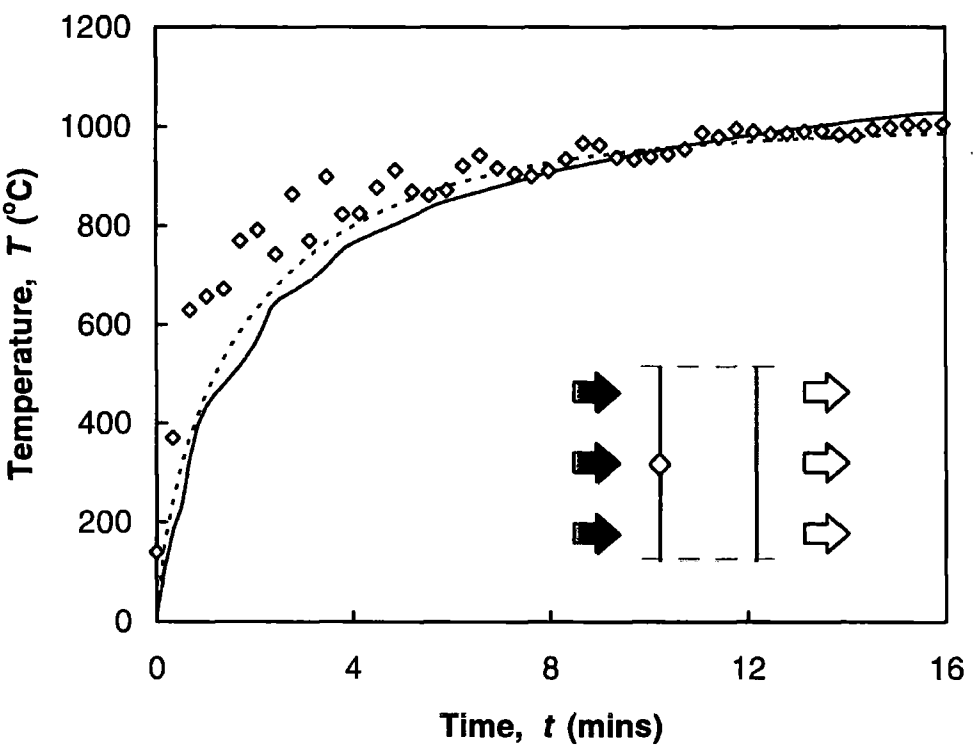

Figure 5.25 Comparison of the computed, empirical and experimental hot surface temperatures. The computed temperatures are shown as a solid line; the empirical temperatures as a dot line and the experimental temperatures as ◇, the position of which is shown in the inset.

At very low temperatures (T<50°C) the effects of radiation, gas mass movement and surface chemical reactions on the hot surface temperature are small. The major contribution is by the convection of heat between fire and the hot surface. At low temperatures (50<T<200°C), the effect of pyrolysis gases flowing away from the hot surface is small since the charring has only just begun. This can be explained by considering the term $\dot{m}_g c_{pg}/h_{c1}$ (Equation 5.35). Variation of the free convection coefficient h_{c1} with temperature is small. When the gas mass flux is very small at the early stage of pyrolysis, the term $\dot{m}_g c_{pg}/h_{c1}$ becomes very small and the blowing factor h_b (Equation 5.35) approaches 1. The convection heat transfer is then governed by the effect of convective coefficient only (Equation 5.36). For higher temperatures, the term $\dot{m}_g c_{pg}/h_{c1}$ becomes larger and the blowing factor approaches zero. At this stage there is no convection heat exchange between fire and the hot surface. This is to be expected since the pyrolysis gases act as a shield between the hot surface and environment and the heat exchange is then governed by radiation heat transfer and surface chemical reactions. At low temperatures, little radiation heat transfer occurs and there are no surface chemical reactions. As temperature rises, the radiation heat transfer begins to contribute more towards the rise of surface temperature compared to convection. With further heating involving high temperatures, the radiation heat transfer plus surface chemical reactions dominate the heat exchange between fire and the hot surface. It is seen that there is a good agreement for longer times and higher temperatures. At even higher temperatures, the effect of the radiation parameters becomes less while the surface chemical reactions play an important role. This is thought to be due to the influence of the gas mass movement on convection heat transfer and the chemical reactions on radiation heat transfer at the surface.

In Figure 5.26 the predicted and experimental temperatures are plotted versus time at various distances. The hot surface temperatures are predicted using the present model including radiation, convection, gas mass flux and surface chemical reactions terms. To compare the present model with Model 3, temperature results of both models are plotted versus time for four locations (Figure 5.27). The results are very close with 5% average difference. The present model predicts the fire resistance to be around 7.5 minutes with just few seconds difference with the experimental. The fire resistance predicted by Model 3 was 7.6 minutes.

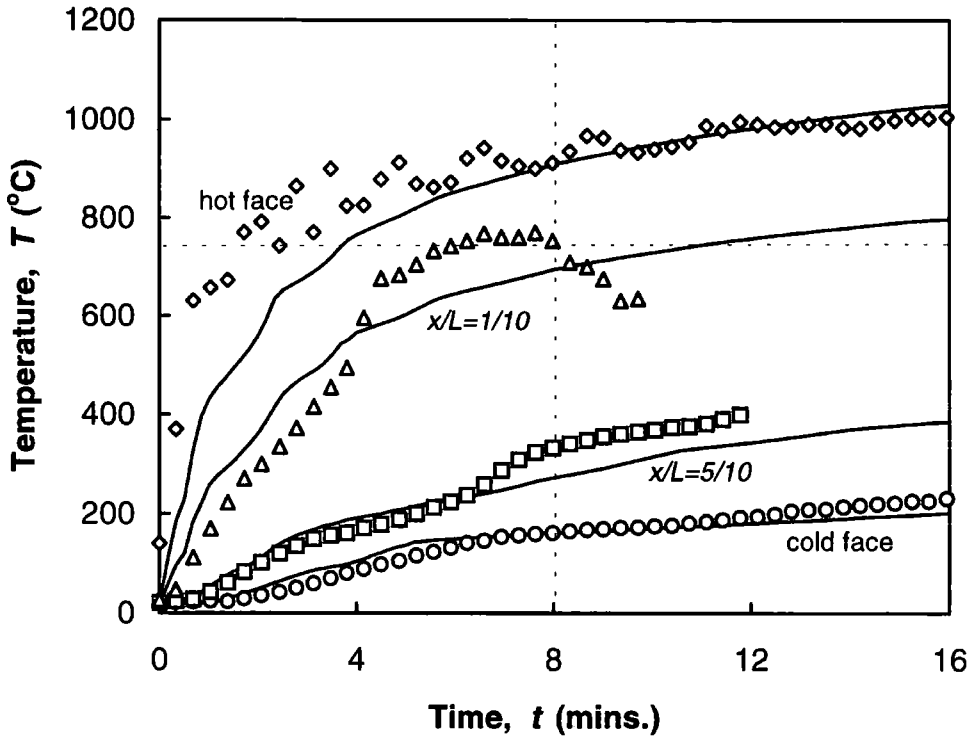

Figure 5.26 Comparisons of the computed and experimental temperatures at four locations. The computed temperatures from Model 4 are shown as solid lines and the experimental results for four sensors as ◇ △ □ ○, the position of which are shown in Figure 5.11. The failure of the inter-laminar sensor has been marked.

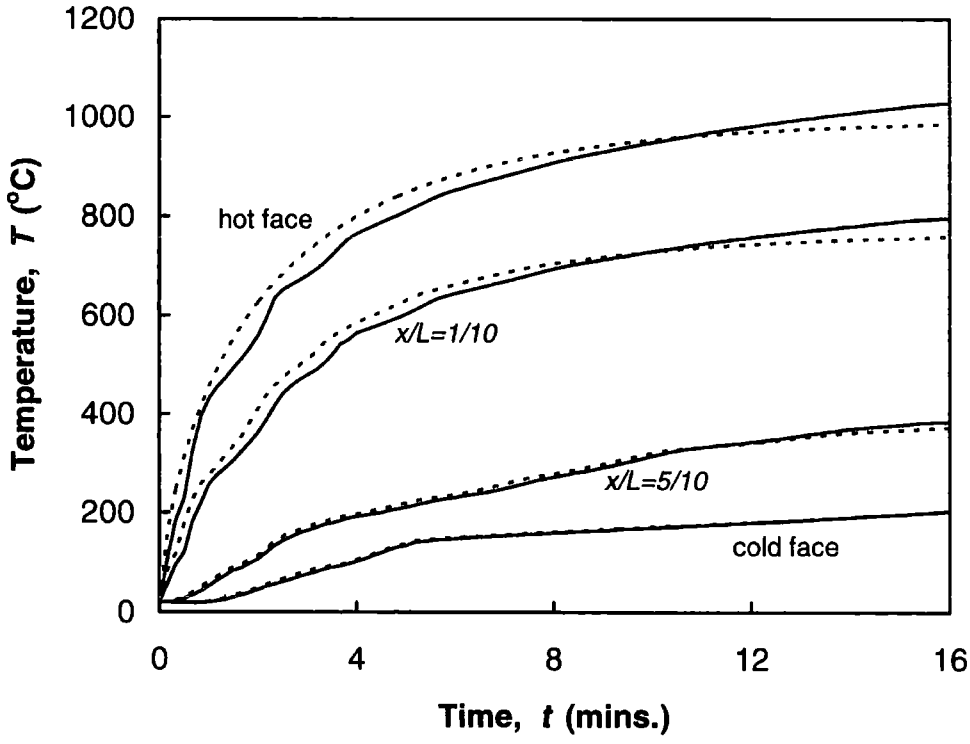

Figure 5.27 Computed temperatures versus time for various distances. The solid lines are from Model 4 including the hot surface phenomena and the dot lines from Model 3 with empirical hot surface boundary condition.

In Figure 5.28 the predicted temperatures of the present model are plotted versus distance for various times with those predicted by Model 3. The results of both models are very similar with 4% average difference.

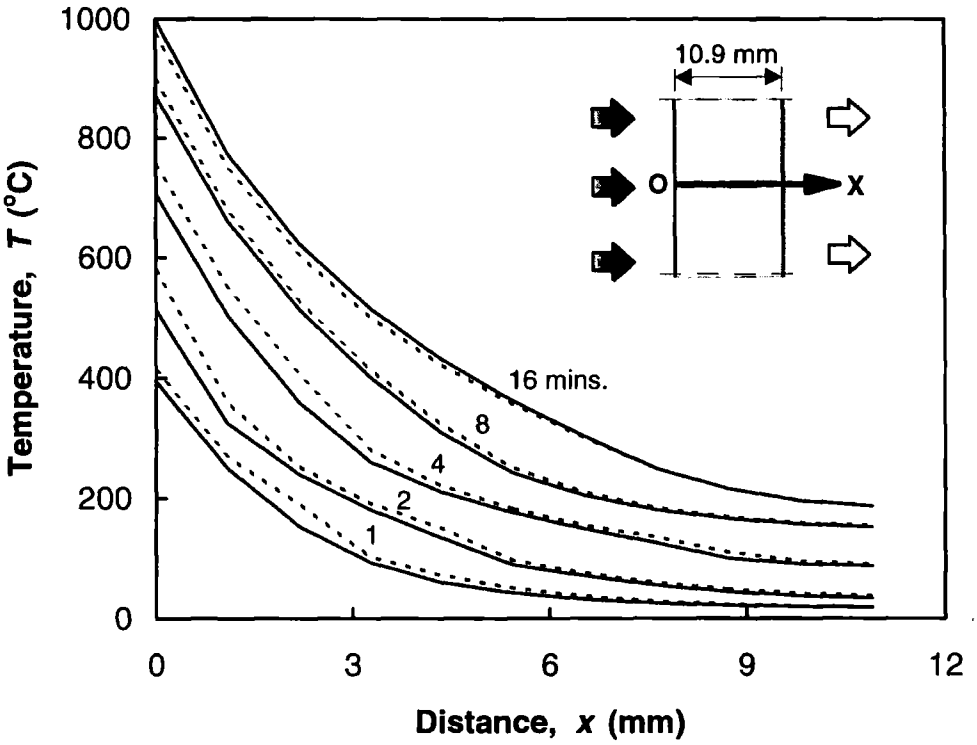

Figure 5.28 Temperature versus distance x for various times (minutes). The solid lines represent the results of Model 4 and the dot lines those of Model 3.

5.6 SUMMARY

This chapter involved the application of the finite element method to the analysis of the thermal response of thick single-skinned glass reinforced plastic (GRP) panels subject to hydrocarbon fire. A one-dimensional mathematical model and an appropriate finite element solution were developed and used to assess the fire resistance of a polyester-based GRP panel with thickness 1.09cm. The mathematical model was developed in four stages (referred to as Models 1,2 3 and 4), at each stage new terms were added. The results were presented and discussed and the relative importance of various terms and their contributions into the fire resistance behaviour of the material were assessed.

Model 1 addressed an infinite vertical panel with finite thickness L exposed to fire on one side. The resin material was assumed to burn away completely at the end of pyrolysis. The hot surface boundary condition was simulated by an empirical formula and the cold surface was assumed to be insulated. The thermal properties were assumed constant throughout fire exposure except for thermal conductivity which was assumed to have a step change at the end of pyrolysis. The computed results were reasonably good compared to the experimental with an overall temperature difference 29.6°C. Using this model, the fire resistance was predicted to occur after 7.9 minutes with 5.6% difference compared to the experimental. The contribution of each term in the modelling was investigated. It was found that the mass loss term, endothermicity and gas mass flux have considerable contributions towards the cooling behaviour and delaying the fire resistance of the material.

Model 2 added: (i) Heat energy (radiation and convection) exchange with the environment at the cold surface and (ii) Different inclinations of the panel, i.e. vertical, horizontal and inclined. It was found that GRP panels used as walls, floors and ceilings behave differently when subject to various boundary conditions. For a given set of radiation and free convection boundary conditions, the worst case in insulation failure was a horizontal panel subject to fire from below. A vertical panel with forced convection and radiation boundary conditions will survive longer than other panels with different inclinations and different boundary conditions. Also, for two identical panels under fire, one used as ceiling fails somewhat quicker than that for flooring. By adding the radiation and convection boundary conditions to the cold surface of Model 1, the difference between predicted and measured fire resistance values was reduced to 2.5%. The average temperature difference between all the predicted and measured temperatures was improved by 17.2% from 29.6°C in Model 1 to 24.5°C in the present model.

Model 3 assumed a vertical panel and added: (i) Variable thermal properties and (ii) 2 to 3% of the resin, remaining at the end of pyrolysis, into the kinetic rate equation. The temperature results showed somewhat better agreement with the experimental including regions of very low or very high temperatures. The average temperature difference between all the predicted and measured temperatures was improved from 24.5°C in Model 2 to 21.4°C in this model. This investigation revealed that the discrepancies at low temperatures were mainly due to the assumption of the constant thermal properties.

The main improvement was due to the variations of the thermal conductivity, which decreases when $T \leq 200^{o}C$ and increases for $T > 200^{o}C$. Significant improvement in temperature predictions were observed when the contribution of 2 to 3% remaining polyester resin at high temperatures were included. A better agreement between predicted and experimental fire resistance was also obtained with a small difference 1.3%.

Model 4 extended Model 3 by applying a theoretical formulation for the simulation of boundary conditions at the hot surface. This includes heat fluxes due to: (i) Radiation, (ii) Convection, (iii) Outward movement of pyrolysis gases and (iv) Surface chemical reactions. The computed hot surface temperatures agreed with the experimental and empirical temperatures by just few percent difference. While at low temperatures ($T \leq 200^{o}C$) convection has the major contribution, at the intermediate temperatures ($200 < T \leq 600^{o}C$) the contribution of the gas mass movement in reducing the convection heat transfer is evident. At this stage radiation heat transfer begins and eventually speeds up the heat exchange between the hot surface and fire. At high temperatures ($600 < T \leq 900^{o}C$) the heat exchange is mainly due to radiation and for even higher temperatures ($T > 900^{o}C$) the surface chemical reactions begin to occur where there is only limited contribution from the other terms.

There were few inconsistencies between the computed temperatures of Model 4, which included all terms, and the experimental results. The major factors were: (i) Some sensors showed somewhat erratic behaviour; (ii) Delamination happened at regions close to the hot surface; (iii) The kinetic properties were approximated including those for the surface chemical reactions; (iv) The volume of material was assumed constant; (v) Accumulation of the pyrolysis gases was not considered; and, finally, (vi) The complete physical and chemical phenomena including heat and mass transfer were not considered.

The present model is able to simulate the thermal response for a wide range of thick single-skinned GRP panels but it can not be used directly for twin-skinned GRP sandwich panels or single-skinned GRP pipes. These will be studied in Chapters 6 and 7.

CHAPTER VI

A ONE-DIMENSIONAL FINITE ELEMENT MODEL FOR THE THERMAL RESPONSE OF GLASS REINFORCED PLASTIC SANDWICH PANELS

6.1 INTRODUCTION

The ability to retain structural integrity and to reduce heat transfer is resulting in a range of new applications for polymer composites in fire sensitive applications. For structural applications, polymer composites have the added advantage that they can easily be fabricated into very strong sandwich components. For example, glass reinforced plastic (GRP) sandwich panels consist of GRP outer skins with various refractory materials sandwiched between. These twin skinned GRP composites, with internal structural elements and refractory fillers, can be used in the design of composite walls, floors and enclosures. These meet mechanical requirements plus stringent fire resistance specifications of 60 and 120 minutes in hydrocarbon fire tests, added advantage include significant weight saving, reduced maintenance costs and appreciable first cost benefit compared to steel structures.

Figure 6.1 shows four types of twin-skinned GRP sandwich panels currently used for passive fire protection applications in the offshore industry. Type (a) includes non-structural refractory sandwich material known as load bearing; whereas types (b) to (d) contain internal structural elements plus refractory sandwich materials (SM) known as non-load bearing. Special construction is required when choosing the sandwich material, as most load bearing sandwich materials have not been developed for high performance in hydrocarbon fires. The sandwich materials with the best thermal performance are ceramics and these tend to be brittle. Two possible options for sandwich materials are: (i) lightweight, non-structural, ceramic insulating materials such as ceramic blanket insulation used in steel fire protection panels, and (ii) structural

sandwich materials with moderate fire resistance such as end-grain balsa which is widely used in marine bulkheads because of its low thermal conductivity and fire resistance properties. The best sandwich material is one with excellent fire resistance properties and load bearing capability. There are several compressed ceramics or cement board materials such as calcium silicate material (Vermiculux). In this work we study type (a) with Vermiculux sandwich material (Figure 6.1).

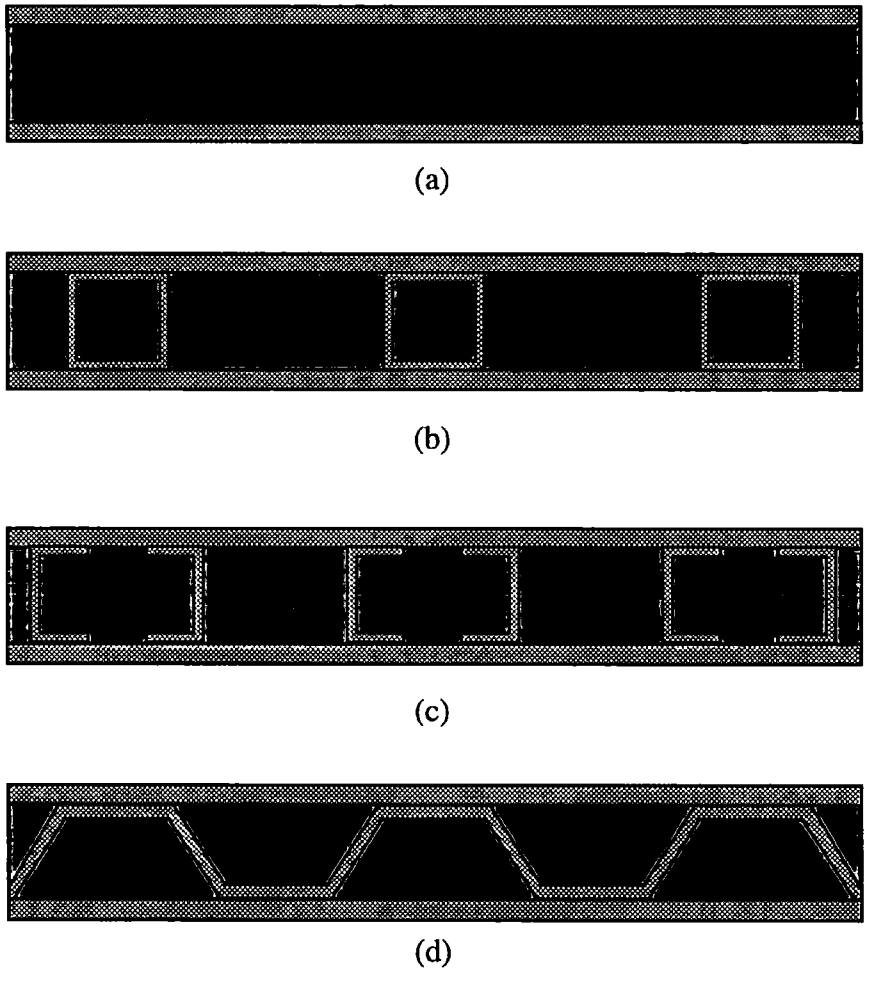

Figure 6.1 Four types of construction for fire resistant sandwich panels; (a) Twin-skinned sandwich panel with load bearing sandwich material; (b), (c) and (d) Twin-skinned sandwich panels with non-load bearing sandwich materials and internal structural elements. In all cases, the outer skins are GRP and the sandwich material can be ceramic blanket insulation, end-grain balsa and Vermiculux of which Vermiculux is the most efficient. The structural elements can be metallic or non-metallic.

In Phases I and II of the Marinetech research programme on "Cost-effective Use of Fibre Reinforced Composites Offshore" some basic work was carried out to quantify the fire performance of composite sandwich panels [Gibson *et al.*, 1992; Spagni & Gibson, 1994]. Panels containing different types of sandwich materials were fire tested. Temperatures were measured on the unexposed (cold) surfaces of various panels until a temperature of 160°C was reached. These were found to be more than 120 minutes for panels with the ceramic sandwich materials. An investigation into the effect of panel thickness on fire resistance (insulation failure) revealed that 120 minutes (H120) is achieved with sandwich thickness at least 3.5cm and 0.9cm skin thickness.

In this chapter, a finite element model is developed to predict the thermal response of twin-skinned GRP sandwich panels subject to fire with object of identifying the best possible panel configurations. Twin-skinned sandwich panels with polyester-based GRP skins and Vermiculux sandwich material are investigated. The model developed previously for single-skinned GRP panels are extended to analyse heat transfer phenomena in GRP skins and refractory sandwich material. Unlike GRP skins, the sandwich material does not undergo any thermochemical decomposition requiring modification of the governing equations for through-the-thickness direction (i.e. from hot to cold surface). Temperature and moisture-dependent thermal properties are included for both GRP and sandwich materials together with realistic boundary conditions. The numerical results are compared with experimental data and discussed.

6.2 MATHEMATICAL MODEL

When two surfaces are brought into contact, the contact surface is imperfect resulting in non-uniform temperature gradients. The temperature difference at the contact depends upon the thermal properties of the materials in contact, the characteristics of the contacting surface and the presence of gaseous and non-gaseous interstitial media along the contact surface.

A bonding process is applied to the surfaces of both GRP and sandwich materials during the fabrication of twin-skinned GRP sandwich panels. This process enhances the GRP/SM/GRP interfacial bonding but imperfections remain and the adherent surfaces are not in perfect contact resulting in heat passing through a limited number of contact spots as shown in Figure 6.2.

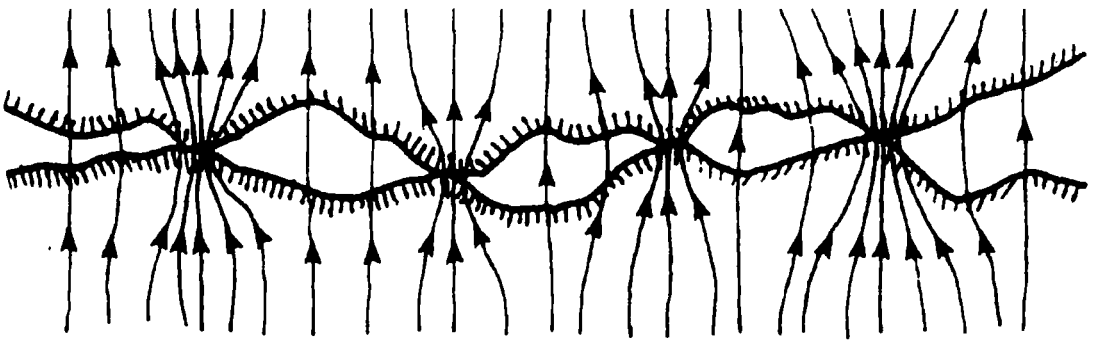

Figure 6.2 Heat flow across a contact surface [from: Fletcher, 1988].

Several successful mathematical models have been developed in recent years which predict the thermal response of composite panels undergoing thermal decomposition [Looyeh & Bettess, 1998a&b; Looyeh *et al.*, 1997; Wang, 1995; Wu *et al.*, 1994]. These have focused on single-skinned composite panels only. Modelling the thermal response of a twin-skinned composite panel demands a detailed knowledge of thermal behaviour of the two adjacent materials. The approach adapted is to formulate the phenomenon of heat transfer through each region individually assuming heat flow in through-the-thickness direction where it remains constant through the whole domain of the panel (Figure 6.3). Thus the model is developed in three parts:

(i) Heat transfer for the two GRP outer skins. The formulation defined in Model 3 of Chapter 5 is used.

(ii) Heat transfer through the sandwich material including temperature dependent and moisture dependent thermal properties.

(iii) Heat transfer at the GRP/SM/GRP interfaces.

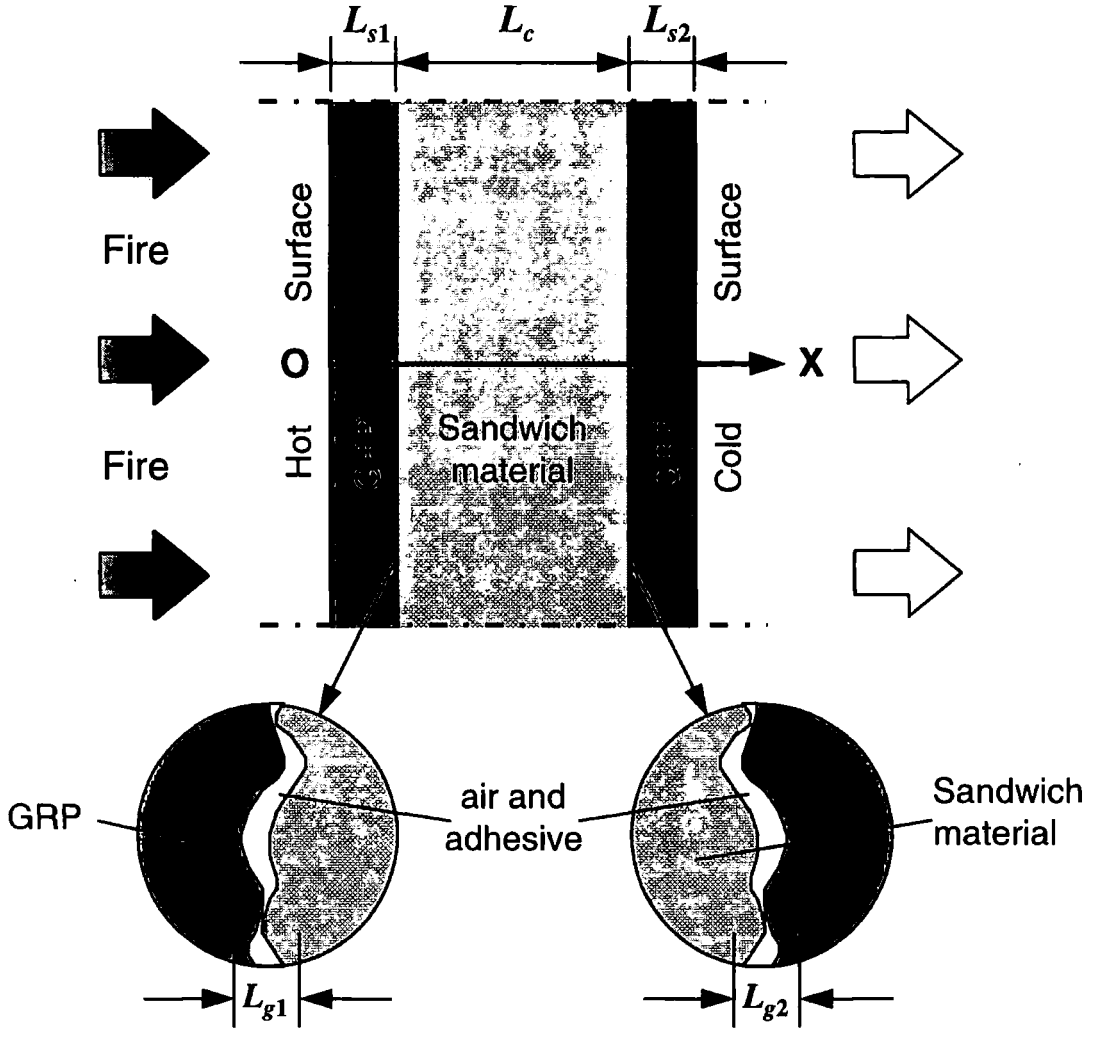

Figure 6.3 Sandwich panel with GRP skins and refractory sandwich material subject to fire from one side.

(i) Heat transfer for the two GRP outer skins

The model extends that for single-skinned GRP panels (Chapter 5-Model 3). It is assumed that no volume contraction/expansion occurs during fire exposure and the characteristics of GRP skins and interfaces are the same. Thus the model can be assumed symmetric. When $L_{s1}=L_{s2}=L_s$ and $L_{g1}=L_{g2}=L_g$, the energy equation for one-dimensional heat transfer through the GRP skins of thicknesses L_s (Figure 6.3) undergoing thermochemical decomposition is given by the following non-linear, second order, partial differential equation, which is valid for both front and back skins:

$$\rho c_p \frac{\partial T}{\partial t} = k\frac{\partial^2 T}{\partial x^2} - \dot{m}_g c_{pg}\frac{\partial T}{\partial x} - \frac{\partial \rho_r}{\partial t}\left(Q + h - h_g\right) \quad \text{for} \quad \begin{matrix} 0 \le x \le L_s \\ L_s + L_c + 2L_g \le x \le L \end{matrix} \qquad (6.1)$$

where

ρ = density of GRP (kgm^{-3})

c_p = specific heat of GRP ($Jkg^{-1}K^{-1}$)

T = temperature (^oC)

t = time (s)

k = thermal conductivity of GRP ($Wm^{-1}K^{-1}$)

x = spatial co-ordinate starting at the hot surface (m)

$\dot{m}_g$ = gas mass flux ($kgm^{-2}s^{-1}$)

c_{pg} = gas specific heat ($Jkg^{-1}K^{-1}$)

ρ_r = density of resin (active) material (kgm^{-3})

Q = heat of decomposition (Jkg^{-1})

h = enthalpy of material (Jkg^{-1})

h_g = enthalpy of gas (Jkg^{-1})

A = pyrolysis constant (s^{-1})

L_s = thickness of the GRP skin (m)

L_c = thickness of sandwich material (m)

L_g = thickness of the void space (m)

L = total thickness of the twin-skinned GRP sandwich panel (m)

= $2L_s+L_c+2L_g$

The initial conditions are given by:

$$\begin{array}{ll} T(x,t)=T_\infty & m(x,t)=m_o \\ c_p=c_{po} & \rho=\rho_o \\ k=k_o & \varepsilon=\varepsilon_o \\ c_{pg}=c_{pgo} & \dot{m}_g=0 \end{array} \quad \text{for} \quad \begin{array}{r} 0\le x\le L_s \\ L_s+L_c+2L_g\le x\le L \\ t=0 \end{array} \tag{6.2}$$

and the boundary conditions by:

$$-k\frac{\partial T}{\partial x}=T_s(t) \quad \text{for} \quad x=0,\ t>0 \tag{6.3}$$

$$-k\frac{\partial T}{\partial x}=h_{TCR}(T_1-T_2) \quad \text{for} \quad x=L_s,\ t>0 \tag{6.4}$$

$$-k\frac{\partial T}{\partial x}=h_{TCR}(T_3-T_4) \quad \text{for} \quad x=L_s+L_c+2L_g,\ t>0 \tag{6.5}$$

$$-k\frac{\partial T}{\partial x}=q_r+q_c\ ,\ \dot{m}_g=0 \quad \text{for} \quad x=L,\ t>0 \tag{6.6}$$

where

m_v = volumetric moisture content

ε = surface emissivity

$T_s(t)$ = hot surface time-dependent temperature (°C)

h_{TCR} = coefficient of thermal contact resistance ($Wm^{-2}K^{-1}$)

T_1 = cold surface temperature of the front GRP skin (°C)

T_2 = hot surface temperature of the sandwich material (°C)

T_3 = cold surface temperature of the sandwich material(°C)

T_4 = hot surface temperature of the back GRP skin (°C)

q_r = radiation heat flux at the cold surface of the back GRP skin (Wm^{-2})

q_c = convection heat flux at the cold surface of the back GRP skin (Wm^{-2})

and subscript o denotes initial quantities.

$T_s(t)$ was introduced in Chapter 3 by an empirical relation [Wu *et al.*, 1994], i.e.:

$$T_s(t) = (T_g - 100)\left\{1 - \exp\left\{-\exp\left[0.71\log\left(\frac{t}{124.8}\right)\right]\right\}\right\} + T_\infty \quad \text{for} \quad t > 0 \qquad (6.7)$$

where T_g is the maximum fire temperature (1100°C) and T_∞ is the ambient temperature (20°C).

h_{TCR} will be explained in detail in part (iii).

q_r and q_c are given by Equations 3.12 and 3.14, i.e.:

$$q_r = h_r(T - T_\infty) \qquad (6.8)$$

$$q_c = h_c(T - T_\infty) \qquad (6.9)$$

where h_r and h_c are the equivalent convection coefficient ($Wm^{-2}K^{-1}$) and the convection coefficient ($Wm^{-2}K^{-1}$) expressed by Equations 3.13 and 3.15, i.e.:

$$h_r = \sigma\varepsilon\left(T_k^2 + T_{\infty k}^2\right)\left(T_k + T_{\infty k}\right) \qquad (6.10)$$

$$h_c = k_{e\infty}\frac{\overline{\mathrm{Nu}}_H}{H} \qquad (6.11)$$

and σ = Stefan-Boltzmann constant (5.669×10^{-8} W $m^{-2}K^{-4}$)

T_k = cold surface temperature (K)

$T_{\infty k}$ = ambient temperature (293K)

$k_{e\infty}$ = thermal conductivity of air at ambient temperature ($Wm^{-1}K^{-1}$)

$\overline{\mathrm{Nu}}_H$ = average Nusselt number (given by Equation 3.16 for vertical panels)

H = height of panel (m)

The rate of resin decomposition, mass flux of pyrolysis gases in the front and back GRP skins and enthalpies of GRP and pyrolysis gases are defined similarly by Equations 2.11, 2.12 and 2.6, i.e.:

$$\frac{\partial \rho_r}{\partial t} = -A\left(\rho_r - \rho_{rf}\right)\exp\left(\frac{-E_A}{RT_k}\right) \tag{6.12}$$

$$\dot{m}_{g1} = \int_{L_s}^{\hat{x}} \frac{\partial \rho_r}{\partial t} dx \qquad \text{for} \qquad 0 \le \hat{x} \le L_s \tag{6.13}$$

$$\dot{m}_{g2} = \int_{L}^{\hat{x}} \frac{\partial \rho_r}{\partial t} dx \qquad \text{for} \qquad L_s + L_c + 2L_g \le \hat{x} \le L \tag{6.13}$$

$$h = \int_{T_\infty}^{T} c_p dT \quad , \quad h_g = \int_{T_\infty}^{T} c_{pg} dT \tag{6.14}$$

where A is the pyrolysis constant (s^{-1}), ρ_{rf} is the final density of resin (kgm^{-3}), E_A is the activation energy ($kJkmole^{-1}$) and R is the gas constant (8.314 $kJkmole^{-1}K^{-1}$).

(ii) Heat transfer through the sandwich material

It is assumed that the sandwich material experiences no thermochemical decomposition. The one-dimensional heat transfer through the sandwich material of thickness L_c is by simple mechanism of transient heat conduction and can be expressed by:

$$\rho_c c_{pc} \frac{\partial T}{\partial t} = k_c \frac{\partial^2 T}{\partial x^2} \qquad \text{for} \qquad L_s + L_g \le x \le L_s + L_g + L_c \tag{6.15}$$

where

ρ_c = density of sandwich material (kgm^{-3})

c_{pc} = specific heat of sandwich material ($Jkg^{-1}K^{-1}$)

k_c = thermal conductivity of sandwich material ($Wm^{-1}K^{-1}$)

The initial conditions are given by:

$$\begin{matrix} \rho_c = \rho_{co} \\ c_{pc} = c_{pco} \\ k_c = k_{co} \end{matrix} \qquad \begin{matrix} T(x,t) = T_\infty \\ m_{vc}(x,t) = m_{vco} \end{matrix} \qquad \text{for} \qquad \begin{matrix} L_s + L_g \le x \le L_s + L_g + L_c \\ t = 0 \end{matrix} \tag{6.16}$$

and the boundary conditions by:

$$-k_c \frac{\partial T}{\partial x} = h_{TCR}(T_1 - T_2) \qquad \text{for} \qquad x = L_s + L_g,\ t > 0 \tag{6.17}$$

$$-k_c \frac{\partial T}{\partial x} = h_{TCR}(T_3 - T_4) \qquad \text{for} \qquad x = L_s + L_g + L_c,\ t > 0 \tag{6.18}$$

As with GRP material, the temperature and moisture dependent properties of sandwich material must be considered. It is important to know that sandwich materials contain high percentage of moisture content and therefore the specific heat and thermal conductivity of these materials vary substantially with moisture gradients. These effects were studied in Chapter 4.

(iii) Heat transfer at the GRP/SM/GRP interfaces

Considerable efforts have been expended in recent years to understand what happens when heat flows across the interface of two materials in contact [Holman, 1997; Fletcher, 1988; Saith *et al.*, 1986; Yovanovich, 1986; Sheffield *et al.*, 1980; Clausing, 1966]. There have also been significant advances in analytical models used to predict the thermal contact resistance at the interface. Models for selected conditions and geometries have been developed and refined with remarkable success [Holman, 1997; Fletcher, 1988]. The diverse nature of the thermal contact conductance phenomenon is such that a generalised prediction technique has not been developed so far.

The contact resistance is due to the area of contact being only a small fraction of the nominal area (Figure 6.2). The contact resistance is defined as the ratio of the temperature drop at the interface to the average heat flux across the junction. The thermal contact resistance is related to the thermal conductance at or across the contact plane which depends on the physical nature of the junction.

GRP sandwich panels are fabricated to achieve the best possible and cost-effective bonding. For fire test purposes and to avoid interfacial failure, the surfaces of the adherents are pre-treated. An angle grinder is used to eliminate release agents and reduce surface roughness. Finally, a degreasing cleaning process is used. Despite this care, the GRP/SM/GRP bondings are not perfect and in this section the effect is investigated. It might be expected that fabrication imperfections might cause variations of temperature across the interfaces.

Performing a one-dimensional energy balance for a sandwich panel, exposed to fire on one side, results in the following energy equations for GRP/SM and SM/GRP interfaces:

$$-k\,\frac{\partial T}{\partial x} = \frac{(T_1 - T_2)}{1/h_{TCR}} \tag{6.19}$$

$$-k_c\,\frac{\partial T}{\partial x} = \frac{(T_3 - T_4)}{1/h_{TCR}} \tag{6.20}$$

where the quantity $1/h_{TCR}$ is the thermal contact resistance per unit area (m^2KW^{-1}).

The surface roughness of both GRP skins and sandwich material are important in determining the thermal contact resistance (Figure 6.4). The principal contributors to the heat transfer through the interfaces are: (i) conduction through the points of contact; (ii) conduction through the adhesive itself and (iii) conduction through entrapped gases. The last represents the major factor in contact resistance calculation. This is the major resistance to heat flow, because the thermal conductivity of entrapped gas is very small compared to those for GRP and sandwich material. Using Fourier's law of heat conduction [Fourier, 1882], the heat flow across the interfaces may be written as:

$$qA = \frac{T_1 - T_2}{\left[L_g/2k(A - A_g)\right] + \left[L_g/2k_c(A - A_g)\right]} + \frac{T_1 - T_2}{L_g/k_g A_g} = \frac{T_1 - T_2}{1/h_{TCR}A} \tag{6.21}$$

$$qA = \frac{T_3 - T_4}{\left[L_g/2k(A - A_g)\right] + \left[L_g/2k_c(A - A_g)\right]} + \frac{T_3 - T_4}{L_g/k_g A_g} = \frac{T_3 - T_4}{1/h_{TCR}A} \tag{6.22}$$

where

q = heat flux (Wm^{-2})

A = total cross-sectional area of sandwich panel (m^2)

A_g = void area (m^2)

k_g = thermal conductivity of entrapped gas in void space ($Wm^{-1}K^{-1}$)

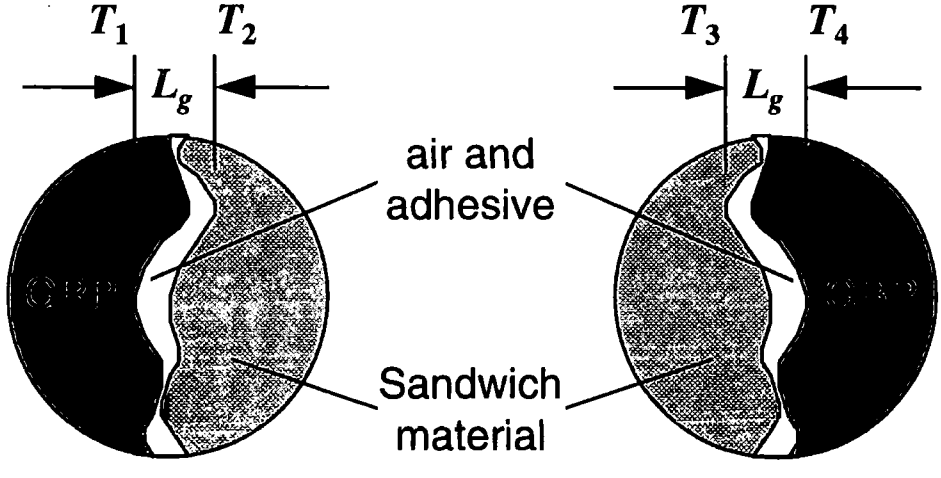

Figure 6.4 Magnification of the imperfect contact and roughness model for the analysis of thermal contact resistance at GRP/Sandwich and Sandwich/GRP interfaces.

Solving Equations 6.21 and 6.22 for h_{TCR} gives [Holman, 1997]:

$$h_{TCR} = \frac{1}{L_g}\left(\left(1-\frac{A_g}{A}\right)\frac{2kk_c}{k+k_c}+\frac{A_g}{A}k_g\right) \tag{6.23}$$

where the thermal conductivity of entrapped gas in the void space, k_g, is small compared with k and k_c. If the contact area is small, the major thermal contact resistance will be from the void space. It is difficult to determine the effective values of A_g/A and L_g for surfaces in contact with accuracy.

6.3 FINITE ELEMENT FORMULATION

The set of governing differential equations, i.e. Equations 6.1, 6.12 to 6.15, 6.19 and 6.20 are solved numerically using the finite element method. Bubnov-Galerkin (weighted residual) approach is adopted. All terms and coefficients are evaluated explicitly using an iterative-updating procedure at each step of computations. Nodal temperatures are computed implicitly using the Crank-Nicolson solution.

6.3.1 Explicit Evaluation of Terms and Coefficients

A general notation $(\ )_j^i$ is used where i represents the time interval and j the spatial position. Time derivative terms are given by forward difference and the spatial variables by central difference, with exception of the gas mass flux term which is represented by backward difference.

Using notation $(\ )_j^i$, Equations 6.1 and 6.15 at each time interval and nodal position can be given by:

$$\rho_j^{i+1}\left(c_p\right)_j^{i+1}\frac{\partial T}{\partial t} = k_j^{i+1}\frac{\partial^2 T}{\partial x^2} - \left(\dot{m}_g\right)_j^{i+1}\left(c_{pg}\right)_j^{i+1}\frac{\partial T}{\partial x} - \left(\frac{\partial \rho_r}{\partial t}\right)_j^{i+1}\left\{Q+\left[\left(c_p\right)_j^{i+1}-\left(c_{pg}\right)_j^{i+1}\right]\left(T-T_\infty\right)\right\} \tag{6.24}$$

$$\rho_c\left(c_{pc}\right)_j^{i+1}\frac{\partial T}{\partial t} = \left(k_c\right)_j^{i+1}\frac{\partial^2 T}{\partial x^2} \tag{6.25}$$

where $$\rho_j^{i+1} = \left\{ (\rho_r)_j^i - A\Delta t\left[(\rho_r)_j^i - \rho_{rf}\right]\exp\left[\frac{-E_A}{R(T_k)_j^i}\right]\right\}(1-V_f) + \rho_{fr}V_f \tag{6.26}$$

$$(\dot{m}_g)_j^{i+1} = \sum_{j=n_x}^{n_T}\left[\frac{(\rho_r)_j^{i+1} - (\rho_r)_j^i}{\Delta t}\right] l_j \tag{6.27}$$

$$\left(\frac{\partial \rho_r}{\partial t}\right)_j^{i+1} = \frac{(\rho_r)_j^{i+1} - (\rho_r)_j^i}{\Delta t} = -A\left[(\rho_r)_j^i - \rho_{rf}\right]\exp\left[\frac{-E_A}{R(T_k)_j^i}\right] \tag{6.28}$$

and

Δt = time step size (s)

V_f = volume fraction

n_x = number of spatial nodes at position x in GRP domain

n_T = total number of spatial nodes in GRP domain

l = element length in GRP domain (m)

Using notation $(\ )_j^i$, Equations 6.19 and 6.20, representing heat transfer across the interfaces, can be given, at each time interval and nodal position, by:

$$-k_j^{i+1}\frac{\partial T}{\partial x} = \frac{(T_1 - T_2)}{1/(h_{TCR})_j^{i+1}} \tag{6.29}$$

$$-(k_c)_j^{i+1}\frac{\partial T}{\partial x} = \frac{(T_3 - T_4)}{1/(h_{TCR})_j^{i+1}} \tag{6.30}$$

where $$(h_{TCR})_j^{i+1} = \frac{1}{L_g}\left(\left(1 - \frac{A_g}{A}\right)\frac{2k_j^{i+1}(k_c)_j^{i+1}}{k_j^{i+1} + (k_c)_j^{i+1}} + \frac{A_g}{A}(k_g)_j^{i+1}\right) \tag{6.31}$$

and expressions for $(c_p)_j^{i+1}$, $(k)_j^{i+1}$ are given in Table 4.3, for $(c_{pg})_j^{i+1}$ in Table 4.4, for $(k_g)_j^{i+1}$ in Table 3.3 (when the entrapped gas is air) and for $(c_{pc})_j^{i+1}$ and $(k_c)_j^{i+1}$ in Table 4.5.

6.3.2 Modelling of Temperature Drop at GRP/SM/GRP Interfaces

Two methods are used: (1) Explicit evaluation of temperature drop using forward difference method and (2) implicit evaluation of temperature drop using finite element method. These methods are explained in detail and then used in conjunction with the governing equations to derive the finite element equations.

(1) Explicit evaluation of temperature drop using forward difference method

The interfacial surfaces of GRP skins and sandwich material, which are numbered from 1 to 4 (Figure 6.5), are assumed to be perfectly in contact, i.e. $L=2L_s+L_c$. The GRP/SM/GRP interfaces are represented by points m and n, respectively. Temperatures corresponding to surfaces 1 and 3 are given by T_{m1} and T_{n3} and those corresponding to surfaces 2 and 4 by T_{m2} and T_{n4} (Figure 6.5). To include the effect of temperature drops, i.e. ΔT_m and ΔT_n, in the finite element equations, the unknown temperatures T_{m2} and T_{n4} must be evaluated while T_{m1} and T_{n3} are known. These temperatures are then used in the corresponding boundary conditions within the finite element equations. This method is repeated over each specific time interval.

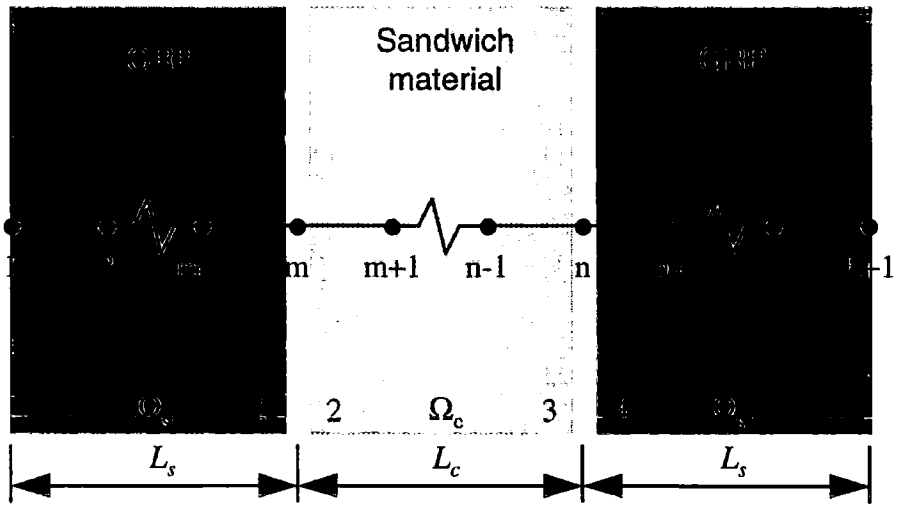

Figure 6.5 Finite element model for the twin-skinned sandwich panel. The model corresponds to the explicit evaluation of the temperature drop including three sub-domains and four contact surfaces. It also includes E linear elements and E+1 nodes. 1, 2, m-1,..., E+1 represent the nodal points where m and n are the nodes at the interfaces.

The equations for the forward difference method are obtained from Equations 6.19 and 6.20 and can be written:

$$-k_m^{i+1}\frac{T_{m1}-T_{m-1}}{l_s}=\left(h_{TCR}\right)_m^{i+1}\left(T_{m1}-T_{m2}\right) \tag{6.32}$$

$$-\left(k_c\right)_n^{i+1}\frac{T_{n3}-T_{n-1}}{l_c}=\left(h_{TCR}\right)_n^{i+1}\left(T_{n3}-T_{n4}\right) \tag{6.33}$$

where

T_{m1} = temperature corresponding to contact surface 1 (°C)

T_{m2} = temperature corresponding to contact surface 2 (°C)

T_{n3} = temperature corresponding to contact surface 3 (°C)

T_{n4} = temperature corresponding to contact surface 4 (°C)

l_s = element length at GRP domain (m)

l_c = element length at sandwich material domain (m)

It is evident that the forward difference method is an approximation to the temperature gradients across the interfaces.

Equations 6.32 and 6.33 are solved for T_{m2} and T_{n4} and can be represented as:

$$T_{m2} = \frac{T_{m1}\left[k_m^{i+1} + \left(h_{TCR}\right)_m^{i+1} l_s\right] - k_m^{i+1} T_{m-1}}{\left(h_{TCR}\right)_m^{i+1} l_s} \tag{6.34}$$

$$T_{n4} = \frac{T_{n3}\left[\left(k_c\right)_n^{i+1} + \left(h_{TCR}\right)_n^{i+1} l_c\right] - \left(k_c\right)_n^{i+1} T_{n-1}}{\left(h_{TCR}\right)_n^{i+1} l_c} \tag{6.35}$$

(2) Implicit evaluation of temperature drop using finite element method

Alternatively, the effect of temperature drop on heat transfer at the GRP/SM/GRP interfaces is modelled by a simple approximation using linear finite elements at the contact boundaries [Zienkiewicz *et al.*, 1978].

Earlier, in the study of the heat transfer across the GRP/SM/GRP interfaces, the boundary conditions for the contact surfaces were introduced (Equations 6.4, 6.5, 6.17 and 6.18). It was assumed that the heat transfer through the GRP/SM/GRP interfaces is directly proportional to the difference in temperatures across them.

Multiply Equations 6.4 and 6.5 by L_g/L_g and rearrange them, the equations become:

$$q = L_g h_{TCR} \frac{(T_1 - T_2)}{L_g} \tag{6.36}$$

$$q = L_g h_{TCR} \frac{(T_3 - T_4)}{L_g} \tag{6.37}$$

These represent Fourier's law of heat conduction where L_g is the length and the term $L_g h_{TCR}$ denotes the thermal conductivity of the bonding domain. Each equation can be modelled using a linear finite element with two nodes, used to couple the GRP and

sandwich material domains. The effect of temperature drop on heat transfer through the GRP/SM/GRP interfaces are therefore modelled by applying two linear elements, i.e. Ω_1 and Ω_2, as shown in Figure 6.6.

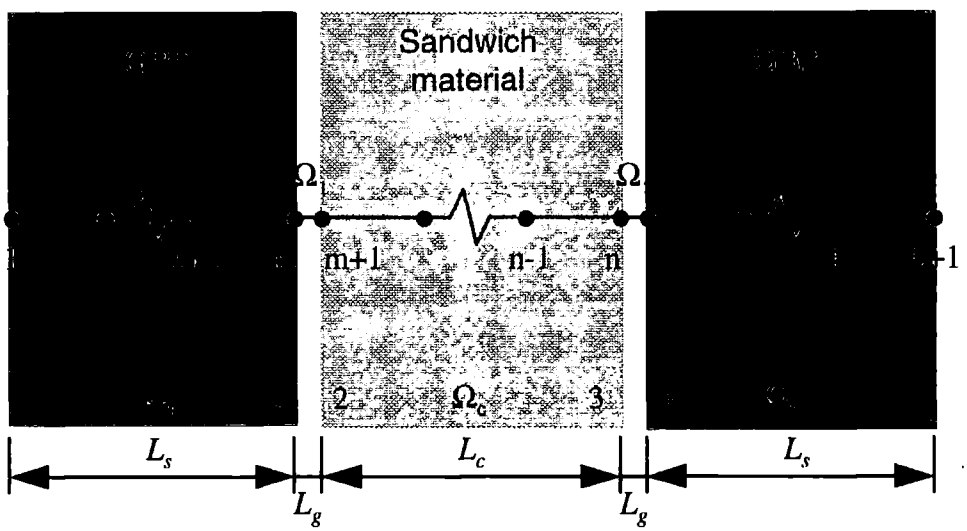

Figure 6.6 Finite element model for the twin-skinned sandwich panel. The model corresponds to the implicit evaluation of the temperature drop including five sub-domains and four contact surfaces. It also includes *E* linear elements including Ω_1 and Ω_2 at the interfaces and *E*+1 nodes.

6.3.3 Finite Element Equations

Using the Bubnov-Galerkin (weighted residual) approach described in Chapter 2, the finite element equations can be given in the form:

$$\mathbf{C}\dot{\mathbf{T}} + \mathbf{K}\mathbf{T} + \mathbf{f} = \mathbf{0} \tag{6.38}$$

where

$\mathbf{C}$	=	element capacitance matrix
$\dot{\mathbf{T}}$	=	vector of temperature derivatives with respect to time
$\mathbf{K}$	=	element conductance matrix
$\mathbf{T}$	=	temperature vector
$\mathbf{f}$	=	element heat load vector

The finite element equations are derived for GRP skins and sandwich material in the same way as explained in Chapter 2.

Finite element equations for Method 1

The solution domain Ω ($=\Omega_{s1}+\Omega_c+\Omega_{s2}$), which is a one-dimensional multi-layered solid of thickness L ($=2L_s+L_c$), is divided into E linear elements of different lengths and two nodes each (Figure 6.5).

Using the Bubnov-Galerkin (weighted residual) approach, the element equation for the front GRP skin, i.e. domain Ω_{s1}, is given by:

$$\left[\int_0^{l_s}\mathbf{N}^{\mathrm{T}}\rho_j^{i+1}\left(c_p\right)_j^{i+1}\mathbf{N}dx\right]\dot{\mathbf{T}}+\left\{\int_0^{l_s}\mathbf{B}^{\mathrm{T}}k_j^{i+1}\mathbf{B}dx\right.$$

$$\left.+\int_0^{l_s}\mathbf{B}^{\mathrm{T}}\left(\dot{m}_g\right)_j^{i+1}\left(c_{pg}\right)_j^{i+1}\mathbf{N}dx+\int_0^{l_s}\mathbf{N}^{\mathrm{T}}\left(\frac{\partial\rho_r}{\partial t}\right)_j^{i+1}\left[\left(c_p\right)_j^{i+1}-\left(c_{pg}\right)_j^{i+1}\right]\mathbf{N}dx\right\}\mathbf{T}$$

$$+\int_0^{l_s}\left(\frac{\partial\rho_r}{\partial t}\right)_j^{i+1}\left\{Q-\left[\left(c_p\right)_j^{i+1}-\left(c_{pg}\right)_j^{i+1}\right]T_\infty\right\}\mathbf{N}^{\mathrm{T}}dx-\begin{bmatrix}-k_j^{i+1}\dfrac{\partial T}{\partial x}(0)\\ -\left(h_{TCR}\right)_m^{i+1}\left(T_{m1}-T_{m2}\right)\end{bmatrix}=\mathbf{0}$$

or
$$\mathbf{C}_s\dot{\mathbf{T}}+\left(\mathbf{K}_{os}+\mathbf{K}_g+\mathbf{K}_d\right)\mathbf{T}+\left(\mathbf{f}_{os}+\mathbf{f}_{b1}\right)=\mathbf{0} \tag{6.39}$$

for the back GRP skin, i.e. domain Ω_{s2}, by:

$$\left[\int_0^{l_s}\mathbf{N}^{\mathrm{T}}\rho_j^{i+1}\left(c_p\right)_j^{i+1}\mathbf{N}dx\right]\dot{\mathbf{T}}+\left\{\int_0^{l_s}\mathbf{B}^{\mathrm{T}}k_j^{i+1}\mathbf{B}dx\right.$$

$$\left.+\int_0^{l_s}\mathbf{B}^{\mathrm{T}}\left(\dot{m}_g\right)_j^{i+1}\left(c_{pg}\right)_j^{i+1}\mathbf{N}dx+\int_0^{l_s}\mathbf{N}^{\mathrm{T}}\left(\frac{\partial\rho_r}{\partial t}\right)_j^{i+1}\left[\left(c_p\right)_j^{i+1}-\left(c_{pg}\right)_j^{i+1}\right]\mathbf{N}dx\right\}\mathbf{T}$$

$$+\int_0^{l_s}\left(\frac{\partial\rho_r}{\partial t}\right)_j^{i+1}\left\{Q-\left[\left(c_p\right)_j^{i+1}-\left(c_{pg}\right)_j^{i+1}\right]T_\infty\right\}\mathbf{N}^{\mathrm{T}}dx-\begin{bmatrix}\left(h_{TCR}\right)_n^{i+1}\left(T_{n3}-T_{n4}\right)\\ -\left(h_{r2}+h_{c2}\right)\left(T-T_\infty\right)\end{bmatrix}=\mathbf{0}$$

or
$$\mathbf{C}_s\dot{\mathbf{T}}+\left(\mathbf{K}_{os}+\mathbf{K}_g+\mathbf{K}_d\right)\mathbf{T}+\left(\mathbf{f}_{os}+\mathbf{f}_{b2}\right)=\mathbf{0} \tag{6.40}$$

and for the sandwich material, i.e. domain Ω_c, by:

$$\left[\int_0^{l_c}\mathbf{N}^{\mathrm{T}}\rho_c\left(c_{pc}\right)_j^{i+1}\mathbf{N}dx\right]\dot{\mathbf{T}}+\left[\int_0^{l_c}\mathbf{B}^{\mathrm{T}}\left(k_c\right)_j^{i+1}\mathbf{B}dx\right]\mathbf{T}-\begin{bmatrix}\left(h_{TCR}\right)_m^{i+1}\left(T_{m1}-T_{m2}\right)\\ -\left(h_{TCR}\right)_n^{i+1}\left(T_{n3}-T_{n4}\right)\end{bmatrix}=\mathbf{0}$$

or
$$\mathbf{C}_c\dot{\mathbf{T}}+\mathbf{K}_c\mathbf{T}+\mathbf{f}_b=\mathbf{0} \tag{6.41}$$

where superscript **T** denotes the transpose quantity and

$\mathbf{N}$ = shape function matrix

$\mathbf{B}$ = shape function derivative matrix

$\mathbf{C_s}$ = element capacitance matrix for GRP skin

$\mathbf{K_{os}}$ = element conductance matrix for GRP skin

$\mathbf{K_g}$ = element gas diffusion matrix

$\mathbf{K_d}$ = element decomposition matrix

$\mathbf{f_{os}}$ = element decomposition vector for GRP skin

$\mathbf{f_{b1}}$ = element boundary conditions vector for the front GRP skin

$\mathbf{f_{b2}}$ = element boundary conditions vector for the back GRP skin

$\mathbf{C_c}$ = element capacitance matrix for sandwich material

$\mathbf{K_{os}}$ = element conductance matrix for sandwich material

$\mathbf{f_b}$ = element boundary conditions vector for sandwich material

N and **B** are given by Equations 2.18a and 2.18b. The vectors $\mathbf{f_{b1}}$, $\mathbf{f_{b2}}$ and $\mathbf{f_b}$ contain the natural boundary conditions in which the prescribed temperature at the hot surface boundary, i.e. Equation 6.7, is introduced to the matrix equation after assembling the element matrices (Appendix C). Also T_{m2} and T_{n4} are evaluated by Equations 6.34 and 6.35 and then used in the boundary conditions vectors, i.e. $\mathbf{f_{b1}}$, $\mathbf{f_{b2}}$ and $\mathbf{f_b}$.

Finite element equations for Method 2

The solution domain Ω ($=\Omega_{s1}+\Omega_1+\Omega_c+\Omega_2+\Omega_{s2}$), which is a one-dimensional multi-layered solid of thickness L ($=2L_s+2L_g+L_c$), is divided into E linear elements of different lengths and two nodes each (Figure 6.6).

The element matrices corresponding to Equations 6.36 and 6.37 are denoted by $\mathbf{K_{TCR1}}$ and $\mathbf{K_{TCR2}}$ and given by the following line integrals:

$$\mathbf{K}_{\mathrm{TCR1}} = \int_{\Omega_1} \mathbf{B}^{\mathrm{T}} L_g \left(h_{TCR}\right)_m^{i+1} \mathbf{B}\, dx = \int_0^{L_g} \mathbf{B}^{\mathrm{T}} L_g \left(h_{TCR}\right)_m^{i+1} \mathbf{B} dx \tag{6.42}$$

$$\mathbf{K}_{\mathrm{TCR2}} = \int_{\Omega_2} \mathbf{B}^{\mathrm{T}} L_g \left(h_{TCR}\right)_n^{i+1} \mathbf{B}\, dx = \int_0^{L_g} \mathbf{B}^{\mathrm{T}} L_g \left(h_{TCR}\right)_n^{i+1} \mathbf{B} dx \tag{6.43}$$

The addition of these terms to the element equations for GRP domains (Equations 6.39 and 6.40) and sandwich domain (Equation 6.41) leads to boundary conditions of the form of Equations 6.4 and 6.5.

Using the Bubnov-Galerkin (weighted residual) approach and Equations 6.42, the element equation for the front GRP skin, i.e. domain Ω_{s1}, is represented by:

$$\left[\int_0^{l_s}\mathbf{N}^{\mathrm{T}}\rho_j^{i+1}\left(c_p\right)_j^{i+1}\mathbf{N}dx\right]\dot{\mathbf{T}}+\left\{\int_0^{l_s}\mathbf{B}^{\mathrm{T}}k_j^{i+1}\mathbf{B}dx+\int_0^{l_s}\mathbf{B}^{\mathrm{T}}\left(\dot{m}_g\right)_j^{i+1}\left(c_{pg}\right)_j^{i+1}\mathbf{N}dx\right.$$

$$\left.+\int_0^{L_g}\mathbf{B}^{\mathrm{T}}L_g\left(h_{TCR}\right)_m^{i+1}\mathbf{B}dx+\int_0^{l_s}\mathbf{N}^{\mathrm{T}}\left(\frac{\partial\rho_r}{\partial t}\right)_j^{i+1}\left[\left(c_p\right)_j^{i+1}-\left(c_{pg}\right)_j^{i+1}\right]\mathbf{N}dx\right\}\mathbf{T}$$

$$+\int_0^{l_s}\left(\frac{\partial\rho_r}{\partial t}\right)_j^{i+1}\left\{Q-\left[\left(c_p\right)_j^{i+1}-\left(c_{pg}\right)_j^{i+1}\right]T_\infty\right\}\mathbf{N}^{\mathrm{T}}dx-\begin{bmatrix}-k_j^{i+1}\dfrac{\partial T}{\partial x}(0)\\ k_j^{i+1}\dfrac{\partial T}{\partial x}(l_s)\end{bmatrix}=\mathbf{0}$$

or
$$\mathbf{C}_s\dot{\mathbf{T}}+\left(\mathbf{K}_{os}+\mathbf{K}_{TCR1}+\mathbf{K}_g+\mathbf{K}_d\right)\mathbf{T}+\left(\mathbf{f}_{os}+\mathbf{f}_{b1}\right)=\mathbf{0} \tag{6.44}$$

for the back GRP skin, i.e. domain Ω_{s2}, by:

$$\left[\int_0^{l_s}\mathbf{N}^{\mathrm{T}}\rho_j^{i+1}\left(c_p\right)_j^{i+1}\mathbf{N}dx\right]\dot{\mathbf{T}}+\left\{\int_0^{l_s}\mathbf{B}^{\mathrm{T}}k_j^{i+1}\mathbf{B}dx+\int_0^{l_s}\mathbf{B}^{\mathrm{T}}\left(\dot{m}_g\right)_j^{i+1}\left(c_{pg}\right)_j^{i+1}\mathbf{N}dx\right.$$

$$\left.+\int_0^{L_g}\mathbf{B}^{\mathrm{T}}L_g\left(h_{TCR}\right)_n^{i+1}\mathbf{B}dx+\int_0^{l_s}\mathbf{N}^{\mathrm{T}}\left(\frac{\partial\rho_r}{\partial t}\right)_j^{i+1}\left[\left(c_p\right)_j^{i+1}-\left(c_{pg}\right)_j^{i+1}\right]\mathbf{N}dx\right\}\mathbf{T}$$

$$+\int_0^{l_s}\left(\frac{\partial\rho_r}{\partial t}\right)_j^{i+1}\left\{Q-\left[\left(c_p\right)_j^{i+1}-\left(c_{pg}\right)_j^{i+1}\right]T_\infty\right\}\mathbf{N}^{\mathrm{T}}dx-\begin{bmatrix}-k_j^{i+1}\dfrac{\partial T}{\partial x}(0)\\ -(h_{r2}+h_{c2})(T-T_\infty)\end{bmatrix}=\mathbf{0}$$

or
$$\mathbf{C}_s\dot{\mathbf{T}}+\left(\mathbf{K}_{os}+\mathbf{K}_{TCR2}+\mathbf{K}_g+\mathbf{K}_d\right)\mathbf{T}+\left(\mathbf{f}_{os}+\mathbf{f}_{b2}\right)=\mathbf{0} \tag{6.45}$$

and for the sandwich material, i.e. domain Ω_c, by:

$$\left[\int_0^{l_c}\mathbf{N}^{\mathrm{T}}\rho_c\left(c_{pc}\right)_j^{i+1}\mathbf{N}dx\right]\dot{\mathbf{T}}+\left[\int_0^{l_c}\mathbf{B}^{\mathrm{T}}\left(k_c\right)_j^{i+1}\mathbf{B}dx\right]\mathbf{T}-\begin{bmatrix}\left(h_{TCR}\right)_m^{i+1}\left(T_1-T_2\right)\\ -\left(h_{TCR}\right)_n^{i+1}\left(T_3-T_4\right)\end{bmatrix}=\mathbf{0}$$

or
$$\mathbf{C}_c\dot{\mathbf{T}}+\mathbf{K}_c\mathbf{T}+\mathbf{f}_b=\mathbf{0} \tag{6.46}$$

6.3.4 Time Step Algorithm

A solution to the matrix equation of the form Equation 6.38 is given by [from: Zienkiewicz & Taylor, 1991 as corrected by Looyeh *et al.*, 1997; Zienkiewicz, Pers. Com., 1995]:

$$\mathbf{T}_{n+1}=\left(\mathbf{C}+\Delta t\Theta\mathbf{K}\right)^{-1}\left\{\left[\mathbf{C}-\Delta t(1-\Theta)\mathbf{K}\right]\mathbf{T}_n-\Delta t\,\bar{\mathbf{f}}\right\} \tag{6.47}$$

where Δt is the time step size (s), Θ is the weighting (time step) parameter, $\bar{\mathbf{f}}$ is the average value of **f** defined by Equation 2.36 and subscripts **n** and **n+1** represent known and unknown quantities.

The time step is based on the critical time step Δt_{cr} which depends on the weighting parameter Θ, the element length l, density ρ, thermal conductivity k and specific heat c_p as given by Equation 2.38 [Zienkiewicz & Taylor, 1991]. For twin-skinned sandwich panels, the critical time steps , i.e. $(\Delta t_{cr})_{GRP}$ and $(\Delta t_{cr})_{SM}$, need to be found for each material region separately. The final critical time step is then chosen as the minimum value of the all computed values:

$$\Delta t_{cr} = \text{Min}\left\langle (\Delta t_{cr})_{GRP}, (\Delta t_{cr})_{SM} \right\rangle \tag{6.48}$$

where

$$(\Delta t_{cr})_{GRP} = \frac{2}{1-2\Theta} \frac{l_s^2 \rho_j^{i+1} \left(c_p\right)_j^{i+1}}{3k_j^{i+1}} \tag{6.49a}$$

$$(\Delta t_{cr})_{SM} = \frac{2}{1-2\Theta} \frac{l_c^2 \rho_c \left(c_{pc}\right)_j^{i+1}}{3\left(k_c\right)_j^{i+1}} \tag{6.49b}$$

The Crank-Nicolson solution, corresponding to Θ=1/2 is used.

6.3.5 The Computer Code Algorithm

Additions are made to the structure of the finite element computer code for single-skinned GRP panels to enable temperature predictions for twin-skinned GRP sandwich panels. The major modification involves inclusion of different material properties for the GRP and sandwich filler. Further additional terms are needed for the effect of imperfect bonding on temperature variations across the interfaces and the evaluation of thermal contact resistance. The key operations flow chart of the modified finite element computer code is shown in Figure 6.7. It is capable of using both methods for computing the effect of the contact resistance on temperature variations.

Main Finite Element Program

1. initialize the system matrices, vectors and principle variables.
2. read finite element mesh data, thermal, kinetic and transport properties for GRP and sandwich material, boundary condition parameters, control ID value for different solutions and method for temperature drop calculations.
3. start time-dependent calculation and determine furnace temperature.
4. set the initial values and calculate additional specific heats and the proportion functions of the moisture contents for both GRP and sandwich material, Eqs. 4.1 to 4.3, 4.6, 4.8, 4.12 and 4.20 to 4.22.
5. determine boundary conditions at the hot surface, cold surface and the GRP/Sandwich/GRP interfaces, Eqs. 6.3 to 6.11, 6.17 and 6.18.
6. calculate the temperature-dependent thermal properties for GRP and sandwich material, Eqs. 4.9, 4.13 to 4.17, 4.23 and 4.26.
7. calculate the effect of moisture content on thermal properties of GRP and sandwich material using additional specific heats obtained in step 4, Eqs. 4.10, 4.11, 4.24 and 4.25.
8. calculate the mass loss rate, instantaneous density and gas mass flux regarding the control ID value for the required solution.
9. calculate thermal conductivity of the gas in the void space and the contact coefficient, Eqs. 3.28 and 6.23 and Table 3.3.
10. calculate the temperature drop at the GRP/Sandwich/GRP interfaces and update the interfaces temperatures (Method 1), Eqs. 6.34 and 6.35.
11. choose a suitable option according to the input element type and create element matrices, **K** and **C**, and element force vector, **f**, Eqs. 6.39 to 6.41 for Method 1 or 6.42 to 6.46 for Method 2.
12. assemble the system matrices and force vector, if any.
13. calculate and update the time step using Eqs. 6.48 and 6.49 or consider the chosen value for the implicit solutions.
14. form system equations according to Eqs. 6.39 to 6.41 or 6.42 to 6.46.
15. apply hot surface, cold surface and interfaces boundary conditions.
16. solve the matrix equation using Eqs. 6.47 and find temperatures, mass loss and moisture profiles.
17. add the time step, determined in step 13, then go to step 4, otherwise stop.

Figure 6.7 Flow chart listing the steps for the main finite element computer code used for twin-skinned GRP sandwich panels including the effect of imperfect bonding on temperature variations.

6.4 FIRE EXPERIMENTS

For comparison with the numerical results, furnace fire experiments were requested from the research groups at the University of Manchester, School of Engineering and the University of Newcastle-upon-Tyne, Centre for Composite Materials Engineering. Three GRP sandwich panels were used, the panels consisting of woven roving glass fibre/polyester resin laminated GRP skins (outside) and Commercial Vermiculux (Calcium Silicate) board (inside) . The outer GRP skins were 0.6cm thick for Panels 1 and 2 and 0.96cm thick for Panel 3. The thickness of Vermiculux boards were 5cm for Panel 1, 6cm for Panel 2 and 4cm for Panel 3. All panels were manufactured by the hand lay-up method (Chapter 1). Polyester resin was used as adhesive to bond the GRP skins to sandwich boards. Four temperature sensors were embedded in each panel during the laminating and bonding processes. They are on the hot and cold surfaces of the GRP skins and at the GRP/Vermiculux/GRP interfaces (Figure 6.8).

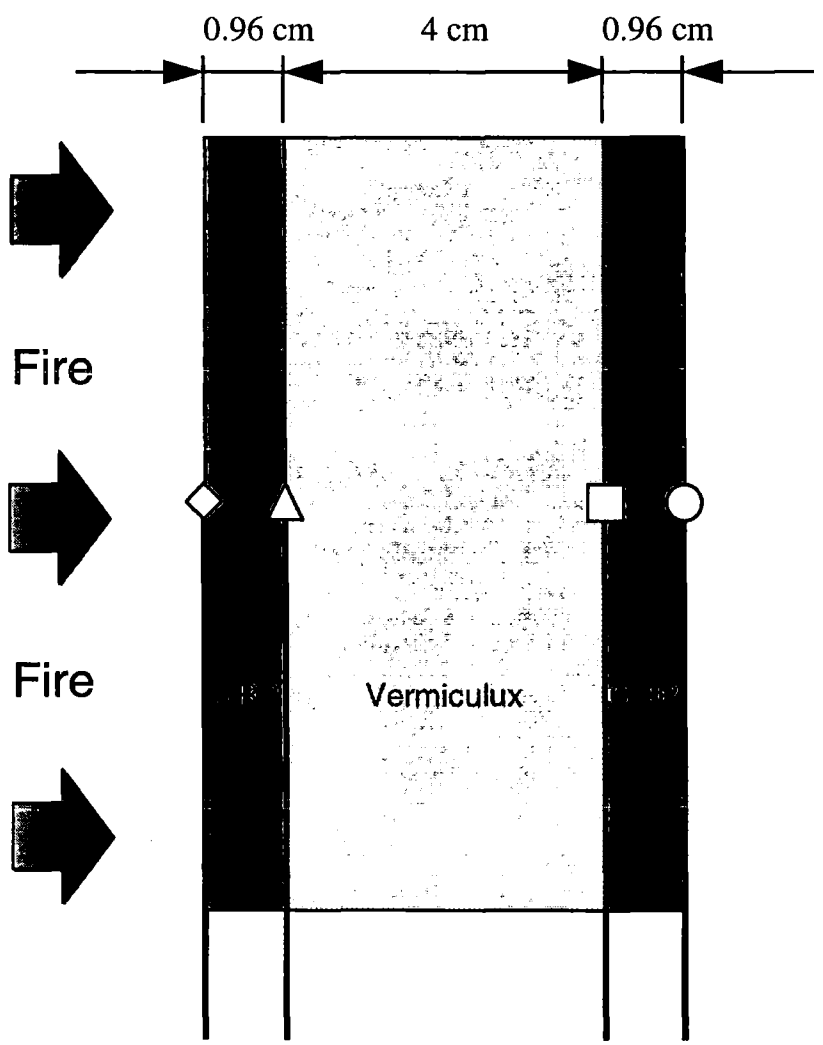

Figure 6.8 Elevation view of the GRP/Vermiculux/GRP sandwich panel (Panel 3) with embedded temperature sensors shown by ◇△□○.

A set of laboratory measurements were carried out in order to find the necessary data for the GRP/Vermiculux/GRP interfaces. These data together with the dimensions of the selected sandwich panels are listed in Table 6.1. Panel 3 is currently being used in the offshore industry.

Table 6.1 Dimensions of sandwich panels with the data for GRP/Vermiculux/GRP interfaces.

Property	Panel 1	Panel 2	Panel 3
Panel dimensions, $L \times W \times H$ (cm)	6.2×30×30	7.2×30×30	5.92×30×30
Thickness of GRP skins, L_s (cm)	0.6	0.6	0.96
Vermiculux thickness, L_c (cm)	5	6	4
Void space thickness, L_g (cm)	4×10^{-4}	4×10^{-4}	4×10^{-4}
Contact index, A_g/A	0.24	0.24	0.24

The prime requirement of the surface preparation processes is to provide surfaces free from contaminants and which will be wetted by the adhesive. In some circumstances it is necessary to include surface treatments to promote bond stability and long term durability. According to recent researches [Spagni & Gibson, 1994; Davies *et al.*, 1994], surface preparation requires: (i) pre-treating of the adherent surfaces; (ii) eliminating the ply from GRP laminates; and (iii) cleaning using a solvent wipe (acetone) just prior to bonding.

The GRP sandwich panels were installed vertically on the door of a ceramic furnace with an active volume of $3.375m^3$ and maximum fire temperature 1100^oC prior to fire experiments [Davies *et al.*, 1994a; Wu *et al.*, 1994]. The panels were then fire tested in furnace conditions controlled by the standard hydrocarbon fire [Spagni & Gibson, 1994; ISO 834, 1975; BS476, 1987]. To understand the behaviour of the Vermiculux under fire two 5cm (one dry and one moist) Vermiculux boards were fire tested.

The results from theses experiments are given in the next section where they are compared with the numerical predictions using the finite element method.

6.5 COMPARISON OF THE FINITE ELEMENT COMPUTATIONS WITH EXPERIMENTAL RESULTS AND DISCUSSION

The finite element formulation developed here with the concept of the thermal contact resistance due to the bonding imperfection is used to compute the thermal response of the GRP/Vermiculux/GRP sandwich panels.

Tables 4.3 and 4.5 list material properties for polyester-based GRP and Vermiculux, respectively. The properties of pyrolysis gases are given in Table 4.4.

The GRP material used for sandwich panels is the same as those for single-skinned panels (Chapter 5-Model 3). The initial density, specific heat and thermal conductivity of the GRP are 1832.4 kgm^{-3}, 1056.84 $Jkg^{-1}K^{-1}$ and 0.322 $Wm^{-1}K^{-1}$, respectively. The variations of these properties with temperature and moisture gradients were studied in Chapters 4 and 5.

Pyrolysis constant, activation energy and heat of decomposition for GRP are evaluated in the same way as explained for Model 3 of Chapter 5 and given by 7525 s^{-1}, 611.5 $MJkmole^{-1}$ and 2.3446 $MJkg^{-1}$, respectively.

The density of Vermiculux is assumed constant given by 470 kgm^{-3}. The initial specific heat and thermal conductivity of Vermiculux are 840 $Jkg^{-1}K^{-1}$, 0.13 $Wm^{-1}K^{-1}$.

The specific heat and thermal conductivity of Vermiculux increase with temperature linearly. The specific heat increases by 21.9% when T = 250°C and by 60% when temperature reaches 650°C. The thermal conductivity increases by 24.7% at T = 250°C and by 67.8% when T = 650°C.

The initial time step is chosen 5 seconds as the minimum value of the critical time steps of GRP and Vermiculux. At the end of each iteration the time step is updated and then applied for the next iteration.

It is helpful to perform a preliminary study on the single-skinned sandwich material such as Vermiculux. The thermal behaviour of the GRP/Vermiculux/GRP sandwich panels can then be more readily appreciated.

6.5.1 Single-Skinned Vermiculux Panels

Vermiculux panels, 5cm thick, are discretized into 50 linear elements of the same length. A Crank-Nicolson solution, corresponding to $\Theta=1/2$, is used with an initial time step of 5 seconds. Figures 6.9 and 6.10 show the comparisons of the numerical and experimental cold surface temperatures for dry and moist Vermiculux panels. It is seen for dry Vermiculux the numerical model gives lower temperatures (compared to Experimental) for exposure times from 15 to 30 minutes and higher temperatures from 45 to 85 minutes (100°C higher at 80 minutes). For Vermiculux with 11.5% moisture, the experimental results are higher for times from 10 to 50 minutes but otherwise the agreement is good. The discrepancies are thought to be due to two factors:

1. In the numerical model, the heat flow through the Vermiculux is assumed to be by heat conduction only with no thermochemical decomposition and no mass change. It is noted that Wu *et al.* [1994] found the sandwich materials experience little decomposition during fire. It is possible that the assumption of transient heat conduction is over-simple as it neglects physical and chemical processes within the material which may be significant. A slower rate of temperature rise in the first 10 to 50 minutes is therefore to be expected since the thermal conductivity of Vermiculux is extremely low, 0.13 $Wm^{-1}K^{-1}$. A thermal gravimetric analysis (TGA) of Vermiculux will reveal the actual mass change during fire exposure and its effect on the heat flow and temperature variations. It is also important to note that inaccuracies in thermal properties could account for the lack of agreement particularly for the case of dry Vermiculux.
2. The first Vermiculux panel was dried to a constant weight at about 110°C before the fire test. Nevertheless, Wang [1995] found that the panel absorbed a substantial amount of moisture in a short period of time before the experiment. The deliquescent behaviour of dry Vermiculux makes it difficult to evaluate its moisture content. It is therefore possible that the disagreement between the computed and measured cold surface temperatures might be due to the effect of moisture evaporation being omitted in the numerical modelling. A slight amount of moisture can significantly change the thermal properties and the time exposed to fire and defer the insulation failure.

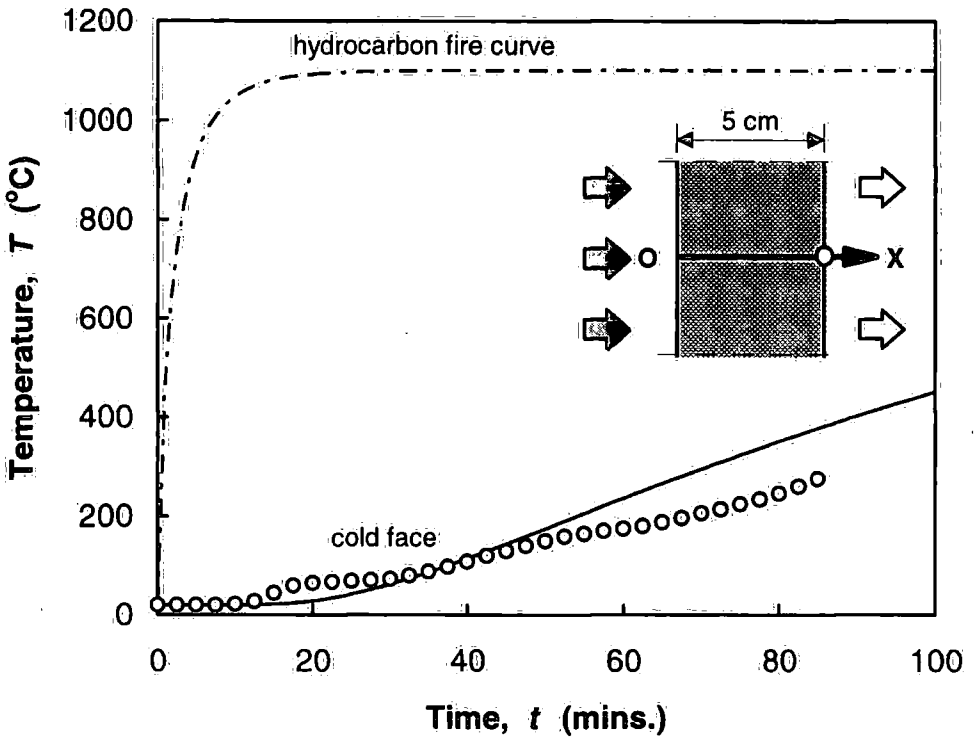

Figure 6.9 Comparison of the computed and experimental cold surface temperatures for dry Vermiculux panel of 5cm thickness. The computed temperatures are shown as a solid line and the experimental temperatures as O.

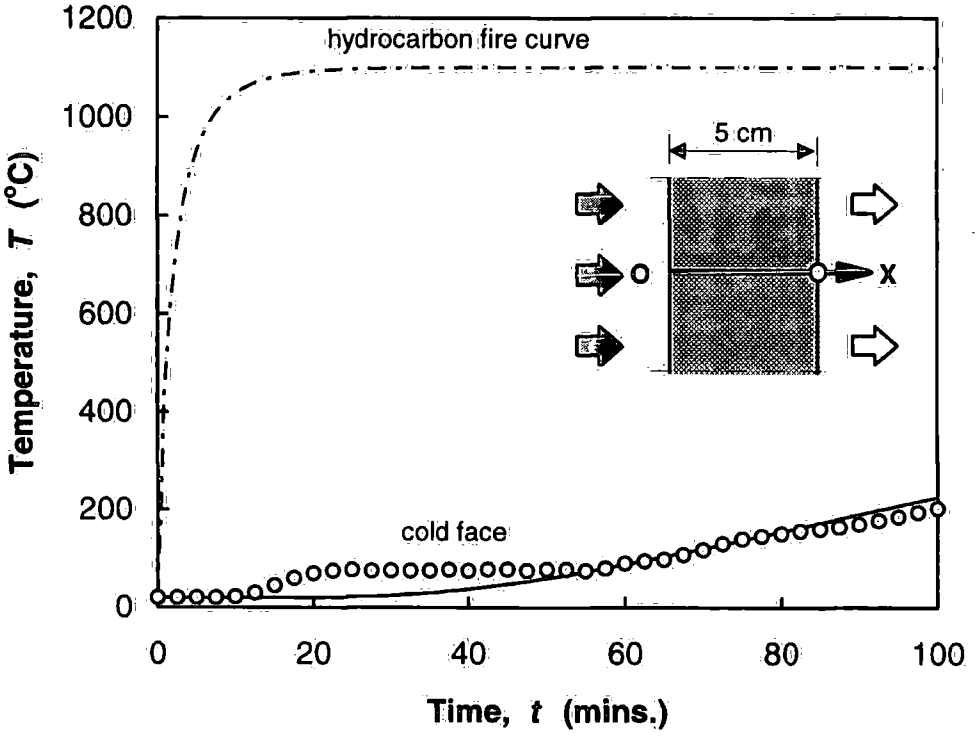

Figure 6.10 Comparison of the computed and experimental cold surface temperatures for Vermiculux panel of 5cm thickness and 11.5% moisture content. The computed temperatures are shown as a solid line and the experimental temperatures as O.

6.5.2 GRP/Vermiculux/GRP Sandwich Panels

To assess the finite element model for sandwich panels, numerical temperature outputs are presented and compared with experimental results for the selected panels as shown in Figures 6.11 to 6.19. All samples achieved the fire resistance (insulation failure) of H60, which means the back face remained below 160°C for at least 60 minutes. Panels 2 and 3 also achieved H120. Panel 3, i.e. 0.96/4/0.96cm, achieved the greatest exposure time with no insulation failure for about 180 minutes. This is despite the fact that this panel is 1.28cm thinner than panel 2. Table 6.2 summarises the finite element specifications for the selected sandwich panels.

Table 6.2 Specifications for the finite element models for the sandwich panels.

Specifications	Panel 1	Panel 2	Panel 3
Thickness, $L_s/L_c/L_s$ (cm)	0.6×5×0.6	0.6×6×0.6	0.96×4×0.96
No. of elements (Method 1)	62	72	60
No. of elements (Method 2)	64	74	62
No. of element sets	2	2	2
Type of elements	2-node linear	2-node linear	2-node linear
Element length, $l_s/l_c/l_s$ (cm)	0.1/0.1/0.1	0.1/0.1/0.1	0.096/0.1/0.096
Gap element length, (cm)	0.001	0.001	0.001
Time step parameter	0.5	0.5	0.5
Critical time step, (s)	6.1	6.1	5.7
Initial time step, (s)	5	5	5

Wu *et al.* [1994] found that the exposure to the furnace fire caused the polyester resin to be burnt out of the front face of the panels leaving behind the glass fibres. The glass fibres in the GRP underwent some decomposition, splitting due to the physical erosive effects of the intensity of the fire. The same effect was found for the Vermiculux; after exposure to the furnace fire the material remained generally intact. Minimal decomposition was only observed after 70 minutes in the Vermiculux particularly in Panel 3 due to its thicker GRP skins. It is therefore important to include all the physical and chemical phenomena to obtain the best numerical predictions.

Panel 1

Figure 6.11 shows computed temperatures plotted versus time for four spatial locations. The effect of bonding imperfections are taken into account at both interfaces using Method 1 of solution (Section 6.3.3). The cold surface temperature profile is compared with the experimental results in Figure 6.12. It is seen that after 20 minutes the numerical results give higher temperatures than the experimental. It is thought this may be related to the behaviour of Vermiculux and inaccuracies in evaluating its thermal properties particularly the effects of moisture evaporation. The simple evaporation-condensation model used for the low-percentage moisture content of GRP skins may not be appropriate for the high percentage of moisture in Vermiculux. Radiation heat transfer across the interfaces may also be important when high temperatures are encountered. The differences get larger after 50 minutes of fire exposure which might point to the necessity to include another term such as for radiation.

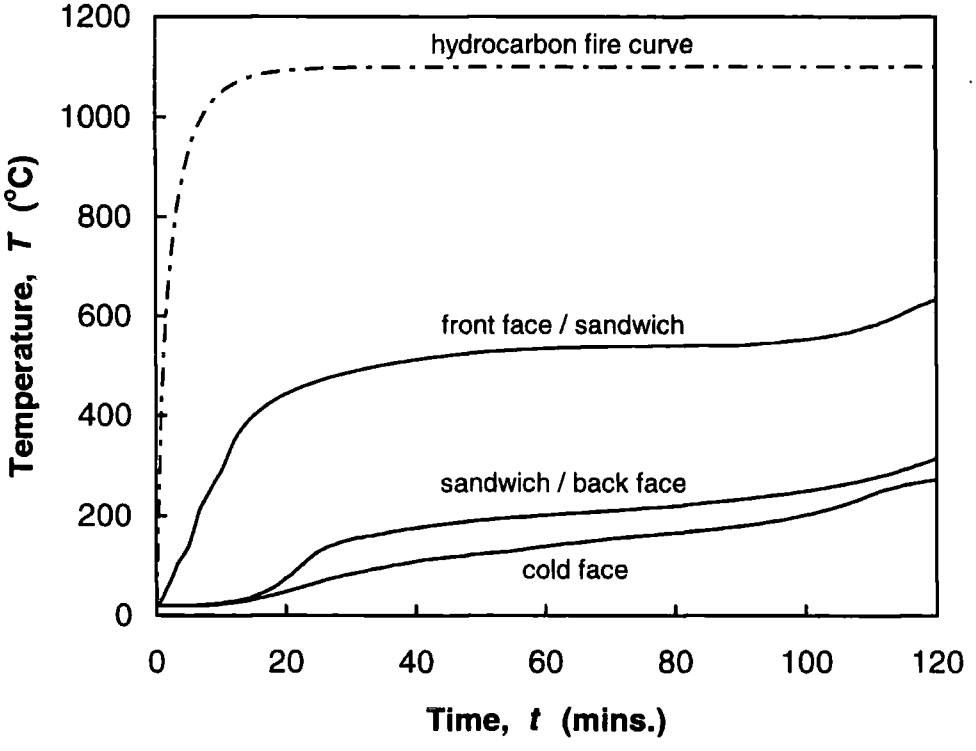

Figure 6.11 Computed temperatures versus time for various distances including the effect of imperfect bonding for Panel 1, i.e. 0.6/5/0.6cm.

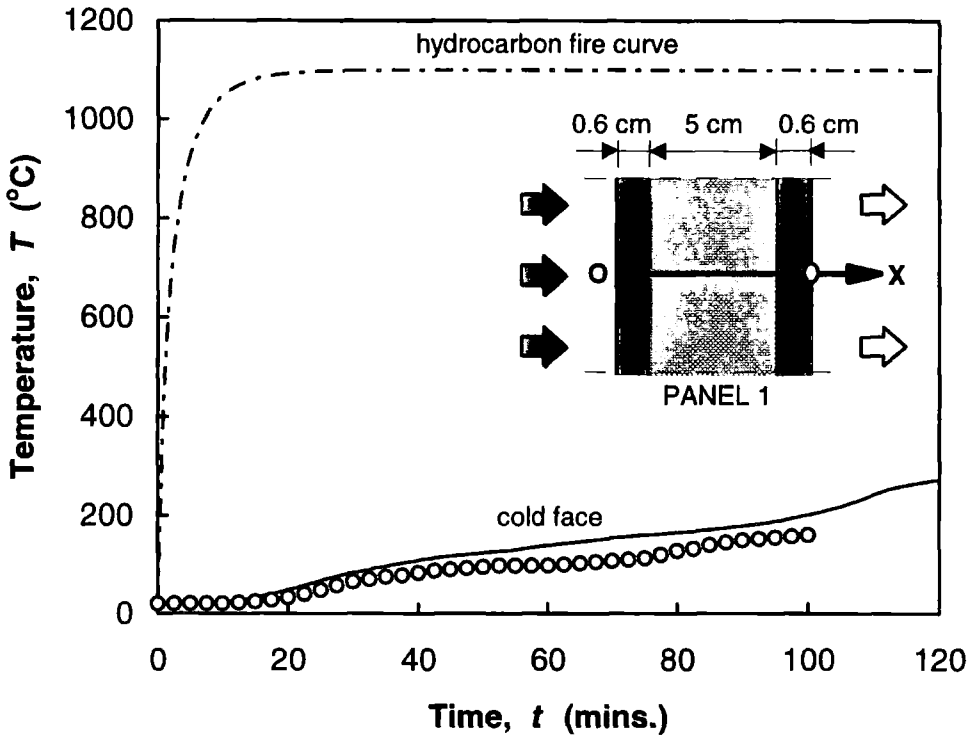

Figure 6.12 Comparison of the computed and experimental cold surface temperatures including the effect of imperfect bonding for Panel 1, i.e. 0.6/5/0.6cm. The computed temperatures are shown as a solid line and the experimental results for a temperature sensor as O, the position of which is shown in the inset.

According to Figure 6.12, the numerical model predicts fire resistance (insulation failure) at about 79 minutes which differs from that of experiment by less than 15 minutes (16.7%).

To investigate how the thermal contact resistance may affect on temperature distributions along the GRP/Vermiculux/GRP interfaces, the computed cold surface temperature profiles for both perfect and imperfect bondings are plotted as functions of time along with the experimental temperatures in Figure 6.13. It is seen that the difference between the two methods is very small (less than 3%). In Method 2 the gap element length is taken 10^{-3}cm which is 2.5 times larger than the actual gap length at the interfaces i.e. 4×10^{-4}cm. This might be the main reason for this difference. The ratio of gap element length to body element length is 1/100. For more complicated problems with larger number of elements, this small ratio may cause problems particularly when time iteration is involved. Method 1 is therefore recommended. The dash-dot line is the

temperature profile for a perfect bonding. Comparison of this profile with that for imperfect bonding (solid line) reveals a difference of 6.8%. The inclusion improves the correlation with the experimental results by 11.1%.

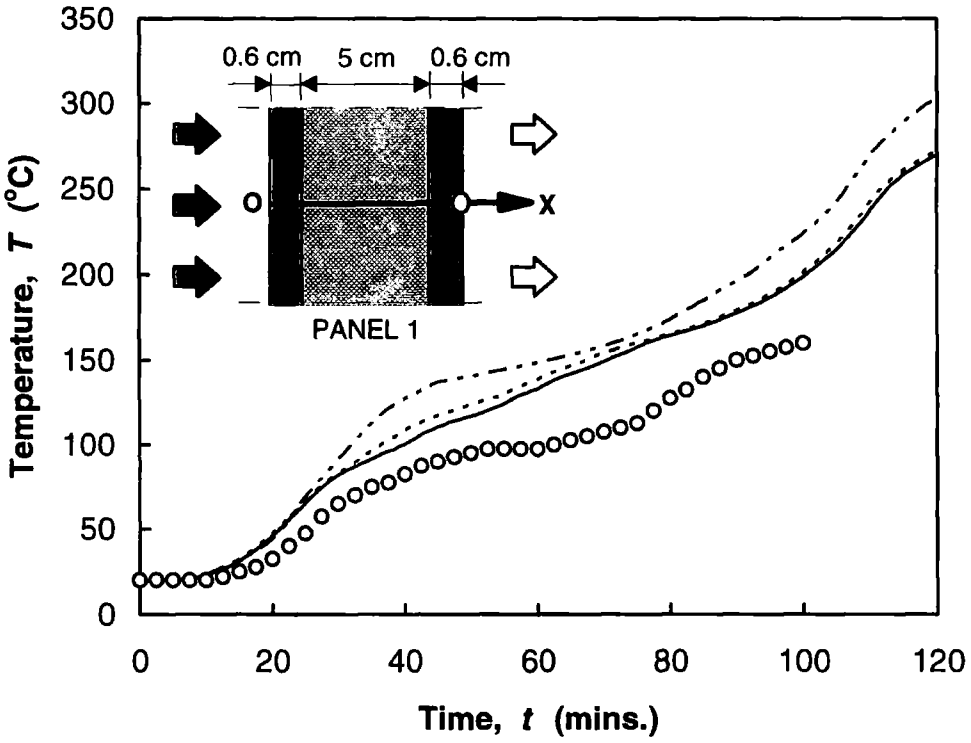

Figure 6.13 Comparison of the computed and experimental cold surface temperatures. The solid and dot lines are for the imperfect bonding using Methods 1 and 2. The computed temperatures for the perfect bonding are shown as dash-dot line. O is the position of the temperature sensor for the experimental results.

Panel 2

The numerical and experimental results for the second sandwich panel, i.e. 0.6/6/0.6cm, are presented in Figures 6.14 and 6.15. The Vermiculux in this panel is 1cm thicker than in Panel 1. This panel easily achieved exacting requirement of 120 minutes insulation failure whereas Panel 1 failed.

In Figure 6.14 temperature profiles are plotted versus time for various locations in the sandwich panel. These are the locations for which temperature sensors were implanted to obtain experimental results.

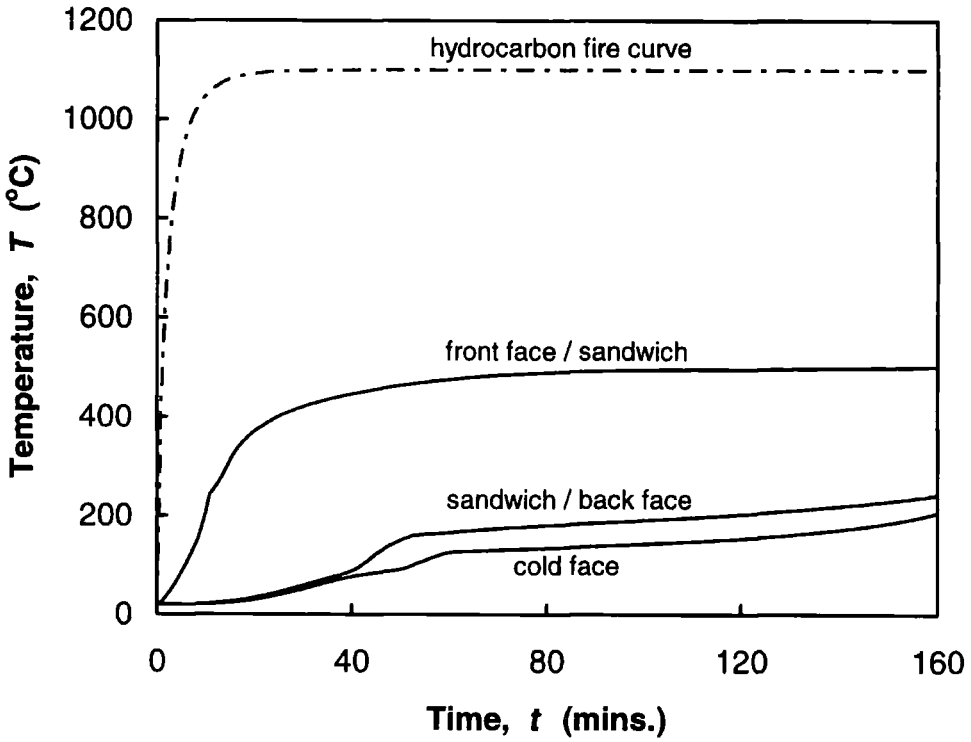

Figure 6.14 Computed temperatures versus time for various distances including the effect of imperfect bonding for Panel 2, i.e. 0.6/6/0.6cm.

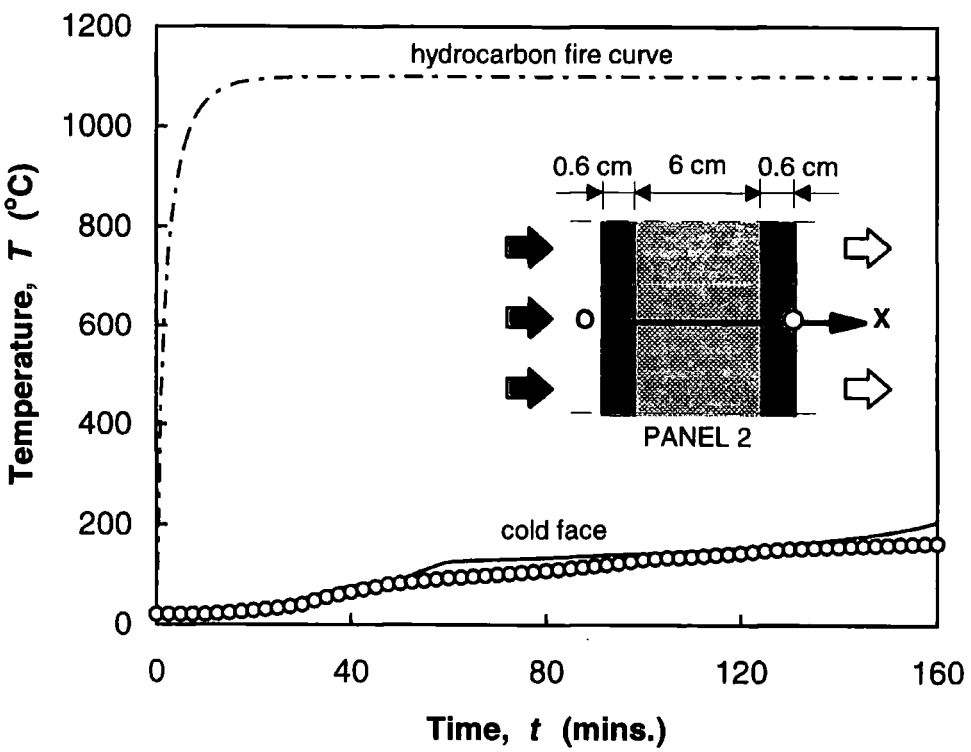

Figure 6.15 Comparison of the computed and experimental cold surface temperatures including the effect of imperfect bonding for Panel 2, i.e. 0.6/6/0.6cm. The computed temperatures are shown as a solid line and the experimental results for a temperature sensor as O, the position of which is shown in the inset.

In Figure 6.15 the numerical cold surface temperatures are compared with the experimental. It is seen that the numerical temperatures are slightly higher for $55<t<95$ minutes and $t>140$ minutes. The differences are much less than for Panel 1 (Figure 6.12). According to Figure 6.15, the numerical model predicts fire resistance (insulation failure) at 129.5 minutes. This is 19.5 minutes or 13% less than from experiments (150 minutes). This is an overall improvement of 54.5 minutes over Panel 1 presumably due to the 1cm thicker Vermiculux.

Panel 3

The numerical and experimental results for Panel 3, i.e. 0.96/4/0.96cm, are shown in Figures 6.16 to 6.19. This panel contains GRP skins of 0.96cm thick and Vermiculux board of 4cm thick. The panel is currently being used in the offshore industry for structural and thermal protection.

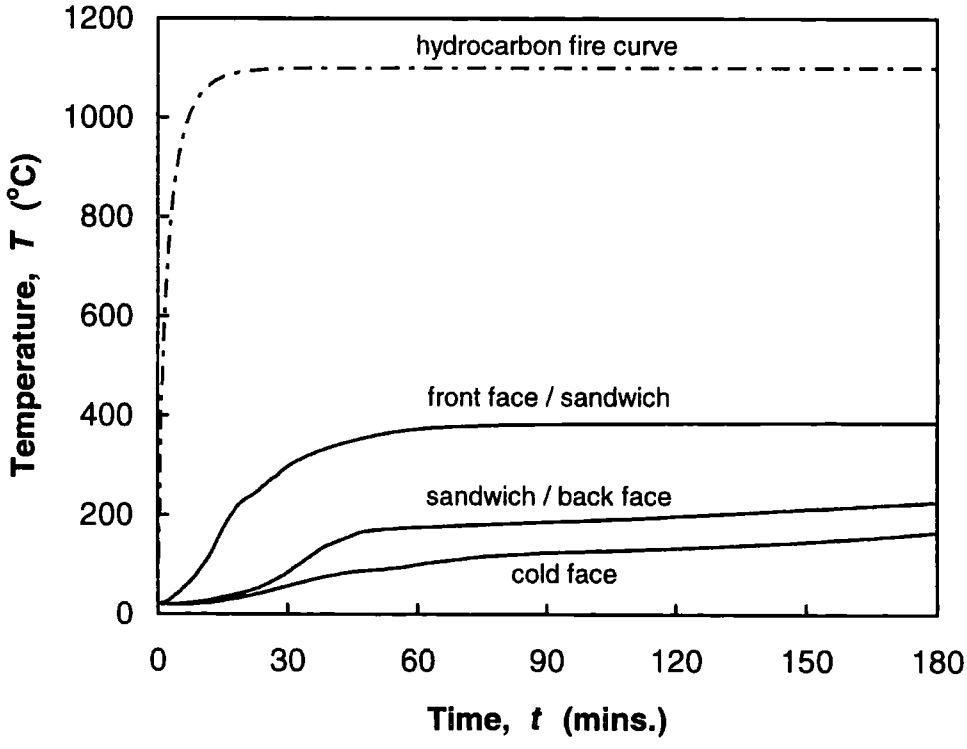

Figure 6.16 Computed temperatures versus time for various distances including the effect of imperfect bonding for Panel 3, i.e. 0.96/4/0.96cm.

Figure 6.16 depicts the computed temperatures versus time for the locations where temperature sensors were implanted in the fire test panel. The steep rise of hydrocarbon fire temperature over the first 10 minutes is, of course, very impressive. The rise in temperature at the cold surface takes 40 minutes mainly due to low thermal conductivity of the GRP (0.322 $Wm^{-1}K^{-1}$) and Vermiculux (0.13 $Wm^{-1}K^{-1}$) and less influence of thermochemical decomposition. As time progresses the contributions from resin decomposition and the movement of pyrolysis gases appear to slow down the temperature rise. Hence, it can been seen that the temperature profiles flatter after about 70 minutes. Comparison of this figure with that of Figure 5.18 for a single-skinned GRP panel reveals a beneficial contribution of the moist Vermiculux which has the effect of producing a cooling process inside the sandwich. It is evident that by using sandwich material the temperature rise will be suppressed significantly and the standard fire resistance (insulation failure) of H120 can be achieved easily.

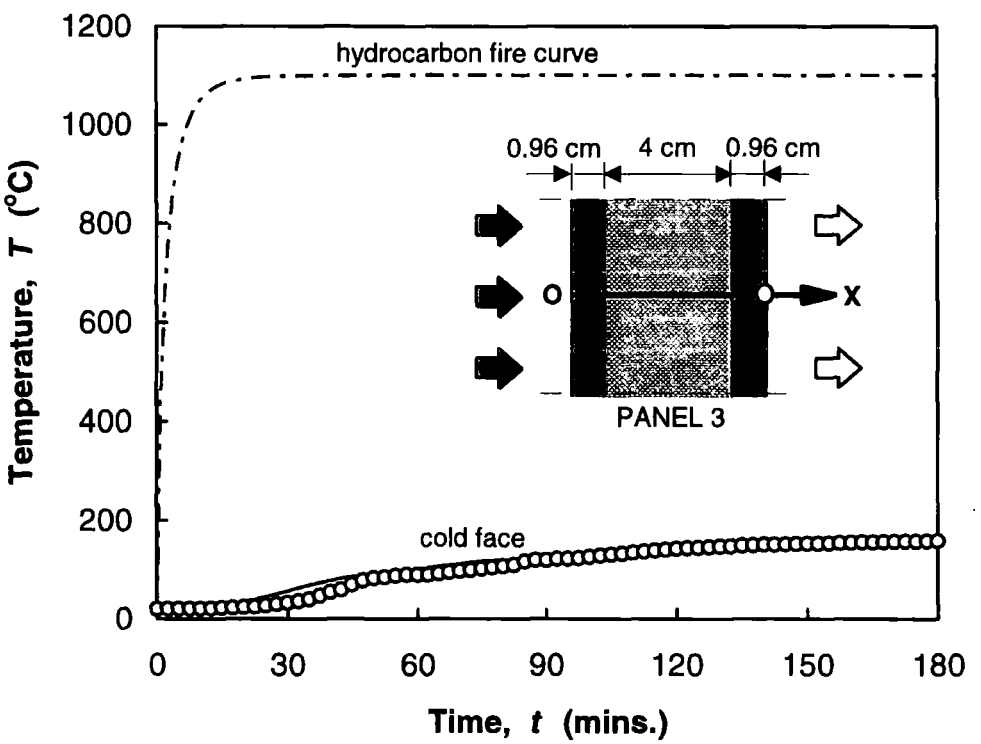

Figure 6.17 Comparison of the computed and experimental cold surface temperatures including the effect of imperfect bonding for Panel 3, i.e. 0.96/4/0.96cm. The computed temperatures are shown as a solid line and the experimental results for a temperature sensor as O, the position of which is shown in the inset.

Figure 6.17 shows the computed and experimental cold surface temperatures over 180 minutes of fire exposure time. Apart from a small difference from 20 and 50 minutes there is very good agreement, and very much better than for Panels 1 and 2. It seems the choice of thicker GRP skins and thinner sandwich board is the main reason for the improvement, the GRP skins having more influence on the heat flow than the sandwich material. The numerical model predicts fire resistance (insulation failure) at about 172.5 minutes which differs from that for experiment by less than 17 minutes or 8.9% (Figure 6.18).

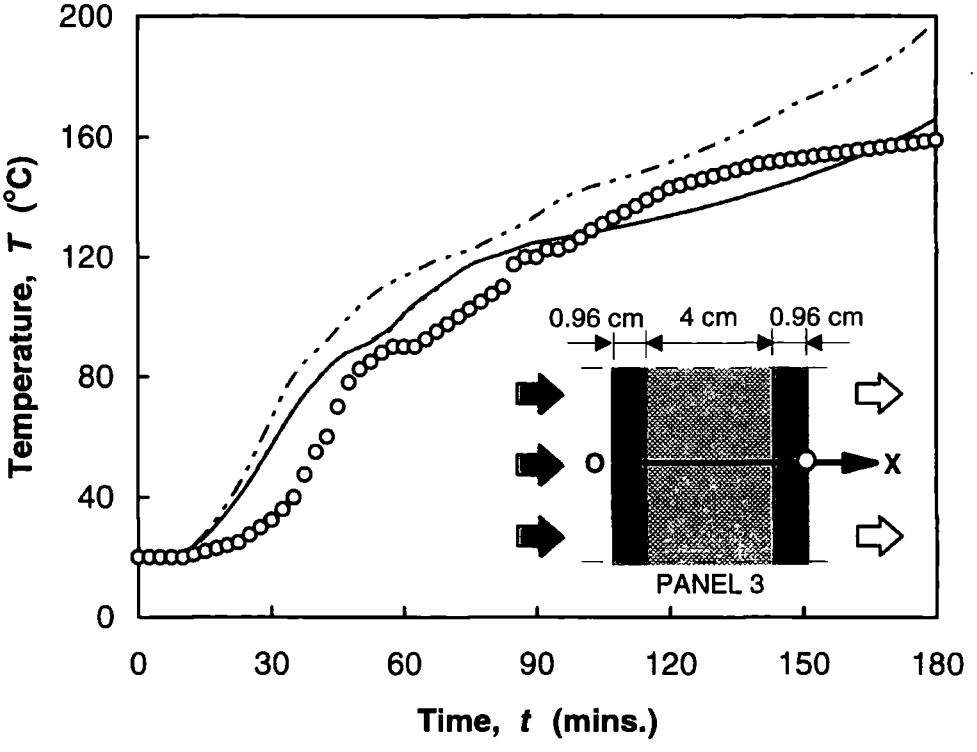

Figure 6.18 Comparison of the computed and experimental cold surface temperatures. The solid and dot lines are for the imperfect bonding using Methods 1 and 2, which are virtually coincident, and the dash-dot line for perfect bonding. O is the position of the temperature sensor for the experimental results.

To study the effect of the thermal contact resistance on the temperature distributions, the computed cold surface temperature profiles for both perfect and imperfect bondings are shown in Figure 6.18. In this figure, the solid and dot lines are for the imperfect bonding using the two methods of solution, i.e. Methods 1 and 2; it is seen they are virtually coincident. The dash-dot line indicates the temperature profile for perfect bonding. It is seen that the computed temperatures are slightly higher than experimental

from 12 to 100 minutes and lower from 100 to 165 minutes. This behaviour is different from Panels 1 and 2 where the computed temperatures were higher for most of fire exposure time. The numerical model including the imperfect bonding formulation agrees with the experiments better than the model using the perfect bonding. Comparison of the profiles for the perfect and imperfect bondings shows a difference of 10.4% and the improvement by including the imperfect bonding formulation is about 13.1%.

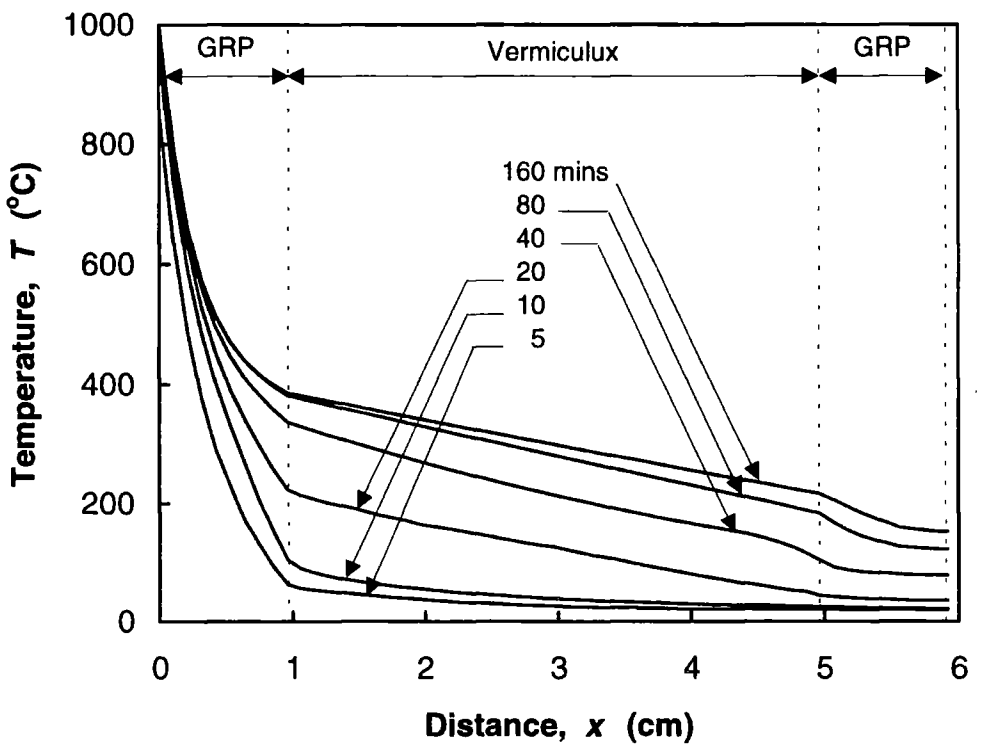

Figure 6.19 Temperature as function of distance x for various times (minutes).

Figure 6.19 shows the computed temperatures versus distance for various time intervals. The figure demonstrates the sharp temperature drop from the hot surface through the front GRP skin with noticeable change in slope at both interfaces where the fall in temperature through Vermiculux becomes linear. It can be concluded that with any decrease in contact coefficient h_{TCR} the contact resistance increases resulting in a decrease in the heat flow (Equations 6.19 to 6.23). The contact coefficient, in turn, depends on surface roughness and the void thermal conductivity.

Improvement in thermal protection requires less conductance and more resistance across the GRP/SM/GRP interfaces. In contrast, to improve the mechanical behaviour

of a sandwich panel across interfaces, it is essential to create greater contact area between surfaces and to make smoother surfaces by improving the surface preparation processes. The quality of the GRP/SM/GRP interfaces must therefore be optimised such that to comply with both requirements.

Table 6.3 Statistical analysis of the computed and experimental cold surface temperatures for the three GRP/Vermiculux/GRP sandwich panels, i.e. Panel 1 (0.6/5/0.6cm), Panel 2 (0.6/6/0.6cm) and Panel 3 (0.96/4/0.96cm).

Analysis type	Panel 1	Panel 2	Panel 3
Average difference (°C)	12.4	13.2	14.4
Standard deviation (°C)	9.6	8.9	8.8
Fire resistance (insulation failure) difference (mins.)	15	19.5	17
Fire resistance (insulation failure) difference (%)	16.7	13	8.9
Perfect bonding difference (%)	40.3	35.6	24.2
Imperfect bonding difference using Method 1 (%)	29.2	24.1	11.1
Improvement made by imperfect bonding (%)	11.1	11.5	13.1

Finally, Table 6.3 summarises the results for the three sandwich panels. The average difference and standard deviation of the computed and experimental results are given in the first two rows. The differences between numerical and experimental fire resistance values are presented in the third and fourth rows. Differences between the numerical results and experimental with perfect and imperfect bondings are given in the fifth and sixth rows, a comparison of these two is given in the last row. The effect of bonding imperfection on temperature results is evident. It can also be seen that the effect of thermal contact resistance on temperature distributions across the interfaces and through the panels varies slightly with the change in dimension and configuration. It is also evident that a panel with reasonably thicker GRP skins will behave better in fire and the standard fire resistance (insulation failure) of H120 can be achieved easily.

6.6 SUMMARY

This chapter involved the application of the finite element method to the analysis of the thermal response of sandwich panels subject to hydrocarbon fire. A one-dimensional

mathematical model and an appropriate finite element solution were developed and used to assess the fire resistance of three GRP/Vermiculux/GRP sandwich panels with thicknesses 6.2, 7.2 and 5.92cm. The model accounted for (i) thermochemical decomposition in the polyester-based GRP skins; (ii) transient heat conduction in Vermiculux and (iii) the effect of thermal contact resistant at the GRP/Vermiculux/GRP interfaces. The thermal contact resistance was found to be important. Two methods were used to include the effect of temperature drop at the interfaces: (i) explicit and (ii) implicit, the former was recommended for complex problems.

Sandwich panels are currently being used in the offshore industry with a variety of GRP, sandwich materials and configurations. In hydrocarbon fires, the twin-skinned sandwich panels with suitable sandwich materials perform well. In such designs the outer GRP skin provides good fire penetration resistance and the sandwich material then provides additional fire resistance aided by its water content. This form of construction offers weight-savings compared to steel or other alloys.

The Vermiculux sandwich material with its low density of 460-540 kg/m^{-3} and low thermal conductivity of 0.13 $Wm^{-1}K^{-1}$ was used with polyester-based GRP in the three panels discussed here. Panels 2 and 3 easily achieved the requirement of 120 minutes (H120) hydrocarbon fire resistance, the latter with fire resistance at about 172.5 minutes. The choice of thicker GRP skins and thinner sandwich board was found as the main factor for the improvement in fire resistance from Panel 2 to Panel 3, the GRP skins having more influence on the heat flow than the sandwich material.

As a general result, it was found that sandwich combinations consisting GRP/Vermiculux/GRP offer good thermal insulation but to achieve H120 suitable combinations of GRP/Vermiculux/GRP thicknesses are required. The results indicate that substantial improvement in delaying insulation failure can be achieved using thicker GRP skins with their low thermal conductivity and thinner sandwich material with its higher percentage of moisture. Also, additional improvement in thermal protection requires less conductance and more resistance across the GRP/SM/GRP interfaces. This is achieved by less contact area and rougher contact surfaces which may result in poor mechanical performance. It is therefore essential to choose an optimised surface quality to satisfy both thermal and mechanical requirements.

CHAPTER VII

AN AXI-SYMMETRIC FINITE ELEMENT MODEL FOR THE THERMAL RESPONSE OF GLASS REINFORCED PLASTIC PIPES

7.1 INTRODUCTION

Experience with glass reinforced plastic (GRP) pipes is currently being gained on several offshore structures, mainly in the Gulf of Mexico and off the coast of Africa [Gibson, 1993]. Although, the use of this material in offshore piping systems is confined mainly to aqueous systems at relatively low pressure (≤1 MPa) [Gibson, 1993], more stringent applications are imminent. With increasing experience and as a result of technology transfer from the chemical industry, where GRP piping systems have already widely been used, further applications can be expected which will involve process fluids and oil and gas at higher pressures (≈10 MPa) as well as aqueous systems.

GRP pipes can be continuously manufactured by wrapping and bonding glass reinforced plastic tapes over an extruded liner. The number of tape layers are chosen based on the required pressure service [Spagni & Gibson, 1994; Johnson Pipes Limited, 1997].

Figure 7.1 shows a typical GRP pipe manufactured by Johnson Pipes Limited [1997]. The twin-layer GRP pipe is lighter, cheaper, stronger and more resistant to corrosion and fire than those made of other materials such as steel and aluminium.

In the oil and gas industry, GRP pipes are used for piping systems and oil, gas and sea water transmissions. The transmission pipes (pipelines) with large diameter (≥10cm) are normally installed inland on special beds made of soil/sand mixture or offshore above the sea bed on special supports (Figure 7.2) [Johnson Pipes Limited, 1997].

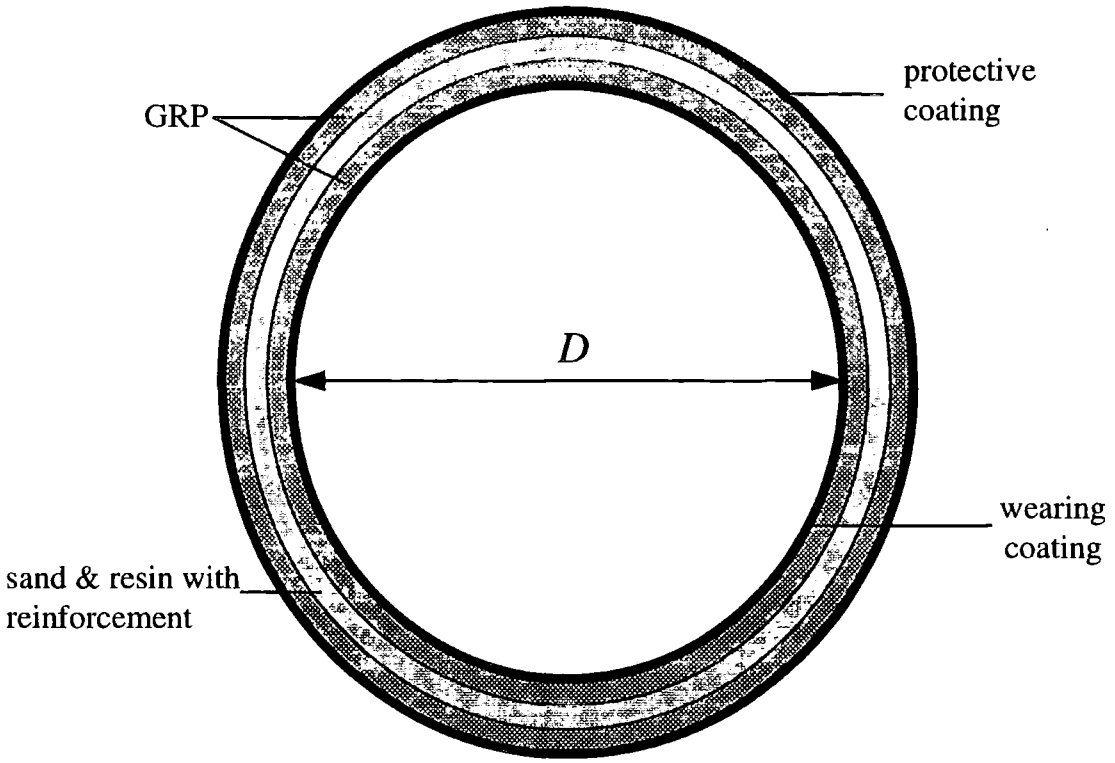

Figure 7.1 Cross-section of a typical GRP pipe for water, sewage and corrosive fluids. The internal diameter can range from 10 to 250cm and the thickness from 0.5 to 6.5cm. It weighs only one-tenth of a similar diameter concrete pipe and one-fifth of a metallic or asbestos cement pipe [from: Johnson Pipes Limited, 1997].

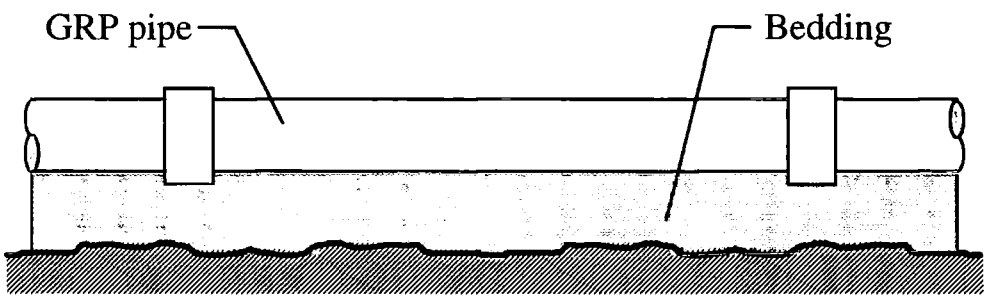

(a) Rock

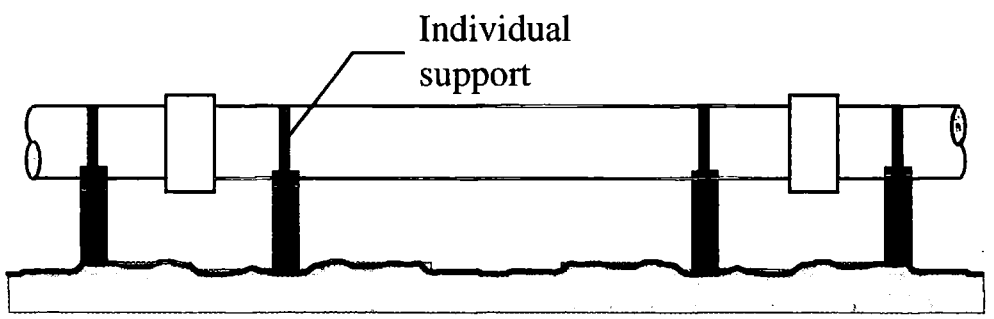

(b) Sea bed

Figure 7.2 Typical methods of installation for large diameter GRP pipes. (a) soil/sand bedding onshore; (b) support arrangement above sea bed [from: Johnson Pipes Limited, 1997].

The fire performance properties of GRP are the major factors in their use in offshore applications particularly piping systems. Moreover, only a few experiments have been carried out which demonstrate the fire performance of small diameter (<10cm) and low pressure (≤1 MPa) GRP pipes with little attempt for numerical modelling [Davies *et al.*, 1998; Gibson *et al.*, 1996; Wang, 1995; Davies *et al.*, 1994; Grim, 1991a&b; Ciraldi *et al.*, 1991; Grim, 1987; Marks, 1987; Guiton, 1987]. In this chapter the thermal response of single-skinned GRP pipes exposed to hydrocarbon fires are modelled including different fluids and a wide range of working pressures using the finite element technique. Two large diameter polyester-based GRP pipes with thicknesses 1.09cm, one with flowing natural gas and the other with sea water are studied in detail. The numerical results are presented and compared with those for a polyester-based GRP panel with the same thickness (1.09cm).

7.2 MATHEMATICAL MODEL

This model extends the one-dimensional model introduced in Chapter 2 for single-skinned GRP panels. The model considered an infinite panel with finite thickness L exposed to fire on one side (Figures 1.6a and 5.1). The differential equation governing the phenomenon of heat transfer in the material, undergoing thermochemical decomposition, was given by Equation 2.10, i.e.:

$$\rho c_p \frac{\partial T}{\partial t} = k \frac{\partial^2 T}{\partial x^2} - \dot{m}_g c_{pg} \frac{\partial T}{\partial x} - \frac{\partial \rho_r}{\partial t}\left(Q + h - h_g\right) \tag{7.1}$$

where

ρ = density of GRP (kgm^{-3})

c_p = specific heat of GRP ($Jkg^{-1}K^{-1}$)

T = temperature (^{o}C)

t = time (s)

k = thermal conductivity of GRP ($Wm^{-1}K^{-1}$)

$\dot{m}_g$ = gas mass flux ($kgm^{-2}s^{-1}$)

c_{pg} = specific heat of gas ($Jkg^{-1}K^{-1}$)

ρ_r = density of resin (active) material (kgm^{-3})

Q = heat of decomposition (Jkg^{-1})

h = enthalpy of GRP (Jkg^{-1})

h_g = enthalpy of gas (Jkg^{-1})

The geometry considered for the present model is shown schematically in Figure 7.3. The GRP pipe is assumed to be exposed to uniform fire on its outer surface (ignoring the effect of supports or bedding shown in Figure 7.2), i.e. axial symmetry is assumed (assumption 1). With this assumption, the phenomenon of heat conduction in the GRP pipe can be easily defined as a one-dimensional axi-symmetric problem. We further assume that the pipe is long and large enough to be analysed as a thin-walled cylinder (assumption 2) and the mass flow of pyrolysis gases is radial only (assumption 3).

To extend Equation 7.1 for the analysis of heat transfer in single-skinned GRP pipes, undergoing thermochemical decomposition, the following transformation from Cartesian co-ordinate x to Polar co-ordinate r is applied (Appendix B):

$$\frac{\partial^2 T}{\partial x^2} = \frac{1}{r}\frac{\partial}{\partial r}\left(r\frac{\partial T}{\partial r}\right) \tag{7.2}$$

where r is the spatial co-ordinate starting at the centre of the pipe (m).

Substituting Equation 7.2 into Equation 7.1 and using assumption 3, gives:

$$\rho c_p \frac{\partial T}{\partial t} = \frac{k}{r}\frac{\partial}{\partial r}\left(r\frac{\partial T}{\partial r}\right) - \dot{m}_g c_{pg}\frac{\partial T}{\partial r} - \frac{\partial \rho_r}{\partial t}\left(Q + h - h_g\right) \tag{7.3}$$

Equation for the rate of decomposition is defined by a first-order kinetic rate Arrhenius equation as given by Equation 2.11 taking into account that a fraction of the resin remains intact at the end of pyrolysis:

$$\frac{\partial \rho_r}{\partial t} = -A\left(\rho_r - \rho_{rf}\right)\exp\left(\frac{-E_A}{RT_k}\right) \tag{7.4}$$

where

A = pyrolysis constant (s^{-1})

ρ_{rf} = final density of resin (kgm^{-3})

E_A = activation energy ($kJkmole^{-1}$)

R = gas constant (8.314 $kJkmole^{-1}K^{-1}$)

T_k = temperature (K)

Using Equation 2.12 and assumption 3, the gas mass flux in r direction becomes:

$$\dot{m}_g = \int_{-R_i}^{\hat{r}} \frac{\partial \rho_r}{\partial t} dr \quad \text{for} \quad -\left(R_i + L\right) \le \hat{r} \le -R_i \tag{7.5}$$

where R_i is the internal radius of pipe (m) and L is the thickness of the pipe wall (m).

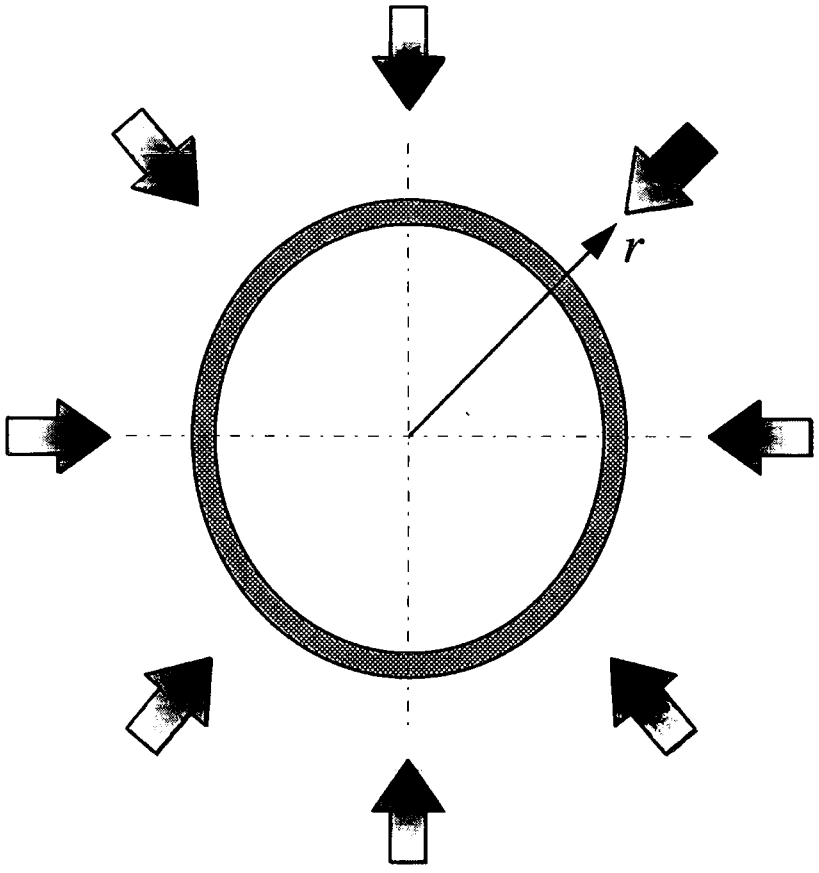

(a)

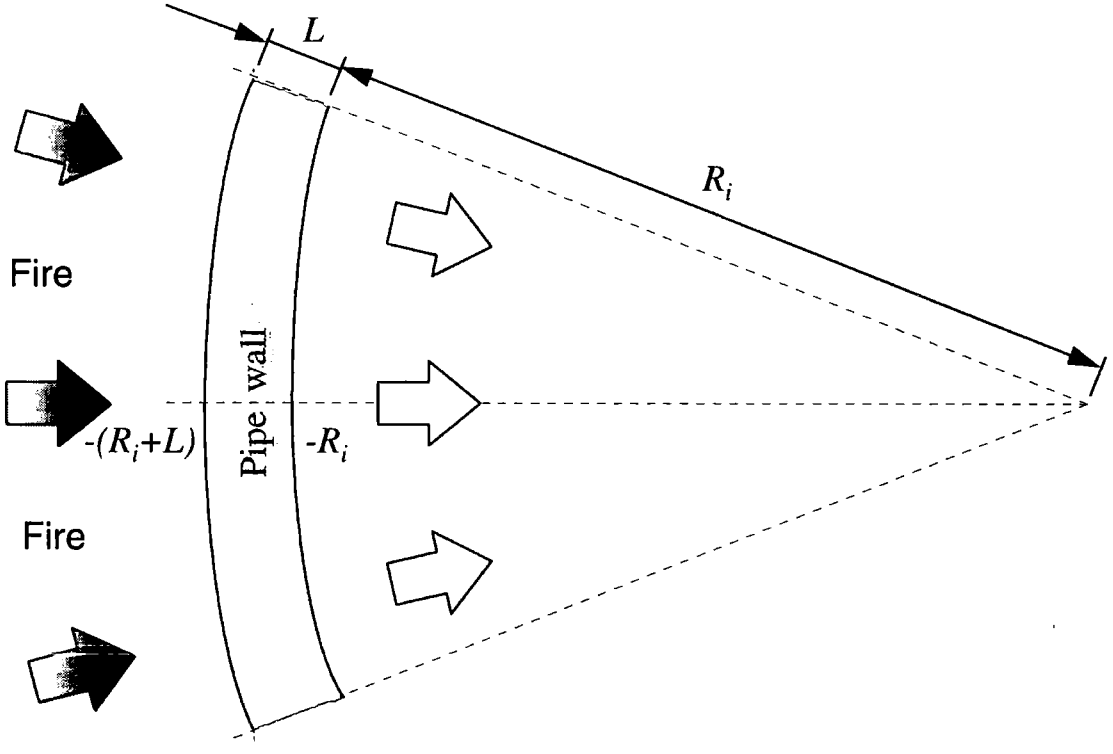

(b)

Figure 7.3 The axi-symmetric geometry of the mathematical model for the GRP pipe subject to uniform fire from outer surface.

The thermal properties are assumed constant throughout fire exposure except for thermal conductivity which is assumed to have a step change at the end of pyrolysis.

The enthalpies of the GRP and pyrolysis gases are defined by Equations 2.22a and 2.22b, i.e.:

$$h = c_p(T - T_\infty) \qquad , \qquad h_g = c_{pg}(T - T_\infty) \tag{7.6}$$

where T_∞ is the ambient temperature (20°C).

Equations 7.3 to 7.6 form a set of non-linear partial differential equations which may be regarded as the complete one-dimensional axi-symmetric mathematical model for single-skinned GRP pipes subject to fire. These equations must be solved simultaneously for T, ρ_r and $\dot{m}_g$ once the initial conditions and appropriate boundary conditions have been defined.

The initial conditions are:

$$\begin{matrix} T(r,t) = T_\infty & \rho = \rho_o \\ \dot{m}_g = 0 & k = k_o \end{matrix} \quad \text{for} \quad \begin{matrix} -(R_i + L) \le r \le -R_i \\ t = 0 \end{matrix} \tag{7.7}$$

where subscript o denotes initial.

The hot surface boundary condition is given by:

$$T(r,t) = T_s(t) \qquad \text{for} \qquad r = -(R_i + L),\ t > 0 \tag{7.8}$$

and the cold surface boundary condition by:

$$\begin{matrix} -k\dfrac{\partial T}{\partial r} = h_c(T_w - T_b) \\ \dot{m}_g = 0 \end{matrix} \qquad \text{for} \qquad r = -R_i,\ t > 0 \tag{7.9}$$

where

$T_s(t)$ = time-dependent hot surface temperature (°C)

h = force convection heat transfer coefficient ($Wm^{-2}K^{-1}$)

T_w = pipe inner surface temperature (°C)

T_b = fluid bulk temperature (°C)

The hot surface time-dependent temperature $T_s(t)$ was introduced in Chapter 3 by an empirical relation, i.e.:

$$T_s(t) = (T_g - 100)\left\{1 - \exp\left\{-\exp\left[0.71\log\left(\frac{t}{124.8}\right)\right]\right\}\right\} + T_\infty \quad \text{for} \quad t > 0 \tag{7.10}$$

where T_g is the maximum fire temperature (1100°C).

The cold surface boundary condition is discussed in detail in the following section.

7.3 FORCED CONVECTION AT THE COLD SURFACE BOUNDARY

To complete the mathematical model, the equation of forced convection heat transfer caused by fluid flow at the internal surface of the pipe needs to be included. This implies that the coefficient of force convection heat transfer h_c and fluid flow bulk temperature T_b appeared in Equation 7.7 should be evaluated. Two types of fluids: (i) natural gas and (ii) sea water are studied.

(i) Natural Gas

The following assumptions are made for natural gas:

1. The natural gas flow is in a state of equilibrium (hydrodynamically and thermally fully developed) (Figure 7.4).
2. The pipe's outer and inner surfaces are considered to remain isothermal during fire exposure.
3. The natural gas flow is assumed to obey the law of ideal gas mixture.
4. The natural gas remains in gaseous phase throughout the fire exposure.
5. No radiative heat transfer occurs between the pipe's inner surface and the gas flow.

A fully developed flow occurs in a region in which the boundary layer is as thick as the pipe internal radius (Figure 7.4). The flow is hydrodynamically developed when the velocity profile is independent from the variable along the pipe axis and its order of magnitude is evaluated based on its mean velocity, i.e. V_m (ms^{-1}). The fluid flow in the boundary layer can be either laminar or turbulent depending on Reynolds number.

Force convection heat transfer coefficient

The force convection heat transfer coefficient h_c is determined using the following formula [Bejan, 1993]:

$$h_c = k_e \frac{\mathrm{Nu_D}}{D} \tag{7.11}$$

where k_e is the fluid thermal conductivity ($Wm^{-1}K^{-1}$), $\mathrm{Nu_D}$ is Nusselt number and D is the pipe internal diameter (m).

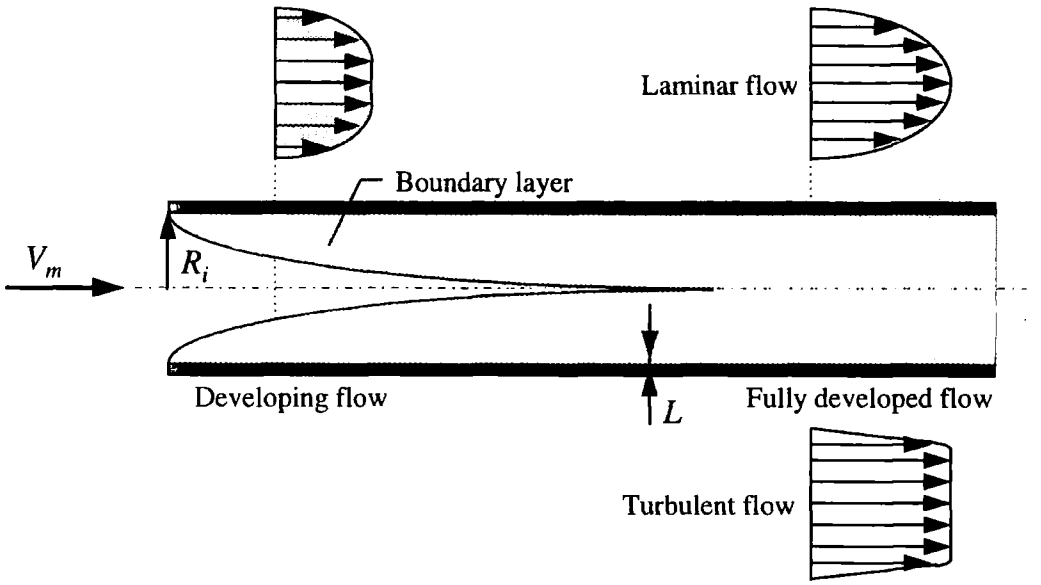

(a)

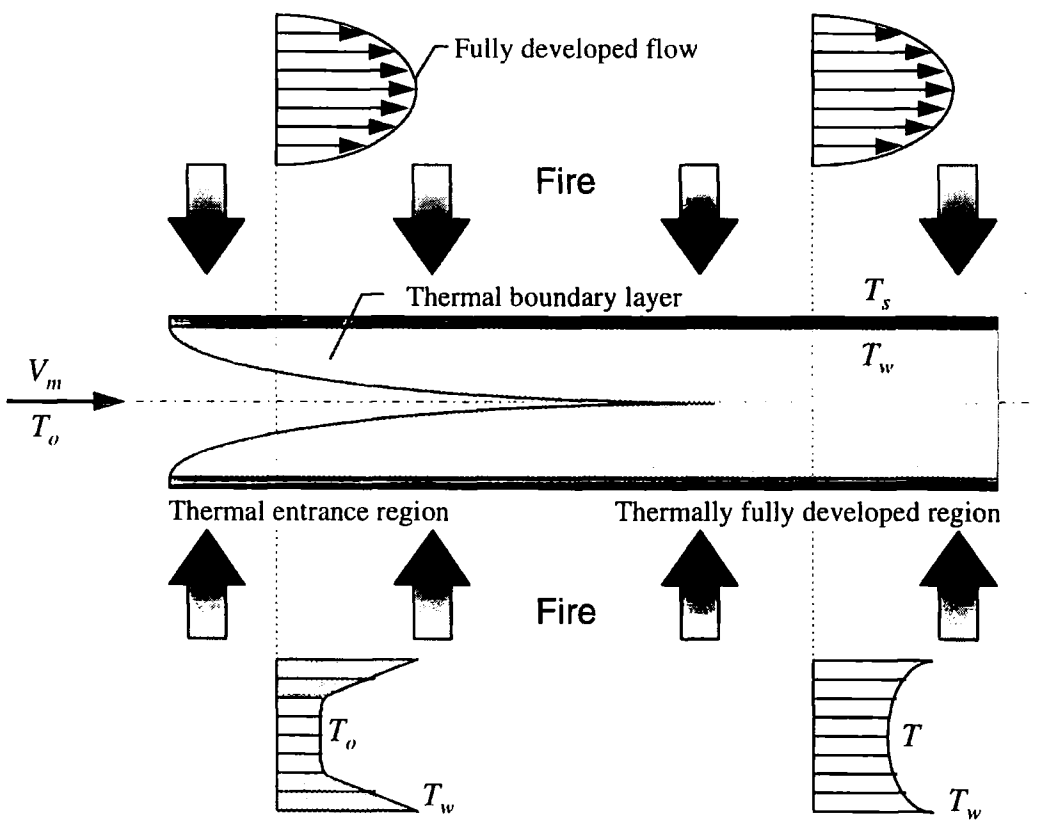

(b)

Figure 7.4 (a) Laminar and turbulent velocity profiles in a fully developed flow region; (b) Temperature profile for a thermally fully developed region [after: Bejan, 1993].

The Reynolds number Re_D is defined as the ratio of inertia force to viscous force by (Appendix B):

$$\mathrm{Re}_D = \frac{\rho_e V_m D}{\mu_e} \tag{7.12}$$

and the Prandtl number Pr as the ratio of viscous diffusion to thermal diffusion by (Appendix B):

$$\mathrm{Pr} = \frac{\mu_e c_{pe}}{k_e} \tag{7.13}$$

where

ρ_e = density of the fluid (kgm^{-3})

μ_e = dynamic viscosity of the fluid (Nsm^{-1})

c_{pe} = specific heat of the fluid ($Jkg^{-1}K^{-1}$)

Experimentally determined values are used for Nusselt number. The empirical relations for the Nusselt number for a laminar flow is given by [Bejan, 1993; Gnielinski, 1976]:

$$\mathrm{Nu}_D = 3.66 \qquad \text{for} \qquad \mathrm{Re}_D < 2\times10^3 \tag{7.14}$$

and for a turbulent flow by [Bejan, 1993; Gnielinski, 1976]:

$$\mathrm{Nu}_D = \frac{(f/2)(\mathrm{Re}_D - 10^3)\mathrm{Pr}}{1+12.7(f/2)^{1/2}(\mathrm{Pr}^{2/3}-1)} \qquad \text{for} \qquad \begin{matrix} 0.5 < \mathrm{Pr} < 10^6 \\ 2.3\times10^3 \le \mathrm{Re}_D \le 5\times10^6 \end{matrix} \tag{7.15}$$

f is the pipe friction factor and represented, for different Reynolds numbers, by [Bejan, 1993]:

$$f = 16\,\mathrm{Re}_D^{-1} \qquad \text{for} \qquad \mathrm{Re}_D < 2\times10^3 \tag{7.16a}$$

$$f \cong 0.079\,\mathrm{Re}_D^{-1/4} \qquad \text{for} \qquad 2\times10^3 \le \mathrm{Re}_D < 2\times10^4 \tag{7.16b}$$

$$f \cong 0.046\,\mathrm{Re}_D^{-1/5} \qquad \text{for} \qquad 2\times10^4 \le \mathrm{Re}_D < 10^6 \tag{7.16c}$$

Bulk temperature and pressure drop

The magnitude of the effective (wall-flow) temperature difference, i.e. (T_w-T_b), depends on the temperature of the inner wall of the pipe and the temperature of the fluid flowing through the pipe. In practice, it will vary along the pipe. Considering assumptions 1 and 2 given similarly for gases or liquids, the temperature difference will decrease exponentially down flow, between a certain value at the pipe inlet and a smaller value at

the pipe outlet (Figure 7.5). The effective temperature difference falls somewhere between ΔT_{in} and ΔT_{out}. Its precise value can be evaluated by deriving the total heat transfer rate per unit area based on thermodynamic analysis. According to this method the total heat transfer rate through the pipe inner wall is given by:

$$q_e = \dot{m}_e c_{pe}\left(T_{out} - T_{in}\right) \tag{7.17}$$

where

q_e = total heat flow through the pipe inner wall (W)

$\dot{m}_e$ = fluid mass flux ($kgm^{-2}s^{-1}$)

T_{out} = outlet temperature of the flow (°C)

T_{in} = inlet temperature of the flow (°C)

To evaluate the flow bulk temperature, it remains to determine the relationship between the heat capacity flow rate $\dot{m}_e c_{pe}$ and convection coefficient, h_c, that appears in the Equation 7.9.

As shown in Figure 7.5b, the bulk temperature of the flow varies exponentially towards the plateau value T_w as z increases. The differential relationship between flow bulk temperature and z [Bejan, 1993] is given by:

$$\frac{dT_b}{T_w - T_b} = \frac{ph_c}{\dot{m}_e c_{pe}} dz \tag{7.18}$$

where p is the pipe inner perimeter defined by $p=2\pi R_i$ (m).

Integrate Equation 7.18 from the inlet (where $T_b = T_{in}$ at $z = 0$) all the way to the outlet (where $T_b = T_{out}$ at $z = L_f$). This gives:

$$\ln\frac{T_w - T_{in}}{T_w - T_{out}} = \frac{h_c A_w}{\dot{m}_e c_{pe}} \tag{7.19}$$

where

A_w = total surface of the pipe swept by flow ($A_w = pL_f$) (m^2)

L_f = overall length of the pipe exposed to fire (m)

By eliminating $\dot{m}_e c_{pe}$ between Equations 7.19 and 7.17, the heat flow rate becomes:

$$q_e = h_c A_w \frac{T_{out} - T_{in}}{\ln\left(\dfrac{T_w - T_{in}}{T_w - T_{out}}\right)} \tag{7.20}$$

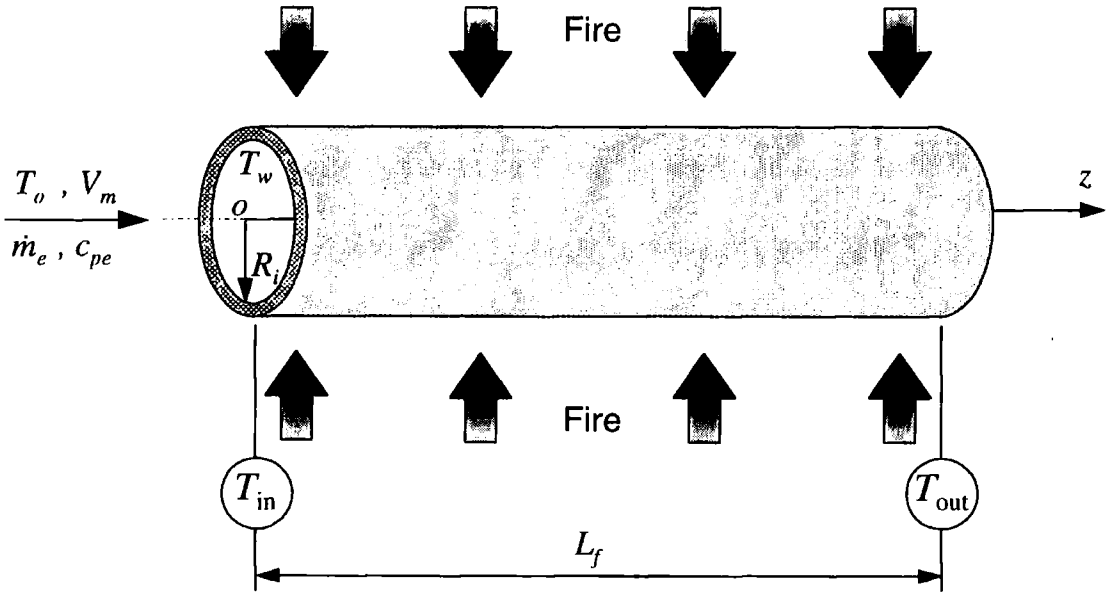

(a)

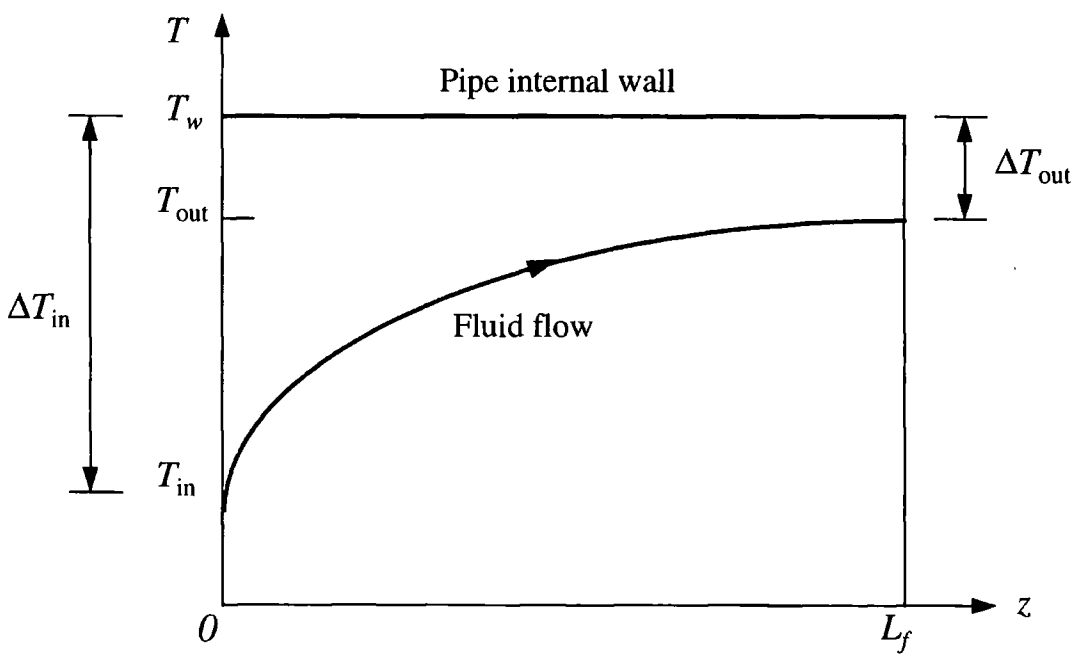

(b)

Figure 7.5 (a) Total heat transfer in terms of inlet and outlet temperatures (given by Equation 7.17) where L_f is the overall length of the pipe exposed to fire, (b) Variation of fluid temperature along the pipe with uniform fire and isothermal wall.

Equations 7.19 and 7.20 can be combined to express the flow bulk temperature:

$$T_b = T_w - \frac{T_{\text{out}} - T_{\text{in}}}{\ln\left(\frac{T_w - T_{\text{in}}}{T_w - T_{\text{out}}}\right)} \tag{7.21}$$

The total heat flow rate can also be evaluated in terms of the inlet temperature, mass flux and force convection coefficient, by combining Equations 7.17 and 7.19, giving:

$$q_e = \dot{m}_e c_{pe}\left(T_w - T_{in}\right)\left[1 - \exp\left(-\frac{h_c A_w}{\dot{m}_e c_{pe}}\right)\right] \tag{7.22}$$

The pressure drop ΔP (kPa) through the length of the pipe exposed to fire is defined, in terms of friction factor f [Bejan, 1993], Equations 7.16a-7.16c, by:

$$\Delta P = f\frac{2L_f}{D}\rho_e V_m^2 \tag{7.23}$$

Density and compressibility factor

Assuming a gaseous phase of the natural gas throughout the fire exposure (assumption 4), the natural gas density can be evaluated, using the real gas law [Hall & Yarborough, 1971], by:

$$\rho_e = \frac{P_e M_e}{zRT_{bk}} \tag{7.24}$$

where

P_e = natural gas pressure (kPa)

M_e = molecular weight (kgkmole^{-1})

z = compressibility factor

T_{bk} = bulk temperature (K)

One particular method for natural gas density estimation is the direct calculation of the compressibility factor. Here, the Hall-Yarborough empirical relation for the compressibility factor is used [Hall & Yarborough, 1971]. This relation is:

$$z = \frac{1 + x + x^2 + x^3 - ax + bx^c}{(1-x)^3} \tag{7.25}$$

where x , a, b and c are given by:

$$x = \frac{\rho_e dM_e}{4} \tag{7.26a}$$

$$a = 14.76t_{cr} - 9.76t_{cr}^2 + 4.58t_{cr}^3 \tag{7.26b}$$

$$b = 90.7t_{cr} - 242.2t_{cr}^2 + 42.4t_{cr}^3 \tag{7.26c}$$

$$c = 1.18 + 2.82t_{cr} \tag{7.26d}$$

d and t_{cr} by:

$$d = 0.245\frac{RT_{cr}}{P_{cr}}\exp\left[-1.2(1-t_{cr})^2\right] \tag{7.26e}$$

$$t_{cr} = \frac{T_{cr}}{T_{bk}} \tag{7.26f}$$

and T_{cr} = critical temperature (K)

P_{cr} = critical pressure (kPa)

Thermo physical properties

To calculate the coefficient of force convection heat transfer h_c and fluid flow bulk temperature T_b, the thermo physical properties of the natural gas must be evaluated.

Mole fractions [Boothby & Vu, Pers. Com., 1995], molecular weights and critical temperatures and pressures [Bradley, 1992] of the components of a standard natural gas are presented in Table 7.1.

Molecular weight and critical temperature and pressure of natural gas composition are evaluated using the law of ideal gas mixture [Bradley, 1992] as:

$$M_e = \sum_{i=1}^{5} y_i M_i \tag{7.27a}$$

$$T_{cr} = \sum_{i=1}^{5} y_i (T_{cr})_i \tag{7.27b}$$

$$P_{cr} = \sum_{i=1}^{5} y_i (P_{cr})_i \tag{7.27c}$$

Lide and Kehiaian [1994] introduced a general formula for the thermo physical properties (TPP) of gases and liquids which can be used for natural gas where $a_6 = 0$. The formula is:

$$\text{TPP} = a_1 + a_2 T_{bk} + a_3 T_{bk}^2 + a_4 T_{bk}^3 + a_5 T_{bk}^4 + a_6 T_{bk}^5 \tag{7.28}$$

where T_{bk} is the bulk temperature (K).

The coefficients a_i (i = 1, 2,..., 5) for natural gas are given in Table 7.2. The valid temperature ranges for thermal conductivity, specific heat and dynamic viscosity are also indicated for each property. These coefficients are obtained using the law of ideal gas mixture.

Table 7.1 Natural gas components and their properties [from: Boothby & Vu, Pers. Com., 1995; Bradley, 1992].

Property	Carbon Dioxide CO_2	Ethane C_2H_6	Methane CH_4	Nitrogen N_2	Propane C_3H_8
Mole fraction, y_i (mole%)	0.2	2.9	90.40	5.80	0.70
Molecular weight, M_i (kgkmole^{-1})	44.01	30.070	16.043	28.013	44.097
Critical temperature, $(T_{cr})_i$ (K)	304.04	305.28	190.4	125.94	369.67
Critical pressure, $(P_{cr})_i$ (kPa)	7384.3	4880.1	4604.3	3399.1	4249.2

Table 7.2 Natural gas a_i coefficients [from: Lide & Kehiaian, 1994].

Coefficient	Thermal Cond., k_e, (Wm^{-1}K^{-1})	Specific Heat, c_{pe}, (Jkg^{-1}K^{-1})	Dynamic Viscosity, μ_e, (Nsm^{-1})
	235-600 K	298-800 K	235-600 K
a_1	0	29.734	0
a_2	1.107×10^{-4}	-9.44×10^{-4}	4.11776×10^{-8}
a_3	-1.322×10^{-7}	1.2469×10^{-4}	6.4239×10^{-13}
a_4	6.017×10^{-10}	-7.4122×10^{-8}	-4.08727×10^{-14}
a_5	-4.761×10^{-13}	0	2.97805×10^{-17}

(ii) Sea water

The following assumptions are made for sea water:

1. The sea water flow is in a state of equilibrium (hydrodynamically and thermally fully developed) (Figure 7.4).
2. The pipe's outer and inner surfaces are considered to remain isothermal during fire exposure.
3. The sea water remains in liquid phase throughout the fire exposure.
4. No radiative heat transfer occurs between the pipe's inner surface and the sea water flow.

Force convection heat transfer coefficient

The force convection heat transfer coefficient h_c for sea water is determined in the same manner as described for natural gas using Equations 7.11 to 7.16.

Bulk temperature and pressure drop

The bulk temperature and pressure drop for sea water are evaluated in the same manner as explained for natural gas using Equations 7.17 to 7.23.

Thermo physical properties

Equation 7.28 introduced by Lide and Kehiaian [1994] is used to evaluate the thermo physical properties of sea water where the coefficients a_i (i = 1, 2,..., 6) are given in Table 7.3.

Table 7.3 Sea water a_i coefficients [from: Lide & Kehiaian, 1994]

Coefficient	Density, ρ_e (kgm^{-3})	Thermal Cond., k_e (Wm^{-1}K^{-1})	Specific Heat, c_{pe} (Jkg^{-1}K^{-1})	Dyn. Viscosity, μ_e (Jkg^{-1}K^{-1})
	273-373 K	273-373 K	273-373 K	273-373 K
a_1	999.84259	0.56052	4216.92	1.76336×10^{-3}
a_2	6.79395×10^{-2}	0.00209	-.04868	-4.7598×10^{-5}
a_3	-9.09529×10^{-3}	-8.37473×10^{-6}	0.079666	5.87405×10^{-7}
a_4	1.00168×10^{-4}	6.66275×10^{-9}	-8.32401×10^{-4}	-2.61556×10^{-9}
a_5	-1.12008×10^{-6}	0	3.40064×10^{-6}	0
a_6	6.53633×10^{-9}	0	0	0

7.4 FINITE ELEMENT FORMULATION

The set of non-linear partial differential equations, Equations 7.3 to 7.6, is solved numerically using Bubnov-Galerkin approach of the finite element method [Zienkiewicz & Taylor, 1994]. All terms and coefficients are evaluated explicitly using an iterative-updating procedure at each step of computations. Nodal temperatures are computed implicitly using the Crank-Nicolson solution.

7.4.1 Explicit Evaluation of Terms and Coefficients

To define the element equations the method presented in Chapter 2 is used. A general notation $(\,)_j^i$ is used where i represents the time interval and j the spatial position. Time derivative terms are given by forward difference and the spatial variables by central difference, with exception of the gas mass flux term which is represented by backward difference.

Using notation $(\,)_j^i$, Equation 7.3 becomes:

$$\rho_j^{i+1} c_p \frac{\partial T}{\partial t} = \frac{k}{r}\frac{\partial}{\partial r}\left(r\frac{\partial T}{\partial r}\right) - \left(\dot{m}_g\right)_j^{i+1} c_{pg}\frac{\partial T}{\partial r} - \left(\frac{\partial \rho_r}{\partial t}\right)_j^{i+1}\left(Q + h - h_g\right) \tag{7.29}$$

where

$$\rho_j^{i+1} = \left\{\left(\rho_r\right)_j^i - A\Delta t\left[\left(\rho_r\right)_j^i - \rho_{rf}\right]\exp\left[\frac{-E_A}{R\left(T_k\right)_j^i}\right]\right\}\left(1 - V_f\right) + \rho_{fr}V_f \tag{7.30}$$

$$\left(\dot{m}_g\right)_j^{i+1} = \sum_{j=n_r}^{n_T}\left[\frac{\left(\rho_r\right)_j^{i+1} - \left(\rho_r\right)_j^i}{\Delta t}\right] l_j \tag{7.31}$$

$$\left(\frac{\partial \rho_r}{\partial t}\right)_j^{i+1} = \frac{\left(\rho_r\right)_j^{i+1} - \left(\rho_r\right)_j^i}{\Delta t} = -A\left[\left(\rho_r\right)_j^i - \rho_{rf}\right]\exp\left[\frac{-E_A}{R\left(T_k\right)_j^i}\right] \tag{7.32}$$

and

Δt = time step size (s)

V_f = volume fraction

l = element length (m)

n_T = total number of spatial nodes

n_r = number of spatial nodes at position r

7.4.2 Finite Element Equations

Consider linear elements with two nodes each and assuming the temperature is the only dependent variable.

The temperature and temperature gradients are approximated within each element by:

$$T(r,t) = \mathbf{N}(r)\mathbf{T}(t) = \sum_{i=1}^{2} N_i(r)T_i(t) \tag{7.33a}$$

$$\frac{\partial T(r,t)}{\partial r} = \mathbf{B}(r)\mathbf{T}(t) = \sum_{i=1}^{2} B_i(r)T_i(t) \tag{7.33b}$$

where

$\mathbf{N}(r)$ = shape function matrix

$\mathbf{T}(t)$ = temperature vector

$N_i(r)$ = the ith element of the shape function matrix

T_i = the ith element of the temperature vector

$\mathbf{B}(r)$ = shape function derivative matrix

$B_i(r)$ = the ith element of shape function derivative matrix defined by $\partial N_i/\partial x$

The shape function and shape function derivative matrices are defined by:

$$\mathbf{N}(r) = \left[\frac{l-r}{l} \quad \frac{r}{l}\right] \tag{7.34a}$$

$$\mathbf{B}(r) = \left[-\frac{1}{l} \quad \frac{1}{l}\right] \tag{7.34b}$$

Applying the Bubnov-Galerkin approach to Equation 7.3 gives:

$$\int_{\Omega^e}\left[\rho c_p \frac{\partial T}{\partial t} - \frac{k}{r}\frac{\partial}{\partial r}\left(r\frac{\partial T}{\partial r}\right) + \dot{m}_g c_{pg}\frac{\partial T}{\partial r} + \frac{\partial \rho_r}{\partial t}\left(Q + h - h_g\right)\right]N_i d\Omega = 0 \qquad i = 1,2$$

or

$$\int_{0}^{l}\left[\rho c_p \frac{\partial T}{\partial t} - \frac{k}{r}\frac{\partial}{\partial r}\left(r\frac{\partial T}{\partial r}\right) + \dot{m}_g c_{pg}\frac{\partial T}{\partial r} + \frac{\partial \rho_r}{\partial t}\left(Q + h - h_g\right)\right]N_i dr = 0 \qquad i = 1,2 \tag{7.35}$$

where 0 and l denote the co-ordinates of the end nodes of the line element within the global co-ordinate system.

Using integration by parts and substituting Equations 7.6 into Equation 7.35, gives:

$$\int_0^l \rho c_p \frac{\partial T}{\partial t} N_i dr - N_i k \frac{\partial T}{\partial r}\Big|_0^l + \int_0^l k \frac{\partial T}{\partial r} B_i dr - \int_0^l \frac{k}{r} \frac{\partial T}{\partial r} N_i dr + \int_0^l \dot{m}_g c_{pg} \frac{\partial T}{\partial r} N_i dr$$

$$+ \int_0^l \frac{\partial \rho_r}{\partial t} (c_p - c_{pg}) T N_i dr + \int_0^l \frac{\partial \rho_r}{\partial t} \left[Q - (c_p - c_{pg}) T_\infty \right] N_i dr = 0 \quad i = 1,2 \qquad (7.36)$$

where the second term in Equation 7.36 represents natural boundary conditions for the element at the boundary node.

Substitute Equations 7.9, 7.33a and 7.33b into Equation 7.36. The resulting equation becomes:

$$\int_0^l \rho c_p \mathbf{N}^T \dot{\mathbf{T}} \mathbf{N} dr + \int_0^l k \mathbf{B}^T \mathbf{T} \mathbf{B} dr - \int_0^l \frac{k}{r} \mathbf{N}^T \mathbf{T} \mathbf{B} dr + \int_0^l \dot{m}_g c_{pg} \mathbf{B}^T \mathbf{T} \mathbf{N} dr$$

$$+ \int_0^l \frac{\partial \rho_r}{\partial t} (c_p - c_{pg}) \mathbf{N}^T \mathbf{T} \mathbf{N} dr + \int_0^l \frac{\partial \rho_r}{\partial t} \left[Q - (c_p - c_{pg}) T_\infty \right] \mathbf{N}^T dr - \begin{bmatrix} -k \dfrac{\partial T}{\partial x}(0) \\ -h(T_w - T_b) \end{bmatrix} = \mathbf{0} \qquad (7.37)$$

where superscript **T** denotes the transpose quantity and the last vector contains the natural boundary conditions in which the second term has been replaced by its equivalent from Equation 7.9. The prescribed temperature at the hot surface boundary, Equation 7.8, is introduced to the matrix equation after assembling the element matrices (Appendix C). Using Equations 7.30 to 7.32 and rearranging Equation 7.37 gives:

$$\left(\int_0^l \mathbf{N}^T \rho_j^{i+1} c_p \mathbf{N} dr \right) \dot{\mathbf{T}} + \left[\int_0^l \mathbf{B}^T k \mathbf{B} dr - \int_0^l \mathbf{N}^T \frac{k}{r} \mathbf{B} dr + \int_0^l \mathbf{B}^T \left(\dot{m}_g \right)_j^{i+1} c_{pg} \mathbf{N} dr \right.$$

$$\left. + \int_0^l \mathbf{N}^T \left(\frac{\partial \rho_r}{\partial t} \right)_j^{i+1} (c_p - c_{pg}) \mathbf{N} dr \right] \mathbf{T} + \int_0^l \left(\frac{\partial \rho_r}{\partial t} \right)_j^{i+1} \left[Q - (c_p - c_{pg}) T_\infty \right] \mathbf{N}^T dr - \begin{bmatrix} -k \dfrac{\partial T}{\partial x}(0) \\ -h(T_w - T_b) \end{bmatrix} = \mathbf{0}$$

or $$\mathbf{C}\dot{\mathbf{T}} + (\mathbf{K_o} + \mathbf{K_g} + \mathbf{K_d} + \mathbf{K_a})\mathbf{T} + (\mathbf{f_o} + \mathbf{f_b}) = \mathbf{0}$$

or $$\mathbf{C}\dot{\mathbf{T}} + \mathbf{K}\mathbf{T} + \mathbf{f} = \mathbf{0} \qquad (7.38)$$

where

$\mathbf{C}$	=	element capacitance matrix
$\mathbf{K_o}$	=	element conductance matrix
$\mathbf{K_g}$	=	element gas diffusion matrix
$\mathbf{K_d}$	=	element decomposition matrix
$\mathbf{K_a}$	=	element matrix due to the term from axi-symmetric definition
$\mathbf{f_o}$	=	element decomposition vector
$\mathbf{f_b}$	=	element boundary conditions vector

The element matrices and element vectors are given, in global co-ordinate r, by:

$$\mathbf{C} = \int_0^l \mathbf{N}^{\mathrm{T}} \rho_j^{i+1} c_p \mathbf{N}\, dr \tag{7.39a}$$

$$\mathbf{K}_{\mathrm{o}} = \int_0^l \mathbf{B}^{\mathrm{T}} k \mathbf{B}\, dr \tag{7.39b}$$

$$\mathbf{K}_{\mathrm{g}} = \int_0^l \mathbf{B}^{\mathrm{T}} \left(\dot{m}_g\right)_j^{i+1} c_{pg} \mathbf{N}\, dr \tag{7.39c}$$

$$\mathbf{K}_{\mathrm{d}} = \int_0^l \mathbf{N}^{\mathrm{T}} \left(\frac{\partial \rho_r}{\partial t}\right)_j^{i+1} \left(c_p - c_{pg}\right) \mathbf{N}\, dr \tag{7.39d}$$

$$\mathbf{K}_{\mathrm{a}} = -\int_0^l \mathbf{N}^{\mathrm{T}} \frac{k}{r} \mathbf{B}\, dr \tag{7.39e}$$

$$\mathbf{f}_{\mathrm{o}} = \int_0^l \mathbf{N}^{\mathrm{T}} \left(\frac{\partial \rho_r}{\partial t}\right)_j^{i+1} \left[Q - \left(c_p - c_{pg}\right) T_\infty\right] dr \tag{7.39f}$$

$$\mathbf{f}_{\mathrm{b}} = -\begin{bmatrix} -k\dfrac{\partial T}{\partial x}(0) \\ -h\left(T_w - T_b\right) \end{bmatrix} \tag{7.39g}$$

where r is expressed as a linear function of nodal values by:

$$r = \mathbf{N}\mathbf{r} = \sum_{i=1}^{2} N_i r_i \tag{7.40}$$

The element matrices and element vectors are then transferred from the global to local co-ordinate in order to be integrated numerically. If the local co-ordinate ξ is chosen to be related to the global co-ordinate r by:

$$r = \frac{l}{2}(1+\xi) \tag{7.41}$$

then the shape function and shape function derivative matrices are given, in the local co-ordinate ξ, by:

$$\mathbf{N}(x) = \begin{bmatrix} \frac{1}{2}(1-\xi) & \frac{1}{2}(1+\xi) \end{bmatrix} \tag{7.42a}$$

$$\mathbf{B}(x) = \begin{bmatrix} -\frac{1}{2} & \frac{1}{2} \end{bmatrix} \tag{7.42b}$$

and the element matrices and element vectors by:

$$\mathbf{C} = \frac{1}{2}\int_{-1}^{1} \mathbf{N}^{\mathrm{T}} \rho_j^{i+1} c_p \mathbf{N}\, d\xi \tag{7.43a}$$

$$\mathbf{K}_{\mathrm{o}} = \frac{1}{2}\int_{-1}^{1} \mathbf{B}^{\mathrm{T}} k \mathbf{B}\, d\xi \tag{7.43b}$$

$$\mathbf{K}_g = \frac{1}{2}\int_{-1}^{1} \mathbf{B}^T \left(\dot{m}_g\right)_j^{i+1} c_{pg} \mathbf{N}\, d\xi \tag{7.43c}$$

$$\mathbf{K}_d = \frac{1}{2}\int_{-1}^{1} \mathbf{N}^T \left(\frac{\partial \rho_r}{\partial t}\right)_j^{i+1} \left(c_p - c_{pg}\right)\mathbf{N}\, d\xi \tag{7.43d}$$

$$\mathbf{K}_a = -\frac{1}{2}\int_{-1}^{1} \mathbf{N}^T \frac{k}{r}\mathbf{B}\, d\xi \tag{7.43e}$$

$$\mathbf{f}_o = \frac{1}{2}\int_{-1}^{1} \mathbf{N}^T \left(\frac{\partial \rho_r}{\partial t}\right)_j^{i+1} \left[Q - \left(c_p - c_{pg}\right)T_\infty\right] d\xi \tag{7.43f}$$

$$\mathbf{f}_b = -\begin{bmatrix} -k\dfrac{\partial T}{\partial x}(0) \\ -h\left(T_w - T_b\right) \end{bmatrix} \tag{7.43g}$$

For numerical integration of the element matrices and vectors, Equations 7.43a to 7.43f, Gauss-Legendre quadrature is used with two Gaussian points (Appendix C).

7.4.3 Time Step Algorithm

A solution to the matrix equation, Equation 7.38, is given by the finite difference time stepping algorithm, Equation 2.37 [from: Zienkiewicz & Taylor, 1991 as corrected by Looyeh *et al.*, 1997; Zienkiewicz, Pers. Com., 1995]:, i.e.:

$$\mathbf{T}_{n+1} = \left(\mathbf{C} + \Delta t \Theta \mathbf{K}\right)^{-1} \left\{\left[\mathbf{C} - \Delta t(1-\Theta)\mathbf{K}\right]\mathbf{T}_n - \Delta t \bar{\mathbf{f}}\right\} \tag{7.44}$$

where Θ is the weighting (time step) parameter, $\bar{\mathbf{f}}$ is given by:

$$\bar{\mathbf{f}} = \bar{\mathbf{f}}_n + \Theta\left(\bar{\mathbf{f}}_{n+1} - \bar{\mathbf{f}}_n\right) \tag{7.45}$$

and subscripts **n** and **n+1** denote know and unknown values, respectively.

A non-symmetric profile matrix solver with active column method is used [Applegarth, 1990]. The Crank-Nicolson solution, corresponding to Θ=1/2, is applied to solve the matrix equation implicitly and compute the nodal temperatures after each iteration.

The time step is based on the critical time step Δt_{cr} given by Equation 2.38 [Zienkiewicz & Taylor, 1991]:

$$\Delta t_{cr} = \frac{2}{1-2\Theta}\frac{l_j^2 \rho_j^{i+1} c_p}{3k} \tag{7.46}$$

7.4.4 The Computer Code Algorithm

Due to the axi-symmetric and force convection terms in Equation 7.38, the finite element computer code for GRP pipes is slightly different from the one underlined for GRP panels (Chapter 5). The key operations flow chart of the finite element computer code developed in this chapter is shown in Figure 7.6. Apart from terms regarding element matrices and vectors, two new subroutines were included to deal with the cold surface boundary condition. The element matrices subroutine was also modified to account for one-dimensional axi-symmetric solution to GRP pipes.

Main Finite Element Program

1. initialize the system matrices, vectors and principle variables.
2. read finite element mesh data, thermal, kinetic and transport properties, pipe data, boundary condition parameters and also control ID value to perform different solutions.
3. start time-dependent calculation and determine furnace temperature.
4. set the initial values for thermal and transport properties, Eqs. 4.1 to 4.3.
5. determine the hot surface boundary condition, Eq. 7.10.
6. determine the cold surface boundary condition, Eqs. 7.11 to 7.28 depending on the fluid.
7. calculate the mass loss rate, instantaneous density and gas mass flux regarding the control ID value for the required solution.
8. choose a suitable option according to the input element type and create element matrices, **K** and **C**, and element force vector, **f**, Eqs. 7.43a to 7.43g.
9. assemble the system matrices and force vector, if any.
10. calculate and update the time step using Eq. 7.46 or consider the chosen value for the implicit solutions.
11. form system equations according to Eq. 7.38.
12. apply hot surface and cold surface boundary conditions.
13. solve the matrix equation using Eqs. 7.44 and find temperatures and mass losses.
14. add the time step, determined in step 10, then go to step 5, otherwise stop.

Figure 7.6 Flow chart listing the steps for the main program of the finite element computer code to perform one-dimensional axi-symmetric heat transfer analysis for GRP pipes.

7.5 GRP, NATURAL GAS, SEA WATER AND PIPE DATA

Table 4.3 lists material properties for polyester-based GRP. The properties of pyrolysis gases are given in Table 4.4. The initial density of the GRP is 1832.4 kgm^{-3}. The density varies with temperature based on a first-order Arrhenius rate equation and the final density is 1203.24 kgm^{-3}. The thermal conductivity is assumed constant throughout the pyrolysis (0.322 $Wm^{-1}K^{-1}$). From the end of pyrolysis and then the transient heat conduction is followed by the thermal conductivity of glass fibre (1.09$Wm^{-1}K^{-1}$). The specific heat of GRP is assumed constant throughout fire exposure (1056.84 $Jkg^{-1}K^{-1}$). Pyrolysis constant, activation energy and heat of decomposition for GRP are given by 7525 s^{-1}, 611.5 $MJkmole^{-1}$ and 2.3446 $MJkg^{-1}$, respectively.

The properties of natural gas and sea water are obtained using Equation 7.28 and Tables 7.1 to 7.3. The standard data for GRP pipes used offshore for natural gas and sea water transmissions [Boothby & Vu, Pers. Com., 1995; Hill, Pers. Com., 1996] are listed in Tables 7.4 and 7.5.

Table 7.4 Pipe size and natural gas data [Boothby & Vu, Pers. Com., 1995; Hill, Pers. Com., 1996]

Property	Value
Nominal pipe size (outer diameter), *OD* (cm)	60.96
Selected pipe thickness, *L* (cm)	1.09
Maximum working pressure, P_M (MPa)	7
Velocity range, *V* (ms^{-1})	10 - 18
Specific gravity, γ_g	5
Normal working temperature range, *T* (°C)	0 - 50

Table 7.5 Pipe size and sea water data [Boothby & Vu, Pers. Com., 1995; Hill, Pers. Com., 1996]

Property	Value
Nominal pipe size (outer diameter), *OD* (cm)	30.48
Selected pipe thickness, *L* (cm)	1.09
Maximum working pressure, P_M (MPa)	2
Maximum velocity, V_M (ms^{-1})	5
Normal working temperature range, *T* (°C)	3 - 35

7.6 FINITE ELEMENT RESULTS AND DISCUSSION

The finite element formulation developed here is used for the axi-symmetric analysis of the thermal response of thin walled, large diameter GRP pipes, i.e. $L/D \leq 1/10$ and $D \geq 10$cm.

Since the fundamental assumptions and principles for deriving the governing equations are the same for both single-skinned GRP pipes and panels, the performance of GRP pipes under fire is expected to be similar to that of GRP panels. This is particularly true when thin-walled large diameter GRP pipes are considered. Some possible differences are expected, among them the following are of great importance:

1. Delamination is not expected to happen in GRP pipes during thermochemical decomposition. This is because the glass fibres are wound helically into the cylindrical shape. This may result in earlier insulation failure in GRP pipes compared to GRP panels. Delamination is the major cause for the sensors separation from the material layers, particularly at the areas near the hot surface. It is therefore expected to gain more accurate experimental results for GRP pipes.
2. The heat exchange at the inner surface of GRP pipes is due to forced convection caused by fluid flow. The fluid flow carries away a part of the heat energy released at the inner surface and therefore performs an efficient cooling process. It is expected that the temperature rise at the inner surface of GRP pipes to be slower compared to that for GRP panels. However, the effect of the additional term in the mathematical model of GRP pipes, i.e. $-(k/r)(\partial T/\partial r)$, on the overall thermal response is unknown and may change the thermal response substantially.

Although there have been a few fire experiments for GRP pipes, these are confined to small diameter ($L<10$cm) empty pipes or those containing stagnant water. It is therefore possible only to discuss the finite element results and compare them with the results of a single-skinned GRP panel which has the same thickness. 2 to 3% of the resin mass is assumed to remain intact after the completion of pyrolysis [Gibson *et al.*, 1996].

In Figure 7.7, the computed temperatures of a GRP pipe and a GRP panel (both with thickness 1.09cm) are plotted versus time for various distances, i.e. $(r-R_i)/L$ or x/L = 0, 1/10, 5/10 and 1. The same hot surface boundary condition is applied to both models. The inner surface of GRP pipe and the back surface of GRP panel are insulated. Evident is the similar trends for temperature profiles at the same positions but faster rate of temperature rise in the GRP pipe with maximum difference 30°C after 16 minutes of fire exposure. It is therefore concluded that for the given set of geometry and boundary conditions, the GRP panel survives longer. The only difference between two mathematical models is an additional term, i.e. $-(k/r)(\partial T/\partial r)$, which is present in the governing equation of the GRP pipe. This is expected to be the source of differences. Important to note is that for very large diameter pipes, the additional term tends to zero, whereas for very small diameter pipes, this term is expected to increase the rate of temperature rise. The variation of this term may also influence the convergence of the finite element program.

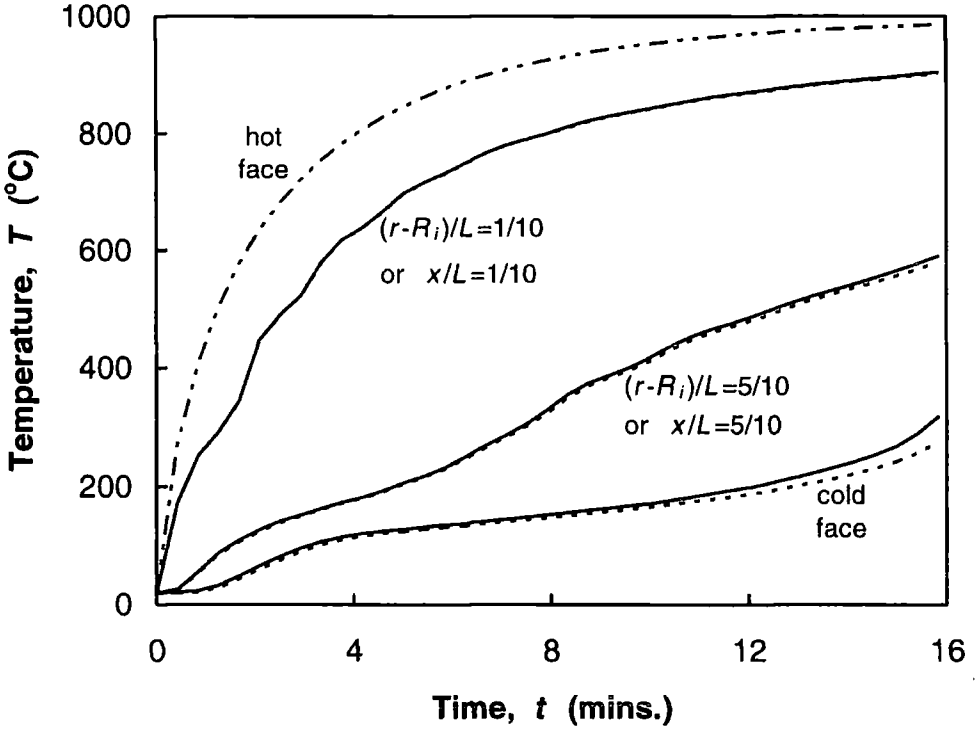

Figure 7.7 Comparison of the computed temperature profiles at various distances. The dash-dot line represents the hot surface temperature profile, the solid lines the temperature results for 1.09cm GRP pipe with an insulated inner surface and the dot lines those for 1.09cm GRP panel insulated at its back surface.

Figure 7.8 shows two set of computed temperature profiles for a GRP pipe subject to different boundary conditions at its inner surface. The first set (solid lines) takes account of forced convection caused by natural gas, whereas the second (dot lines) deals with an insulated surface. Faster temperature rise in the insulated GRP pipe is noticeable. The difference between the cold surface temperatures of two models after 16 minutes of fire exposure is about 20°C. The insulated GRP pipe reaches insulation failure (time to 160°C) after 9 minutes and the GRP pipe with natural gas forced convection after 9.4 minutes.

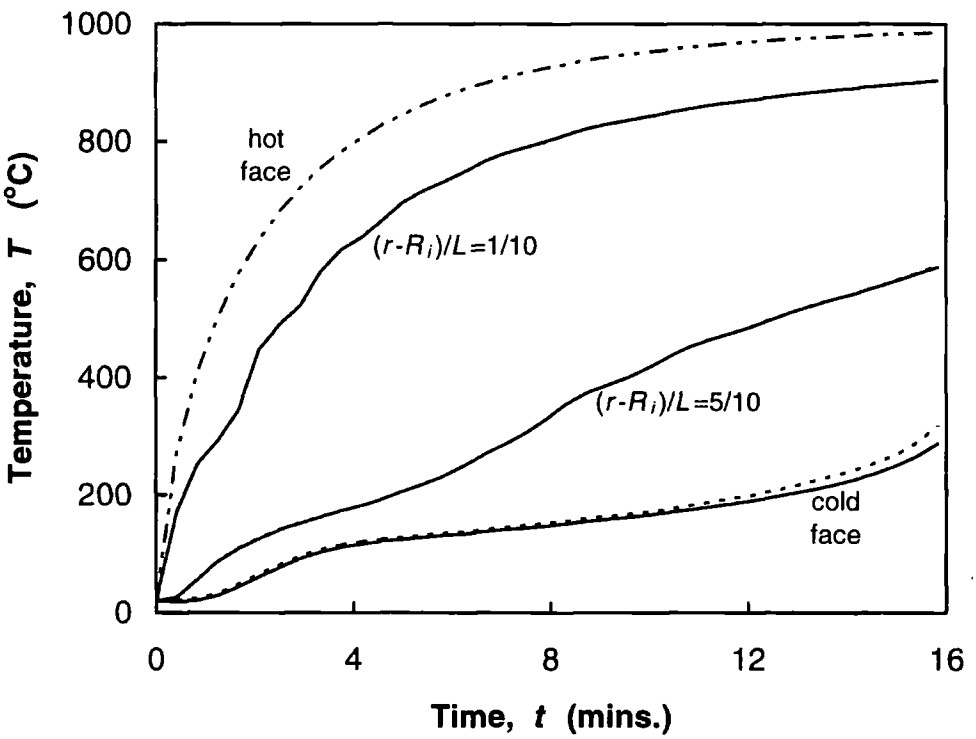

Figure 7.8 Computed temperatures versus time for various distances. The dash-dot line represents the hot surface temperature profile, the solid lines the temperature results for 1.09cm GRP pipe subject to natural gas forced convection at its inner surface and the dot lines those for 1.09cm GRP pipe with an insulated inner surface.

Figure 7.9 shows a combination of Figures 7.7 and 7.8 where the cold surface temperature profiles are only presented. These profiles are: (i) GRP pipe with insulated inner surface (dash-dot line); (ii) GRP pipe with natural gas forced convection at its inner surface (solid line); (iii) GRP panel with insulated cold surface (dot line). It is

seen that the effect of the additional term $-(k/r)(\partial T/\partial r)$, which causes the difference between profile (i) and profile (iii) is greater than that for the forced convection which shifts profile (i) to profile (ii). This suggests that the former term has an important role in the design of fire protected pipes.

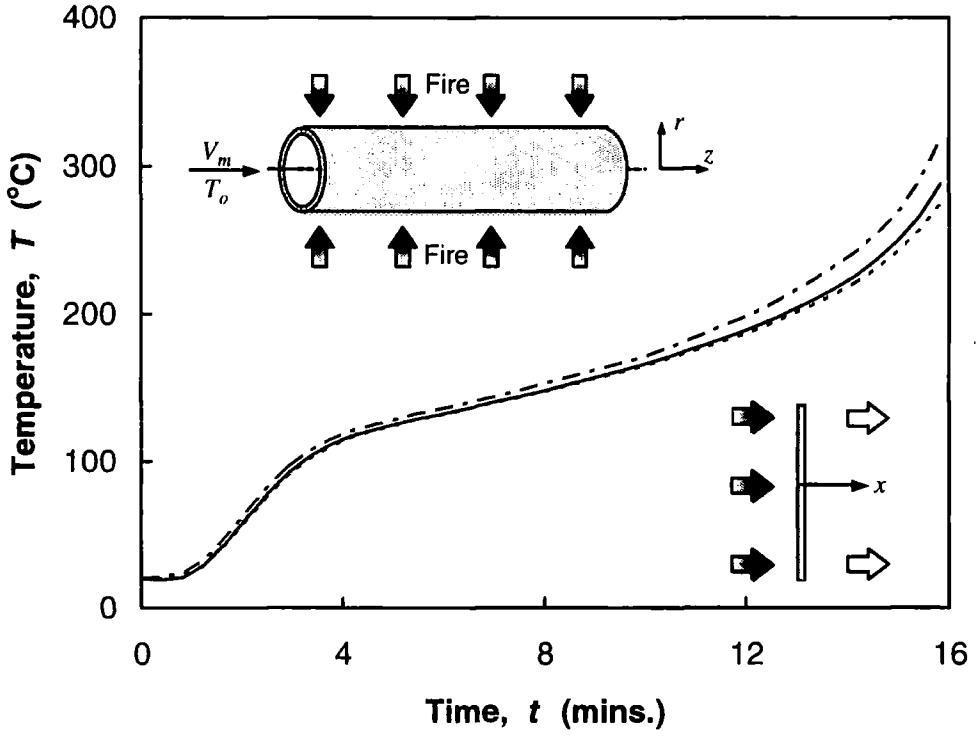

Figure 7.9 Comparison of the computed cold surface temperatures. The dash-dot line represents the results for 1.09cm GRP pipe insulated at its inner surface, the solid line that for 1.09cm GRP pipe subject to natural gas forced convection and the dot line that for 1.09cm GRP panel insulated at its back surface.

Figure 7.10 is similar to Figure 7.8 with the exception that sea water is flowing through the pipe. Sea water flow has lower velocity (5 ms^{-1}) compared to that of natural gas (14 ms^{-1}). It is expected to reach smaller Reynolds number for the flowing sea water and thus less heat loss at the pipe inner surface compared to that for natural gas. The difference between the cold surface temperatures of the insulated GRP pipe and that for the GRP pipe with flowing sea water after 16 minutes of fire exposure is less than 8°C. This differs from that of Figure 7.8 by 12°C. The GRP pipe with flowing sea water reaches insulation failure (time to 160°C) after 9.1 minutes. This is 1.1% greater than that for an insulated GRP pipe and 3.3% less than that for GRP pipe with flowing natural gas (Figure 7.11).

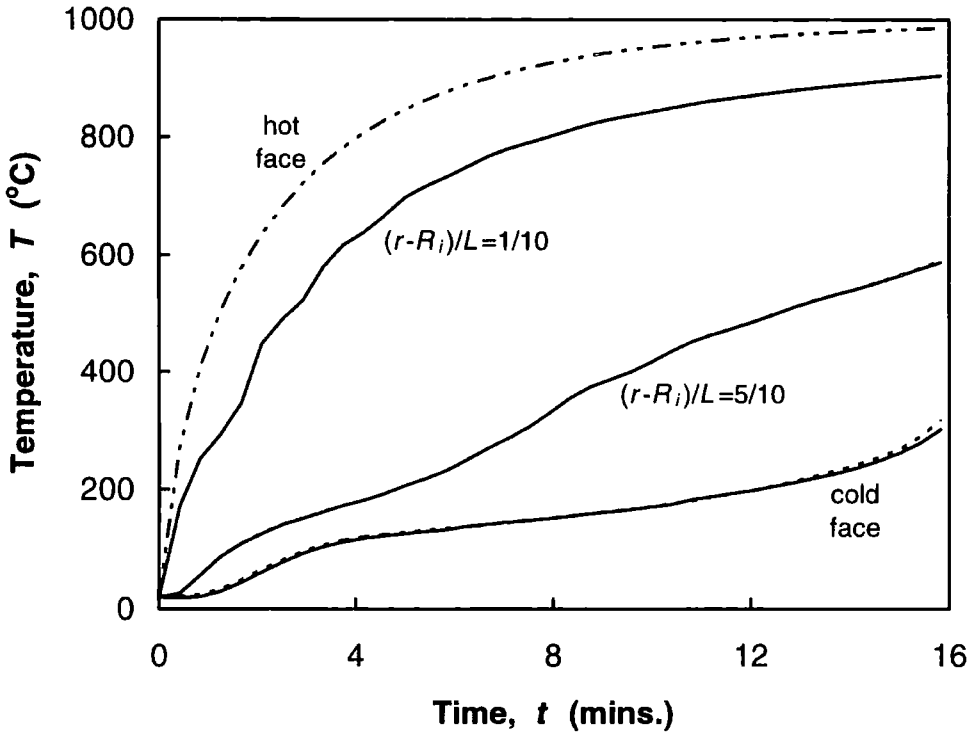

Figure 7.10 Computed temperatures versus time for various distances. The dash-dot line represents the hot surface temperature profile, the solid lines the temperature results for 1.09cm GRP pipe subject to sea water forced convection and the dot lines those for 1.09cm GRP pipe insulated at its inner surface.

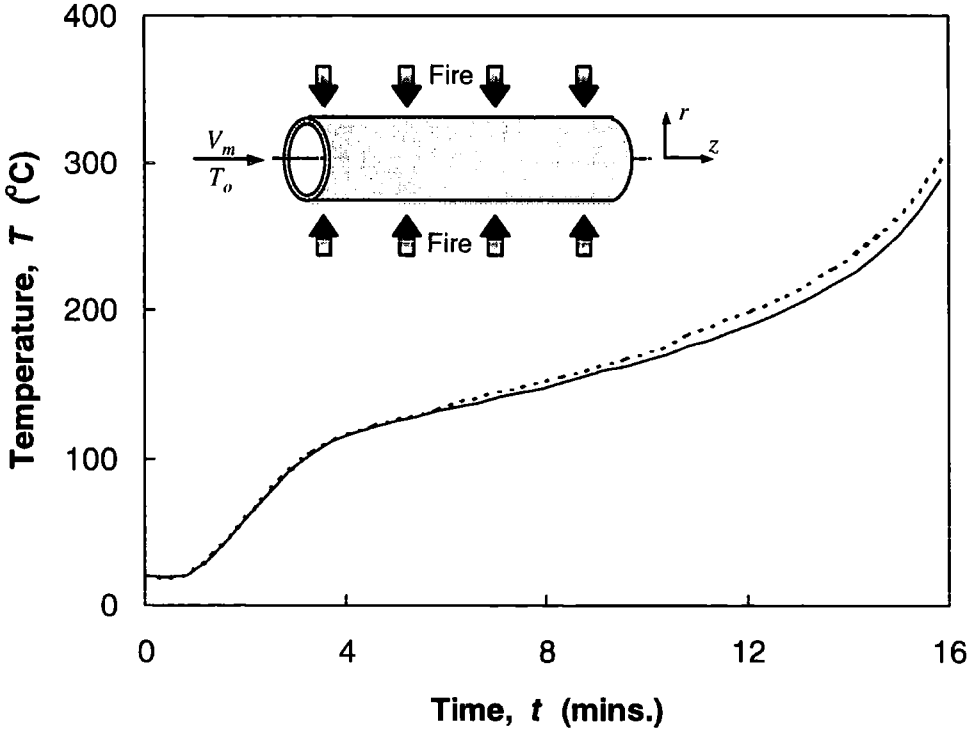

Figure 7.11 Comparison of the computed cold surface temperatures. The solid line represents the results for 1.09cm GRP pipe subject to natural gas forced convection and the dot line that for 1.09cm thick GRP pipe subject to sea water forced convection.

7.7 SUMMARY

The well known advantages of high strength-to-weight ratio and excellent fire, corrosion, impact and fatigue resistance of GRP find ready applications offshore particularly as pipes, pipelines and risers.

In this chapter, axi-symmetric mathematical and finite element models were developed to quantify the thermal response of thin-walled, large diameter GRP pipes, used for natural gas and sea water transmissions, subject to hydrocarbon fires. The mathematical model was based on a one-dimensional model developed for single-skinned GRP panels and include: (i) transient heat conduction; (ii) radial gas mass movement; (iii) mass loss and Arrhenius rate decomposition of resin material and (iv) endothermicity of the decomposition process.

The results revealed that for a given set of dimensions and boundary conditions, GRP pipes reach insulation failure (time to 160°C) earlier than GRP panels. It was found that the additional term in the governing equation of a GRP pipe, i.e. $-(k/r)(\partial T/\partial r)$, may be considered as the likely reason for this behaviour. The effect of forced convection heat exchange was found to be less compared to that of the additional term even if high velocity fluid flow are encountered. This model is able to simulate the fire performance of GRP pipes including different types of fluids and a wide range of working pressures. Despite the lack of experimental data, the result can be used to assess the feasibility of using GRP for offshore pipes and pipelines where severe fire conditions may occur.

The model is sensitive to the magnitude of pipe diameter and merits further investigation and a sensitivity analysis for various diameters. It is also required to implement a set of furnace fire tests for comparison with the numerical results.

CHAPTER VIII

A TWO-DIMENSIONAL FINITE ELEMENT MODEL FOR THE THERMAL RESPONSE OF GLASS REINFORCED PLASTIC JOINS

8.1 INTRODUCTION

A unique property of glass reinforced plastics (GRP) is that almost any desired shape of structure may be produced by the use of an appropriately shaped mould. However, large and complex structures such as offshore components, which can not be formed in one process, require several elements to be joined to produce the completed structure. Joins also become necessary due to cost restrictions and the need for access within the structure during its working life and maintenance. Figure 8.1 shows a variety of adhesively bonded joins used in the offshore industry. Some of the existing applications are topside deck, partition walls, boxes, housing, walkways (Figure 8.1a), tanks, vessels, water piping systems and pipelines (Figure 8.1b).

Structural integrity is the major requirement that a join must meet when the structure is subject to mechanical loading, high temperatures or other environmental conditions. This chapter is involved with a two-dimensional analysis of thin GRP joins subject to hydrocarbon fires. A join is assumed to be thin when its thickness to length ratio is less than 1/10.

Over the past few years, a number of researchers [Gibson *et al.*, 1996; Wang, 1995; Spagni & Gibson, 1994; Wu *et al.*, 1994; Davies *et al.*, 1994] have developed mathematical and numerical models and performed substantial experiments to predict the thermal response of GRP components for offshore applications. These researches have been limited to simple geometries such as single-skinned GRP panels and pipes and their applicability to complex components is questionable. The thermal response of GRP is complicated and can be affected by its structural complexity and the interactions between elements. So far, the thermal and structural failure of GRP exposed to severe hydrocarbon fires has not been quantitatively assessed for more complicated components such as panel-panel, panel-pipe and pipe-pipe joins.

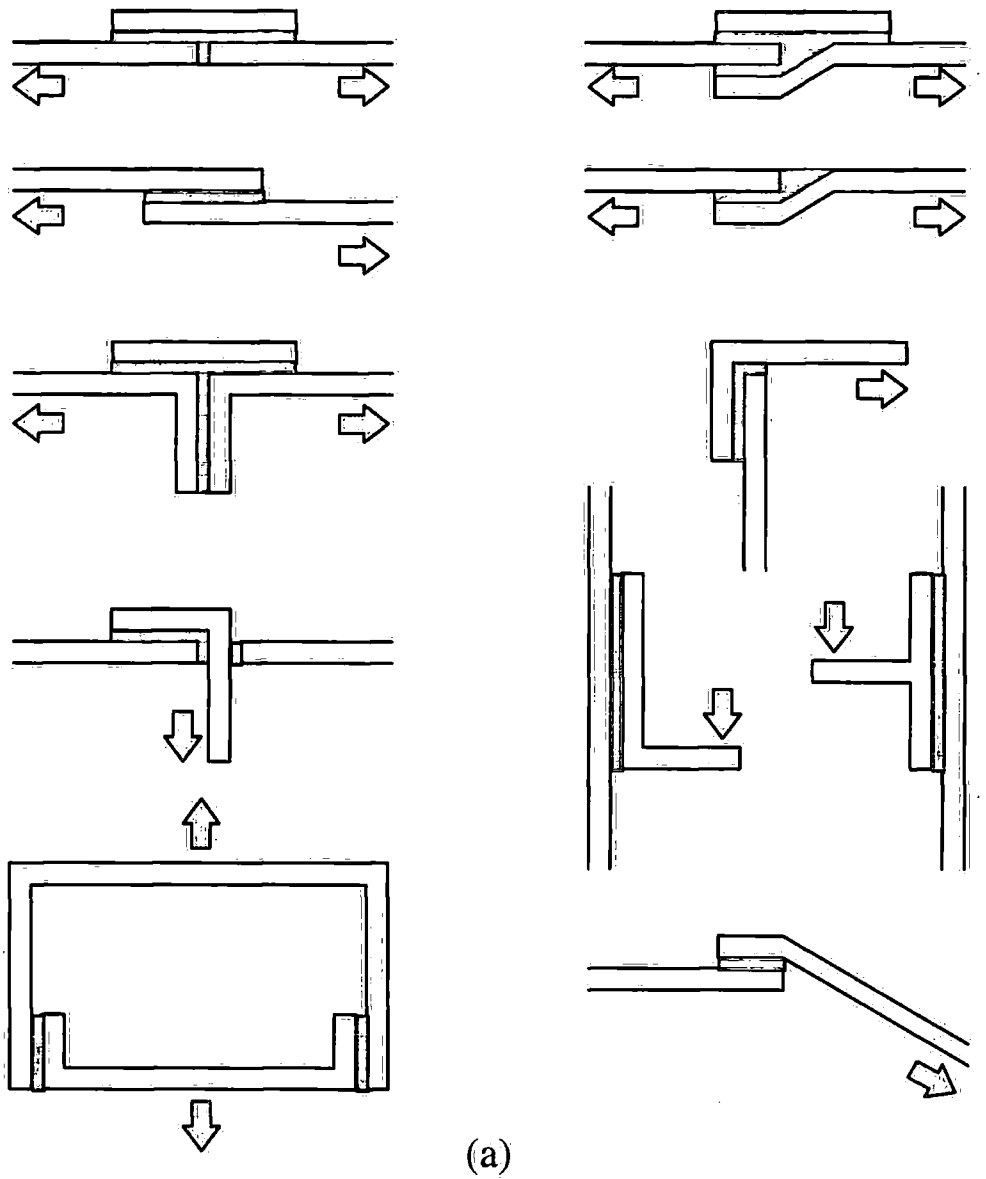

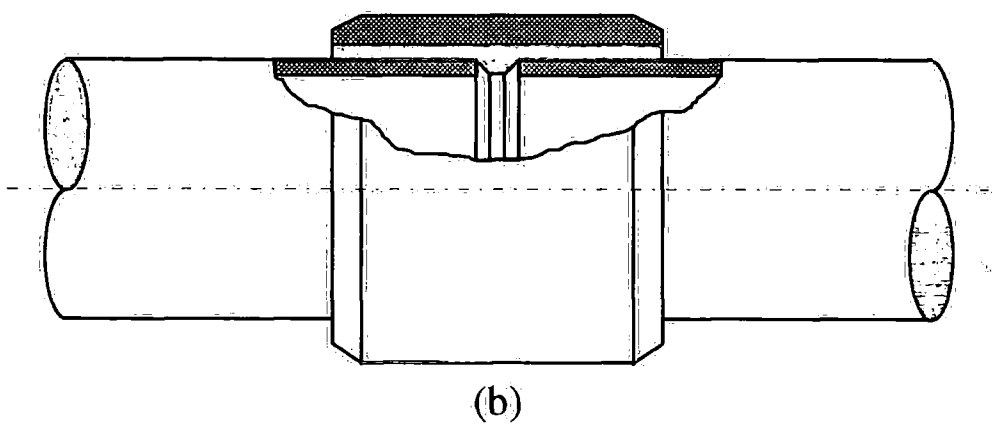

Figure 8.1 Various types of joins used in the offshore industry all using adhesive bonding (black), i.e. they are not machined joints; (a) panel-panel joins with the directions of mechanical loading [from: Shenoi & Willicome, 1993b]; (b) pipe-pipe join [from: Johnston Pipes Limited, 1997].

The one-dimensional numerical models developed in Chapters 5 and 7 for GRP panels and pipes can be used to approximate the thermal response of panel-panel, panel-pipe and pipe-pipe joins in fire but the accuracy of the predictions is unknown. A numerical model which accounts for heat transfer in more than one dimension is required to analyse the behaviour of these joins in fire.

In this chapter, a two-dimensional finite element model, simulating heat flow and material break-down in thin GRP joins is developed [Looyeh *et al.*, 1998c]. An extensive programme of fire experiments on thin GRP step panels, representing thin GRP joins, has been performed and the results have been compared with the numerical modelling. The one-dimensional finite element formulation developed in Chapter 5 is used. This is extended to two dimensions as the heat flow is no longer uniform. The two-dimensional equations governing the thermal and gaseous diffusion are derived using conservation of energy and the continuity equation. These include equations for material mass loss and the creation of gas mass flux using a first order kinetic rate Arrhenius equation (assuming the resin does not burn completely in pyrolysis). It is assumed that the mass of the pyrolysis gases diffuse in the fire direction only which in practice is very unlikely. The fire-exposed surface boundary condition is fixed by a time-dependent empirical formula [Wu *et al.*, 1994]; for the unexposed surface, time-dependent non-linear radiative and convective boundary conditions are used. The numerical model employs the Bubnov-Galerkin finite element approach with quasi-linearisation of the terms and coefficients. It is used to examine the heat flow through a thin step panel consisting of three GRP laminates, glued from one side, and to predict temperature distributions in two perpendicular directions.

The two-dimensional finite element model is flexible and can be applied to a wide range of two-dimensional geometries such as GRP joins. A numerical test is performed for a step panel made of polyester-based GRP with thicknesses 0.54 and 1.26cm and thickness to length ratio about 1/24. The temperature results are also computed for an equivalent one-dimensional model. In Chapter 5 the mass of the pyrolysis gases was found to be important in the one-dimensional thermal analysis of GRP panels during thermochemical decomposition. This term will expect to have a similar effect in the two-dimensional model. Figure 8.2 shows the experimental furnace set up for the GRP step panel.

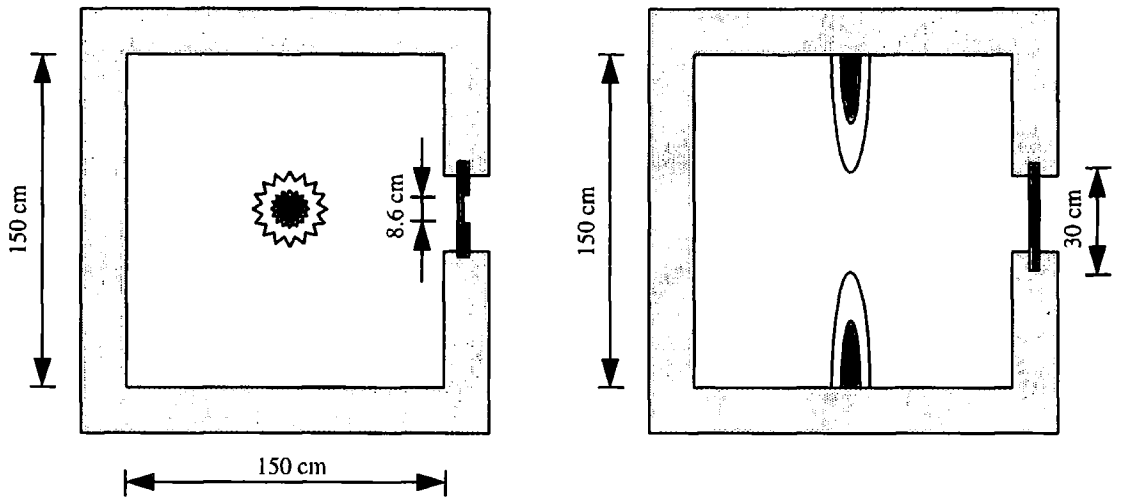

Figure 8.2 Elevation and plan views of the experimental furnace set up. The furnace is made of ceramic with an active volume of 3.375m^3. The GRP step panel with thicknesses 0.54 and 1.26cm is fitted on the door of the furnace.

8.2 MATHEMATICAL MODEL

An example of step panels with different thicknesses is shown in Figure 8.3a. Ignoring the temperature variations in the transverse direction z, the problem of three-dimensional heat transfer is reduced to two dimensions (Figure 8.3b) where temperature varies along through-the-thickness direction x and longitudinal direction y.

A woven roving GRP laminate is assumed to be homogenous and orthotropic with two different thermal conductivities in mutually perpendicular directions, i.e. on the plane of the material and perpendicularly through the material (Figure 8.3b). The Fourier's law of heat conduction [Fourier, 1882] is given, in x and y directions, by (Appendix B):

$$q_x = -k_T \frac{\partial T}{\partial x} \quad , \quad q_y = -k_L \frac{\partial T}{\partial y} \tag{8.1}$$

where

q_x = heat flux in through-the-thickness direction x (Wm^{-2})

k_T = through-the-thickness thermal conductivity (Wm^{-1}K^{-1})

T = temperature (^{o}C)

x = spatial co-ordinate representing through-the-thickness direction (m)

q_y = heat flux in the longitudinal direction y (Wm^{-2})

k_L = longitudinal thermal conductivity (Wm^{-1}K^{-1})

y = spatial co-ordinate representing the longitudinal direction (m)

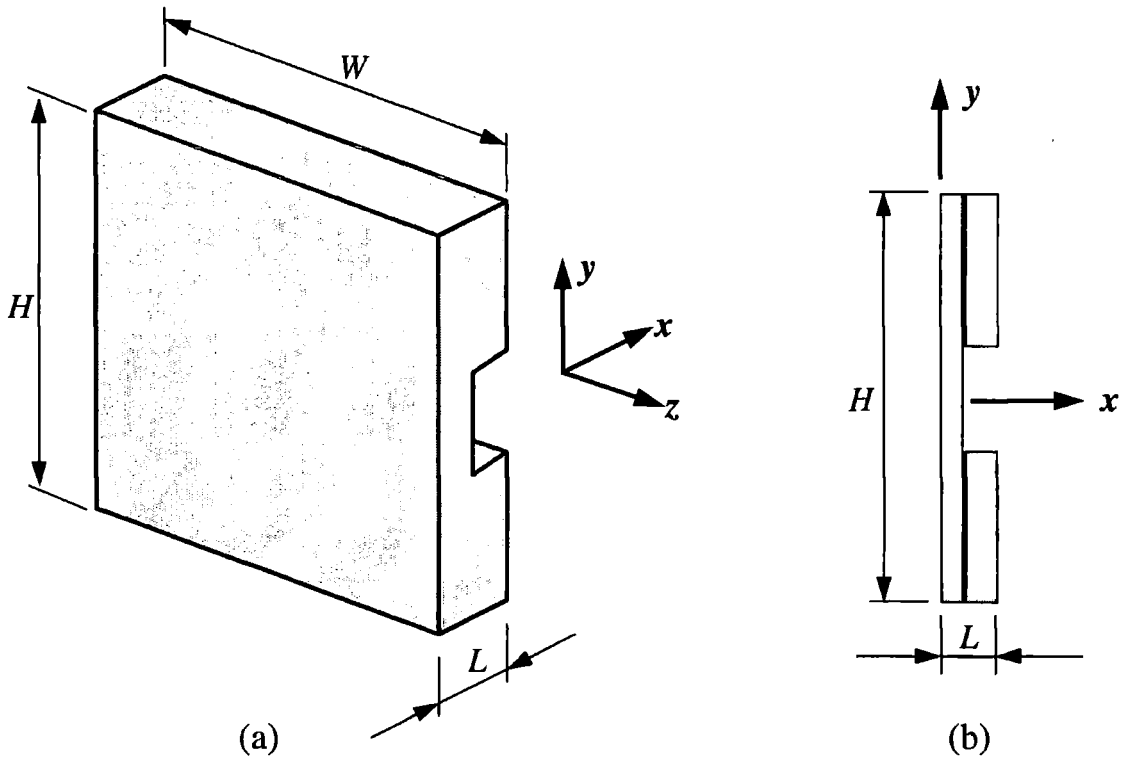

Figure 8.3 Schematic of GRP step panel; (a) three-dimensional view where *L*, *H* and *W* are the thickness, length and width of the step panel and *x*, *y* and *z* represent through-the-thickness, longitudinal and transverse directions, (b) two-dimensional view. The panel consists of three woven roving GRP laminates joined using adhesive (black).

With internal heat generation, assuming conservation of energy, the differential equation describing the two-dimensional transient heat conduction is given by:

$$\rho c_p \frac{\partial T}{\partial t} = -\frac{\partial q_x}{\partial x} - \frac{\partial q_y}{\partial y} + \dot{q} \tag{8.2}$$

where

ρ = density of GRP (kgm^{-3})

c_p = specific heat of GRP ($Jkg^{-1}K^{-1}$)

t = time (s)

$\dot{q}$ = internally generated heat per unit volume (Wm^{-3})

The method for the modelling of single-skinned GRP panels can be used for the two-dimensional mathematical model. The model is now extended to include non-uniform heat flow in the longitudinal direction of the panel. The bondings are assumed perfect. For simplicity, it is assumed that the pyrolysis gases diffuse in through-the-thickness direction only.

For a step domain Ω bounded by a closed curve $\Gamma=S_1+S_2+S_3+S_4+S_5+S_6$ (Figure 8.4), undergoing thermochemical decomposition, the transient heat conduction equation, i.e. Equation 8.2, becomes:

$$\rho c_p \frac{\partial T}{\partial t} = k_T \frac{\partial^2 T}{\partial x^2} + k_L \frac{\partial^2 T}{\partial y^2} - \dot{m}_g c_{pg} \frac{\partial T}{\partial x} - \frac{\partial \rho_r}{\partial t}\left(Q + h - h_g\right) \tag{8.3}$$

where

$\dot{m}_g$ = gas mass flux ($kgm^{-2}s^{-1}$)

c_{pg} = gas specific heat ($Jkg^{-1}K^{-1}$)

ρ_r = density of resin (active) material (kgm^{-3})

Q = heat of decomposition (Jkg^{-1})

h = enthalpy of GRP (Jkg^{-1})

h_g = enthalpy of gas (Jkg^{-1})

The term on left represents the rate of change of internal energy per unit volume. On the right, the first and second terms represent two-dimensional heat conduction; the third, convection of energy resulting from the pyrolysis gases flowing back through the porous charring layer along x axis (this term is always negative) and the fourth term represents the rate of heat generation resulting from the decomposition of the material.

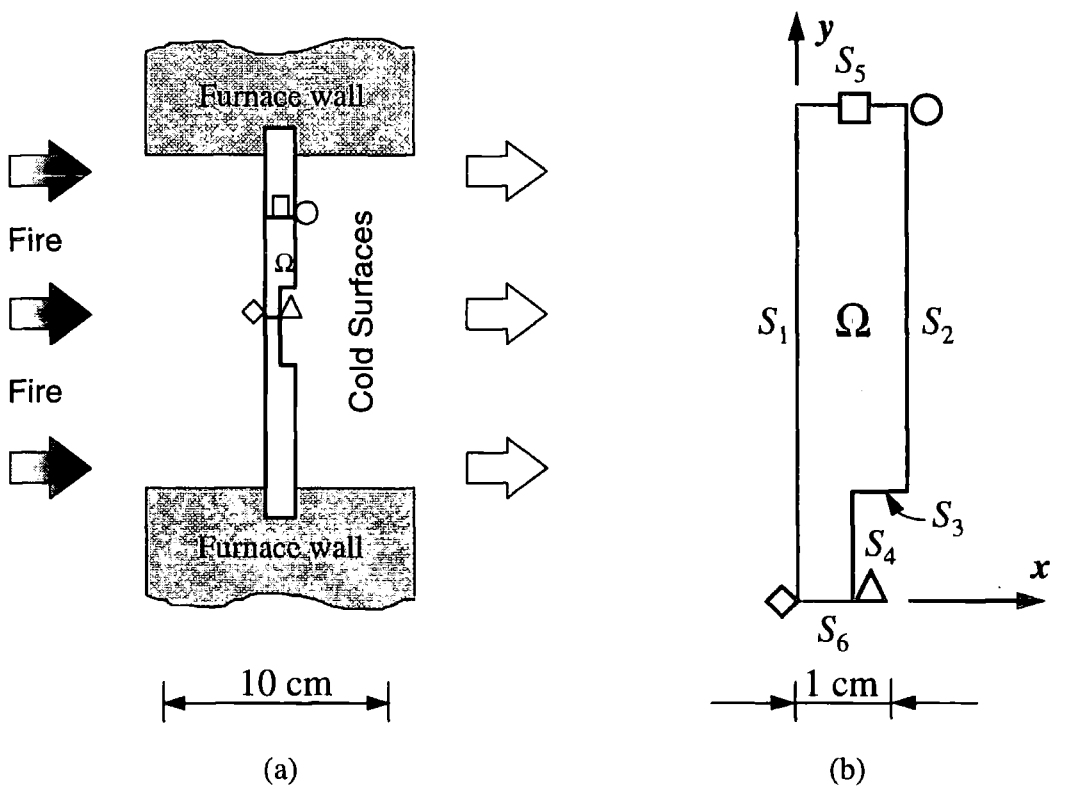

Figure 8.4 (a) Elevation view of the step panel used in experiment and mathematical modelling. (b) The geometry and notation used in the mathematical model. The locations of the temperature sensors are shown as ◇△□○.

The initial conditions are given by:

$$\begin{aligned} T(x,y,t) &= T_\infty \quad & m_v(x,y,t) &= m_{vo} \\ \dot{m}_g &= 0 & \rho &= \rho_o \\ k_T &= k_{To} & k_L &= k_{Lo} \\ c_p &= c_{po} & c_{pg} &= c_{pgo} \\ \varepsilon &= \varepsilon_o \end{aligned} \qquad \text{for} \quad \Omega,\ t = 0 \tag{8.4}$$

where

T_∞ = ambient temperature (20°C)

m_v = volumetric moisture content

ε = surface emissivity

and subscript o denotes initial quantities.

The boundary conditions are given by:

$$T(x,y,t) = T_s(t) \qquad \text{for} \quad S_1,\ t > 0 \tag{8.5a}$$

$$-k_T \frac{\partial T}{\partial x} = q_{r2} + q_{c2}\ ,\ \dot{m}_g = 0 \qquad \text{for} \quad S_2,\ t > 0 \tag{8.5b}$$

$$-k_L \frac{\partial T}{\partial y} = q_{r3} + q_{c3}\ ,\ \dot{m}_g = 0 \qquad \text{for} \quad S_3,\ t > 0 \tag{8.5c}$$

$$-k_T \frac{\partial T}{\partial x} = q_{r4} + q_{c4}\ ,\ \dot{m}_g = 0 \qquad \text{for} \quad S_4,\ t > 0 \tag{8.5d}$$

$$\frac{\partial T}{\partial x} = 0\ ,\ \dot{m}_g = 0 \qquad \text{for} \quad S_5 \text{ and } S_6,\ t > 0 \tag{8.5e}$$

where

$T_s(t)$ = hot surface time-dependent temperature (°C)

q_{rj} = radiation heat flux at the cold surfaces S_j, $j = 2,3,4$ (Wm^{-2})

q_{cj} = convection heat flux at the cold surfaces S_j, $j = 2,3,4$ (Wm^{-2})

$T_s(t)$ was introduced in Chapter 3 by an empirical relation [Wu *et al.*, 1994], i.e.:

$$T_s(t) = (T_g - 100)\left\{1 - \exp\left\{-\exp\left[0.71\log\left(\frac{t}{124.8}\right)\right]\right\}\right\} + T_\infty \quad \text{for} \quad t > 0 \tag{8.6}$$

where T_g is the maximum fire temperature (1100°C).

q_{rj} and q_{cj} (j = 2, 3, 4) are given by Equations 3.12 and 3.14, i.e.:

$$q_{rj} = h_{rj}(T - T_\infty) \qquad \text{for} \quad j = 2,3,4 \tag{8.7}$$

$$q_{cj} = h_{cj}(T - T_\infty) \qquad \text{for} \quad j = 2,3,4 \tag{8.8}$$

where h_{rj} and h_{cj} are the equivalent convection coefficient ($Wm^{-2}K^{-1}$) and the convection coefficient ($Wm^{-2}K^{-1}$) expressed by Equations 3.13 and 3.15, i.e.:

$$h_{rj} = \sigma\varepsilon\left(T_{kj}^2 + T_{\infty k}^2\right)\left(T_{kj} + T_{\infty k}\right) \quad \text{for} \quad j = 2,3,4 \tag{8.9}$$

$$h_{cj} = k_{e\infty}\frac{\overline{\mathrm{Nu}}_{wj}}{W} \quad \text{for} \quad j = 2,3,4 \tag{8.10}$$

and

σ = Stefan-Boltzmann constant (5.669×10^{-8} $Wm^{-2}K^{-4}$)

T_{kj} = cold surface temperature (K)

$T_{\infty k}$ = ambient temperature (293K)

$k_{e\infty}$ = thermal conductivity of air at ambient temperature ($Wm^{-1}K^{-1}$)

$\overline{\mathrm{Nu}}_{wj}$ = average Nusselt number

W = width of step panel (m)

An empirical relation that is valid for all Rayleigh and Prandtl numbers has been introduced by Churchill and Chu [1975] for Nusselt number. This relation is:

$$\overline{\mathrm{Nu}}_{wj} = \left\{0.825 + \frac{0.387\mathrm{Ra}_{wj}^{1/6}}{\left[1+(0.492/\mathrm{Pr})^{9/16}\right]^{8/27}}\right\}^2 \qquad \begin{matrix} 10^{-1} < \mathrm{Ra}_{wj} < 10^{12} \\ \text{for all Pr,}\ j = 2,3,4 \end{matrix} \tag{8.11}$$

where Ra_W denotes Rayleigh number and Pr denotes Prandtl number (Appendix B).

Assuming no expansion of the material due to decomposition, the rate of resin decomposition can be expressed by Equation 2.11, i.e.:

$$\frac{\partial \rho_r}{\partial t} = -A\left(\rho_r - \rho_{rf}\right)\exp\left(\frac{-E_A}{RT_k}\right) \tag{8.12}$$

where

A = pyrolysis constant (s^{-1})

ρ_{rf} = the final density of resin (kgm^{-3})

E_A = activation energy ($kJkmole^{-1}$)

R = gas constant (8.314 $kJkmole^{-1}K^{-1}$)

It is assumed that the pyrolysis gases diffuse in through-the-thickness direction only. The mass flux of pyrolysis gases is defined similarly by Equation 2.12, i.e.:

$$\dot{m}_g = \int_L^{\hat{x}} \frac{\partial \rho_r}{\partial t} dx \quad \text{for} \quad 0 \le \hat{x} \le L \tag{8.13}$$

The enthalpies of GRP and pyrolysis gases are given by Equations 2.6, i.e.:

$$h = \int_{T_\infty}^{T} c_p dT \qquad , \qquad h_g = \int_{T_\infty}^{T} c_{pg} dT \tag{8.14}$$

Equations 8.3 and 8.12 to 8.14 form a set of non-linear partial differential equations which must be solved simultaneously using the initial and boundary conditions, i.e. Equations 8.3 and 8.4, for ρ, $\dot{m}_g$ and T.

8.3 FINITE ELEMENT FORMULATION

The set of governing differential equations, i.e. Equations 8.3 and 8.12 to 8.14 are solved numerically using the finite element method. The Bubnov-Galerkin (weighted residual) approach is adopted. All terms and coefficients are evaluated explicitly using an iterative-updating procedure at each step of computations. Nodal temperatures are computed implicitly using the Crank-Nicolson solution.

8.3.1 Explicit Evaluation of Terms and Coefficients

A general notation $(\ )^i_{j,k}$ is used where i represents the time interval and j and k the spatial positions. Time derivative terms are given by forward difference and the spatial variables by central difference, with exception of the gas mass flux term which is represented by backward difference.

Using notation $(\ )^i_{j,k}$, Equation 8.3 at each time interval and nodal position can be given by:

$$\rho^{i+1}_{\bar{j},\bar{k}} \left(c_p\right)^{i+1}_{\bar{j},\bar{k}} \frac{\partial T}{\partial t} = \left(k_T\right)^{i+1}_{\bar{j},\bar{k}} \frac{\partial^2 T}{\partial x^2} + \left(k_L\right)^{i+1}_{\bar{j},\bar{k}} \frac{\partial^2 T}{\partial y^2}$$

$$-\left(\dot{m}_g\right)^{i+1}_{\bar{j},\bar{k}} \left(c_{pg}\right)^{i+1}_{\bar{j},\bar{k}} \frac{\partial T}{\partial x} - \left(\frac{\partial \rho_r}{\partial t}\right)^{i+1}_{\bar{j},\bar{k}} \left\{Q + \left[\left(c_p\right)^{i+1}_{\bar{j},\bar{k}} - \left(c_{pg}\right)^{i+1}_{\bar{j},\bar{k}}\right]\left(T - T_\infty\right)\right\} \tag{8.15}$$

where

$$\rho^{i+1}_{\bar{j},\bar{k}} = \left\{\left(\rho_r\right)^i_{\bar{j},\bar{k}} - A\Delta t\left[\left(\rho_r\right)^i_{\bar{j},\bar{k}} - \rho_{rf}\right]\exp\left[\frac{-E_A}{R\left(T_k\right)^i_{\bar{j},\bar{k}}}\right]\right\}\left(1 - V_f\right) + \rho_{fr} V_f \tag{8.16}$$

$$\left(\dot{m}_g\right)_{\bar{j},\bar{k}}^{i+1} = \sum_{j=n_x}^{n_T}\left[\frac{\left(\rho_r\right)_{\bar{j},\bar{k}}^{i+1} - \left(\rho_r\right)_{\bar{j},\bar{k}}^{i}}{\Delta t}\right] l_j \tag{8.17}$$

$$\left(\frac{\partial \rho_r}{\partial t}\right)_{\bar{j},\bar{k}}^{i+1} = -A\left[\left(\rho_r\right)_{\bar{j},\bar{k}}^{i} - \rho_{rf}\right]\exp\left[\frac{-E_A}{R\left(T_k\right)_{\bar{j},\bar{k}}^{i}}\right] \tag{8.18}$$

and

Δt = time step size (s)

V_f = volume fraction

n_x = number of mesh seeds at location x

n_T = total number of mesh seeds in x direction

l = element length (m)

subscripts $\bar{j}$ and $\bar{k}$ specify the position of the centre of each element and notation $(\,)_{\bar{j},\bar{k}}$ represents the average of all the nodal values.

Expressions for thermal conductivity and specific heat of GRP and specific heat of pyrolysis gases at each time and spatial position are given in Tables 4.3 and 4.4.

8.3.2 Finite Element Equations

The solution domain Ω, which is a two-dimensional step panel with maximum thickness L and length H, is divided into E quadrilateral elements of different lengths and widths with 4 nodes each. The governing differential equation, i.e. Equation 8.15, is cast into a matrix equation by applying the weighted residual approach of the finite element method. Within each element the temperature and temperature gradients are approximated by:

$$T(x,y,t) = \mathbf{N}(x,y)\mathbf{T}(t) \tag{8.20}$$

$$\begin{Bmatrix} \dfrac{\partial T}{\partial x}(x,y,t) \\ \dfrac{\partial T}{\partial y}(x,y,t) \end{Bmatrix} = \mathbf{B}(x,y)\mathbf{T}(t) \tag{8.21}$$

where

$\mathbf{N}(x,y)$ = shape function matrix

$\mathbf{T}(t)$ = temperature vector

$\mathbf{B}(x,y)$ = shape function derivative matrix

The element shape function matrix **N** and the shape function derivative matrix **B** are expressed by:

$$\mathbf{N}(x,y)=\begin{bmatrix}N_1 & N_2 & N_3 & N_4\end{bmatrix} \tag{8.22}$$

$$\mathbf{B}(x,y)=\begin{bmatrix}N_{1x} & N_{2x} & N_{3x} & N_{4x}\\ N_{1y} & N_{2y} & N_{3y} & N_{4y}\end{bmatrix} \tag{8.23}$$

where N_i (i = 1,...,4) are given, in global co-ordinates, by (Appendix C):

$$N_1(x,y)=1-\frac{x}{l}-\frac{y}{h}+\frac{xy}{lh} \tag{8.24a}$$

$$N_2(x,y)=\frac{x}{l}-\frac{xy}{lh} \tag{8.24b}$$

$$N_3(x,y)=\frac{xy}{lh} \tag{8.24c}$$

$$N_4(x,y)=\frac{y}{h}-\frac{xy}{lh} \tag{8.24d}$$

and l and h are the length and width of each element which may vary from one element to another. The elements of the **B** matrix are calculated by differentiation of the shape functions with respect to x and y.

To perform the finite element computations, the element matrices are derived in local co-ordinates, a co-ordinate system associated with each element. The element shape functions and shape function derivative matrix may therefore be represented, in local co-ordinates, as:

$$N_1(\xi,\eta)=\frac{1}{4}(1-\xi)(1-\eta) \tag{8.25a}$$

$$N_2(\xi,\eta)=\frac{1}{4}(1+\xi)(1-\eta) \tag{8.25b}$$

$$N_3(\xi,\eta)=\frac{1}{4}(1+\xi)(1+\eta) \tag{8.25c}$$

$$N_4(\xi,\eta)=\frac{1}{4}(1-\xi)(1+\eta) \tag{8.25d}$$

and

$$\mathbf{B}(\xi,\eta)=\frac{1}{4}\begin{bmatrix}-(1-\eta) & (1-\eta) & (1+\eta) & -(1+\eta)\\ -(1-\xi) & -(1+\xi) & (1+\xi) & (1+\xi)\end{bmatrix} \tag{8.26}$$

where ξ and η denote the local co-ordinates which are related to the global co-ordinates by:

$$x=\frac{1}{2}(1+\xi) \quad , \quad y=\frac{1}{2}(1+\eta) \tag{8.27}$$

Consider Equation 8.3, the weighted residual approach requires:

$$\int_{\Omega^e}\left\{\rho c_p\frac{\partial T}{\partial t}-k_T\frac{\partial^2 T}{\partial x^2}-k_L\frac{\partial^2 T}{\partial y^2}+\dot{m}_g c_{pg}\frac{\partial T}{\partial x}\right.$$

$$\left.+\frac{\partial \rho_r}{\partial t}\left[Q+\left(c_p-c_{pg}\right)\left(T-T_\infty\right)\right]\right\}N_i d\Omega^e=0 \qquad i=1,\ldots,4 \tag{8.28}$$

where Ω^e denotes the domain for element e.

Equation 8.28 expresses the desired averaging of the residual at the element boundaries but it does not represent the influence of the boundary conditions. Integration by parts using Green's theorem (Appendix C):

$$\int_{\Omega^e} u\,(\nabla.\mathbf{v})d\Omega=\int_{\Gamma^e} u\,(\mathbf{v}.\mathbf{n})d\Gamma-\int_{\Omega^e}\mathbf{v}.\nabla u\,d\Omega \tag{8.29}$$

with u=N_i and

$$\mathbf{v}=-k_T\frac{\partial T}{\partial x}\hat{i}-k_L\frac{\partial T}{\partial y}\hat{j} \tag{8.30}$$

and separating each term, gives expressions containing lower order derivatives:

$$\int_{\Omega^e}\rho c_p\frac{\partial T}{\partial t}N_i d\Omega-\int_{\Gamma^e}\begin{bmatrix}n_x & n_y\end{bmatrix}\begin{Bmatrix}k_T\dfrac{\partial T}{\partial x}\\ k_L\dfrac{\partial T}{\partial y}\end{Bmatrix}N_i d\Gamma$$

$$+\int_{\Omega^e}\begin{bmatrix}\dfrac{\partial N_i}{\partial x} & \dfrac{\partial N_i}{\partial y}\end{bmatrix}\begin{Bmatrix}k_T\dfrac{\partial T}{\partial x}\\ k_L\dfrac{\partial T}{\partial y}\end{Bmatrix}d\Omega+\int_{\Omega^e}\dot{m}_g c_{pg}\frac{\partial T}{\partial x}N_i d\Omega$$

$$+\int_{\Omega^e}\frac{\partial \rho_r}{\partial t}\left(c_p-c_{pg}\right)TN_i d\Omega+\int_{\Omega^e}\frac{\partial \rho_r}{\partial t}\left[Q-\left(c_p-c_{pg}\right)T_\infty\right]N_i d\Omega=0 \quad i=1,\ldots,4 \tag{8.31}$$

where

$$\mathbf{n}=n_x\hat{i}+n_y\hat{j} \tag{8.32}$$

and the second term represents natural boundary conditions for the element. The natural boundary conditions are taken into account when the element matrices are assembled. During assembly, these will cancel at all interior nodes of the solution domain leaving only the natural boundary conditions to be evaluated at the hot and cold surfaces, i.e. S_1, S_2, S_3 and S_4. This implies that the second term of Equation 8.31 actually represents the surface boundary conditions defined by Equations 8.5a to 8.5d where the prescribed temperature at the hot surface boundary, i.e. Equation 8.5a, is introduced to the matrix equation after assembling the element matrices (Appendix C).

Introducing the boundary conditions to the element equation, the resulting equation becomes:

$$\int_{\Omega^e} \rho c_p \frac{\partial T}{\partial t} N_i d\Omega + \int_{\Omega^e} \begin{bmatrix} \frac{\partial N_i}{\partial x} & \frac{\partial N_i}{\partial y} \end{bmatrix} \begin{Bmatrix} k_T \frac{\partial T}{\partial x} \\ k_L \frac{\partial T}{\partial y} \end{Bmatrix} d\Omega + \int_{\Omega^e} \dot{m}_g c_{pg} \frac{\partial T}{\partial x} N_i d\Omega$$

$$+ \int_{\Omega^e} \frac{\partial \rho_r}{\partial t} (c_p - c_{pg}) T N_i d\Omega + \sum_{j=2}^{4} \int_{S_j} (h_{rj} + h_{cj}) T N_i d\Gamma - \int_{S_1} \begin{bmatrix} n_x & n_y \end{bmatrix} \begin{Bmatrix} k_T \frac{\partial T}{\partial x} \\ k_L \frac{\partial T}{\partial y} \end{Bmatrix} N_i d\Gamma$$

$$- \sum_{j=2}^{4} \int_{S_j} (h_{rj} + h_{cj}) T_\infty N_i d\Gamma + \int_{\Omega^e} \frac{\partial \rho_r}{\partial t} \left[Q - (c_p - c_{pg}) T_\infty \right] N_i d\Omega = 0 \quad i = 1,\ldots,4 \qquad (8.33)$$

Substitute Equations 8.20 and 8.21 into Equation 8.33, it becomes:

$$\int_{\Omega^e} \rho c_p \mathbf{N}^{\mathrm{T}} \dot{\mathbf{T}} \mathbf{N} d\Omega + \int_{\Omega^e} k_T \mathbf{N}_{\mathrm{x}}^{\mathrm{T}} \mathbf{T} \mathbf{N}_{\mathrm{x}} d\Omega + \int_{\Omega^e} k_L \mathbf{N}_{\mathrm{y}}^{\mathrm{T}} \mathbf{T} \mathbf{N}_{\mathrm{y}} d\Omega + \int_{\Omega^e} \dot{m}_g c_{pg} \mathbf{N}_{\mathrm{x}}^{\mathrm{T}} \mathbf{T} \mathbf{N} d\Omega$$

$$+ \int_{\Omega^e} \frac{\partial \rho_r}{\partial t} (c_p - c_{pg}) \mathbf{N}^{\mathrm{T}} \mathbf{T} \mathbf{N} d\Omega + \sum_{j=2}^{4} \int_{S_j} (h_{rj} + h_{cj}) \mathbf{N}^{\mathrm{T}} \mathbf{T} \mathbf{N} d\Gamma + \int_{S_1} (\mathbf{q}.\mathbf{n}) \mathbf{N}^{\mathrm{T}} d\Gamma$$

$$- \sum_{j=2}^{4} \int_{S_j} (h_{rj} + h_{cj}) T_\infty \mathbf{N}^{\mathrm{T}} d\Gamma + \int_{\Omega^e} \frac{\partial \rho_r}{\partial t} \left[Q - (c_p - c_{pg}) T_\infty \right] \mathbf{N}^{\mathrm{T}} d\Omega = \mathbf{0} \qquad (8.34)$$

where superscript **T** denotes the transpose. Rearranging Equation 8.34 results in:

$$\left(\int_{\Omega^e} \mathbf{N}^{\mathrm{T}} \rho c_p \mathbf{N} d\Omega \right) \dot{\mathbf{T}} + \left[\int_{\Omega^e} \mathbf{N}_{\mathrm{x}}^{\mathrm{T}} k_T \mathbf{N}_{\mathrm{x}} d\Omega + \int_{\Omega^e} \mathbf{N}_{\mathrm{y}}^{\mathrm{T}} k_L \mathbf{N}_{\mathrm{y}} d\Omega + \int_{\Omega^e} \mathbf{N}_{\mathrm{x}}^{\mathrm{T}} \dot{m}_g c_{pg} \mathbf{N} d\Omega \right.$$

$$\left. + \int_{\Omega^e} \mathbf{N}^{\mathrm{T}} \frac{\partial \rho_r}{\partial t} (c_p - c_{pg}) \mathbf{N} d\Omega + \sum_{j=2}^{4} \int_{S_j} \mathbf{N}^{\mathrm{T}} (h_{rj} + h_{cj}) \mathbf{N} d\Gamma \right] \mathbf{T} + \int_{S_1} \mathbf{N}^{\mathrm{T}} (\mathbf{q}.\mathbf{n}) d\Gamma$$

$$- \sum_{j=2}^{4} \int_{S_j} \mathbf{N}^{\mathrm{T}} (h_{rj} + h_{cj}) T_\infty d\Gamma + \int_{\Omega^e} \mathbf{N}^{\mathrm{T}} \frac{\partial \rho_r}{\partial t} \left[Q - (c_p - c_{pg}) T_\infty \right] d\Omega = \mathbf{0}$$

or $$\mathbf{C}\dot{\mathbf{T}} + (\mathbf{K}_{\mathrm{x}} + \mathbf{K}_{\mathrm{y}} + \mathbf{K}_{\mathrm{g}} + \mathbf{K}_{\mathrm{d}} + \mathbf{K}_{\mathrm{c}})\mathbf{T} + (\mathbf{f}_{\mathrm{b}} + \mathbf{f}_{\mathrm{c}} + \mathbf{f}_{\mathrm{o}}) = \mathbf{0}$$

or $$\mathbf{C}\dot{\mathbf{T}} + \mathbf{K}\mathbf{T} + \mathbf{f} = \mathbf{0} \qquad (8.35)$$

where

$\mathbf{C}$	=	element capacitance matrix
$\dot{\mathbf{T}}$	=	vector of temperature derivative with respect to time
$\mathbf{K}_x$	=	element conductance matrix with respect to conduction in x direction
$\mathbf{K}_y$	=	element conductance matrix with respect to conduction in y direction

$\mathbf{K_g}$ = element gas diffusion matrix

$\mathbf{K_d}$ = element decomposition matrix

$\mathbf{K_c}$ = element radiation and convection matrix with respect to cold surfaces

$\mathbf{f_b}$ = element vector with respect to prescribed temperature at hot surface

$\mathbf{f_c}$ = element radiation and convection vector with respect to cold surfaces

$\mathbf{f_o}$ = element decomposition vector

Using the material properties for the element centre point given by Equations 8.15 to 8.18 and Tables 4.3 and 4.4, the element matrices and vectors are represented, in global co-ordinates, as:

$$\mathbf{C} = \int_{\Omega^e} \mathbf{N}^{\mathrm{T}} \rho_{\bar{j},\bar{k}}^{i+1} \left(c_p\right)_{\bar{j},\bar{k}}^{i+1} \mathbf{N} d\Omega \tag{8.36a}$$

$$\mathbf{K_x} = \int_{\Omega^e} \mathbf{N_x^{\mathrm{T}}} \left(k_T\right)_{\bar{j},\bar{k}}^{i+1} \mathbf{N_x} d\Omega \tag{8.36b}$$

$$\mathbf{K_y} = \int_{\Omega^e} \mathbf{N_y^{\mathrm{T}}} \left(k_L\right)_{\bar{j},\bar{k}}^{i+1} \mathbf{N_y} d\Omega \tag{8.36c}$$

$$\mathbf{K_g} = \int_{\Omega^e} \mathbf{N}^{\mathrm{T}} \left(\dot{m}_g\right)_{\bar{j},\bar{k}}^{i+1} \left(c_{pg}\right)_{\bar{j},\bar{k}}^{i+1} \mathbf{N}_x d\Omega \tag{8.36d}$$

$$\mathbf{K_d} = \int_{\Omega^e} \mathbf{N}^{\mathrm{T}} \left(\frac{\partial \rho_r}{\partial t}\right)_{\bar{j},\bar{k}}^{i+1} \left(c_p - c_{pg}\right)_{\bar{j},\bar{k}}^{i+1} \mathbf{N} d\Omega \tag{8.36e}$$

$$\mathbf{K_c} = \sum_{j=2}^{4} \int_{S_j} \mathbf{N}^{\mathrm{T}} \left(h_{rj} + h_{cj}\right) \mathbf{N} d\Gamma \tag{8.36f}$$

$$\mathbf{f_b} = \int_{S_1} \mathbf{N}^{\mathrm{T}} (\mathbf{q}.\mathbf{n}) d\Gamma \tag{8.36g}$$

$$\mathbf{f_c} = -\sum_{j=2}^{4} \int_{S_j} \mathbf{N}^{\mathrm{T}} \left(h_{rj} + h_{cj}\right) T_\infty d\Gamma \tag{8.36h}$$

$$\mathbf{f_o} = \int_{\Omega^e} \mathbf{N}^{\mathrm{T}} \left(\frac{\partial \rho_r}{\partial t}\right)_{\bar{j},\bar{k}}^{i+1} \left[Q - \left(c_p - c_{pg}\right)_{\bar{j},\bar{k}}^{i+1} T_\infty\right] d\Omega \tag{8.36i}$$

The element matrices and vectors are evaluated numerically using the Gauss-Legendre quadrature (Appendix C).

The numerical solution of the present problem requires solving the set of first order simultaneous ordinary differential equations of the form Equation 8.35.

8.3.3 Time Step Algorithm

A solution to the matrix equation of the form Equation 8.35 is given by [from: Zienkiewicz & Taylor, 1991 as corrected by Looyeh *et al.*, 1997; Zienkiewicz, Pers. Com., 1995]:

$$\mathbf{T}_{n+1} = (\mathbf{C} + \Delta t \Theta \mathbf{K})^{-1} \left\{ [\mathbf{C} - \Delta t(1-\Theta)\mathbf{K}]\mathbf{T}_n - \Delta t\, \bar{\mathbf{f}} \right\} \tag{8.37}$$

where Δt is the time step size (s), Θ is the weighting (time step) parameter, $\bar{\mathbf{f}}$ is the average value of **f** defined by Equation 2.36 and subscripts **n** and **n+1** represent known and unknown quantities.

The time step is based on the critical time step Δt_{cr} which depends on the weighting parameter Θ, the element length l and width h, density ρ, through-the-thickness thermal conductivity k_T, longitudinal thermal conductivity k_L and specific heat c_p. The critical time step needs to be found for the smallest element in the solution domain, i.e.:

$$\Delta t_{cr} = \frac{2}{1-2\Theta} \frac{[\text{Min} < l_m, h_m >]^2 (\rho)_{j,\bar{k}}^{i+1} \left(c_p\right)_{j,\bar{k}}^{i+1}}{3\ \text{Max} < \left(k_T\right)_{j,\bar{k}}^{i+1}, \left(k_L\right)_{j,\bar{k}}^{i+1} >} \tag{8.38}$$

where Δt_{cr} is the critical time step, l_m and h_m are the length and width of the smallest element within the finite element mesh and the operators Min< > and Max< > choose the minimum and maximum quantities, respectively.

The Crank-Nicolson solution, corresponding to Θ = 1/2, with a non-symmetric matrix solver [Applegarth, 1990] are used to solve matrix equation implicitly and compute the nodal temperatures after each iteration.

8.3.4 The Computer Code Algorithm

Additions are made to the structure of the finite element computer code for single-skinned GRP panels to enable temperature predictions for thin GRP step panels and facilitate both one- and two-dimensional finite element analyses. Also, a new subroutine is added to the computer code to evaluate element matrices and vectors. The operations flow chart of the finite element computer code developed in this chapter is shown in Figure 8.5, only those sections concerned with two-dimensional analysis are presented.

Main Finite Element Program

1. initialize the system matrices, vectors and principle variables.
2. read finite element mesh data, thermal, kinetic and transport properties, boundary condition parameters and also control ID value to perform different two-dimensional solutions.
3. start time-dependent calculation and determine furnace temperature.
4. set the initial values and calculate additional specific heat and the proportion function of the moisture content, Eqs. 4.1 to 4.3, 4.6 and 4.8 to 4.12.
5. determine the hot and cold surface boundary conditions, Eqs. 8.5 to 8.11.
6. specify the edges of the two-dimensional geometry with respect to Fig. 8.4b.
7. calculate the temperature-dependent thermal properties, Eqs. 4.9 and 4.13 to 4.17.
8. calculate the effect of moisture content on thermal properties using additional specific heat obtained in step 4, Eqs. 4.10 and 4.11.
9. calculate the mass loss rate, instantaneous density and gas mass flux for the control ID value of the required solution.
10. choose a suitable option according to the input element type and create element matrices, **K** and **C**, and element force vector, **f**, Eqs. 8.36a to 8.36i.
11. assemble the system matrices and force vector, if any.
12. calculate and update the time step using Eq. 8.38 or consider the chosen value for an implicit solution.
13. form system equations according to Eq. 8.35.
14. apply hot surface and cold surface boundary conditions.
15. solve the matrix equation using Eq. 8.39 and find temperature distributions, mass loss and moisture loss profiles.
16. add the time step, determined in step 13, then go to step 4, otherwise stop.

Figure 8.5 Flow chart listing the steps for the main finite element computer code to perform two-dimensional transient heat conduction analysis for thin GRP step panels.

8.4 FIRE EXPERIMENTS

For comparison with the numerical results, furnace fire experiments were requested from the research groups at the University of Manchester, School of Engineering and the University of Newcastle-upon-Tyne, Centre for Composite Materials Engineering. Two step and two single-skinned GRP panels were manufactured (Figure 8.6). Three GRP laminates were used to form each GRP step panel using polyester resin adhesive (Figure 8.3b). All GRP laminates, made of woven roving glass fibres and polyester resin using the hand lay-up method (Chapter 1), comply with homogeneous and orthotropic characteristics.

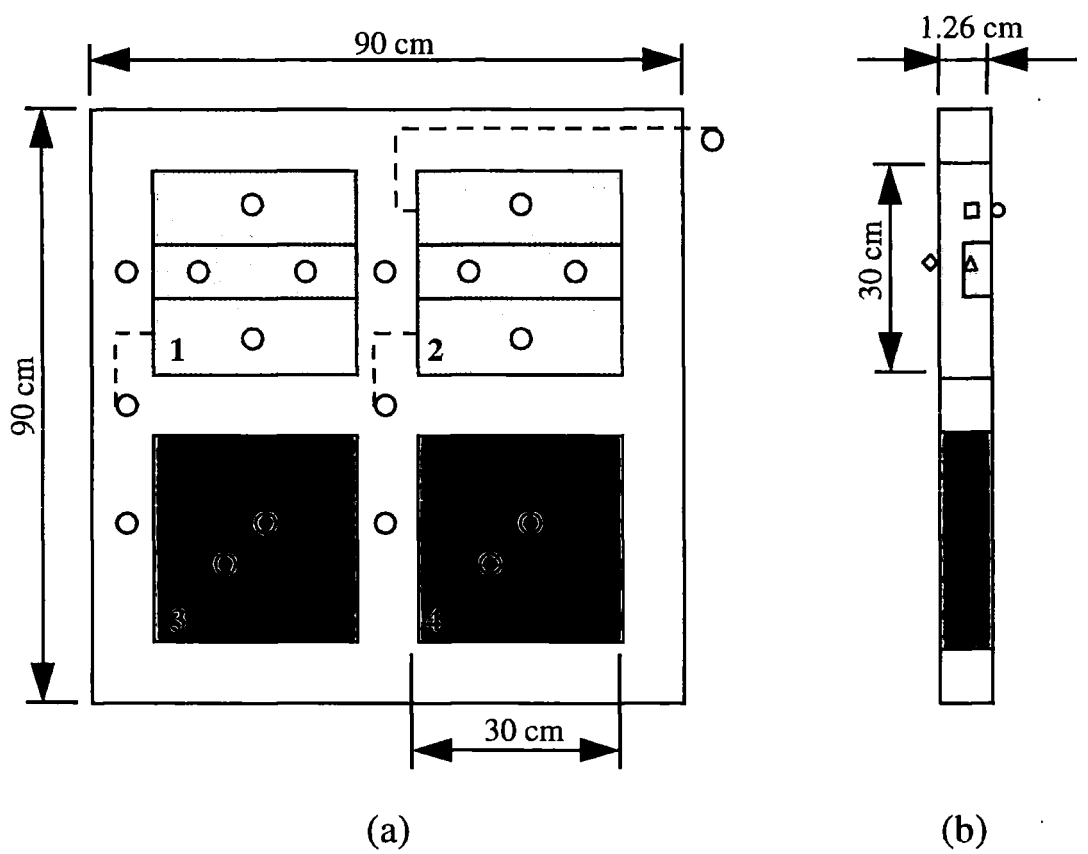

Figure 8.6 Elevation and side views of the fire test GRP panels. (a) 1 and 2 are step panels and 3 and 4 are single-skinned with the lay out of 19 temperature sensors. (b) key temperature sensors of the selected step panel, shown as ◇△□○, used for comparison of the measured and computed temperatures.

The step panels, i.e. Panels 1 and 2, were similar with maximum thickness 1.26cm and minimum thickness 0.54cm. The single-skinned panels, i.e. Panels 3 and 4, were also similar with thickness 1.26cm. All panels were then cut into 30×30cm pieces to fit into the door of a ceramic furnace (Figure 8.6a), with an active volume of $3.375m^3$ and maximum fire temperature 1100°C, prior to fire experiments [Davies *et al.*, 1994a; Wu *et al.*, 1994]. 19 temperature sensors were implanted inter-laminarly at the suitable points through the panels, 4 as the key sensors for Panel 1 (Figure 8.6b). The panels were then fire tested in the furnace involved with a simulated hydrocarbon fire [Spagni & Gibson, 1994; ISO 834, 1975; BS476, 1987]. For Panels 1 and 2, the whole body undergoes the same heat flux from the furnace but due to different thicknesses the heat transfer is different.

The experimental results from Panels 1 and 3 are presented in the next section where they are compared with the numerical predictions using the finite element method.

8.5 COMPARISON OF THE FINITE ELEMENT COMPUTATIONS WITH EXPERIMENTAL RESULTS AND DISCUSSION

The finite element formulation developed here is used to compute the thermal response of a thin GRP step panel.

Table 4.3 lists material properties for polyester-based GRP. The properties of pyrolysis gases are given in Table 4.4.

The GRP material used for step panels is the same as those for single-skinned panels (Chapter 5, Component 3). The initial density and specific heat of the GRP are 1832.4 kgm^{-3}, 1056.84 $Jkg^{-1}K^{-1}$. Thermal conductivities of GRP step panel in the through-the-thickness and longitudinal directions are 0.322 $Wm^{-1}K^{-1}$ and 0.614 $Wm^{-1}K^{-1}$. The variations of these properties with temperature and moisture gradients were studied in Chapters 4 and 5.

Pyrolysis constant, activation energy and heat of decomposition for GRP are 7525 s^{-1}, 611.5 $MJkmole^{-1}$ and 2.3446 $MJkg^{-1}$, respectively.

The length of Panel 1 is 30cm, 24 times greater than the thickness of the panel at the thickest area (1.26cm) and 55 times greater at the thinnest (0.54cm). A two-dimensional model which includes the whole area of the step panel is therefore not necessary, since this would require a huge number of elements and gives similar results to a one-dimensional model in the areas well away from the step region. The two-dimensional behaviour of the step panel occurs near the step region and its effect on isotherms decreases rapidly in the longitudinal direction away from the step region. For an optimised solution and to understand how temperature varies around the step region, only a small area of the step panel including the middle corner needs to be discretised. The chosen two-dimensional finite element domain contains the same length and thickness, i.e. 1.26cm. Four types of meshes with the same type of elements but different numbers of elements and nodes are created in the step region as shown in Figures 8.7a to 8.7d. Specifications and comparisons are given in Table 8.1. Apart from the first mesh which contains uniformly coarse elements, the rest are non-uniform patterns with finer elements around the corners particularly near the middle corner. Figures 8.8a to 8.8d show the isotherms for the different meshes after 4 minutes of fire exposure. It is seen that the contour plot for (d) is superior to the others but (b) with fewer elements is almost as good and takes less time and might be considered satisfactory.

Table 8.1 Specifications of the finite element meshes, time steps and iterations after 4 minutes.

Specifications	Mesh 1	Mesh 2	Mesh 3	Mesh 4
Type of mesh	uniform	non-uniform	non-uniform	non-uniform
Number of elements	37	37	109	333
Number of nodes	52	52	134	376
Type of elements	quad4*	quad4*	quad4*	quad4*
Initial time step (s)	5	1	0.2	0.1
Number of iterations	48	240	1200	2400
Ave. diff. with mesh 1 (%)	0	9	13	14

* 4 node quadrilateral

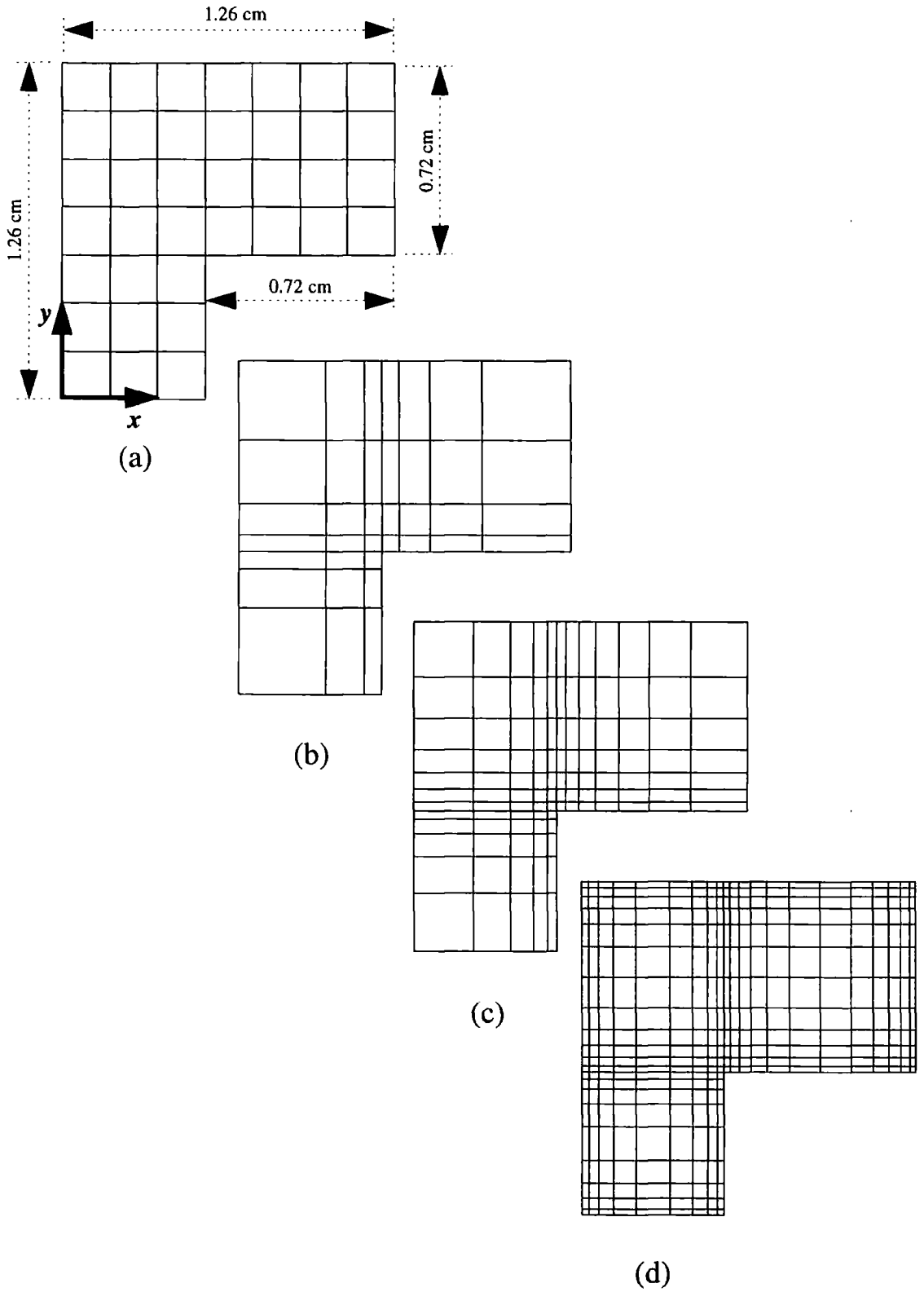

Figure 8.7 Various two-dimensional finite element meshes for GRP step panel; (a) uniformly coarse mesh with 52 nodes and 37 elements; (b) non-uniformly coarse mesh with 52 nodes and 37 elements; (c) non-uniformly medium mesh with 134 nodes and 109 elements; (d) non-uniformly fine mesh with 376 nodes and 333 elements.

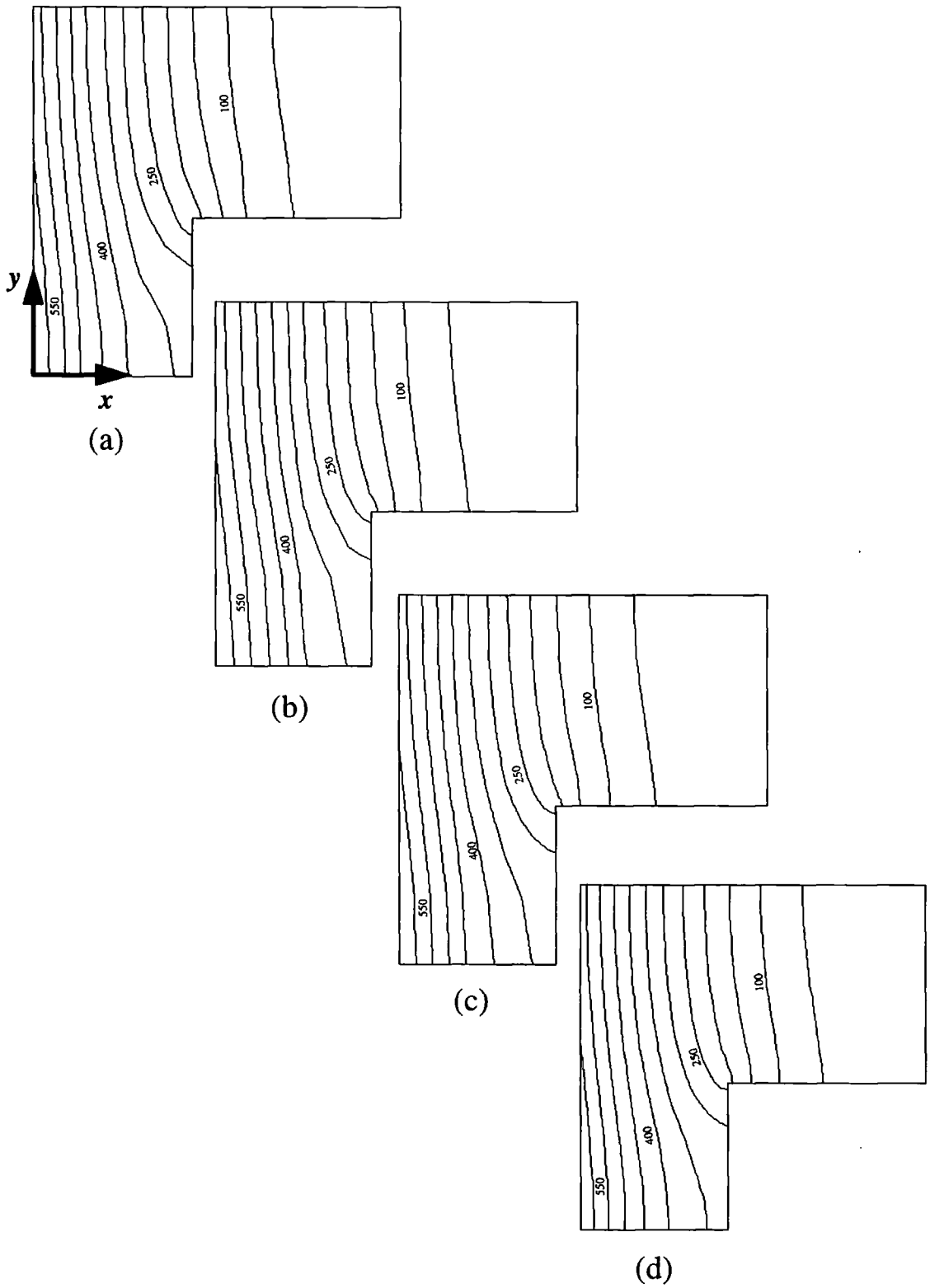

Figure 8.8 Temperature contour plots after 4 minutes of fire exposure for various finite element meshes; (a) uniformly coarse mesh with 52 nodes and 37 elements; (b) non-uniformly coarse mesh with 52 nodes and 37 elements; (c) non-uniformly medium mesh with 134 nodes and 109 elements; (d) non-uniformly fine mesh with 376 nodes and 333 elements (all temperatures in °C).

In Figures 8.9a to 8.9c isotherms are plotted after 4, 10 and 16 minutes of fire exposure time for the second mesh (Figure 8.7b).

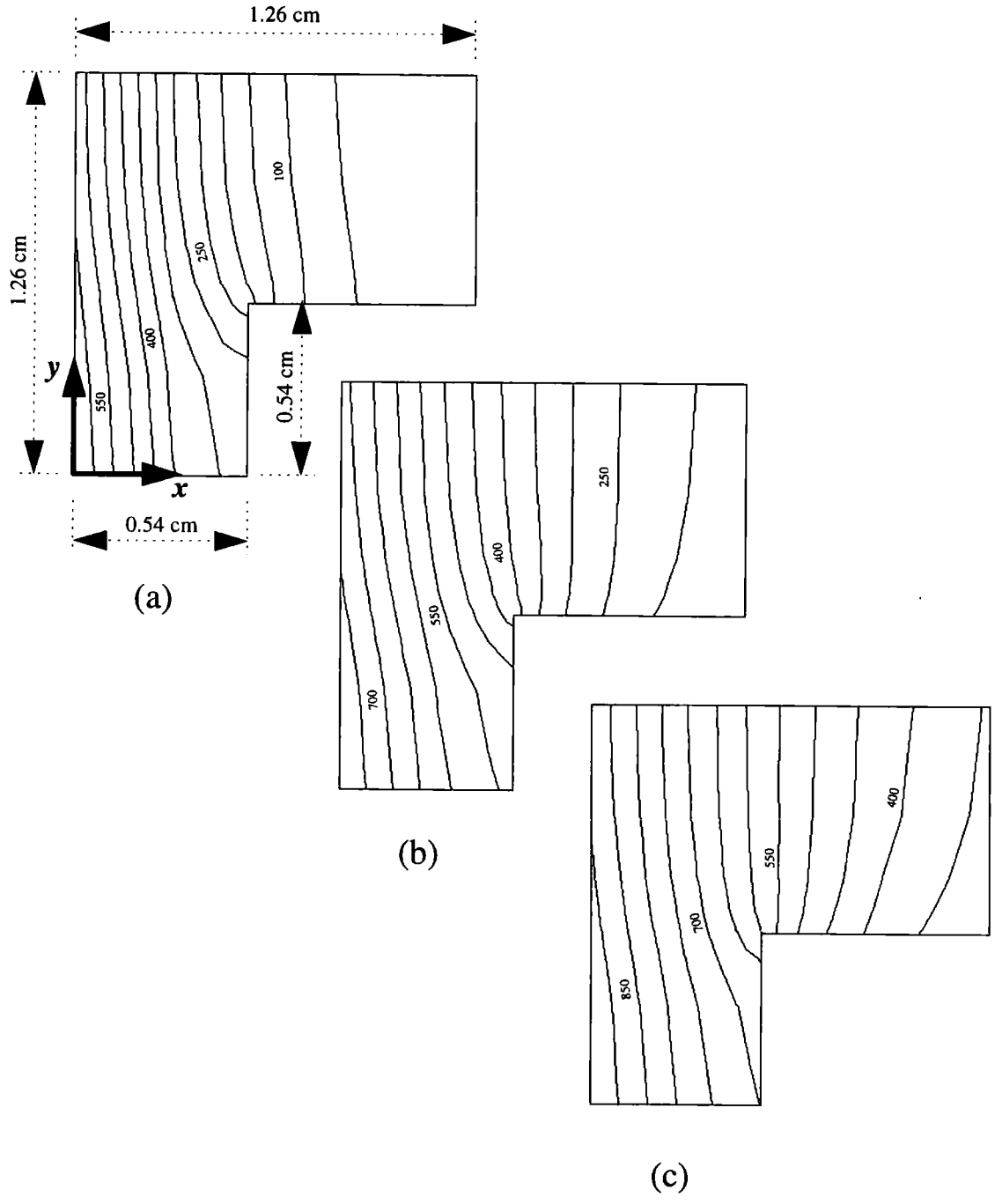

Figure 8.9 Temperature contour plots after (a) 4, (b) 10 and (c) 16 minutes of fire exposure, i.e. 6-minute increments. The results are obtained using the second finite element mesh which contains 52 nodes and 37 non-uniform elements (all temperatures in ^{o}C).

The following are noticeable:

1. The isotherms in the thin region, i.e. $0 \leq x \leq 0.54$cm and $0 \leq y \leq 0.54$cm, are somewhat different from those in the thick region, i.e. $0 \leq x \leq 1.26$cm and $0.54 \leq y \leq 1.26$cm. In the thin region, the temperature gradient is steeper (more isotherm). It is seen that for similar inter-laminar positions the material gets warmer in this region. For example, for $x \approx 0.27$cm, Figure 8.9a gives $T \approx 450^{\circ}$C at $y = 0$, whereas it gives $T \approx 350^{\circ}$C at $y \approx 0.27$cm. These variations are more noticeable around the middle corner.
2. For the inter-laminar and cold surface sensors of the step panel, i.e. △ □ ○ (Figure 8.4b), embedded far away from the middle corner, it is unlikely to see much differences between the experimental and numerical results of the single-skinned panel and those for the step panel.

A one-dimensional model should therefore be sufficient to predict temperatures away from the middle corner where only a time-dependent fire temperature is applied.

To compute temperatures at the key sensors, a finite element mesh is created with a length (9.9cm) to thickness (1.26cm) ratio of greater than 7, 348 nodes and 285 non-uniform elements. A comparison of the temperatures computed using this mesh with those for Mesh 2, with 52 nodes and 37 non-uniform elements (Figure 8.7b), reveals less than 5% difference. The latter is recommended for further comparison with experiments.

In Figure 8.10 the computed temperatures are plotted as a function of time for various distances. It is seen that at the thin region ($0 \leq x \leq 0.54$cm) the cold surface at $x = 0.54$cm gets warmer than at the same distance of the inter-laminar of the thick part ($0 \leq x \leq 1.26$cm); this is due to protective and cooling effects of GRP. This figure also shows a slower rate of temperature rise for the cold surface and inter-laminar at $x = 0.54$cm between 4 and 8 minutes compared to that for $t < 4$ minutes. This is expected as at this stage the heat flow is mostly governed by the decomposition of the material which acts as a coolant. Lastly, the fire-resistance (insulation failure) is predicted to occur after about 10.4 minutes.

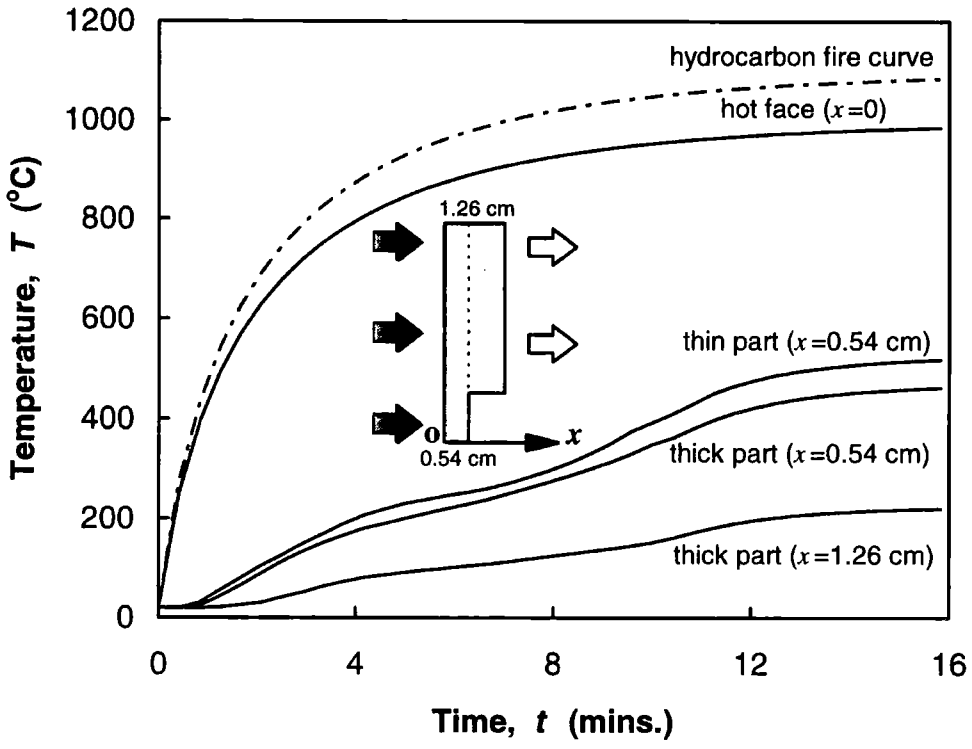

Figure 8.10 Computed temperatures versus time for various distances using Mesh 2 (solid lines).

In Figures 8.11 and 8.12 the computed and experimental temperatures of the two-dimensional model are plotted versus time for various positions of temperature sensors in the experiments. A remarkably good agreement is seen for the cold surface at the thick region (x = 1.26cm). The numerical model predicts fire resistance (insulation failure) at about 10.4 minutes which differs from that of experiment by less than 0.7 minutes or 6.7% (Figure 8.12). Erratic behaviours are observed for the cold surface sensor Δ (x = 0.54cm) at the thin region and the inter-laminar sensor □ (x = 0.54cm) at the thick region, making it difficult to compare the numerical predictions with the experimental results. For the inter-laminar sensor □, the experimental temperature rise is much less steep than for the computed profile and closer to the behaviour of the cold surface sensor O at the thick region. The same behaviour can be seen for the cold surface sensor Δ at the thin region, this sensor being no longer in touch with the surface at T>300°C and t>8.3 minutes. Also, the agreement is less good for the hot surface specially for T>760°C when there is sharp drop of temperature probably due to the sensor becoming detached. Comparison of all four suggests there may be something amiss with the model for these sensors.

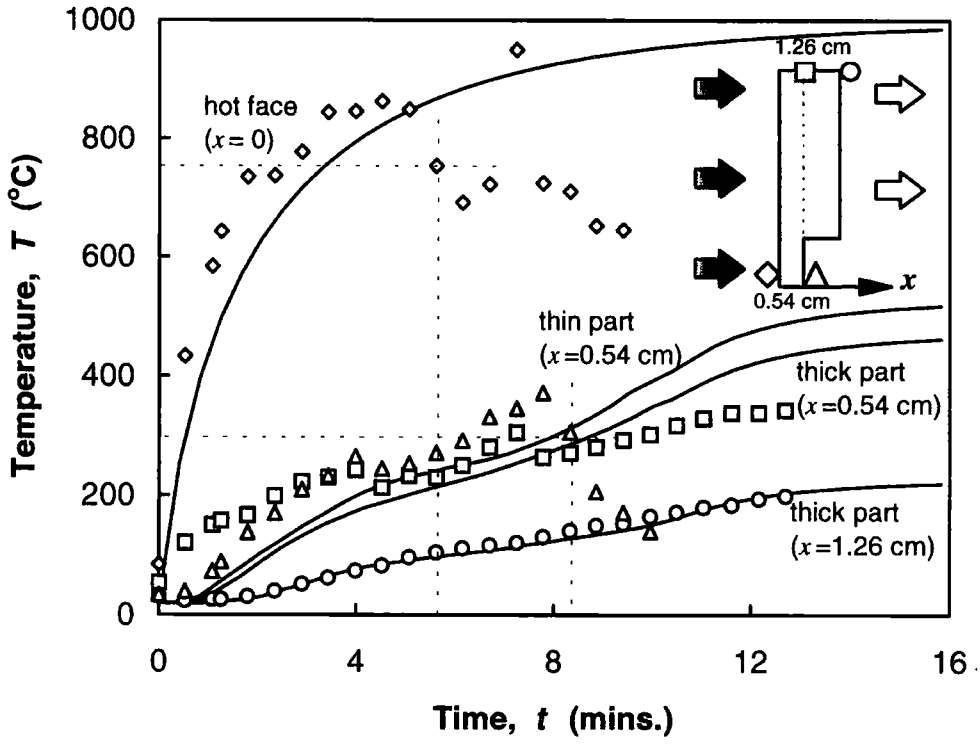

Figure 8.11 Comparison of the computed with experimental temperatures at four distances. The computed temperatures are shown as solid lines and the experimental results for four sensors ◇ △ □ ○, the position of which are shown in the inset. The temperature sensors ◇ △ become detached after 5.5 and 8.3 minutes.

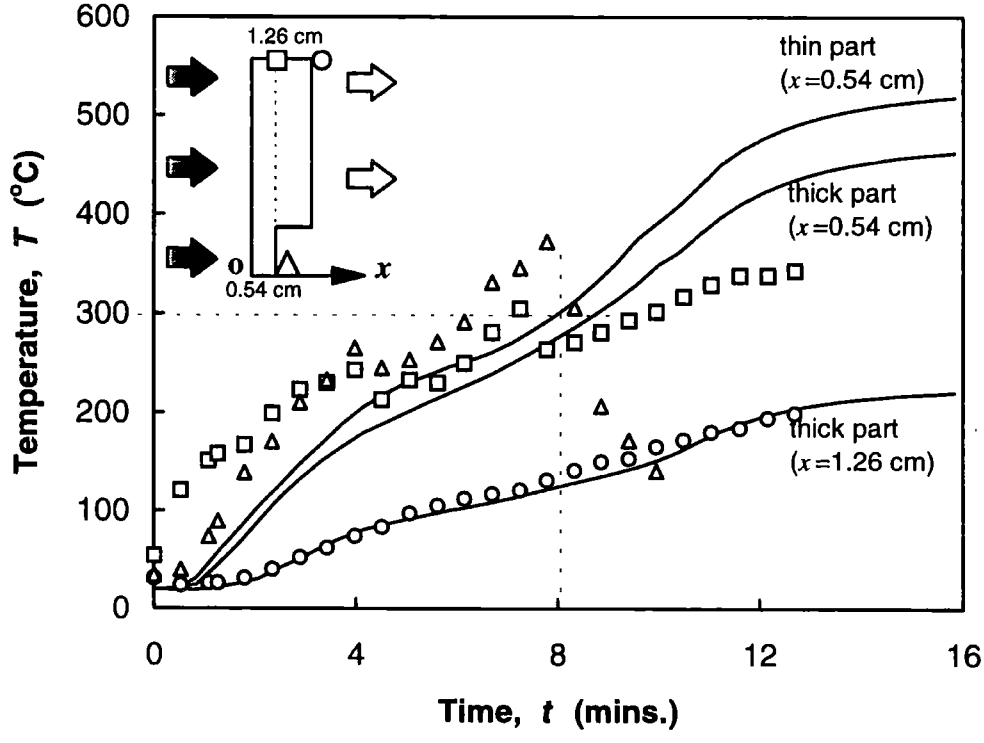

Figure 8.12 Comparison of the computed with experimental temperatures. The computed temperatures are shown as solid lines and the experimental results for four sensors △ □ ○, the position of which are shown in the inset.

In Figure 8.13 the computed temperature profiles for the one- and two-dimensional finite element models for the same thicknesses (1.26cm) are compared. It is seen that for both cold surface and inter-laminar positions the one-dimensional model over-predicts temperatures for times less than 10 minutes compared to the two-dimensional model but after this time it tends to under-predict. It is also seen that the one-dimensional inter-laminar temperature profile shows much less steep rise of temperature throughout fire exposure compared to that for the two-dimensional model. Earlier (Figure 8.9) the thin region of the step panel where $0 \leq x \leq 0.54$cm and $0 \leq y \leq 0.54$cm showed a faster rate of temperature rise but a lower rate in the thick region with $0 \leq x \leq 1.26$cm and $0.54 \leq y \leq 1.26$cm. Figures 8.9a to 8.9c, which show isotherms after 4, 10 and 16 minutes, can be used to explain why the two-dimensional model behaves differently. After 4 minutes of fire exposure, the thin region experiences a decreasing rate of temperature rise which lasts for a few more minutes. After 10 minutes of fire exposure, the rate of temperature rise speeds up particularly for $x = y \geq 0.54$cm where the inter-laminar and cold surface temperature sensors are mounted. This can be seen in Figures 8.9b and 8.9c.

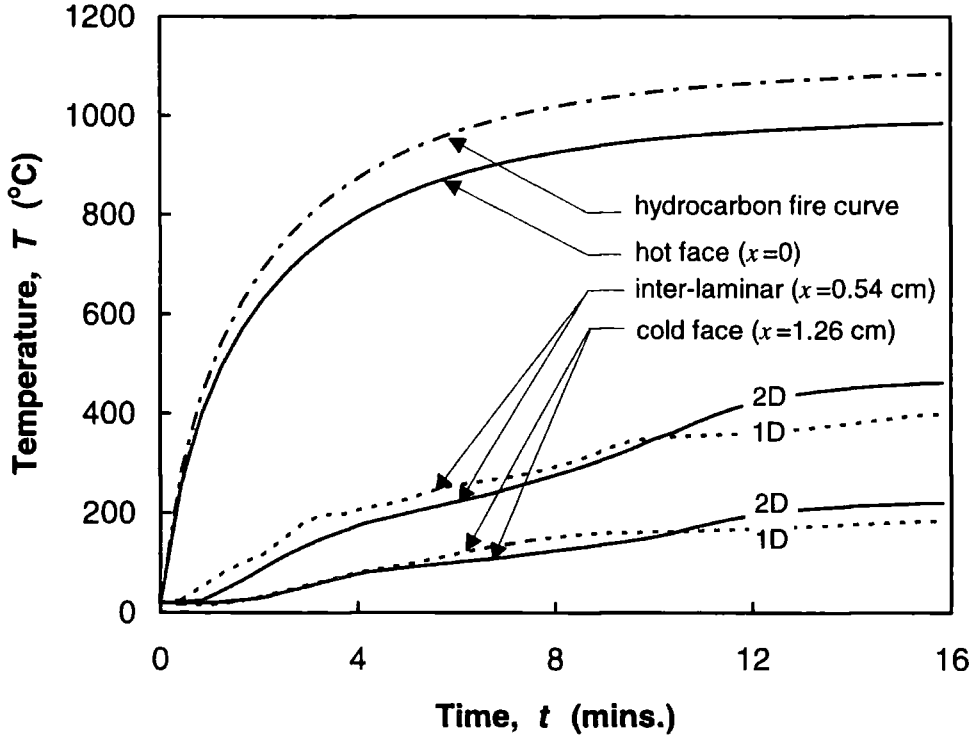

Figure 8.13 Comparison of one- and two-dimensional computed temperature profiles at various distances. The solid lines represent the two-dimensional temperatures, the dot lines the one-dimensional temperatures and dash-dot line the hydrocarbon fire curve.

The one- and two-dimensional models have the same through-the-thickness thermal conductivities, i.e. 0.322 $Wm^{-1}K^{-1}$ but the longitudinal thermal conductivity of the two-dimensional model is 0.614 $Wm^{-1}K^{-1}$ which is nearly twice larger. Average temperature difference 8.6°C between the cold surface temperatures, predicted by these models, reveals that even with higher heat conduction in the longitudinal direction a less effect is seen on the cold surface temperatures and the fire resistance (insulation failure) of the thin step panel. Important to note is that the pyrolysis gases, which have cooling effects, are assumed to influence heat conduction in through-the-thickness direction only.

Figure 8.14 shows the temperatures computed by one- and two-dimensional models along with the measured values of the cold surface in detail. It is seen that the experimental results are very close to the two-dimensional profile (solid line) but at variance with the one-dimensional profile (dot line).

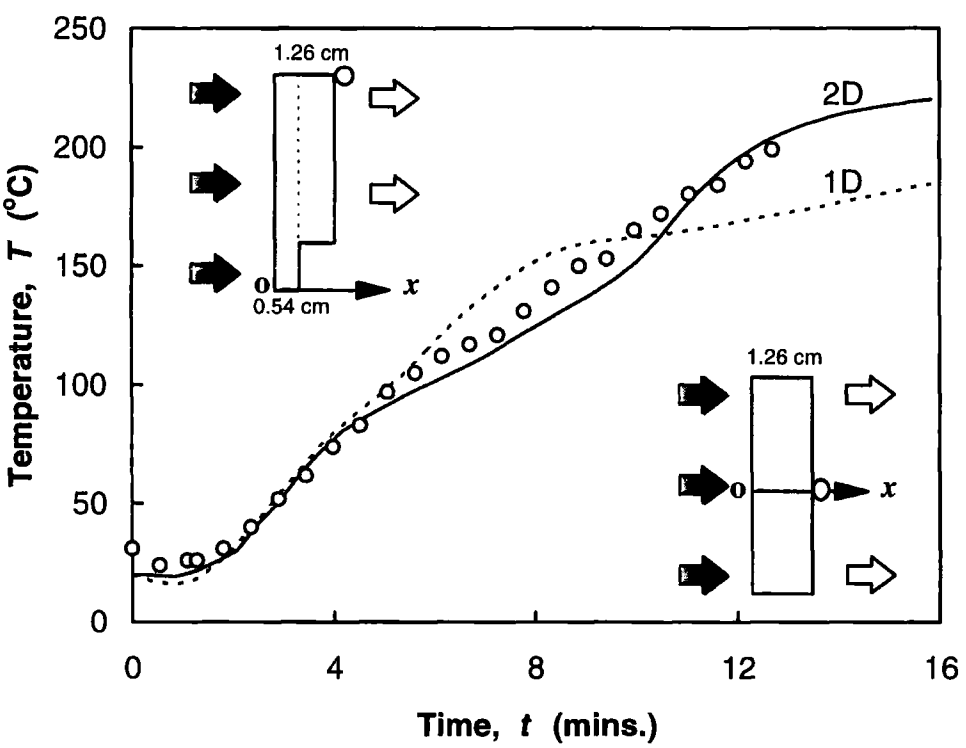

Figure 8.14 Comparison of the computed and experimental cold surface temperatures. The dot and solid lines are the results of one- and two-dimensional numerical models and the experimental temperatures are shown as ○.

Table 8.2 lists comparisons of the one- and two-dimensional finite element models. A longer fire resistance is predicted by the one-dimensional model. This value (11.9 minutes) differs from the two-dimensional experimental value by 22.1%. Table 8.3 shows the standard deviation for the one-dimensional model is almost three times larger than that for the two-dimensional model. Nevertheless, with 8.6°C average difference between the one- and two-dimensional cold surface temperatures, one-dimensional modelling of thin GRP step panels seems to give satisfactory results with less than 15% error.

Table 8.2 Comparisons of the one- and two-dimensional finite element models for a the thin polyester-based GRP step panel.

Specifications	1D model	2D model
Thickness (es) (cm)	1.26	0.54/1.26
Length (s) (cm)	-	0.54/1.26
Width (cm)	30	30
Total number of elements	7	37
Total number of Nodes	8	52
Initial time step (s)	5	1
Fire resistance (time to 160°C) (mins.)	11.9	10.4
Difference with experiment (%)	22.1	7.2
Standard deviation (°C)	14.2	4.7

Figure 8.15 summarises the results for the step panel by plotting the predicted temperatures as functions of distance for various times obtained from the two-dimensional finite element model. The steep variations of temperature profiles are evident from this figure at the thin region. To see the decreasing rate of heat transfer as the decomposition process progresses, a constant time interval (3 minutes) is used. It is therefore seen that as time progresses the two adjacent profiles get closer.

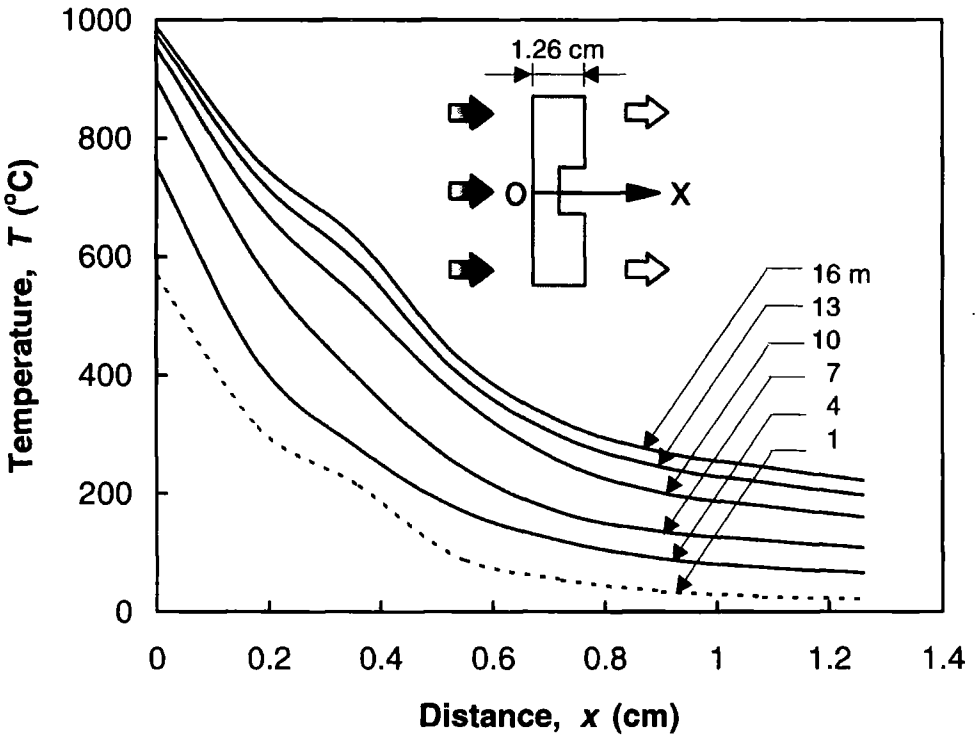

Figure 8.15 Temperatures versus distance x for various times (minutes). The results are computed using the two-dimensional finite element model for a GRP step panel as shown in the inset.

8.6 SUMMARY

This chapter involved the application of the finite element method to the analysis of the thermal response of thin GRP joins subject to hydrocarbon fire. A two-dimensional mathematical model and an appropriate finite element solution were developed and used to assess the fire resistance of a thin GRP step panel with maximum and minimum thicknesses 1.26 and 0.54cm. The GRP step panel was made of three woven rovings glass fibre/polyester laminates where polyester resin was used as adhesive and the bonding was assumed perfect. The model accounted for (i) non-uniform heat flow in the plane of GRP; (ii) two-dimensional transient heat conduction; (iii) thermochemical decomposition of the material; (iv) one-dimensional gas mass diffusion. The numerical temperatures obtained from two-dimensional model were compared with experimental results. These results were also compared with those for an equivalent one-dimensional model.

Results were obtained for: (i) the cold surface at the thick region in which the agreement was within a few degrees; (ii) the cold surface at the thin region and the inter-laminar at the thick region where the agreements were fairly poor particularly for the first 6 minutes of fire exposure with an average difference of 22.2°C; (iii) the hot surface where the agreement is good for $T \leq 760$°C but breaks down at higher temperatures which might be due to the temperature sensor disconnecting. Here the predicted fire resistance (time to 160°C) differs from the experiment for 0.7 minutes (6.7%).

A comparison between the one- and two-dimensional models of the same thicknesses and material properties revealed an average temperature difference of 8.6°C at the cold surface. The two-dimensional numerical prediction differs from the experiment with a standard deviation of 4.7°C but for the one-dimensional model it is three times larger (14.2°C).

For thin GRP joins (thickness to length ratio less than 1/10) heat flows mainly in through-the-thickness direction. One-dimensional models were therefore found to reach satisfactory results when quick and cost-effective analyses are required. These models may cause errors up to 15%.

The diffusion of the pyrolysis gases, which was modelled with a one-dimensional equation, needs to be extended to two dimensional as it is likely to play an important role in the longitudinal direction particularly when thicker GRP joins are considered. Evident is the large discrepancy between the predicted and experimental temperatures at the inter-laminar position.

The finite element model was found to be sensitive to the specifications at the corners of the unexposed surfaces. This requires a sensitivity analysis for different configurations.

For the case investigated the thickness to length ratio was about 1/24. This small ratio caused some problems with the design of experiments and in the finite element computations.

Further investigations are required to include: (i) thick GRP joins and their effects on temperature predictions and (ii) two-dimensional gas mass diffusion.

CHAPTER IX

A COUPLED FINITE ELEMENT SOLUTION FOR HEAT AND MASS TRANSFER IN GLASS REINFORCED PLASTIC JOINS

9.1 INTRODUCTION

In the last chapter, it was assumed that the pyrolysis gases diffuse in through-the-thickness direction only with no diffusion in other directions and no accumulation of gases in the material. Although, the numerical model temperature profiles and experimental results agreed reasonably well for thin GRP step panels, a few inconsistencies were seen. We therefore extend the previous two-dimensional model to take account of thermochemical decomposition involving the two-dimensional energy and gas diffusion equations and the interactive effect of the gas pressures on the pores. The material mass loss is obtained using a first-order kinetic rate Arrhenius equation and the mass flux of the pyrolysis gases from Darcy's equation. A first-order exponential equation is employed for permeability [Fredlund, 1988].

The GRP step panel used in the last chapter for the numerical modelling and experiments (with thickness 1.26cm) was not thick enough to study the two-dimensional heat flow within the material. Here, thick GRP step panels (thickness to length ratio greater than 1/10) are studied. A thick GRP step panel with thickness 9.6cm and thickness to length ratio greater than 1/4 is used.

The fire-exposed boundary condition is again assumed to be the empirical hydrocarbon fire curve given by ISO 834 [1975]. Radiative and convective heat transfer boundary conditions are maintained at the unexposed surface. To derive the appropriate element equations, the Bubnov-Galerkin finite element approach is applied to the coupled set of energy and mass conservation equations. The finite element formulation is used for simultaneous solution of pore pressures and temperatures at each step of the computations. The non-linear terms and coefficients are quasi-linearised. A finite

element computer code has been developed based on an efficient solution algorithm using the finite difference approximation and variable time step. This has been used to yield an accurate prediction of the thermal response of GRP joins under fire. An extensive programme of experimental fire measurements, performed on thick step panels with regions of different thicknesses, is used to test the numerical modelling (Figure 9.1). The numerical results, presented for a thick polyester-based GRP step panel with maximum thickness 9.6cm, are compared with the experiments and include temperature, pore pressure and fraction mass profiles.

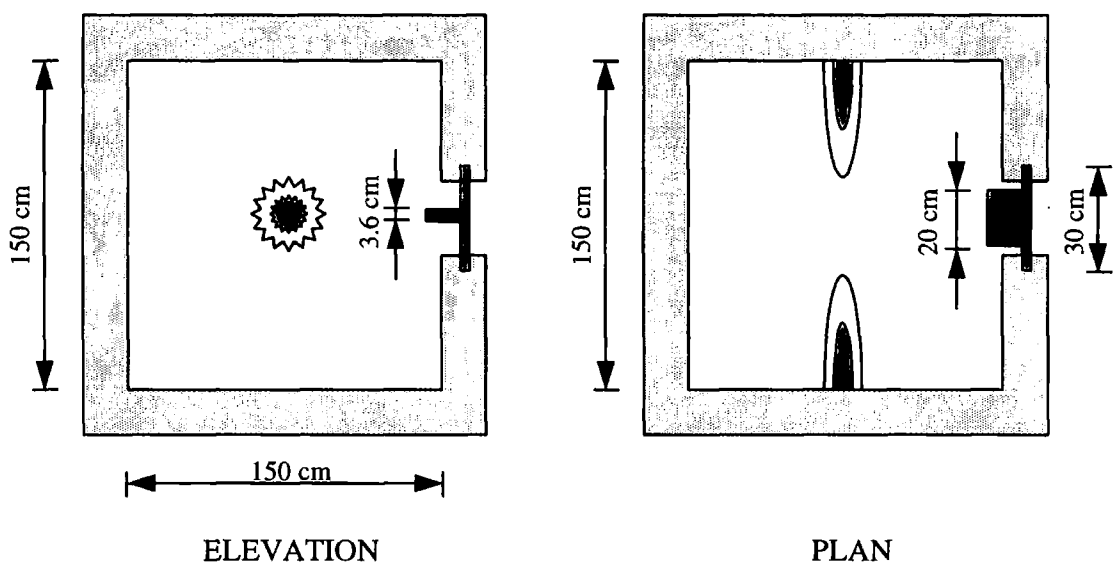

Figure 9.1 Elevation and plan views of the experimental furnace set up. The furnace is made of ceramic with an active volume of 3.375m^3. The thick GRP step panel with thicknesses 1.2 and 9.6cm is fitted on the door of the furnace.

9.2 MATHEMATICAL MODEL

The geometry of the model is shown in Figure 9.2. If the temperature variations are ignored in the transverse, z, direction, the problem of three-dimensional heat transfer (Figure 9.2a) can be reduced to two dimensions (Figure 9.2b), i.e. temperature varies along through-the-thickness and longitudinal directions only, i.e. x and y. Unlike the last chapter where a thin step panel (with thickness 1.26cm) was used, here we use a thick step panel with thickness 9.6cm.

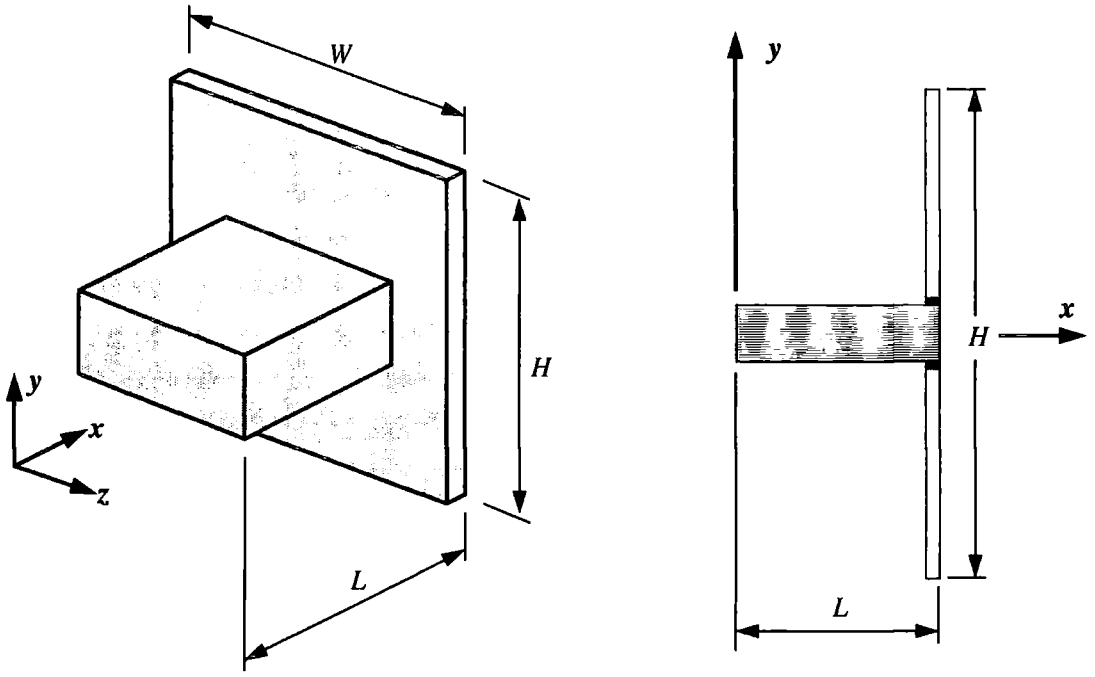

(a) (b)

Figure 9.2 Sketch of thick GRP step panel (right rectangular prism); (a) three-dimensional view where *L*, *H* and *W* are the thickness, length and width of the step panel and *x*, *y* and *z* represent through-the-thickness, longitudinal and transverse directions; (b) two-dimensional elevation view, the step panel consists of two woven-roving GRP laminates joined using adhesive (black).

A woven roving GRP laminate is homogenous and orthotropic but the selected step panel, made of two GRP laminates as shown in Figure 9.2b, is non-homogeneous and anisotropic (Appendix A). To derive the governing equations, the step panel is assumed homogeneous and orthotropic in the plane of the step domain.

Figure 9.3 shows an elevation section of a GRP step panel (right rectangular prism) set into the furnace wall.

The fundamental energy equation introduced in Chapter 8 for the two-dimensional modelling of thick GRP step panels can be extended to formulate the present mathematical model by taking into account the change in internal energy of the material influenced by both active material and pyrolysis gases due to the porous nature of the composite. The pyrolysis gases diffuse in two directions due to the change in their enthalpy in both through-the-thickness and longitudinal directions. To derive the two-dimensional formulation for heat and mass transfer a new step panel of thickness L and length H is used. For a step domain Ω bounded by a closed curve $\Gamma=S_1+S_2+S_3+S_4+S_5+S_6$ (Figure 9.4), the phenomena of heat and mass transfer is given by two equations: (i) energy equation and (ii) gas diffusion equation.

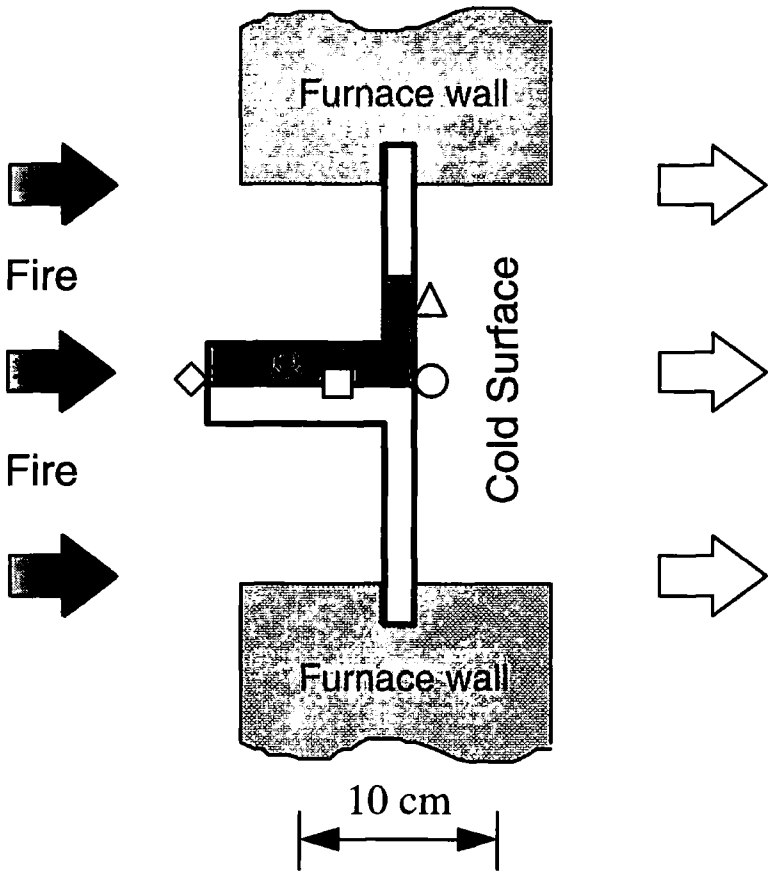

Figure 9.3 Elevation section of the step panel used in the mathematical modelling and experiments. The panel is made of two single-skinned GRP laminates inset into the wall of a ceramic furnace. The locations of the temperature sensors are shown as ◇□○△.

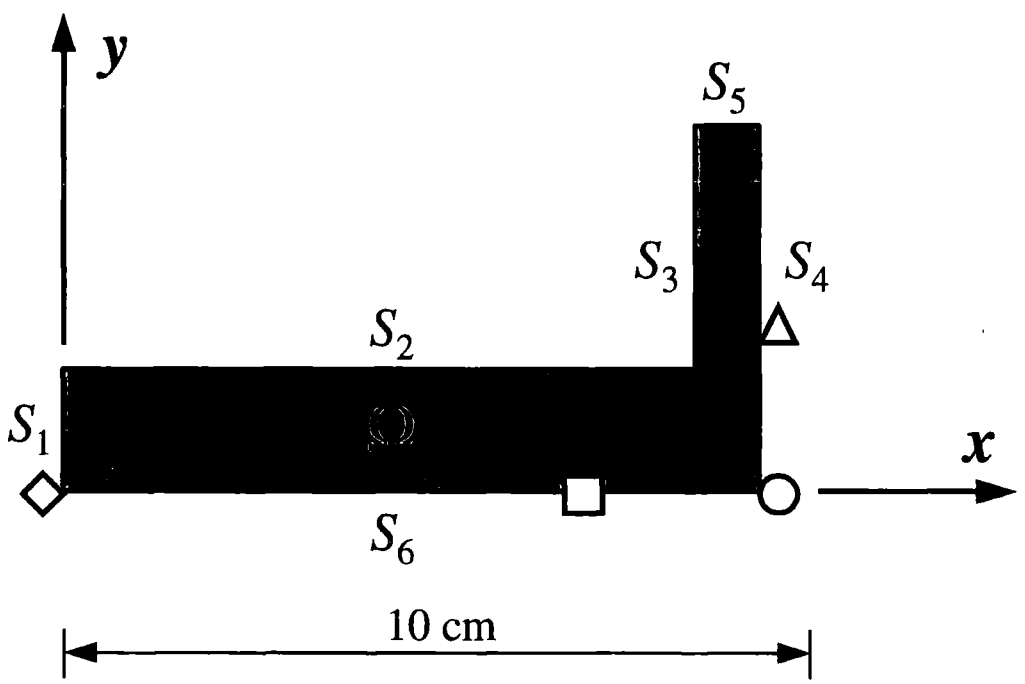

Figure 9.4 The simplified geometry and notation for mathematical model. The locations of temperature sensors are shown as ◇□○△.

(i) Energy equation

The conservation of energy in a two dimensional porous body is given by:

$$\left[(1-\phi)\rho c_p + \phi \rho_g c_{pg}\right]\frac{\partial T}{\partial t} = -\frac{\partial q_x}{\partial x} - \frac{\partial q_y}{\partial y} + \dot{q} \tag{9.1}$$

where ϕ = porosity

ρ = density of GRP (kgm^{-3})

c_p = specific heat of GRP ($Jkg^{-1}K^{-1}$)

ρ_g = density of the pyrolysis gases (kgm^{-3})

c_{pg} = specific heat of pyrolysis gases ($Jkg^{-1}K^{-1}$)

T = temperature (°C)

t = time (s)

q_x = heat flux in through-the-thickness direction (Wm^{-2})

x = spatial co-ordinate representing through-the-thickness direction (m)

q_y = heat flux in the longitudinal direction (Wm^{-2})

y = spatial co-ordinate representing the longitudinal direction (m)

$\dot{q}$ = internally generated heat per unit volume (Wm^{-3})

In Equation 9.1, the term at the left hand side is the rate of change of internal energy in the material; the first two terms on the right hand side are the energy flow rate per unit area and the third one is the heat generated internally per unit volume. In this equation, ρc_p and $\rho_g c_{pg}$ also represent the heat capacities of the solid and pyrolysis gases, respectively.

Heat fluxes in x and y directions include two terms, i.e. heat conduction and gas mass movement:

$$q_x = -\bar{k}_T \frac{\partial T}{\partial x} + \dot{m}_{gx} h_g \tag{9.2a}$$

$$q_y = -\bar{k}_L \frac{\partial T}{\partial y} + \dot{m}_{gy} h_g \tag{9.2b}$$

where

$\bar{k}_T$ = thermal conductivity of solid/gas mixture in x direction ($Wm^{-1}K^{-1}$)

$\dot{m}_{gx}$ = gas mass flux in x direction ($kgm^{-2}s^{-1}$)

h_g = enthalpy of pyrolysis gases (Jkg^{-1})

$\bar{k}_L$ = thermal conductivity of solid/gas mixture in y direction ($Wm^{-1}K^{-1}$)

$\dot{m}_{gy}$ = gas mass flux in y direction ($kgm^{-2}s^{-1}$)

The first terms on the right hand sides of Equations 9.2a and 9.2b indicate the heat energy transferred by conduction and the second terms denote the heat energy flows due to the gas mass movement.

The heat energy generated during decomposition process is independent from the geometry of the solid, therefore, it is the same for both one- and two-dimensional model given by:

$$\dot{q} = -\frac{\partial \rho_r}{\partial t}\left(Q + h - h_g\right) \tag{9.3}$$

where

ρ_r = density of resin (active) material (kgm^{-3})

Q = heat of decomposition (Jkg^{-1})

h = enthalpy of GRP (Jkg^{-1})

h_g = enthalpy of pyrolysis gases (Jkg^{-1})

Taking account of the assumption of local thermal equilibrium between virgin material and pyrolysis gases and using the term of the internal heat generation (Equation 9.3) and Equations 9.2a and 9.2b into Equation 9.1, the differential equation which governs the flow of energy through a decomposing, porous body takes the final form:

$$\begin{aligned}\left[(1-\phi)\rho c_p + \phi \rho_g c_{pg}\right]\frac{\partial T}{\partial t} = {} & \frac{\partial}{\partial x}\left(\bar{k}_T \frac{\partial T}{\partial x}\right) + \frac{\partial}{\partial y}\left(\bar{k}_L \frac{\partial T}{\partial y}\right) \\ & - c_{pg}\left(\dot{m}_{gx}\frac{\partial T}{\partial x} + \dot{m}_{gy}\frac{\partial T}{\partial y}\right) \\ & - \frac{\partial \rho_r}{\partial t}\left(Q + h - h_g\right)\end{aligned} \tag{9.4}$$

where the left hand side represents the rate of change of internal energy of the material. The first and second terms on the right hand side indicate the heat conduction across the boundary; the third term represents energy transferred due to gas mass diffusion which is evaluated in terms of pressure gradients and assumed to conform to Darcy's law and the last term accounts for internal heat energy which is released due to endothermic decomposition process.

The thermal conductivities of solid/gas mixture in through-the-thickness and longitudinal directions are given by:

$$\bar{k}_T = (1-\phi)k_T + \phi k_g \tag{9.5a}$$

$$\bar{k}_L = (1-\phi)k_L + \phi k_g \tag{9.5b}$$

where

k_T = thermal conductivity of material in x direction ($Wm^{-1}K^{-1}$)

k_g = thermal conductivity of the pyrolysis gases ($Wm^{-1}K^{-1}$)

k_L = thermal conductivity of material in y direction ($Wm^{-1}K^{-1}$)

The porosity is defined as the ratio of void volume to total volume (solid+void) calculated as a weighted function of the instantaneous mass fraction F:

$$\phi = \phi_0 F + \phi_1 (1-F) \tag{9.6}$$

where ϕ_0 is the initial porosity, ϕ_1 is the curve fit coefficient and F is defined by:

$$F = \frac{\rho_r - \rho_{rf}}{\rho_{ro} - \rho_{rf}} \tag{9.7}$$

where ρ_{rf} is the final density of resin (kgm^{-3}) and ρ_{ro} is the initial density of resin (kgm^{-3}).

The rate of decomposition is formulated upon the rate of change of the resin density, $\partial\rho_r/\partial t$, which conforms to a first-order kinetic rate Arrhenius equation given by:

$$\frac{\partial \rho_r}{\partial t} = -A\left(\rho_r - \rho_{rf}\right) \exp\left(\frac{-E_A}{RT_k}\right) \tag{9.8}$$

where

A = pyrolysis constant (s^{-1})

E_A = activation energy ($kJmole^{-1}$)

R = gas constant (8.314 $kJkmole^{-1}K^{-1}$)

T_k = temperature (K)

Heat of decomposition Q is evaluated experimentally and h and h_g are given by:

$$h = \int_{T_\infty}^{T} c_p dt \tag{9.9a}$$

$$h_g = \int_{T_\infty}^{T} c_{pg} dt \tag{9.9b}$$

where T_∞ is the ambient temperature (20°C).

(ii) Gas diffusion equation

The gas diffusion equation assumes conservation of gas mass with only two dependent variables related to pore pressure and temperature, respectively.

The gas mass flow is dependent upon the temperature and pressure gradients; the first from Fourier's law of conduction [Fourier, 1882] and the second from Darcy's law of diffusion [Bejan, 1993]. For materials with high percentage of moisture, the pressure change caused by the gaseous products in a constant volume can be small compared with that caused by the effect of moisture evaporation. However, earlier we saw that due to the low percentage of moisture in GRP the water vapour does not merge with pyrolysis gases and therefore makes no contribution into the pressure rise and gas diffusion equation.

The model presented here for the diffusion of the pyrolysis gases assumes the gas flow is driven by pressure gradients. Darcy's law of diffusion states that the flow is proportional to the pressure gradients. Thus:

$$\dot{m}_{gx} = -\frac{\gamma_x \rho_g}{\mu_g \phi} \frac{\partial P}{\partial x} \tag{9.10a}$$

$$\dot{m}_{gy} = -\frac{\gamma_y \rho_g}{\mu_g \phi} \frac{\partial P}{\partial y} \tag{9.10b}$$

where γ_x = permeability in x direction (m^2)

ρ_g = density of pyrolysis gases (kgm^{-3})

P = pore pressure (Pa)

μ_g = dynamic viscosity of pyrolysis gases (Nsm^{-2})

γ_y = permeability in y direction (m^2)

Differentiation of Equations 9.10a and 9.10b with respect to x and y result in:

$$\frac{\partial \dot{m}_{gx}}{\partial x} = -\frac{\partial}{\partial x}\left(\frac{\gamma_x \rho_g}{\mu_g \phi} \frac{\partial P}{\partial x}\right) \tag{9.11a}$$

$$\frac{\partial \dot{m}_{gy}}{\partial y} = -\frac{\partial}{\partial y}\left(\frac{\gamma_y \rho_g}{\mu_g \phi} \frac{\partial P}{\partial y}\right) \tag{9.11b}$$

The density of the pyrolysis gases can be obtained using the ideal gas equation, i.e.:

$$\rho_g = \frac{P M_g \phi}{R T_k} \tag{9.12}$$

where M_g is the gas molecular weight ($kgkmole^{-1}$).

The change in the density of the pyrolysis gases in the porous solid is evaluated from the continuity equation, i.e.:

$$\frac{\partial \rho_g}{\partial t} = -\frac{\partial \rho_r}{\partial t} - \frac{\partial \dot{m}_{gx}}{\partial x} - \frac{\partial \dot{m}_{gy}}{\partial y} \tag{9.13}$$

By differentiating Equation 9.12 with respect to t, the variation of gas density with pressure and temperature is given by:

$$\frac{\partial \rho_g}{\partial t} = \frac{M_g \phi}{RT_k}\frac{\partial P}{\partial t} - \frac{PM_g \phi}{RT_k^2}\frac{\partial T}{\partial t} \tag{9.14}$$

Using the ideal gas equation, i.e. Equation 9.12, this becomes:

$$\frac{\partial \rho_g}{\partial t} = \frac{\rho_g}{P}\frac{\partial P}{\partial t} - \frac{\rho_g}{T_k}\frac{\partial T}{\partial t} \tag{9.15}$$

Substituting Equations 9.11a, 9.11b and 9.15 into Equation 9.13, the differential equation which governs the diffusion of the pyrolysis gases through a two-dimensional decomposing, porous solid is given by:

$$\frac{\rho_g}{P}\frac{\partial P}{\partial t} = \frac{\partial}{\partial x}\left(\frac{\gamma_x \rho_g}{\mu_g \phi}\frac{\partial P}{\partial x}\right) + \frac{\partial}{\partial y}\left(\frac{\gamma_y \rho_g}{\mu_g \phi}\frac{\partial P}{\partial y}\right) + \frac{\rho_g}{T_k}\frac{\partial T}{\partial t} - \frac{\partial \rho_r}{\partial t} \tag{9.16}$$

where the left hand side denotes the gas storage in the pore system. The first and second terms on the right hand side represent the gas mass flux moving across the boundary; the third term accounts for variation of pore pressure with temperature and the last term is the contribution to the pore pressure due to decomposition and the generation of the pyrolysis gases.

According to Darcy's law (Equations 9.10a and 9.10b), the gas mass fluxes are proportional to the pressure gradients. The transferred terms, i.e. $\gamma_x \rho_g / \mu_g \phi$ and $\gamma_y \rho_g / \mu_g \phi$, depend on permeabilities γ_x and γ_y, which are functions of the pore system, porosity and the properties of the gas mixture. The permeability used here is obtained from a best fit empirical formulation given by Equation 4.19:

$$\gamma = \gamma_o \exp[\gamma_1 (1 - F)] \tag{9.17}$$

where γ_0 is the initial permeability (m^2) and γ_1 is the curve fit coefficient. This was proposed by Fredlund [1988] for wood and is considered as a temporary solution to evaluate the permeability of the GRP here in both through-the-thickness and longitudinal directions, i.e. $\gamma_x = \gamma_y = \gamma$.

It is noted the variations of pore pressure of GRP is sensitive to the value of permeability and it is essential to apply the best possible value for initial permeability and the curve fit coefficient. A prediction-correction method may also be used [Wang, 1995]. As a first step, the approximate values are derived from literature, then refined by numerical techniques through systematically fitting the results given by computation to the results of the fire experiments. Once these values have been determined, the thermal behaviour of the material under a variety of environments and configurations can then be modelled. This method can only be used to obtain the value of one property at a time.

Initial and boundary conditions

It is assumed all the boundaries are at atmospheric pressure and no gas mass movement occurs across the boundaries during exposure to fire. At the hot and cold surfaces both radiative and convective heat transfer occurs.

The initial conditions are given by:

$$\begin{array}{lll} T(x,y,t)=T_\infty & m(x,y,t)=m_{vo} & P(x,y,t)=P_\infty \\ c_p=c_{po} & c_{pg}=c_{pgo} & k_g=k_{go} \\ \rho=\rho_o & \rho_g=0 & \phi=\phi_o \\ k_T=k_{To} & \dot{m}_{gx}=0 & \gamma=\gamma_o \\ k_L=k_{Lo} & \dot{m}_{gy}=0 & \varepsilon=\varepsilon_o \end{array} \quad \text{for} \quad \Omega,\ t=0 \qquad (9.18)$$

where

P_∞ = ambient pressure (0.1 MPa)

m_v = volumetric moisture content

ε = surface emissivity

and subscript o denotes initial quantities.

The boundary condition for the hot surfaces, i.e. S_1, S_2 and S_3, is given by:

$$\begin{array}{l} T(x,y,t)=T_s(t) \\ P(x,y,t)=P_\infty \end{array} \quad \text{for} \quad S_1,\ S_2 \text{ and } S_3,\ t>0 \qquad (9.19)$$

for the cold surface S_4 by:

$$\begin{array}{l} -k_T\dfrac{\partial T}{\partial x}=q_r+q_c \\ P(x,y,t)=P_\infty \\ \dot{m}_g=0 \end{array} \quad \text{for} \quad S_4,\ t>0 \qquad (9.20)$$

and for S_5 and S_6 by:

$$\begin{aligned} \frac{\partial T}{\partial y} &= 0 \\ P(x,y,t) &= P_\infty \\ \dot{m}_g &= 0 \end{aligned} \qquad \text{for} \qquad S_5 \text{ and } S_6,\ t>0 \tag{9.21}$$

where

$T_s(t)$ = hot surface time-dependent temperature (°C)

q_r = radiation heat flux at the cold surface S_4 (Wm^{-2})

q_c = convection heat flux at the cold surface S_4 (Wm^{-2})

$T_s(t)$ was introduced in Chapter 3 by an empirical relation [Wu *et al.*, 1994], i.e.:

$$T_s(t) = (T_g - 100)\left\{1 - \exp\left\{-\exp\left[0.71\log\left(\frac{t}{124.8}\right)\right]\right\}\right\} + T_\infty \quad \text{for} \quad t>0 \tag{9.22}$$

where T_g is the maximum fire temperature (1100°C).

q_r and q_c are given by Equations 3.12 and 3.14:

$$q_r = h_r(T - T_\infty) \tag{9.23}$$

$$q_c = h_c(T - T_\infty) \tag{9.24}$$

where h_r and h_c are the equivalent convection coefficient ($Wm^{-2}K^{-1}$) and the convection coefficient ($Wm^{-2}K^{-1}$) expressed by Equations 3.13 and 3.15:

$$h_r = \sigma\varepsilon\left(T_k^2 + T_{\infty k}^2\right)\left(T_k + T_{\infty k}\right) \tag{9.25}$$

$$h_c = k_{e\infty}\frac{\overline{\mathrm{Nu}}_W}{W} \tag{9.26}$$

and σ = Stefan-Boltzmann constant (5.669×10^{-8} W $m^{-2}K^{-4}$)

T_{kj} = cold surface temperature (K)

$T_{\infty k}$ = ambient temperature (293K)

$k_{e\infty}$ = thermal conductivity of air at ambient temperature ($Wm^{-1}K^{-1}$)

$\overline{\mathrm{Nu}}_{Wj}$ = average Nusselt number

W = width of step panel (m)

An empirical relation that is valid for all Rayleigh and Prandtl numbers has been introduced by Churchill and Chu [1975] for Nusselt number. This relation is:

$$\overline{\mathrm{Nu}}_W = \left\{0.825 + \frac{0.387\mathrm{Ra}_W^{1/6}}{\left[1+(0.492/\mathrm{Pr})^{9/16}\right]^{8/27}}\right\}^2 \qquad \begin{matrix} 10^{-1} < \mathrm{Ra}_W < 10^{12} \\ \text{for all Pr} \end{matrix} \tag{9.27}$$

where Ra_W denotes Rayleigh number and Pr denotes Prandtl number (Appendix B).

Equations 9.4, 9.5, 9.8 to 9.10, 9.12, 9.13, 9.16 and 9.17 form a set of non-linear partial differential equations which must be solved simultaneously using the initial and boundary conditions, i.e. Equations 9.18 to 9.21, for ρ, T, $\dot{m}_{gx}$, $\dot{m}_{gy}$ and P.

9.3 FINITE ELEMENT FORMULATION

The set of non-linear partial differential equations, i.e. Equations 9.4, 9.5, 9.8 to 9.10, 9.12, 9.13, 9.16 and 9.17, which represent the two-dimensional heat and mass transfer problem in thick GRP step panels, are solved numerically for temperature and pore pressure distributions at any time during fire exposure. The Bubnov-Galerkin finite element approach is used to solve the equations simultaneously. All terms and coefficients are evaluated explicitly using an iterative-updating procedure and nodal temperatures and pore pressures are computed implicitly using the Crank-Nicolson solution.

9.3.1 Explicit Evaluation of Terms and Coefficients

A general notation $(\ )^{i}_{j,k}$ is used where i represents the time interval and j and k denote the spatial positions. Time derivative terms are given by forward difference and the spatial variables by central difference.

Using notation $(\ )^{i}_{j,k}$, the energy and gas diffusion equations, i.e. Equations 9.4 and 9.16, are given, at a particular time and position, by:

$$\left[\left(1-\phi^{i+1}_{\bar{j},\bar{k}}\right)\left(\rho c_p\right)^{i+1}_{\bar{j},\bar{k}}+\phi^{i+1}_{\bar{j},\bar{k}}\left(\rho_g c_{pg}\right)^{i+1}_{\bar{j},\bar{k}}\right]\frac{\partial T}{\partial t}=\frac{\partial}{\partial x}\left[\left(\bar{k}_T\right)^{i+1}_{\bar{j},\bar{k}}\frac{\partial T}{\partial x}\right]+\frac{\partial}{\partial y}\left[\left(\bar{k}_L\right)^{i+1}_{\bar{j},\bar{k}}\frac{\partial T}{\partial y}\right]$$

$$-\left(c_{pg}\right)^{i+1}_{\bar{j},\bar{k}}\left[\left(\dot{m}_{gx}\right)^{i+1}_{\bar{j},\bar{k}}\frac{\partial T}{\partial x}+\left(\dot{m}_{gy}\right)^{i+1}_{\bar{j},\bar{k}}\frac{\partial T}{\partial y}\right]-\left(\frac{\partial \rho_r}{\partial t}\right)^{i+1}_{\bar{j},\bar{k}}\left\{Q+\left[\left(c_p\right)^{i+1}_{\bar{j},\bar{k}}-\left(c_{pg}\right)^{i+1}_{\bar{j},\bar{k}}\right]\left(T-T_\infty\right)\right\} \quad (9.28)$$

and

$$\frac{\left(\rho_g\right)^{i+1}_{\bar{j},\bar{k}}}{P^{i}_{\bar{j},\bar{k}}}\frac{\partial P}{\partial t}=\frac{\partial}{\partial x}\left[\left(\frac{\gamma p_g}{\mu_g \phi}\right)^{i+1}_{\bar{j},\bar{k}}\frac{\partial P}{\partial x}\right]+\frac{\partial}{\partial y}\left[\left(\frac{\gamma p_g}{\mu_g \phi}\right)^{i+1}_{\bar{j},\bar{k}}\frac{\partial P}{\partial y}\right]$$

$$+\frac{\left(\rho_g\right)^{i+1}_{\bar{j},\bar{k}}}{\left(T_k\right)^{i}_{\bar{j},\bar{k}}}\frac{\partial T}{\partial t}-\left(\frac{\partial \rho_r}{\partial t}\right)^{i+1}_{\bar{j},\bar{k}} \quad (9.29)$$

where Δt is the time step size (s), subscripts $\bar{j}$ and $\bar{k}$ specify the position of the centre of each element and notation $(\ )_{\bar{j},\bar{k}}$ represents the average of all the nodal values.

Required throughout the finite element program are the density, porosity, instantaneous mass fraction, thermal conductivities of the solid/gas mixture, gas mass fluxes, mass loss rate, gas density and permeability. These are approximated at particular time and position explicitly using Equations 4.1, 9.5 to 9.8, 9.10, 9.12 and 9.17:

$$\rho_{j,k}^{i+1} = \left\{ (\rho_r)_{j,k}^{i} - A\Delta t\left[(\rho_r)_{j,k}^{i} - \rho_{rf}\right]\exp\left[\frac{-E_A}{R(T_k)_{j,k}^{i}}\right]\right\}(1-V_f) + \rho_{fr}V_f \tag{9.30a}$$

$$\phi_{j,k}^{i+1} = \phi_o F_{j,k}^{i+1} + \phi_1\left(1 - F_{j,k}^{i+1}\right) \tag{9.30b}$$

$$F_{j,k}^{i+1} = \frac{(\rho_r)_{j,k}^{i+1} - \rho_{rf}}{\rho_{ro} - \rho_{rf}} \tag{9.30c}$$

$$\left(\bar{k}_T\right)_{j,k}^{i+1} = \left(1-\phi_{j,k}^{i+1}\right)\left(k_T\right)_{j,k}^{i+1} + \phi_{j,k}^{i+1}\left(k_g\right)_{j,k}^{i+1} \tag{9.30d}$$

$$\left(\bar{k}_L\right)_{j,k}^{i+1} = \left(1-\phi_{j,k}^{i+1}\right)\left(k_L\right)_{j,k}^{i+1} + \phi_{j,k}^{i+1}\left(k_g\right)_{j,k}^{i+1} \tag{9.30e}$$

$$\left(\dot{m}_{gx}\right)_{j,k}^{i+1} = -\frac{\gamma_{j,k}^{i+1}\,\rho_{j,k}^{i+1}}{\left(\mu_g\right)_{j,k}^{i+1}\,\phi_{j,k}^{i+1}}\left(\frac{P_{j+1,k}^{i+1} - P_{j,k}^{i+1}}{l_j}\right) \tag{9.30f}$$

$$\left(\dot{m}_{gy}\right)_{j,k}^{i+1} = -\frac{\gamma_{j,k}^{i+1}\,\rho_{j,k}^{i+1}}{\left(\mu_g\right)_{j,k}^{i+1}\,\phi_{j,k}^{i+1}}\left(\frac{P_{j,k+1}^{i+1} - P_{j,k}^{i+1}}{h_k}\right) \tag{9.30g}$$

$$\left(\frac{\partial \rho_r}{\partial t}\right)_{j,k}^{i+1} = -A\left[(\rho_r)_{j,k}^{i} - \rho_{rf}\right]\exp\left[\frac{-E_A}{R(T_k)_{j,k}^{i}}\right] \tag{9.30h}$$

$$\left(\rho_g\right)_{j,k}^{i+1} = \frac{P_{j,k}^{i} M_g \phi_{j,k}^{i+1}}{R(T_k)_{j,k}^{i}} \tag{9.30i}$$

$$\gamma_{j,k}^{i+1} = \gamma_o \exp\left[\gamma_1\left(1 - F_{j,k}^{i+1}\right)\right] \tag{9.30j}$$

where V_f is the volume fraction, l is the element length (m) and h is the element width (m). The length and width of each element may vary from one element to another.

Expressions for thermal conductivity and specific heat of GRP and specific heat and dynamic viscosity of pyrolysis gases at particular time and position are given in Tables 4.3 and 4.4.

9.3.2 Finite Element Equations

The solution domain Ω, which is a two-dimensional step panel with maximum thickness L and length H, is divided into E quadrilateral elements of different lengths and widths with 4-nodes each. The governing differential equations, i.e. Equations 9.28 and 9.29, are cast into a coupled matrix equation by applying the weighted residual approach of the finite element method. Within each element, the temperature, pore pressure and their gradients are approximated by:

$$T(x,y,t) = \mathbf{N}(x,y)\mathbf{T}(t) \quad , \quad \begin{Bmatrix} \frac{\partial T}{\partial x}(x,y,t) \\ \frac{\partial T}{\partial y}(x,y,t) \end{Bmatrix} = \mathbf{B}(x,y)\mathbf{T}(t) \tag{9.31}$$

$$P(x,y,t) = \mathbf{N}(x,y)\mathbf{P}(t) \quad , \quad \begin{Bmatrix} \frac{\partial P}{\partial x}(x,y,t) \\ \frac{\partial P}{\partial y}(x,y,t) \end{Bmatrix} = \mathbf{B}(x,y)\mathbf{P}(t) \tag{9.32}$$

where

$\mathbf{N}(x,y)$	=	shape function matrix
$\mathbf{T}(t)$	=	temperature vector
$\mathbf{P}(x,y)$	=	pressure vector
$\mathbf{B}(x,y)$	=	shape function derivative matrix

The element shape function and shape function derivative matrices are given by:

$$\mathbf{N}(x,y) = \begin{bmatrix} N_1 & N_2 & N_3 & N_4 \end{bmatrix} \tag{9.33a}$$

$$\mathbf{B}(x,y) = \begin{bmatrix} N_{1x} & N_{2x} & N_{3x} & N_{4x} \\ N_{1y} & N_{2y} & N_{3y} & N_{4y} \end{bmatrix} \tag{9.33b}$$

where N_i (i = 1,...,4) are given, in global co-ordinates, by:

$$N_1(x,y) = 1 - \frac{x}{l} - \frac{y}{h} + \frac{xy}{lh} \tag{9.34a}$$

$$N_2(x,y) = \frac{x}{l} - \frac{xy}{lh} \tag{9.34b}$$

$$N_3(x,y) = \frac{xy}{lh} \tag{9.34c}$$

$$N_4(x,y) = \frac{y}{h} - \frac{xy}{lh} \tag{9.34d}$$

The elements of the **B** matrix are evaluated by differentiating the shape functions with respect to x and y.

To perform the finite element computations, the element matrices are derived in local co-ordinates, a co-ordinate system associated with each element. The element shape functions and shape function derivative matrix may therefore be represented, in local co-ordinates, as:

$$N_1(\xi,\eta)=\frac{1}{4}(1-\xi)(1-\eta) \tag{9.35a}$$

$$N_2(\xi,\eta)=\frac{1}{4}(1+\xi)(1-\eta) \tag{9.35b}$$

$$N_3(\xi,\eta)=\frac{1}{4}(1+\xi)(1+\eta) \tag{9.35c}$$

$$N_4(\xi,\eta)=\frac{1}{4}(1-\xi)(1+\eta) \tag{9.35d}$$

and

$$\mathbf{B}(\xi,\eta)=\frac{1}{4}\begin{bmatrix}-(1-\eta) & (1-\eta) & (1+\eta) & -(1+\eta)\\ -(1-\xi) & -(1+\xi) & (1+\xi) & (1+\xi)\end{bmatrix} \tag{9.36}$$

where ξ and η denote the local co-ordinates which are related to the global co-ordinates by:

$$x=\frac{1}{2}(1+\xi) \quad , \quad y=\frac{1}{2}(1+\eta) \tag{9.37}$$

Consider Equations 9.4 and 9.16, the weighted residual approach requires:

$$\int_{\Omega^e}\left\{\left[(1-\phi)\rho c_p+\phi\rho_g c_{pg}\right]\frac{\partial T}{\partial t}-\bar{k}_T\frac{\partial^2 T}{\partial x^2}-\bar{k}_L\frac{\partial^2 T}{\partial y^2}\right.$$

$$\left.+c_{pg}\left(\dot{m}_{gx}\frac{\partial T}{\partial x}+\dot{m}_{gy}\frac{\partial T}{\partial y}\right)+\frac{\partial \rho_r}{\partial t}\left[Q+\left(c_p-c_{pg}\right)\left(T-T_\infty\right)\right]\right\}N_i\,d\Omega=0 \quad i=1,\ldots,4 \tag{9.38}$$

for the energy equation and

$$\int_{\Omega^e}\left[\frac{\rho_g}{P}\frac{\partial P}{\partial t}-\frac{\partial}{\partial x}\left(\frac{\gamma p_g}{\mu_g\phi}\frac{\partial P}{\partial x}\right)-\frac{\partial}{\partial y}\left(\frac{\gamma p_g}{\mu_g\phi}\frac{\partial P}{\partial y}\right)\right.$$

$$\left.-\frac{\rho_g}{T_k}\frac{\partial T}{\partial t}+\frac{\partial \rho_r}{\partial t}\right]N_i\,d\Omega=0 \quad i=1,\ldots,4 \tag{9.39}$$

for the gas diffusion equation where Ω^e denotes the domain for element e.

Equations 9.38 and 9.39 express the desired averaging of the residual at the element boundaries for both temperature and pore pressure but they do not represent the influence of the boundary conditions. Integration by parts using Green's theorem (Appendix C):

$$\int_{\Omega^e} u\,(\nabla.\mathbf{v})d\Omega = \int_{\Gamma^e} u\,(\mathbf{v}.\mathbf{n})d\Gamma - \int_{\Omega^e} \mathbf{v}.\nabla u\,d\Omega \tag{9.40}$$

with $u=N_i$ and

$$\mathbf{v} = -k_T \frac{\partial T}{\partial x}\hat{i} - k_L \frac{\partial T}{\partial y}\hat{j} \tag{9.41a}$$

for the energy equation and

$$\mathbf{v} = -\frac{\gamma\rho_g}{\mu_g \phi}\left(\frac{\partial P}{\partial x}\hat{i} + \frac{\partial P}{\partial y}\hat{j}\right) \tag{9.41b}$$

for the gas diffusion equation and separating each term, gives expressions containing lower order derivatives, i.e.:

(i) Energy

$$\int_{\Omega^e}\left[(1-\phi)\rho c_p + \phi\rho_g c_{pg}\right]\frac{\partial T}{\partial t}N_i d\Omega - \int_{\Gamma^e}\begin{bmatrix} n_x & n_y \end{bmatrix}\begin{Bmatrix} \bar{k}_T \dfrac{\partial T}{\partial x} \\ \bar{k}_L \dfrac{\partial T}{\partial y} \end{Bmatrix} N_i d\Gamma$$

$$+\int_{\Omega^e}\begin{bmatrix} \dfrac{\partial N_i}{\partial x} & \dfrac{\partial N_i}{\partial y} \end{bmatrix}\begin{Bmatrix} \bar{k}_T \dfrac{\partial T}{\partial x} \\ \bar{k}_L \dfrac{\partial T}{\partial y} \end{Bmatrix} d\Omega - \int_{\Omega^e} c_{pg}\left(\frac{\gamma\rho_g}{\mu_g\phi}\right)\begin{bmatrix} \dfrac{\partial P}{\partial x} & \dfrac{\partial P}{\partial y} \end{bmatrix}\begin{Bmatrix} \dfrac{\partial T}{\partial x} \\ \dfrac{\partial T}{\partial y} \end{Bmatrix} N_i d\Omega$$

$$+\int_{\Omega^e}\frac{\partial\rho_r}{\partial t}\left(c_p - c_{pg}\right)TN_i d\Omega + \int_{\Omega^e}\frac{\partial\rho_r}{\partial t}\left[Q - \left(c_p - c_{pg}\right)T_\infty\right]N_i d\Omega = 0 \quad i = 1,\ldots,4 \tag{9.42}$$

(ii) Gas diffusion

$$\int_{\Omega^e}\frac{\rho_g}{P}\frac{\partial P}{\partial t}N_i d\Omega - \int_{\Gamma^e}\frac{\gamma\rho_g}{\mu_g\phi}\begin{bmatrix} n_x & n_y \end{bmatrix}\begin{Bmatrix} \dfrac{\partial P}{\partial x} \\ \dfrac{\partial P}{\partial y} \end{Bmatrix} N_i d\Gamma + \int_{\Omega^e}\frac{\gamma\rho_g}{\mu_g\phi}\begin{bmatrix} \dfrac{\partial N_i}{\partial x} & \dfrac{\partial N_i}{\partial y} \end{bmatrix}\begin{Bmatrix} \dfrac{\partial P}{\partial x} \\ \dfrac{\partial P}{\partial y} \end{Bmatrix} d\Omega$$

$$-\int_{\Omega^e}\frac{\rho_g}{T_k}\frac{\partial T}{\partial t}N_i d\Omega + \int_{\Omega^e}\frac{\partial\rho_r}{\partial t}N_i d\Omega = 0 \quad i = 1,\ldots,4 \tag{9.43}$$

where

$$\mathbf{n} = n_x\hat{i} + n_y\hat{j} \tag{9.44}$$

and Γ^e denotes the boundary of element e.

The second terms of Equations 9.42 and 9.43 represent natural boundary conditions for the element. The natural boundary conditions are taken into account when the element matrices are assembled. During assembly, these will cancel at all interior nodes of the solution domain leaving only the natural boundary conditions to be evaluated at the hot and cold surfaces, i.e. S_1, S_2, S_3 and S_4. This implies that the second terms of Equations 9.42 and 9.43 actually represent the surface boundary conditions defined by Equations 9.19 to 9.21 where the prescribed temperature at the hot surface boundary, i.e. Equation 9.19, is introduced to the matrix equation after assembling the element matrices (Appendix C).

Introducing the boundary conditions to the element equations result in:

(i) Energy

$$\int_{\Omega^e}\left[(1-\phi)\rho c_p+\phi\rho_g c_{pg}\right]\frac{\partial T}{\partial t}N_i d\Omega+\int_{\Omega^e}\begin{bmatrix}\frac{\partial N_i}{\partial x} & \frac{\partial N_i}{\partial y}\end{bmatrix}\begin{Bmatrix}\bar{k}_T\frac{\partial T}{\partial x}\\ \bar{k}_L\frac{\partial T}{\partial y}\end{Bmatrix}d\Omega$$

$$-\int_{\Omega^e}c_{pg}\left(\frac{\gamma\rho_g}{\mu_g\phi}\right)\begin{bmatrix}\frac{\partial P}{\partial x} & \frac{\partial P}{\partial y}\end{bmatrix}\begin{Bmatrix}\frac{\partial T}{\partial x}\\ \frac{\partial T}{\partial y}\end{Bmatrix}N_i d\Omega+\int_{\Omega^e}\frac{\partial\rho_r}{\partial t}\left(c_p-c_{pg}\right)TN_i d\Omega$$

$$+\int_{S_4}\left(h_r+h_c\right)TN_i d\Gamma-\sum_{j=1}^{3}\int_{S_i}\begin{bmatrix}n_x & n_y\end{bmatrix}\begin{Bmatrix}\bar{k}_T\frac{\partial T}{\partial x}\\ \bar{k}_L\frac{\partial T}{\partial y}\end{Bmatrix}N_i d\Gamma$$

$$+\int_{\Omega^e}\frac{\partial\rho_r}{\partial t}\left[Q-\left(c_p-c_{pg}\right)T_\infty\right]N_i d\Omega-\int_{S_4}\left(h_r+h_c\right)T_\infty N_i d\Gamma=0\qquad i=1,\ldots,4\qquad(9.45)$$

(i) Gas diffusion

$$\int_{\Omega^e}\frac{\rho_g}{P}\frac{\partial P}{\partial t}N_i d\Omega+\int_{\Omega^e}\frac{\gamma\rho_g}{\mu_g\phi}\begin{bmatrix}\frac{\partial N_i}{\partial x} & \frac{\partial N_i}{\partial y}\end{bmatrix}\begin{Bmatrix}\frac{\partial P}{\partial x}\\ \frac{\partial P}{\partial y}\end{Bmatrix}d\Omega-\int_{\Omega^e}\frac{\rho_g}{T_k}\frac{\partial T}{\partial t}N_i d\Omega$$

$$+\int_{\Omega^e}\frac{\partial\rho_r}{\partial t}N_i d\Omega-\sum_{j=1}^{4}\int_{S_j}\frac{\gamma\rho_g}{\mu_g\phi}\begin{bmatrix}n_x & n_y\end{bmatrix}\begin{Bmatrix}\frac{\partial P}{\partial x}\\ \frac{\partial P}{\partial y}\end{Bmatrix}N_i d\Gamma=0\qquad i=1,\ldots,4\qquad(9.46)$$

Substitute Equations 9.31 and 9.32 into Equations 9.45 and 9.46, the resulting equations become:

(i) Energy

$$\int_{\Omega^e}\left[(1-\phi)\rho c_p+\phi\rho_g c_{pg}\right]\mathbf{N}^{\mathrm{T}}\dot{\mathbf{T}}\mathbf{N}d\Omega+\int_{\Omega^e}\bar{k}_T\mathbf{N}_{\mathrm{x}}^{\mathrm{T}}\mathbf{T}\mathbf{N}_{\mathrm{x}}d\Omega+\int_{\Omega^e}\bar{k}_L\mathbf{N}_{\mathrm{y}}^{\mathrm{T}}\mathbf{T}\mathbf{N}_{\mathrm{y}}d\Omega$$

$$-\int_{\Omega^e}\frac{\gamma}{\mu_g\phi}\rho_g c_{pg}P_x\mathbf{N}_{\mathrm{x}}^{\mathrm{T}}\mathbf{T}\mathbf{N}_{\mathrm{x}}d\Omega-\int_{\Omega^e}\frac{\gamma}{\mu_g\phi}\rho_g c_{pg}P_y\mathbf{N}_{\mathrm{y}}^{\mathrm{T}}\mathbf{T}\mathbf{N}_{\mathrm{y}}d\Omega$$

$$+\int_{\Omega^e}\frac{\partial\rho_r}{\partial t}\left(c_p-c_{pg}\right)\mathbf{N}^{\mathrm{T}}\mathbf{T}\mathbf{N}d\Omega+\int_{S_4}\left(h_r+h_c\right)\mathbf{N}^{\mathrm{T}}\mathbf{T}\mathbf{N}d\Gamma+\sum_{j=1}^{3}\int_{S_j}(\mathbf{q}.\mathbf{n})\mathbf{N}^{\mathrm{T}}d\Gamma$$

$$+\int_{\Omega^e}\frac{\partial\rho_r}{\partial t}\left[Q-\left(c_p-c_{pg}\right)T_\infty\right]\mathbf{N}^{\mathrm{T}}d\Omega-\int_{S_2}\left(h_r+h_c\right)T_\infty\mathbf{N}^{\mathrm{T}}\,d\Gamma=\mathbf{0} \qquad (9.47)$$

(ii) Gas diffusion

$$\int_{\Omega^e}\frac{\rho_g}{P}\mathbf{N}^{\mathrm{T}}\dot{\mathbf{P}}\mathbf{N}d\Omega+\int_{\Omega^e}\frac{\gamma p_g}{\mu_g\phi}\mathbf{N}_{\mathrm{x}}^{\mathrm{T}}\mathbf{P}\mathbf{N}_{\mathrm{x}}d\Omega+\int_{\Omega^e}\frac{\gamma p_g}{\mu_g\phi}\mathbf{N}_{\mathrm{y}}^{\mathrm{T}}\mathbf{P}\mathbf{N}_{\mathrm{y}}d\Omega$$

$$-\int_{\Omega^e}\frac{\rho_g}{T_k}\mathbf{N}^{\mathrm{T}}\dot{\mathbf{T}}\mathbf{N}d\Omega+\int_{\Gamma^e}\frac{\partial\rho_r}{\partial t}\mathbf{N}^{\mathrm{T}}d\Gamma+\sum_{j=1}^{4}\int_{S_j}\left(\dot{\mathbf{m}}_{\mathbf{g}}.\mathbf{n}\right)\mathbf{N}^{\mathrm{T}}d\Gamma=\mathbf{0} \qquad (9.48)$$

where

$\dot{\mathbf{T}}$	=	vector of temperature derivatives with respect to time
$\mathbf{N_x}$	=	shape function derivative matrix with respect to x
$\mathbf{N_y}$	=	shape function derivative matrix with respect to y
$\mathbf{q}$	=	two-dimensional heat load vector
$\dot{\mathbf{m}}_{\mathbf{g}}$	=	two-dimensional gas mass flux vector

and subscript **T** denotes the transpose. Rearranging Equations 9.47 and 9.48 results in:

(i) Energy

$$\left\{\int_{\Omega^e}\mathbf{N}^{\mathrm{T}}\left[(1-\phi)\rho c_p+\phi\rho_g c_{pg}\right]\mathbf{N}d\Omega\right\}\dot{\mathbf{T}}+\left[\int_{\Omega^e}\mathbf{N}_{\mathrm{x}}^{\mathrm{T}}\bar{k}_T\mathbf{N}_{\mathrm{x}}d\Omega+\int_{\Omega^e}\mathbf{N}_{\mathrm{y}}^{\mathrm{T}}\bar{k}_L\mathbf{N}_{\mathrm{y}}d\Omega\right.$$

$$-\int_{\Omega^e}\mathbf{N}_{\mathrm{x}}^{\mathrm{T}}\frac{\gamma}{\mu_g\phi}\rho_g c_{pg}P_x\mathbf{N}_{\mathrm{x}}d\Omega-\int_{\Omega^e}\mathbf{N}_{\mathrm{y}}^{\mathrm{T}}\frac{\gamma}{\mu_g\phi}\rho_g c_{pg}P_y\mathbf{N}_{\mathrm{y}}d\Omega$$

$$\left.+\int_{\Omega^e}\mathbf{N}^{\mathrm{T}}\frac{\partial\rho_r}{\partial t}\left(c_p-c_{pg}\right)\mathbf{N}d\Omega+\int_{S_4}\mathbf{N}^{\mathrm{T}}\left(h_r+h_c\right)\mathbf{N}d\Gamma\right]\mathbf{T}+\sum_{j=1}^{3}\int_{S_j}\mathbf{N}^{\mathrm{T}}(\mathbf{q}.\mathbf{n})d\Gamma$$

$$+\int_{\Omega^e}\mathbf{N}^{\mathrm{T}}\frac{\partial\rho_r}{\partial t}\left[Q-\left(c_p-c_{pg}\right)T_\infty\right]d\Omega-\int_{S_2}\mathbf{N}^{\mathrm{T}}\left(h_r+h_c\right)T_\infty d\Gamma=\mathbf{0} \qquad (9.49)$$

(ii) Gas diffusion

$$\left(\int_{\Omega^e}\mathbf{N}^{\mathrm{T}}\frac{\rho_g}{P}\mathbf{N}d\Omega\right)\dot{\mathbf{P}}+\left(\int_{\Omega^e}\mathbf{N}_x^{\mathrm{T}}\frac{\gamma p_g}{\mu_g\phi}\mathbf{N}_x d\Omega+\int_{\Omega^e}\mathbf{N}_y^{\mathrm{T}}\frac{\gamma p_g}{\mu_g\phi}\mathbf{N}_y d\Omega\right)\mathbf{P}$$

$$\left(-\int_{\Omega^e}\mathbf{N}^{\mathrm{T}}\frac{\rho_g}{T_k}\mathbf{N}d\Omega\right)\dot{\mathbf{T}}+\int_{\Gamma^e}\mathbf{N}^{\mathrm{T}}\frac{\partial\rho_r}{\partial t}d\Gamma+\sum_{j=1}^{4}\int_{S_j}\mathbf{N}^{\mathrm{T}}\left(\dot{\mathbf{m}}_g.\mathbf{n}\right)d\Gamma=\mathbf{0} \qquad (9.50)$$

Since temperature and pore pressure interact, an independent solution for either temperature or pore pressure is impossible without simultaneous solution of the other, i.e. the temperature and pore pressure are inter-dependent variables and neither can be eliminated at the differential equation level. Equations 9.49 and 9.50 have therefore to be solved as a coupled formulation. These equations can be rearranged and combined into a coupled matrix equation as:

$$\begin{bmatrix}\mathbf{C}_{11} & \mathbf{0}\\ \mathbf{C}_{21} & \mathbf{C}_{22}\end{bmatrix}\frac{d}{dt}\begin{Bmatrix}\mathbf{T}\\ \mathbf{P}\end{Bmatrix}+\begin{bmatrix}\mathbf{K}_{11} & \mathbf{0}\\ \mathbf{0} & \mathbf{K}_{22}\end{bmatrix}\begin{Bmatrix}\mathbf{T}\\ \mathbf{P}\end{Bmatrix}+\begin{Bmatrix}\mathbf{f}_1\\ \mathbf{f}_2\end{Bmatrix}=\begin{Bmatrix}\mathbf{0}\\ \mathbf{0}\end{Bmatrix}$$

or

$$\mathbf{C}\dot{\mathbf{X}}+\mathbf{K}\mathbf{X}+\mathbf{f}=\mathbf{0} \qquad (9.51)$$

where

$\mathbf{C}_{11}$ = element capacitance matrix for the rate of change of internal energy

$\mathbf{C}_{21}$ = element capacitance matrix for the molar capacity of the pore system

$\mathbf{C}_{22}$ = element capacitance matrix for the thermal expansion of gas volume

$\mathbf{K}_{11}$ = element conductance matrix for heat conduction

$\mathbf{K}_{22}$ = element conductance matrix for gas mass diffusion and flow gradients

$\mathbf{f}_1$ = element heat load vector for pyrolysis and boundary conditions

$\mathbf{f}_2$ = element heat load vector for mass loss rate

$\mathbf{X}$ = vector of unknown variables

$\dot{\mathbf{X}}$ = vector of the derivatives of unknown variables with respect to time

Using the material properties for the element centre point given by Equations 9.28 to 9.30 and Tables 4.3 and 4.4, the element matrices and vectors are represented, in global co-ordinates, as:

$$\mathbf{C}_{11}=\int_{\Omega^e}\mathbf{N}^{\mathrm{T}}\left[\left(1-\phi_{\bar{j},\bar{k}}^{i+1}\right)\rho_{\bar{j},\bar{k}}^{i+1}\left(c_p\right)_{\bar{j},\bar{k}}^{i+1}+\phi_{\bar{j},\bar{k}}^{i+1}\left(\rho_g\right)_{\bar{j},\bar{k}}^{i+1}\left(c_{pg}\right)_{\bar{j},\bar{k}}^{i+1}\right]\mathbf{N}d\Omega \qquad (9.52a)$$

$$\mathbf{C}_{21}=-\int_{\Omega^e}\mathbf{N}^{\mathrm{T}}\frac{\left(\rho_g\right)_{\bar{j},\bar{k}}^{i+1}}{\left(T_k\right)_{\bar{j},\bar{k}}^{i}}\mathbf{N}d\Omega \qquad (9.52b)$$

$$\mathbf{C}_{22} = \int_{\Omega^e} \mathbf{N}^{\mathrm{T}} \frac{\left(\rho_g\right)_{\bar{j},\bar{k}}^{i+1}}{P_{\bar{j},\bar{k}}^{i}} \mathbf{N} d\Omega \tag{9.52c}$$

$$\mathbf{K}_{11} = \int_{\Omega^e} \mathbf{N}_{\mathrm{x}}^{\mathrm{T}} \left(\bar{k}_T\right)_{\bar{j},\bar{k}}^{i+1} \mathbf{N}_{\mathrm{x}} d\Omega + \int_{\Omega^e} \mathbf{N}_{\mathrm{y}}^{\mathrm{T}} \left(\bar{k}_L\right)_{\bar{j},\bar{k}}^{i+1} \mathbf{N}_{\mathrm{y}} d\Omega$$

$$- \left(c_{pg}\right)_{\bar{j},\bar{k}}^{i+1} \left[\int_{\Omega^e} \mathbf{N}_{\mathrm{x}}^{\mathrm{T}} \left(\dot{m}_{gx}\right)_{\bar{j},\bar{k}}^{i+1} \mathbf{N}_{\mathrm{x}} d\Omega + \int_{\Omega^e} \mathbf{N}_{\mathrm{y}}^{\mathrm{T}} \left(\dot{m}_{gy}\right)_{\bar{j},\bar{k}}^{i+1} \mathbf{N}_{\mathrm{y}} d\Omega \right]$$

$$+ \int_{\Omega^e} \mathbf{N}^{\mathrm{T}} \left(\frac{\partial \rho_r}{\partial t} \right)_{\bar{j},\bar{k}}^{i+1} \left(c_p - c_{pg}\right)_{\bar{j},\bar{k}}^{i+1} \mathbf{N} d\Omega + \int_{S_4} \mathbf{N}^{\mathrm{T}} \left(h_r + h_c\right) \mathbf{N} d\Gamma \tag{9.52d}$$

$$\mathbf{K}_{22} = \frac{\gamma_{\bar{j},\bar{k}}^{i+1} \left(\rho_g\right)_{\bar{j},\bar{k}}^{i+1}}{\left(\mu_g\right)_{\bar{j},\bar{k}}^{i+1} \phi_{\bar{j},\bar{k}}^{i+1}} \left(\int_{\Omega^e} \mathbf{N}_{\mathrm{x}}^{\mathrm{T}} \mathbf{N}_{\mathrm{x}} d\Omega + \int_{\Omega^e} \mathbf{N}_{\mathrm{y}}^{\mathrm{T}} \mathbf{N}_{\mathrm{y}} d\Omega \right) \tag{9.52e}$$

$$\mathbf{f}_1 = \int_{\Omega^e} \mathbf{N}^{\mathrm{T}} \left(\frac{\partial \rho_r}{\partial t} \right)_{\bar{j},\bar{k}}^{i+1} \left[Q - \left(c_p - c_{pg}\right)_{\bar{j},\bar{k}}^{i+1} T_\infty \right] d\Omega$$

$$+ \sum_{j=1}^{3} \int_{S_j} \mathbf{N}^{\mathrm{T}} \left(\mathbf{q}.\mathbf{n}\right) d\Gamma - \int_{S_4} \mathbf{N}^{\mathrm{T}} \left(h_r + h_c\right) T_\infty d\Gamma \tag{9.52f}$$

$$\mathbf{f}_2 = \int_{\Omega^e} \mathbf{N}^{\mathrm{T}} \left(\frac{\partial \rho_r}{\partial t} \right)_{\bar{j},\bar{k}}^{i+1} d\Omega + \sum_{j=1}^{4} \int_{S_j} \mathbf{N}^{\mathrm{T}} \left(\dot{\mathbf{m}}_{\mathrm{g}}.\mathbf{n}\right) d\Gamma \tag{9.52g}$$

The element matrices and vectors are evaluated numerically using Gauss-Legendre quadrature (Appendix C).

The numerical solution of the present problem requires solving the set of coupled differential equations of the form Equation 9.51.

9.3.3 Time Step Algorithm

A solution to the matrix equation of the form Equation 9.51 is given by [from: Zienkiewicz & Taylor, 1991 as corrected by Looyeh *et al.*, 1997; Zienkiewicz, Pers. Com., 1995]:

$$\mathbf{X}_{\mathbf{n+1}} = \left(\mathbf{C} + \Delta t \Theta \mathbf{K}\right)^{-1} \left\{ \left[\mathbf{C} - \Delta t (1 - \Theta) \mathbf{K}\right] \mathbf{X}_{\mathbf{n}} - \Delta t \, \bar{\mathbf{f}} \right\} \tag{9.53}$$

where Δt is the time step size (s), Θ is the weighting (time step) parameter, $\bar{\mathbf{f}}$ is the average value of $\mathbf{f}$ defined by Equation 2.36 and subscripts **n** and **n+1** represent known and unknown quantities.

The time step is based on the critical time step Δt_{cr} which depends on the weighting parameter Θ, the element length l and width h, density ρ, gas density ρ_g, porosity ϕ, through-the-thickness thermal conductivity k_T, longitudinal thermal conductivity k_L, specific heat c_p and gas specific heat c_{pg}. The critical time step needs to be found for the smallest element in the solution domain, i.e.:

$$\Delta t_{cr} = \frac{2}{1-2\Theta} \frac{\left[\text{Min} < l_m, h_m >\right]^2 \left[\left(1-\phi_{\bar{j},\bar{k}}^{i+1}\right)\left(\rho\right)_{\bar{j},\bar{k}}^{i+1} \left(c_p\right)_{\bar{j},\bar{k}}^{i+1} - \phi_{\bar{j},\bar{k}}^{i+1}\left(\rho_g\right)_{\bar{j},\bar{k}}^{i+1} \left(c_{pg}\right)_{\bar{j},\bar{k}}^{i+1}\right]}{3 \text{ Max} < \left(\bar{k}_T\right)_{\bar{j},\bar{k}}^{i+1}, \left(\bar{k}_L\right)_{\bar{j},\bar{k}}^{i+1} >} \tag{9.54}$$

where Δt_{cr} is the critical time step, l_m and h_m are the length and width of the smallest element within the finite element mesh and the operators Min< > and Max< > choose the minimum and maximum quantities, respectively.

The Crank-Nicolson solution, corresponding to Θ = 1/2, with a non-symmetric matrix solver [Applegarth, 1990] are used to solve matrix equation implicitly and compute the nodal temperatures and pressures after each iteration.

9.3.4 The Computer Code Algorithm

To perform the two-dimensional coupled finite element analysis for the transient heat and mass transfer in thick GRP step panels, additions are made to the structure of the finite element computer code developed in the last chapter (Figure 9.5). Only the sections of the main program which are relevant to the present work are shown. A new subroutine is also added to the computer code to create the element matrices and vectors for the gas diffusion equation. During an iteration, this subroutine is called by the main program before the similar subroutine which corresponds to the energy equation. The gas mass fluxes in through-the-thickness and longitudinal directions are then evaluated. The next step is the creation of the element matrices and vectors for the energy equation. This process is continued until the element matrices and vector are formed for all elements with respect to energy and gas diffusion equations. The element matrices and vectors are then assembled in final form as a coupled equation which is required for the simultaneous solution of both nodal temperatures and pore pressures.

Main Finite Element Program

1. initialize the system matrices, vectors and principle variables.
2. read finite element mesh data, thermal, kinetic and transport properties, boundary condition parameters and also control ID value to perform different two-dimensional solutions.
3. start time-dependent calculation and determine furnace temperature.
4. set the initial values and calculate additional specific heat, the proportion function of the moisture content and gas density, Eqs. 4.1 to 4.3, 4.6, 4.8 to 4.12 and 9.12.
5. determine the hot and cold surface boundary conditions, Eqs. 9.19 to 9.27.
6. specify the edges of the two-dimensional geometry with respect to Fig. 9.4.
7. calculate the temperature-dependent thermal properties, Eqs. 4.9 and 4.13 to 4.17.
8. calculate the effect of moisture content on thermal properties using additional specific heat obtained in step 4, Eqs. 4.10 and 4.11.
9. calculate the mass loss rate and instantaneous density for the control ID value of the required solution, Eqs. 9.30a and 9.30h.
10. determine instantaneous mass fraction, porosity and permeability, Eqs. 9.30b, 9.30c and 9.30j.
11. calculate gas density and solid/gas mixture thermal conductivities, Eqs. 9.30d, 9.30e and 9.30i and update pore pressure and temperature values.
12. create element matrices, $\mathbf{C}_{21}$, $\mathbf{C}_{22}$ and $\mathbf{K}_{22}$, and element force vector, $\mathbf{f}_2$, for gas diffusion equation, Eqs. 9.52b, 9.52c, 9.52e and 9.52g.
13. calculate gas mass fluxes, Eqs. 9.30f and 9.30g.
14. create element matrices, $\mathbf{C}_{11}$ and $\mathbf{K}_{11}$, and element force vector, $\mathbf{f}_1$, for energy equation, Eqs. 9.52a, 9.52d and 9.52f.
15. assemble the system matrices, $\mathbf{K}$ and $\mathbf{C}$, and force vector, $\mathbf{f}$.
16. calculate and update the time step using Eq. 9.54 or consider the chosen value for an implicit solution.
17. form coupled system equations according to Eq. 9.51.
18. apply hot surface and cold surface boundary conditions.
19. solve the matrix equation using Eq. 9.53 and find temperature and pore pressure distributions and mass loss and moisture loss profiles.
20. add the time step, determined in step 16, then go to step 4, otherwise stop.

Figure 9.5 Flow chart listing the steps for the main finite element computer code to perform two-dimensional coupled heat and mass transfer analysis for GRP step panels.

9.4 FIRE EXPERIMENTS

For comparison with the numerical results, a furnace fire experiment was requested from the research groups at the University of Manchester, School of Engineering and the University of Newcastle-upon-Tyne, Centre for Composite Materials Engineering.

To manufacture a thick GRP step panel (right rectangular prism), two pieces of GRP (Figure 9.6a), one a rectangular prism (step) and the other a rectangular laminate (wall) were initially made by woven roving glass fibres and polyester resin using the hand lay-up method. A rectangular hole was then cut in the centre of the wall in which the rectangular prism was fitted and glued using polyester resin (Figure 9.6b). 4 temperature sensors were implanted at the suitable points of the panel (Figure 9.7). The step panel was fitted into the door of a ceramic furnace (Figure 9.1), with active volume of 3.375m^3 and maximum fire temperature 1100°C, prior to fire experiment [Dodds & Gibson, Pers. Com., 1997]. The panel was then fire tested in the furnace involved with a simulated hydrocarbon fire [Spagni & Gibson, 1994; ISO 834, 1975; BS476, 1987]. For this panel the whole body undergoes the same heat flux from the furnace but due to different thicknesses the heat transfer is different.

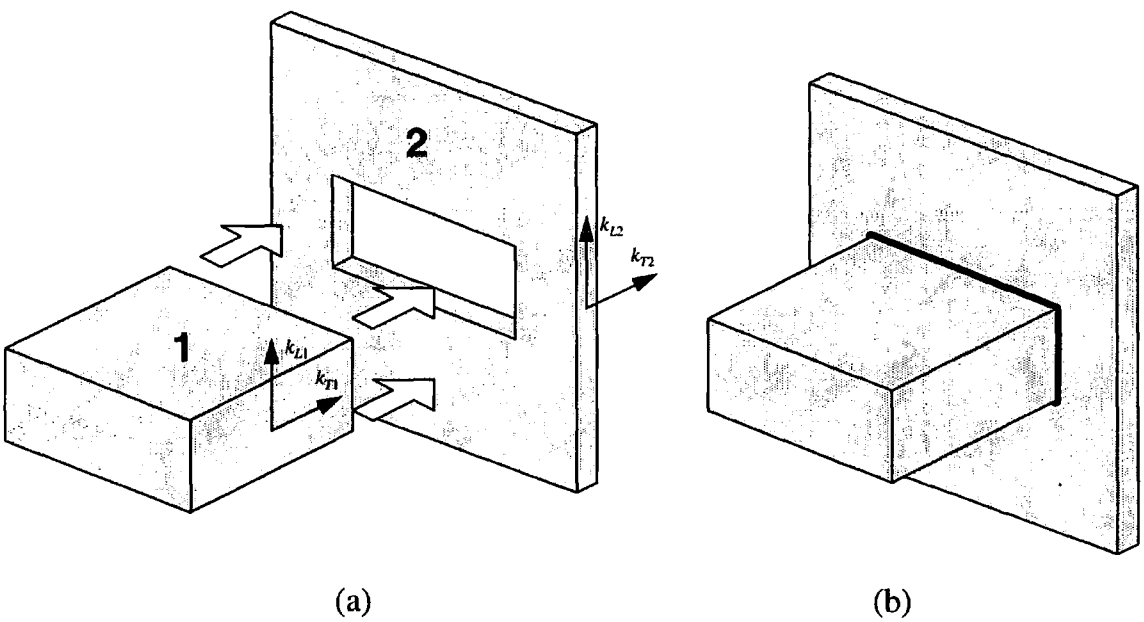

Figure 9.6 The procedure in which the thick GRP step panel is manufactured; (a) 1 and 2 are single-skinned GRP panels which are joined in the direction shown, k_{T1} and k_{T2} represent thermal conductivities in through-the-thickness direction and k_{L1} and k_{L2} those of the longitudinal direction; (b) GRP step panel.

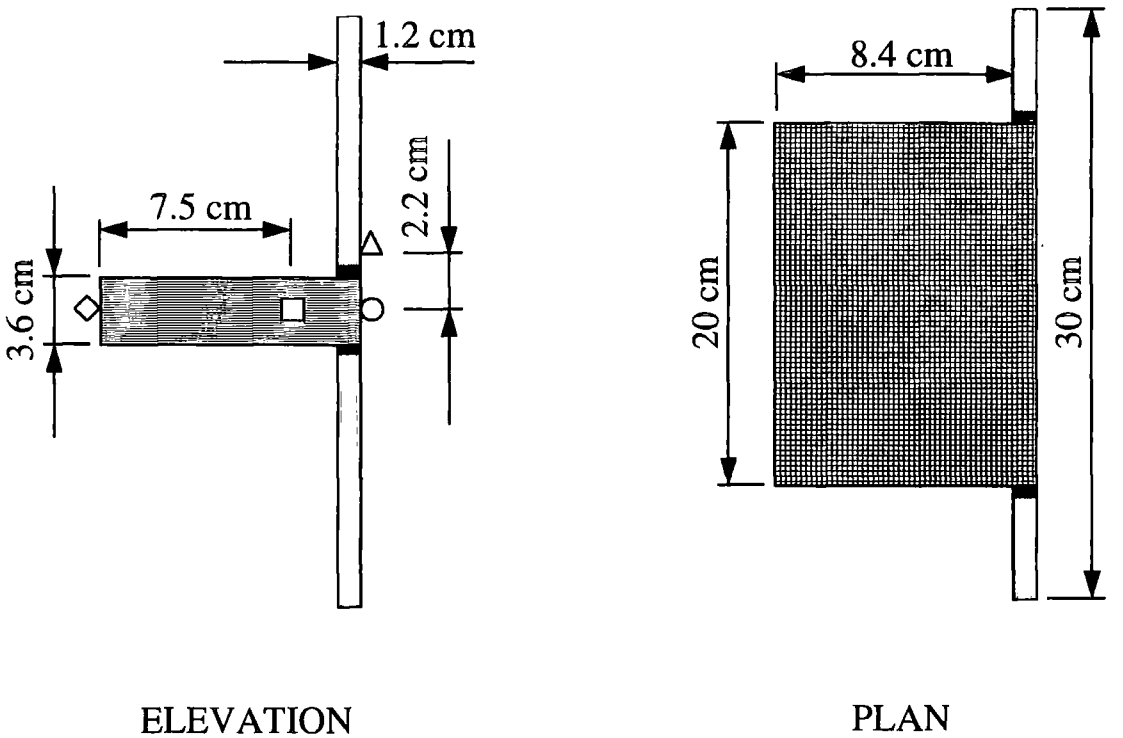

Figure 9.7 Elevation and plan sections of the GRP step panel used in the fire test. The panel is inset into the door of a ceramic furnace (Figure 9.1). The locations of the temperature sensors are shown as ◇□○△.

The experimental results from the thick GRP step panel are presented in the next section where they are compared with the numerical predictions obtained from the finite element method.

9.5 COMPARISON OF THE FINITE ELEMENT COMPUTATIONS WITH EXPERIMENTAL RESULTS AND DISCUSSION

The coupled finite element formulation developed here is used to compute the thermal response of GRP step panels with various thicknesses. A thick GRP step panel with maximum thickness 9.6cm and thickness to length ratio greater than 1/4 is used.

Table 4.3 lists material properties for polyester-based GRP. The properties of pyrolysis gases are given in Table 4.4.

The GRP material used for the step panel is the same as those for single-skinned panels (Chapter 5-Model 3). The initial density and specific heat of the GRP are 1832.4 kgm^{-3} and 1056.84 $Jkg^{-1}K^{-1}$. The thermal conductivities of GRP step panel in through-the-thickness and longitudinal directions are 0.322$Wm^{-1}K^{-1}$ and 0.614$Wm^{-1}K^{-1}$. The variations of these properties with temperature and moisture gradients were discussed in Chapters 4 and 5.

Pyrolysis constant, activation energy and heat of decomposition for GRP are 7525 s^{-1}, 611.5 $MJkmole^{-1}$ and 2.3446 $MJkg^{-1}$, respectively.

To find suitable mesh pattern and optimised number of elements, the same procedure is used as in the last chapter (Figures 9.8a to 9.8d). All meshes contain 4-node quadrilateral elements but they differ in number of nodes and elements. Apart from the first mesh with uniformly coarse elements, the rest are non-uniform with finer elements around the corners in particular near the middle corner.

Figures 9.9a to 9.9d show the isotherms for the corresponding meshes after 4 minutes of fire exposure. It is seen that the contour plot for (d) is superior to the others as it displays smoother isotherms around the middle corner, but (c) with fewer elements takes less time and might be considered satisfactory.

Figures 9.10a to 9.10c display the isotherms after 4, 10 and 16 minutes of fire exposure for mesh (d). These figures may be compared with Figures 8.9a to 8.9c. If contours of heat flow (perpendicular to the isotherms) are drawn for both cases, substantial variations can be pictured for the thick step panel. For the thin step panel these variations are much smaller. This is partly due to the step side of the thick panel exposed to fire being affected by the contributions from gas mass flux and the accumulation of the pyrolysis gases, i.e. more uniform temperature distribution is obtained by employing the two-dimensional gas mass diffusion in the mathematical model. It is seen that the mathematical model for thick step panels formulates the heat flow phenomena more accurately.

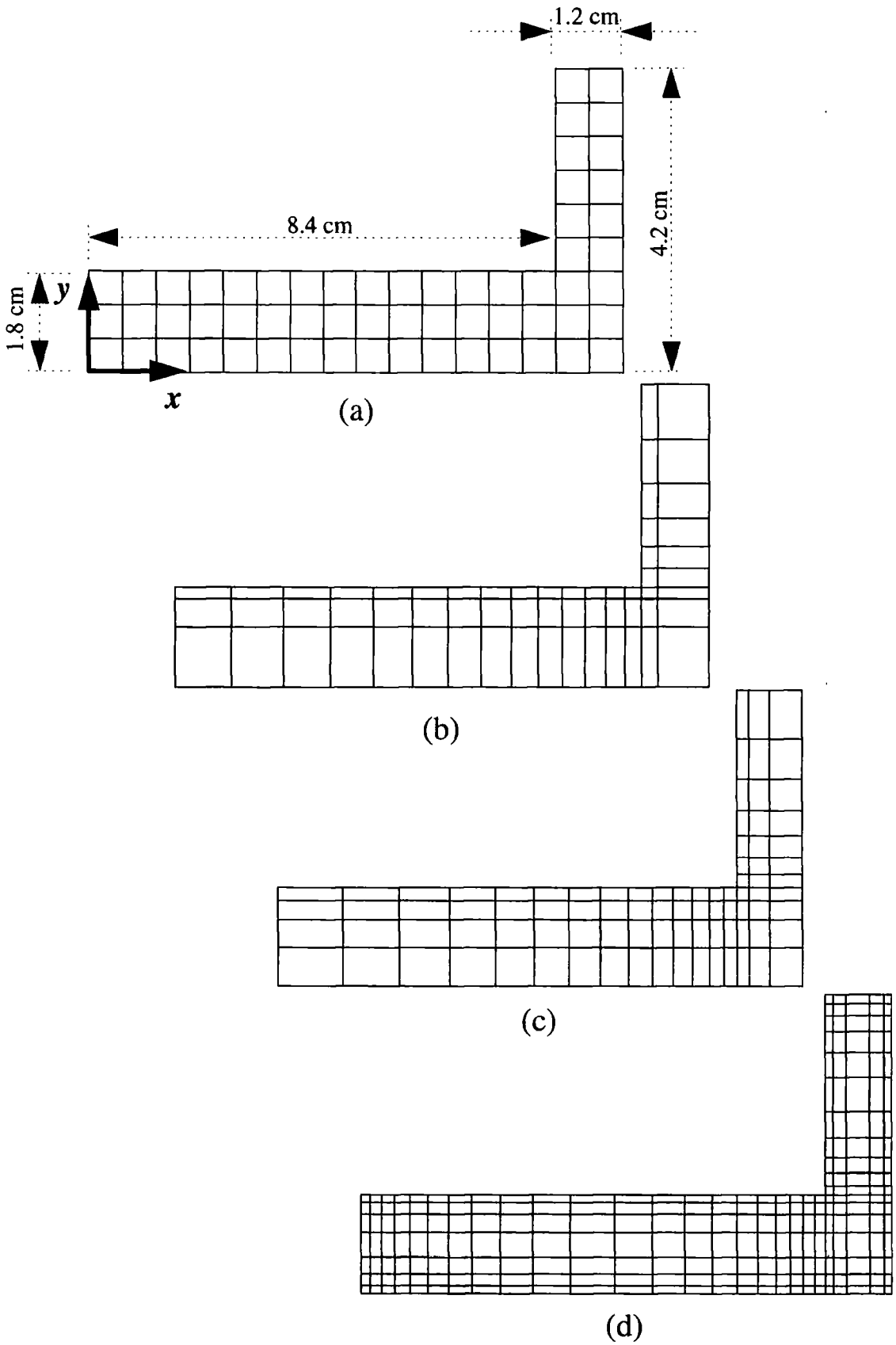

Figure 9.8 Various two-dimensional finite element meshes for thick GRP step panel; (a) uniformly coarse mesh with 86 nodes and 60 elements; (b) non-uniformly coarse mesh with 86 nodes and 60 elements; (c) non-uniformly medium mesh with 118 nodes and 89 elements; (d) non-uniformly fine mesh with 282 nodes and 237 elements.

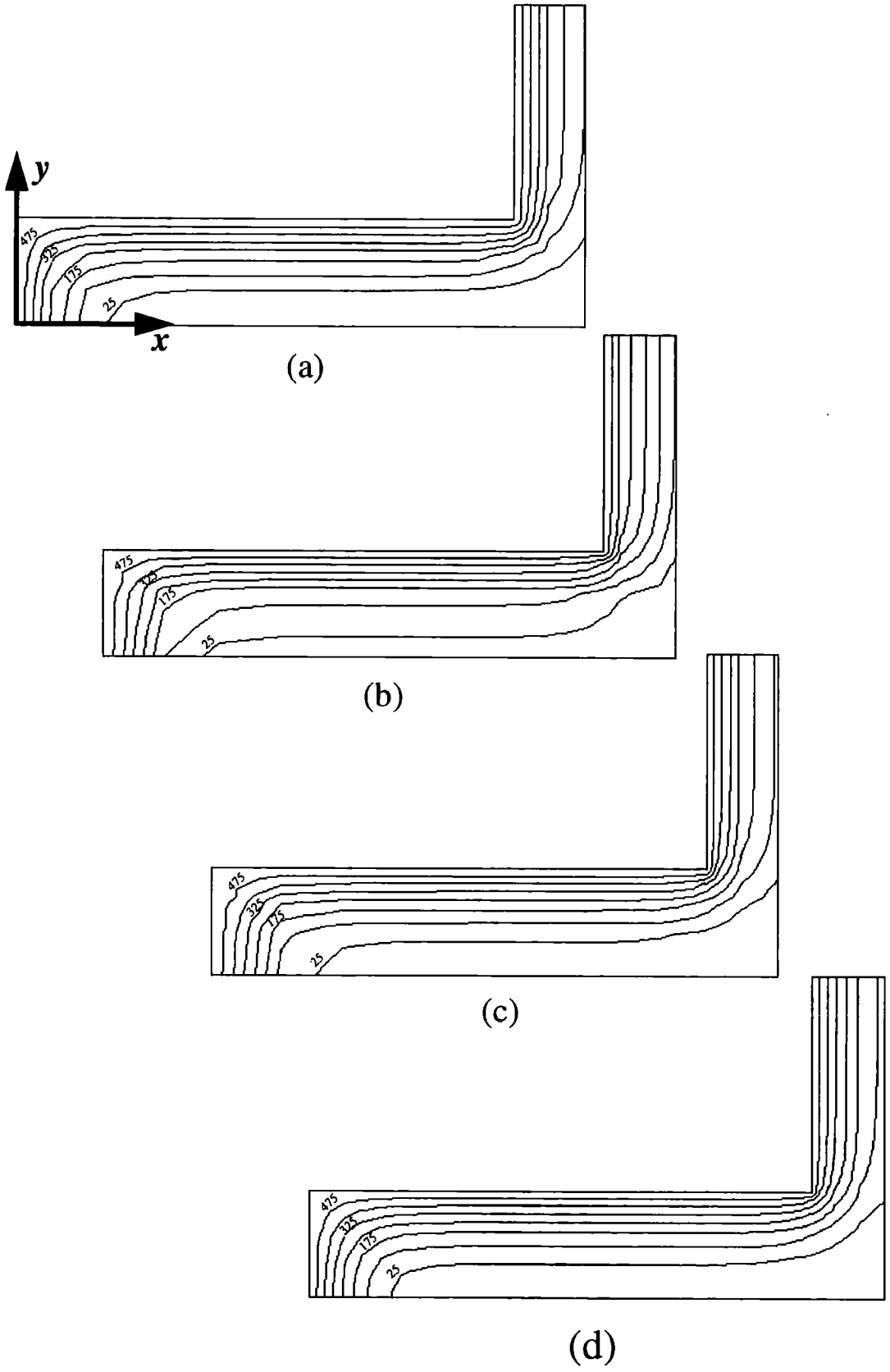

Figure 9.9 Temperature contour plots after 4 minutes of fire exposure for various finite element meshes; (a) uniformly coarse mesh with 86 nodes and 60 elements; (b) non-uniformly coarse mesh with 86 nodes and 60 elements; (c) non-uniformly medium mesh with 118 nodes and 89 elements; (d) non-uniformly fine mesh with 282 nodes and 237 elements.

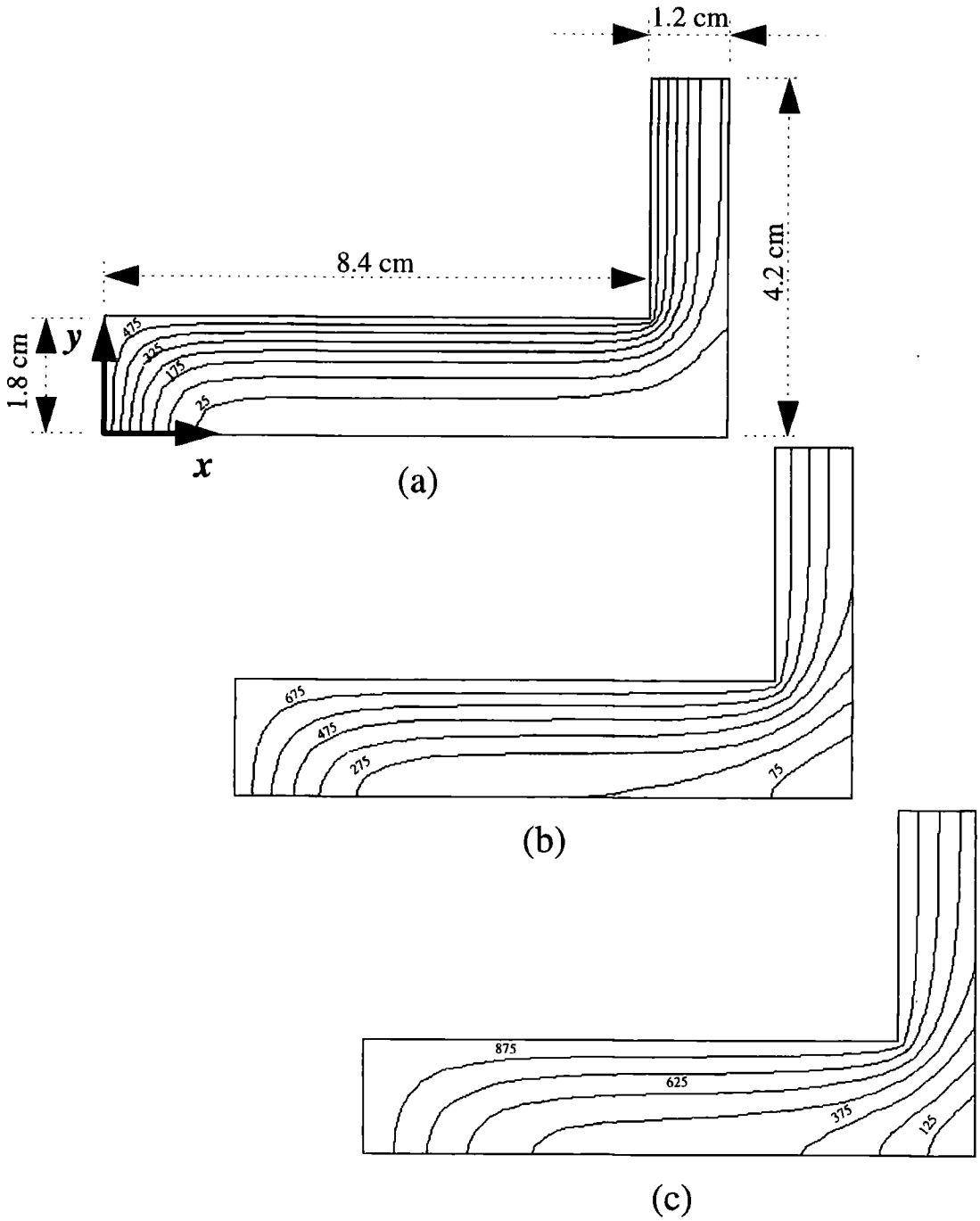

Figure 9.10 Temperature contour plots after (a) 4 (b) 10 and (c) 16 minutes of fire exposure. The finite element mesh contains 282 nodes and 237 non-uniform elements (Figure 9.8d).

In Figure 9.11, temperatures obtained by the finite element method are compared with some experimental data. It is seen that there is good agreement for the inter-laminar sensor □ except temperatures for the numerical model are up to 5°C higher than the experimental between 5 and 9 minutes. The variation of pore pressure, gas mass movement, thermal conductivity, the decomposition of material and endothermicity are the major terms which dominate the variation of temperature in the material. In the previous chapters, we discussed the effect of each term but the pore pressure. It is likely that the slight disagreement (between 5 and 9 minutes) is due to less accuracy in the permeability which is approximated by a temporary model. Important to note is that any slight change in permeability may cause considerable changes in pore pressure and temperature. The errors in the through-the-thickness and longitudinal thermal conductivities are unlikely to be a major source for the disagreement as it occurs only for part of fire exposure (between 5 and 9 minutes).

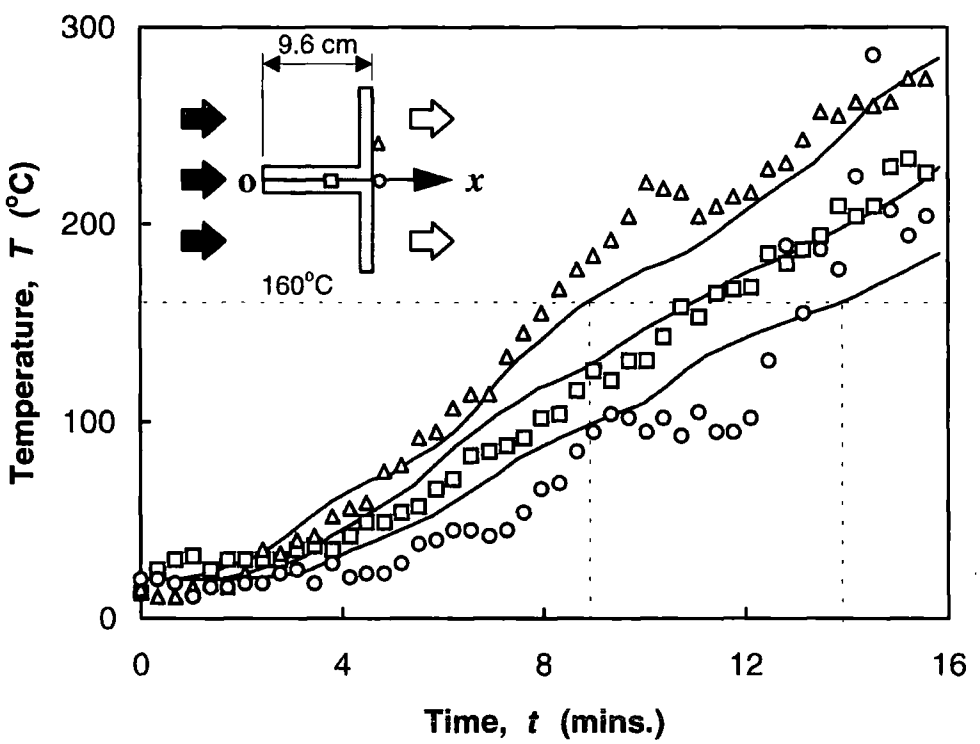

Figure 9.11 Comparisons of computed and experimental temperatures. The solid lines represent computed temperatures and □, ○ and △ indicate experimental results at the temperature sensors implanted into the material (Figure 9.7). The numerical results agree with the experimental but there are inconsistencies for the sensors on the external wall.

The two sensors on the external wall showed somewhat erratic behaviour especially for $t>4$ minutes (Figure 9.11) making it difficult to compare the finite element computations with experiment. It is seen that the experimental temperatures for sensor O are mostly lower than those computed by the finite element method and those for sensor Δ are mostly higher. For $x<10$ minutes the experimental temperatures for the two sensors are inconsistent with each other and for $x>10$ minutes it appears both were affected by external influences especially cooling at about 11 minutes (e.g. someone opened door and there was a blast of cold air!). Ignoring the erratic behaviour of these sensors, a possible reason for under-prediction at O and over-prediction at Δ might be the errors in the through-the-thickness and longitudinal thermal conductivities. These sensors are located in two different regions (Figure 9.6a), sensor O in region 1 (step) and sensor Δ in region 2 (wall). The step panel is basically non-homogeneous and anisotropic (Figure 9.7) for which $k_{T1} = k_{L2} = 0.614$ $Wm^{-1}K^{-1}$ and $k_{L1} = k_{T2} = 0.322$ $Wm^{-1}K^{-1}$ (Figure 9.6a). For simplicity, we assumed that the step panel is homogeneous and orthotropic where $k_{T1} = k_{T2} = 0.614$ $Wm^{-1}K^{-1}$ and $k_{L1} = k_{L2} = 0.322$ $Wm^{-1}K^{-1}$. It is very likely that this choice of thermal conductivities have had the greatest effect.

For the external wall the finite element model predicts fire resistance (time to reach 160°C) to be around 9 minutes at sensor Δ and 13 minutes at sensor O with 44.4% difference. The insulation failures can also be found from Figures 9.10a to 9.10c.

Figure 9.12 illustrates the variation of temperature with distance along the x axis for various times. It is seen that the temperature profiles appear to be very steep for $0<x<2$cm of the step. This is primarily due to the low thermal conductivity of the GRP. In fact, the same effect was seen for the one-dimensional models.

Figure 9.13 shows the variations in pore pressure with distance along the x axis of the right rectangular prism (centre line) at various times. As can be seen the peak pressure advances further into the material moving away from the fire-exposed surface as fire exposure time increases. Since the accumulation of gaseous products occurs at the pyrolysis zone, it is expected that for a given time the peak pressure occurs at the same zone, i.e. peak pressure is related to the propagation of the char (hence peak pressure increases steadily as fire exposure time increases). According to Figure 9.13, the pore pressure arrives at a maximum of approximately 27 MPa after 16 minutes. It is thought that these high pressures are primarily due to low porosity and permeability in the region of the decomposition.

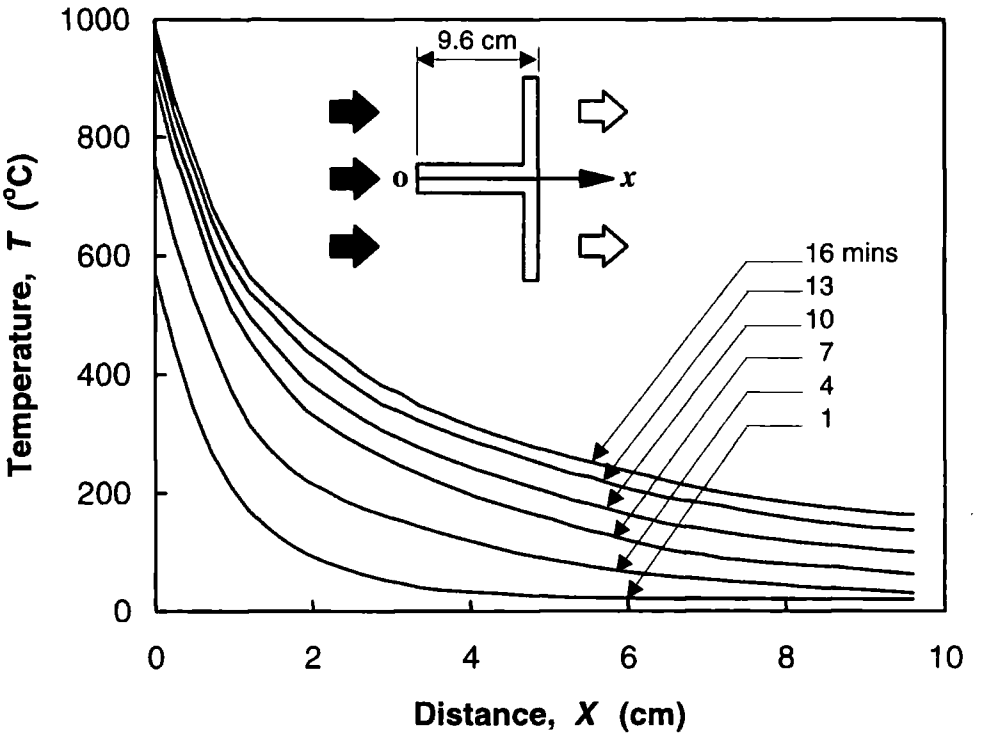

Figure 9.12 Temperature as a function of distance along the x axis for various times (minutes). The results are computed at 27 points along the line of symmetry (Figure 9.8d).

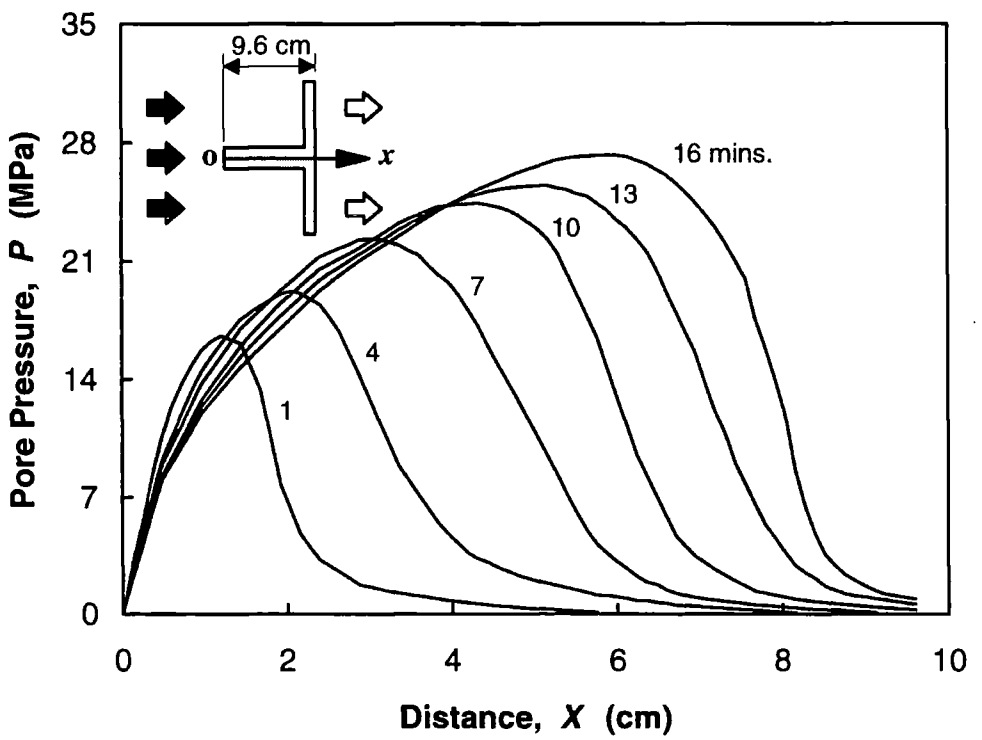

Figure 9.13 Pore-pressure as a function of distance along the x axis for various times (minutes). The maximum pressure occurs along the line of symmetry moving from the fire-exposed surface towards the external wall.

In Figures 9.14 and 9.15, the porosity and permeability of the material are plotted versus distance along the x axis at various times using Equations 9.6 and 9.17. It is seen that porosity increases faster than permeability. At the early stage of pyrolysis, the porosity increases slightly as the virgin material breaks down into char and gaseous products. At this stage the pore pressure increases rapidly due to the high rate of generation of pyrolysis gases and less volume available for storage.

At 4 minutes of fire exposure the peak pressure occurs at about 2cm away from the hot surface (Figure 9.13) where the porosity is about 0.17 with 13% increase (Figure 9.14) and there is no change in permeability (Figure 9.15).

At 16 minutes of fire exposure the pore pressure is at maximum 6cm from the fire-exposed surface (Figure 9.13). At the same time (16 minutes) there has been less increase in porosity (Figure 9.14) where half of the material has experienced no rise in permeability (Figure 9.15).

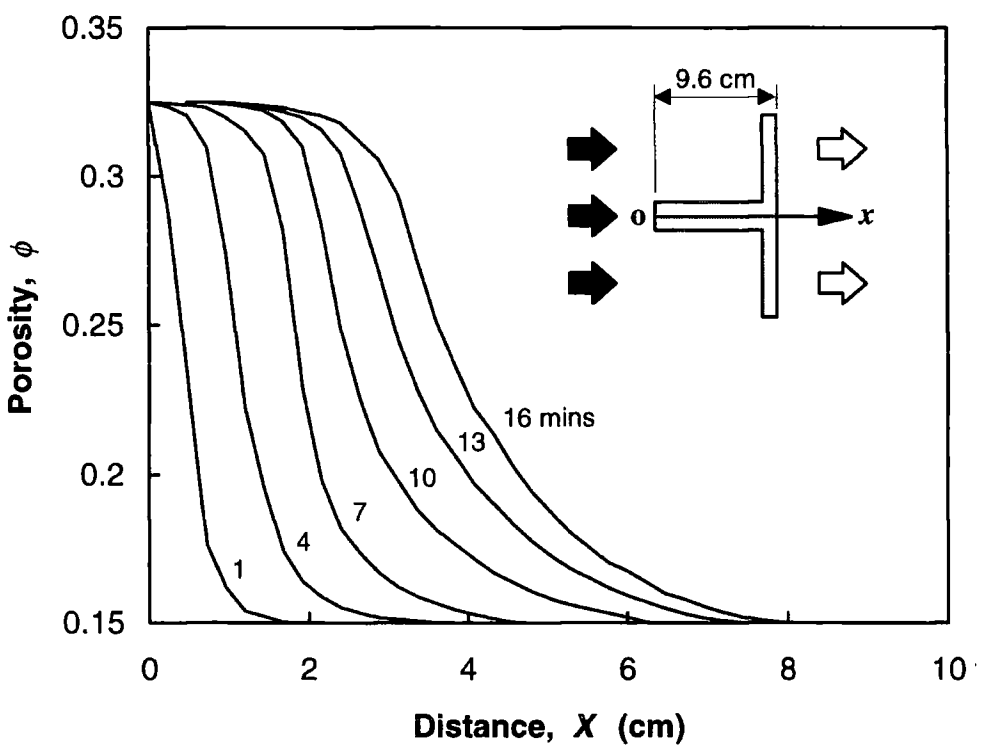

Figure 9.14 Porosity as a function of distance along the x axis for various times (minutes).

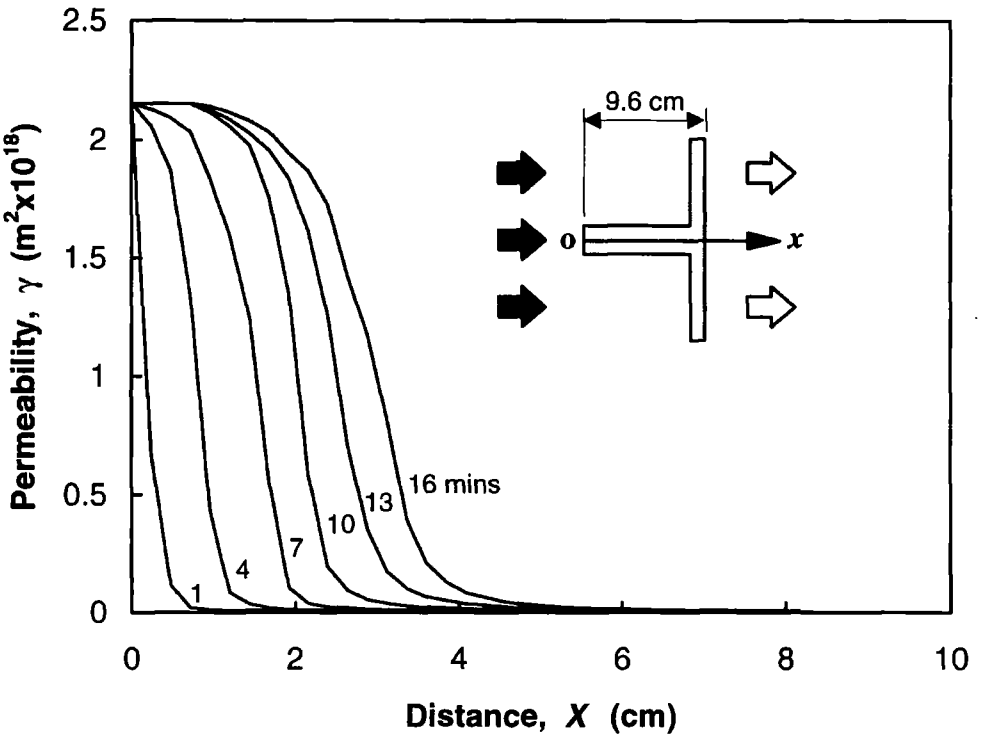

Figure 9.15 Permeability as a function of distance along the x axis for various times (minutes).

Figure 9.16 shows the mass loss profiles for various times. Comparison with Figure 9.12 reveals that the pyrolysis reactions are initiated at $T \geq 200^{\circ}C$ and reach completion for $T \leq 700^{\circ}C$. Figure 9.16 also shows that the completion of pyrolysis occurs at $\rho_r / \rho_{ro} = 0.02$ or $\rho / \rho_o \cong 0.66$. It is evident that for $t > 1$ minutes pyrolysis reaches completion at the hot surface of the step panel (as expected). At 16 minutes, the pyrolysis zone has not reached 8cm (1.6cm from the back of the panel). Comparison of Figures 9.13 and 9.16 shows the peak pore pressure at a given time occurs just after the onset of pyrolysis. The peak pore pressure occurs at this early stage of decomposition because less material has burnt out and the porosity of the solid remains quite small with less available volume for the storage of the generated gases. It is also evident that the pore pressure remains high in the solid in the region close to the cold surface prior to the onset of pyrolysis. This is due to: (i) the gas pressure in the pores of the solid increases with temperature, and (ii) a small amount of the generated gases advances into the solid.

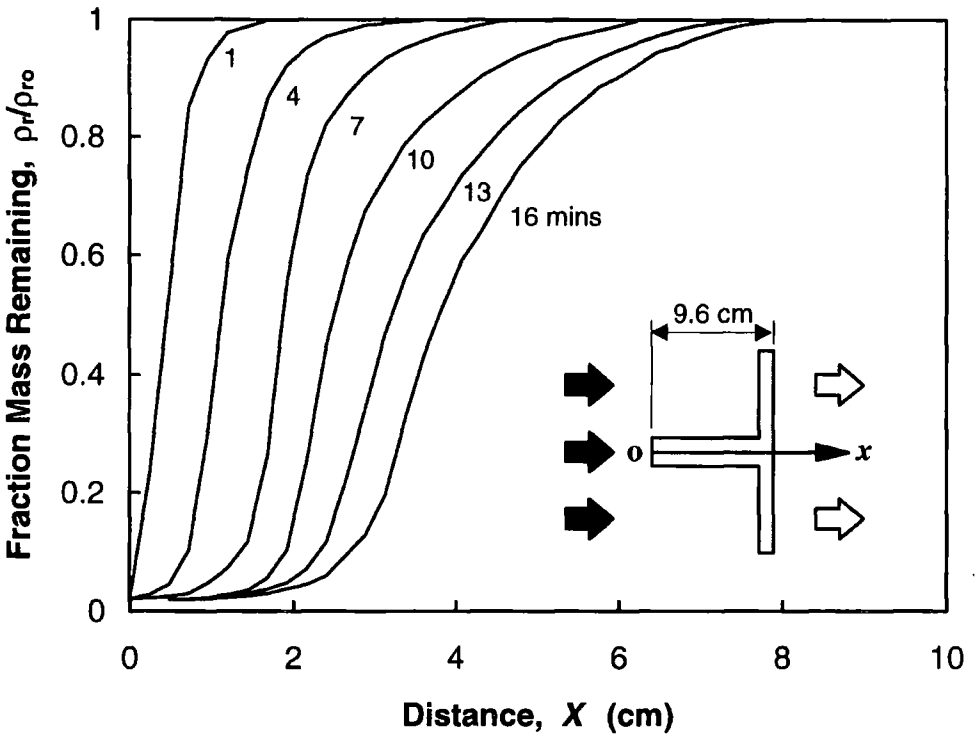

Figure 9.16 Mass fraction of the resin material as a function of distance along the x axis (see inset) for various times (minutes). It can be seen that after 16 minutes of fire exposure there is still a layer of 1.8cm of the material along the line of symmetry which has been left intact.

9.6 SUMMARY

This chapter involved the application of the finite element method to the analysis of heat and mass transfer in thick GRP joins subject to hydrocarbon fire. A two-dimensional mathematical model and an appropriate finite element formulation were developed and used to assess the fire resistance of a thick GRP step panel (right rectangular prism) with maximum and minimum thicknesses 9.6 and 1.2cm. The GRP step panel was made of two woven roving glass fibre/polyester laminates where polyester resin was used as adhesive and the bonding was assumed perfect. The numerical model introduced a coupled finite element method for the simultaneous solution of temperatures and pore pressures. The mathematical model includes: (i) the conservation of energy equation; (ii) two-dimensional gas mass diffusion; (iii) the kinetic rate Arrhenius equation; (iv) the continuity equation; (v) Darcy's equation and (vi) the ideal gas equation. A first-order

exponential formula was used for permeability. The numerical temperatures obtained from the two-dimensional model were compared with the experimental results.

The numerical model revealed that the fire resistance of thick step panels can vary substantially from one point to another, e.g. for a 9.6cm polyester-based GRP step panel, there is a difference of 4 minutes (44.4%) between two points 2.2cm apart along the wall, i.e. points Δ and O (Figure 9.7a). The numerical model predicts insulation failure around 9 minutes. This model also gives more accurate isotherms than the previous two-dimensional model.

Comparison of the computed temperatures with some experimental results showed: (i) For the inter-laminar sensor, the numerical and experimental results agreed within a few degrees. (ii) For the sensors mounted on the external wall, it is difficult to make any comparisons particularly for t>4 minutes.

In the two-dimensional analysis of the GRP step panel, the variation of temperature is dominated by the variation of pore pressure, gas mass movement, the variation of thermal conductivity, the decomposition of material and endothermicity. It was found that the variation of the thermal conductivities and permeability are the main sources of disagreements between computations and experiments.

The model accounts for the variation of pore pressure and two-dimensional gas mass diffusion which are thought to play significant roles in the physical and chemical processes in the material. This is confirmed as the decompositional behaviour of the material can be more clearly observed and explained. It is possible to employ this model, in conjunction with force-displacement data, to predict the failure of GRP due to internal pressure. Unfortunately, the pore pressure could not be verified due to the lack of experimental data. Accurate measurement of pore pressure is difficult and needs high technology. This highlights one of the most significant obstacles in this area and merits further investigation.

CHAPTER X

CONCLUSIONS AND RECOMMENDATIONS FOR FUTURE WORK

Since the Piper Alpha disaster in 1988, there has been an increasing demand in the offshore industry for suitable materials to replace steel and aluminium. A survey of the literature revealed that glass reinforced plastics (GRP) are useful alternatives where low weight and low cost are desirable but their applications to the marine environment, especially fire hazards, need further investigation. High temperatures experienced in fires result in loss of strength and stability and subsequent structural failure. It is therefore important to determine the fire performance of GRP components in order to re-assess and improve technical and safety specifications especially as GRP displays complex thermochemical decomposition (pyrolysis). Analytical solutions are only available for very simple cases, making it essential to use numerical techniques for problems of practical interest. A comprehensive numerical technique is required and the finite element technique was selected as being superior.

The research presented here covered four principal subjects:

1. The development of mathematical models for the analysis of heat transfer in decomposing polymer composites affected by fire.
2. The development of numerical solutions for these models using the finite element technique and designing appropriate computer codes.
3. Application of the computer codes to some simple cases.
4. Comparison of the computed outputs with experimental results where available.

One- and two-dimensional mathematical and numerical models have been developed with associated computer codes to predict the fire performance of GRP in the form of panels, pipes and joints (step panels). The research concentrated on the physical and chemical processes of importance in the material exposed to hydrocarbon fires under various configurations and environmental conditions.

10.1 MATHEMATICAL MODELS

Single-skinned GRP panels

A one-dimensional mathematical model was developed in 4 stages to include: (i) transient heat conduction, (ii) gas mass movement and internal heat convection of the decomposition gases, (iii) mass loss and Arrhenius rate decomposition of the resin material into gases and residual char and (iv) endothermicity of the decomposition process. The first stage (Model 1) addresses an infinite vertical panel with finite thickness L exposed to fire on one side. The resin material is assumed to burn away completely at the end of pyrolysis. The hot surface boundary condition is simulated by an empirical formula and the cold surface is assumed to be insulated. The thermal properties are assumed constant throughout fire exposure except for thermal conductivity which is assumed to have a step change at the end of pyrolysis. The second stage (Model 2) adds: (i) heat energy (radiation and convection) exchange with the environment at the cold surface and (ii) different inclinations of the panel, i.e. vertical, horizontal and inclined. The third stage (Model 3) assumes a vertical panel and adds: (i) variable thermal properties, and (ii) 2 to 3% of the resin, remaining at the end of pyrolysis, into the kinetic rate equation. Finally, the fourth stage (Model 4) extends Model 3 by applying a theoretical formulation for simulating the boundary condition at the hot surface. This includes heat fluxes due to: (i) radiation, (ii) convection, (iii) outward movement of pyrolysis gases and (iv) surface chemical reactions. Model 4 is considered to be the most complete model.

Twin-skinned GRP sandwich panels

A one-dimensional mathematical model was developed to include: (i) thermochemical decomposition in GRP skins (as explained for the single-skinned GRP panels), (ii) transient heat conduction in the sandwich material, and (iii) the effect of thermal contact resistance at the GRP/SM/GRP interfaces due to imperfect bonding.

Single-skinned GRP pipes

An axi-symmetric mathematical model was developed for thin-walled, large diameter GRP pipes carrying high velocity fluids. The model is based on that for the single-skinned GRP panels and includes: (i) transient heat conduction, (ii) radial gas mass

movement, (iii) mass loss and Arrhenius rate decomposition of the resin material, and (iv) endothermicity of the decomposition process.

Thin GRP step panels (thickness to length ratio smaller than 1/10)

A two-dimensional mathematical model was developed to include: (i) non-uniform heat flow in the plane of the GRP, (ii) two-dimensional transient heat conduction, (iii) thermochemical decomposition of the material, and (iv) one-dimensional gas mass diffusion. The model extends that for the single-skinned GRP panels and assumes perfect bonding at the interfaces.

Thick GRP step panels (thickness to length ratio greater than 1/10)

A two-dimensional mathematical model was developed to include: (i) the conservation of energy equation in two dimensions, (ii) two-dimensional gas mass diffusion and internal pressurisation of the material, (iii) mass loss and the kinetic rate Arrhenius equation, (iv) the continuity equation, (v) Darcy's equation, and (vi) the ideal gas equation. The model is developed for homogeneous and orthotropic step panels and assumes perfect bonding at the interfaces. A first-order exponential formula is used for permeability.

10.2 FINITE ELEMENT MODELS AND COMPUTER CODES

Single-skinned GRP panels

A one-dimensional finite element model (associated with a computer code) was developed using the weighted residual approach. Two node linear elements are used. All terms and coefficients are evaluated explicitly using an iterative-updating procedure and nodal temperatures implicitly using a Crank-Nicolson solution. For Models 1 and 2 constant time steps and for Models 3 and 4 variable time steps are used. The finite difference time stepping algorithm is used for the iterative computations. Gauss-Legendre quadrature with two points is used for numerical integration and a non-symmetric profile matrix solver for the system equation. An efficient coding system is applied to enable various analyses for heat transfer.

Twin-skinned GRP sandwich panels

Additions were made to the finite element model of the single skinned GRP panels to include: (i) the analysis of multi-layered panels with different material properties, and (ii) the effect of imperfection at the interfaces. Two methods are used to include the effect of imperfect bonding: (i) explicit method in which the unknown temperature at each interface is found by forward difference, and (ii) implicit method in which a linear finite element is used for modelling each interface.

Single-skinned GRP pipes

The finite element model of the single-skinned GRP panels was modified to account for Polar co-ordinates. Forced convection at the pipe internal surface is applied to the model.

Thin GRP step panels

This extended the finite element model of the single-skinned GRP panels to two dimensions. For the inclusion of boundary conditions an element edging method is used plus four node quadrilateral elements and variable time step. Gauss-Legendre quadrature with two points in each direction is used for numerical integration.

Thick GRP step panels

A coupled two-dimensional finite element model (associated with a computer code) was developed using the weighted residual approach. Two finite element formulations are developed for the energy equation and gas diffusion equation. Since temperature and pore pressure interact, an independent solution for either temperature or pore pressure is impossible without simultaneous solution of the other and therefore a coupled formulation is introduced and incorporated into the computer code. Four node quadrilateral elements and variable time steps are used. All terms and coefficients are evaluated explicitly using an iterative-updating procedure and nodal temperatures and pressures are evaluated implicitly using a Crank-Nicolson solution. Gauss-Legendre quadrature with two points in each direction is used for numerical integration and a non-symmetric profile matrix solver for system equation.

10.3 MAIN RESULTS OF FINITE ELEMENT NUMERICAL ANALYSES

Results of the finite element numerical analyses are plotted in the form of temperature versus time for various spatial locations in GRP panels, pipes and joins. These can be chosen to facilitate comparison with any available experimental data (next section). Desirable outputs are temperature profiles for the front hot and back cold surface plus intermediary positions to enable a full study of the behaviour of the material and design up to 20 minutes of fire exposure for single-skinned GRP panels and pipes and GRP step panels and up to 180 minutes for GRP/SM/GRP sandwich panels.

The results are also presented in the form of temperature versus distance from the fire-exposed surface for various times after onset of the fire. Instantaneous resin mass, resin mass rate, pore pressure, and moisture content can be presented as sets of time or distance curves in assessing pyrolysis and fire resistance.

Single-skinned GRP panels

A single-skinned GRP panel made of woven roving glass fibres and polyester resin with thickness 1.09cm was studied. The numerical results are presented in Figures 5.12 to 5.28 and discussed in detail in Section 5.5. The main results are given in Table 10.1.

Table 10.1 Main results for 1.09cm polyester-based GRP panel.

Model 1	Fire resistance time (no decomposition)	2.9 mins.
	Fire resistance time (gas mass term included)	4 mins.
	Fire resistance time (mass loss included)	4.9 mins.
	Fire resistance time (full decomposition)	7.9 mins.
	Completion of pyrolysis at hot surface	2 mins.
	Full pyrolysis	15 mins.
Model 2	Fire resistance time (full decomposition)	7.7 mins.
	Overall temperature difference with Model 1	5.1°C
	Contribution from radiation and convection at cold surface	6.8%
Model 3	Fire resistance time (full decomposition)	7.6 mins.
	Overall temperature difference with Model 1	8.2°C
	Contribution from variable thermal properties	14.3%
Model 4	Fire resistance time (full decomposition)	7.6 mins.
	Ave. diff. (empirical and theoretical hot surface temp.)	3.2%

The results of Model 1 show that the decomposition of the material, endothermicity of pyrolysis with movement of pyrolysis gases make substantial contributions towards the cooling behaviour and delaying the fire resistance of the material. The results of Model 2 reveal that for a given set of dimensions and boundary conditions, a horizontal panel heated from below will fail quicker than other panels, i.e. panels used as ceilings than for floors quicker than walls. In Model 3, the inclusion of the variable thermal properties changes the results substantially. The results of Model 4 reveal that for $T \leq 200^{\circ}C$ convection plays a major role; for $200 < T \leq 600^{\circ}C$ the effect of gas mass flux reduces convection where radiation has just begun; for $600 < T \leq 900^{\circ}C$ the heat exchange is mainly driven by radiation and for $T > 900^{\circ}C$ surface chemical reactions begin to occur. Due to the hot surface chemical reactions in which the residual glass fibres react with residual carbon and are eventually consumed, the behaviour of very thin laminates (<0.5cm) can not be modelled in the same procedure. The erosive effect of furnace environment may also influence this process.

Twin-skinned GRP sandwich panels

Three Sandwich panels with thicknesses 6.2, 7.2, 5.92cm composed of polyester-based GRP skins and Vermiculux sandwich materials were studied. The numerical results are presented in Figures 6.9 to 6.19 and Tables 6.2 and 6.3 and discussed in detail in Section 6.5. The main results are given in Table 10.2.

Table 10.2 Computed fire resistance results of perfect and imperfect bonding for Panel 1(0.6/5/0.6cm), Panel 2 (0.6/6/0.6cm) and Panel 3 (0.96/4/0.96cm).

	Panel 1	Panel 2	Panel 3
Fire resistance time (perfect bonding)	74 mins.	113 mins	145 mins.
Fire resistance time (imperfect bonding)	83 mins.	129 mins	172 mins.
Difference (w.r.t. perfect bonding)	+12.2%	+14.2%	+18.6%

The results reveal that sandwich panels consisting of GRP/SM/GRP offer good thermal insulation. To achieve 120 minutes of fire resistance an optimised combination of GRP/Sandwich/GRP, consists of GRP skins with low thermal conductivity

(<0.5 $Wm^{-1}K^{-1}$) and thicknesses between 0.8 to 1.2cm and sandwich material with high moisture (>10%) and thicknesses between 3.5 to 4.5cm, is required. Passive thermal protection requires sandwich panels with less conductance and more resistance across the interfaces. The thermal contact resistance at an imperfect bonding was found to be important. Two methods are introduced to model the temperature gradients across the interfaces. Both were found efficient to within few percent difference. The explicit method is recommended because of simplicity. It was shown that less conductance can be achieved by less contact area and rougher contact surfaces but it may result in poorer mechanical performance. It is therefore essential to arrive to an optimal design to satisfy both thermal and mechanical requirements.

Single-skinned GRP pipes

Two pipes with thickness 1.09cm, one with natural gas and diameter 60.96cm and the other with sea water and diameter 30.48cm were studied. The numerical results are presented in Figures 7.7 to 7.11 and discussed in detail in Section 7.6. The results reveal that for a given set of dimensions and boundary conditions, GRP pipes reach insulation failure earlier than GRP panels. The additional term in the governing equation of a GRP pipe, i.e. $-(k/r)(\partial T/\partial r)$, is considered as the likely reason for this behaviour. The effect of forced convection heat exchange is found to be less compared to that of the additional term even if high velocity fluid flow (e.g. natural gas with 14ms^{-1}) is involved. The present results can be used to assess the feasibility of using GRP for offshore pipes and pipelines where severe fire conditions may occur.

Thin GRP step panels

A step panel with length 30cm and maximum and minimum thicknesses 1.26 and 5.4cm was studied. Four finite element meshes are introduced to verify the convergence of the finite element model with respect to mesh type, number of elements and time step size. A non-uniform mesh of 37 elements with finer elements at the step region and 1 second initial time step is found suitable for the numerical computations. The numerical results are presented in Figures 8.7 to 8.15 and Tables 8.1 and 8.2 and discussed in detail in Section 8.5. The main results are given in Table 10.3.

Table 10.3 One and two-dimensional numerical results for a thin GRP step panel with maximum thickness 1.26cm.

Fire resistance time (two-dimensional)	10.4 mins.
Fire resistance time (one-dimensional)	11.9 mins.
Difference (with respect to two-dimensional)	+14.4%
Computation time for fire resistance (two-dimensional)	2.06 mins.
Computation time for fire resistance (one-dimensional)	0.36 mins.
Difference (with respect to two-dimensional)	-82.5%

The model is found to be sensitive to the specification of the corners particularly at the step region where oscillation of isotherms are seen for coarse meshes. Table 10.3 shows that one- and two-dimensional model agree by less than 15%. For thinner step panels this difference reduces considerably and therefore, a one-dimensional model should be adequate for the thermal response of thin GRP step panels.

Thick GRP step panels

A step panel with length 30cm and maximum and minimum thicknesses 9.6 and 1.2cm was studied. An investigation into the effect of the type and size of mesh reveal a requirement for very fine meshes in order to enable accurate evaluation of the steep variation of pore pressure. A non-uniform mesh of 282 elements with finer elements at the step region is found suitable with little oscillation in the isotherms. The numerical results are presented in Figures 9.8 to 9.16 and discussed in detail in Section 9.5. The main results are given in Table 10.4.

Table 10.4 Two-dimensional numerical results for a thick GRP step panel with maximum thickness 9.6cm.

Fire resistance time (shown by O in Figure 9.7)	13 mins.
Fire resistance time (shown by Δ in Figure 9.7)	9 mins.
Maximum pore pressure (at 16 mins.)	27 MPa
Amount of pyrolysis (at 16 mins.)	83.3%
Increase in porosity (at 6cm and 16 mins)	13%

The temperature distribution in the thick step panel is dominated by the variation of thermal conductivity, the variation of pore pressure, gas mass flux, the decomposition of the material and endothermicity. It was shown that the result may change substantially with a slight change in the permeability. The major source of uncertainty was the lack of sufficient information to model permeability and porosity of the material.

10.4 COMPARISON OF NUMERICAL AND EXPERIMENTAL RESULTS

Single-skinned GRP panels

For Model 1, good agreement is found between computed and experimental cold surface temperatures with 5.6% difference between the fire resistance values. A sudden change of thermal conductivity from 0.322 $Wm^{-1}K^{-1}$ to 1.09 $Wm^{-1}K^{-1}$ due to completion of pyrolysis is found to be the main source of disagreement particularly for high exposure times. By applying free convection and radiation boundary conditions to the cold surface boundary of a vertical panel, the agreement between computed and experimental fire resistance is improved by 37.5% (compared to Model 1). For Model 3, The computed temperatures show better overall agreement with experiments by 12.6% over Model 1 and the difference between the fire resistance values is reduced to 2.5%. The disagreement at high temperatures (T>600°C) is found to be mainly due to the assumption of constant thermal properties where the variation of thermal conductivity has a major effect, i.e. at 600°C, a thermal conductivity increase of 53.4% and specific heat increase of 11.7%. Thermal properties also change with moisture, e.g. with 1.8% moisture in polyester-based GRP the specific heat increases by more than 100% from 90 to 120°C. For Model 4, The computed hot surface temperatures agree with the experimental by a few percent.

The main factors causing disagreements between computed and experimental temperatures are: (i) the delamination at the regions close to the hot surface which causes some sensors to separate from the surface; (ii) ignoring the expansion of the material during decomposition; (iii) assuming local thermal equilibrium; (iv) ignoring the accumulation of pyrolysis gases and internal pressurisation of the material and (v) assuming some of the material properties such as pyrolysis constant, activation energy and gas specific heat.

Twin-skinned GRP sandwich panels

The numerical results agree reasonably well with the experimental data. For Panel 3, i.e. 0.96/4/0.96cm, the numerical model predicts fire resistance by less than 8.9% difference compared to the experiment. By the inclusion of the thermal contact resistance due to imperfect bonding into the formulation, the agreement between the computed temperatures and experimental results is improved by 12% compared to a perfect bonding.

Thin GRP step panels

The numerical results agree well with experimental at the cold surface by less than a few degrees. There is poor agreement for the inter-laminar sensor. This is thought to be mainly due to the occurrence of the delamination in the experiments.

Thick GRP step panels

The temperature results are satisfactory and agree with experimental at the inter-laminar sensor to within few degrees. Sensors on the external wall showed erratic behaviour making it difficult to do a detail comparison. It is likely that these were affected by an external source of disturbance. Ignoring the erratic behaviour of these sensors, a possible reason for the overall differences between the computed and experimental temperatures are thought to be mainly due to the errors in estimates of the through-the-thickness and longitudinal thermal conductivities.

10.5 CONCLUSIONS

1. Numerical modelling of the fire performance of GRP has two major benefits: (i) it facilitates and reduces the cost of the design process and (ii) it improves our knowledge of how these materials behave when exposed to fire.
2. The inclusion of a theoretical boundary condition at the hot surface into the mathematical model (Chapter 5-Model 4) was found to be a complex phenomenon involving heat and mass transfer and it is a success compared to the empirical formula [Wu *et al.*, 1994] given only for furnace conditions. The model can now be used for any environmental conditions.

3. The inclusion of the non-linear decomposition terms and a variety of non-linear mixed boundary conditions into the finite element model (Chapter 5) revealed interesting results for polyester-based GRP (below) and provide a base for further investigation for other composites. The incorporation of the variable time step gave more efficient computation with less cost.

   Polyester-based GRP is found to be surprisingly reliable for fire hazard areas despite its combustibility. It exhibits complex thermal behaviour when heated to high temperatures (1100°C). Its good fire resistance (7.6 minutes for a 1.09cm thick panel) is mainly due to its low thermal conductivity, i.e. 0.322 $Wm^{-1}K^{-1}$, decomposition of the material, endothermicity of pyrolysis and the movement of pyrolysis gases where the last two act as coolants and perform a key role in delaying the burn-through. For polyester-based GRP, pyrolysis is completed when the material reaches 600 to 700°C. At this stage about 98% of polyester or 36% of the GRP has burned away. Although a part of the volume reduction is countered by the expansion of the material due to high temperatures and internal pressurisation, the assumption of constant volume throughout fire exposure can be a significant source of error in the fire performance computations. Surface chemical reactions occur when the temperature reaches $T \geq 900$°C. At this stage, the residual glass fibres react with residual carbon and are eventually consumed. As a result, the solid mass decreases by more than 80% of its original value with a corresponding severe contraction. The porosity increases significantly with a corresponding rise in permeability. One of the observations from the fire tests is the delamination of polyester-based GRP laminates near the hot surface. Delamination caused some sensors to disconnect in some experiments and hence give unreliable measurements. It may also increase the risk of weakness in the structural integrity and premature failure. Nevertheless, it is beneficial as it acts as a thermal shield against fire. The thermal response of polyester-based GRP is affected by the amount of moisture in the polyester. Moisture may reduce the mechanical strength and increase risk of corrosion. Some properties such as thermal conductivity increase with increasing moisture content. During fire, a considerable part of the heat is used to drive off the moisture with correspondingly less heat energy available to move through the material. For a given set of dimensions and boundary conditions a horizontal panel heated from below fails quicker than at other

orientations. Since most of offshore fires occur in compartments, thicker panels must be used for ceiling than for walls and floors.

4. The finite element method is particularly useful for studying the thermal contact resistance in GRP sandwich panels and for simultaneous solution of pore pressure and temperature in thick step panels. The computer code can be easily used to study the influence of each term or parameter on heat and mass transfer. It enables the study of various materials and configurations and aids production of optimal designs.
5. The idea that imperfect bonding in sandwich panels has negligible effect on the thermal integrity is proven to be wrong. Thermal contact resistance due to bonding imperfections in the mathematical model of GRP/Vermiculux/GRP reveals a minimum 12% improvement in the fire performance predictions (Chapter 6). The term was successfully included in the finite element model using the explicit forward difference method and implicit finite element method. It can be used widely for further investigations into other materials. The Thermal contact resistance is found to be beneficial for delaying the fire resistance but it may result in poorer mechanical performance. This might also encourage the use of double-laminating (with air gap) in the design of sandwich panels for the offshore industry.
6. The axi-symmetric modelling of thin-walled, large diameter (≥10cm) GRP pipes, including thermochemical decomposition and the complex phenomenon of forced convection, revealed that for a given set of dimensions and boundary conditions, the polyester-based GRP pipe reaches insulation failure earlier than the GRP panel. It was suggested that the additional term in the governing equation of a GRP pipe, i.e. $-(k/r)(\partial T/\partial r)$, may be likely reason for this behaviour. The effect of forced convection heat exchange was found to be less compared to that of the additional term even if high velocity fluid flow is present. It is evident that for pipes with stagnant water or low velocity flow and for small diameter pipes (<10cm) the fire resistance will decrease considerably.
7. Thin and thick GRP step panels were found to behave differently (Chapters 8 and 9). One- and two-dimensional modelling of a thin GRP step panel undergoing thermochemical decomposition were carried out (Chapter 8) and showed that a one-dimensional prediction is adequate where less than 15% error is allowable and involves more than 82% time saving.

8. The two-dimensional mathematical model developed for heat and mass transfer in thick GRP panels (Chapter 9) is the most complete model of its type so far. Introducing a coupled finite element formulation and incorporating it into the computer code is considered as the most interesting part of this thesis. The model revealed that the fire resistance of thick panels can vary substantially from one point to another, e.g. for a 9.6cm polyester-based GRP step panel (Section 10.3), there is a difference of 4 minutes (44.4%) between two points 2.2cm apart along the wall. It is therefore concluded that unlike thin step panels, thick step panels must be modelled two-dimensionally to achieve reasonable predictions. The coupled model may be used in a wide range of materials and it is capable of giving simultaneous solutions for temperature, pore pressure, mass loss rate and gas mass flux. Using this model, it is possible to increase our knowledge in the structural integrity of offshore components more rapidly.
9. It is evident from the numerical results that small time steps and small elements are required for convergence with no oscillation if steep pressure or temperature gradients are to be computed. Such selections require more iterations and elements which increase the time and cost of computations. Variable time steps and optimised number of elements were used for all finite element models in this work. The models allow for a non-uniform mesh with a maximum 500 elements.

10.6 RECOMMENDATIONS FOR FUTURE WORK

Development of mathematical models

1. Three major obstacles in the modelling of the thermal response of polymer composites are: (i) the complexity of the radiative heat exchange between fire and the exposed surface, (ii) the lack of sufficient information on material properties at the elevated temperatures, and (iii) finding an efficient method to configurate the large number of terms and parameters required to model pyrolysis numerically. These merit further work.
2. The models presented do not incorporate: (i) the expansion of the material due to high temperatures, (ii) the internal pressurisation caused by the accumulation of the pyrolysis gases within the pore network, and (ii) the contraction of the material due

to the consumption of the resin material during pyrolysis. Future work requires the development of models which include terms containing the rate of expansion and contraction for varying temperature and pore pressure. Facilities to include the accurate variation of permeability and porosity are also required.

3. A first-order kinetic rate Arrhenius equation suitable for mass loss-temperature data for polyester resin, from thermo gravimetric analysis (TGA), may not be good for other materials. For some polymers such as phenolic, there may be two or more stages of decomposition. In these cases the TGA data are grouped into two or more stages. Kinetic properties are then obtained by fitting an Arrhenius type equation to each group. A continuation of this work should include a multi-stage decomposition facility.
4. The assumption of local-thermal equilibrium between virgin material and pyrolysis gases may be a source of error in the predicted temperatures, pore pressures and mass losses and cause some errors in the analysis of the thermomechanical behaviour of the material at high temperatures. A model which avoids this assumption is required.
5. The methods introduced to obtain the hot surface temperature, used the Norwegian Petroleum Directorate (NPD) hydrocarbon fire curve which dose not represent conditions for a real fire. High gas velocity, high level of oxygen consumption and thermal shocks are encountered in real fires and also need to be taken into account.
6. The prescribed time-dependent temperature formula, used as the fire-exposed surface boundary condition, does not represent the actual characteristics of the thermal loading. This formula is empirical and depends on the furnace design. It is therefore important to quantify the rate of heat irradiated from fire and the proportion received at the surface such that fires can be modelled by different heating rates. The accuracy of a model can also be verified by using different heating rates where the kinetic properties are independent of heating rate.
7. Surface chemical reactions are complicated and have not been investigated in detail. Further work is required on surface chemical reactions at temperatures >1000°C, e.g. carbon-silica reactions. The erosive effect of hydrocarbon fires which may considerably alter the reactions needs investigating. The corresponding reaction products are dependent on temperature, pore pressure, heating rate and the

concentration of the reactants. The evaluation of the thermal and kinetic properties may require design and implementation of advanced experiments.

8. The formation of the pyrolysis reaction zone progressing from the front/hot to the back/cold surface and interacting with the charring and virgin layers at two boundaries needs detailed investigation involving the progression of the moving charred boundary.
9. The conduction-convection formulation used to model the effect of imperfect bonding on heat transfer across contact surfaces may be further improved by adding the effect of radiation heat transfer particularly at very high temperatures.
10. The models presented in this work enable analysis of composites with homogenous and orthotropic behaviour with respect to thermal as well as mechanical properties. The development of the models for any composite behaviour requires non-homogenous and anisotropic facilities.
11. It is known that heat transfer can be deformed by magnetic or electrical fields. It is interesting to know if such property can be used to delay the burn-through during fire.
12. To determine the effect of fire on the overall performance of an offshore structure, the temperature distribution must be evaluated. This can then be used in designs for passive fire protection and evacuation systems. This includes modelling the spread of fire and requires knowledge of the thermal response of the individual elements. Other parameters such as interaction between elements might be involved and requires study.
13. Linearisation of radiative heat transfer, which results in introducing an equivalent convective coefficient, is valid only for simple cases and may cause some errors in practical problems.
14. Further investigations are required for offshore pipes to study: (i) small diameter, thick-walled empty GRP pipes or those containing stagnant water, (ii) vertical and inclined pipes with various types of fluids, (iii) the use of GRP as insulation rather than structural material (e.g. steel pipes with GRP coating), and (iv) the effect of radiative heat exchange between internal surface of the pipe and stagnant or flowing fluid.
15. The effect of thickness on the thermal response of single-skinned GRP panels has not been studied and needs investigation.

16. It is interesting to know how unique the GRP are compared to other materials such as steel, which heats up rapidly with no pyrolysis, or timber, which decomposes differently from GRP.

Development of numerical models

1. Little attempt has been made in the use of numerical methods other than finite element technique. For comparison purposes, it is interesting to perform numerical modelling using finite difference, boundary element or finite volume methods.
2. The finite element computer codes are confined to one- and two-dimensional problems for specific GRP configurations, environmental conditions and limited meshes (<500 elements). More work is required to make the computer codes more versatile and accessible for other users. Although, many practical problems in the offshore industry may be addressed by two-dimensional modelling, there is considerable potential for the application of three-dimensional simulations of complex structures. Large three-dimensional finite element models might be beyond the capability of direct solution methods and more innovative methods need to be found. These require new mathematical models with efficient computer codes.
3. To meet the demand in the offshore industry, a specialised numerical tool needs to be developed to perform thermomechanical analyses.
4. Linearisation of the non-linear terms and coefficients and evaluating them by explicit forward difference method may be a disadvantage in the finite element models. It is possible to evaluate all or some of the main terms such as instantaneous mass, mass loss rate, permeability and gas mass flux coupled with temperature and pressure by developing implicit solutions.
5. The numerical models are sensitive to the variations of some terms such as thermal conductivity and permeability. Studies are needed to reveal to what extend they may affect the final results and the convergence of the finite element solutions (known as sensitivity analysis).
6. The application of the present numerical tools are restricted to the thermal analysis of GRP for offshore use. Extra terms are needed to extend the use to other materials. Some examples are: (i) fabrication processing of polymer composites which are mostly exothermic so that in the model the endothermic heat of

decomposition term can be replaced by an exothermic term, (ii) concrete or natural composites such as timber, for which water vapour has an important role in the internal pressurisation, require an extra term in the gas mass diffusion equation, (iii) carbon-carbon composites for which different stages of decomposition are required, and (iv) metal matrix and ceramic matrix composites which do not undergo thermochemical decomposition and therefore the decomposition term should be removed.

Development of fire experiments

1. A set of furnace and hydrocarbon fire tests at various heating rates are required for currently used polymer composites with various configurations. For such experiments more implanted temperature sensors with high sensitivity are required.
2. Pore pressure and its effect on gas mass diffusion requires experimental data for comparison with numerical results.
3. Thermomechanical response of polymer composites subject to hydrocarbon fires is an important issue in evaluating the structural integrity and should be investigated in detail. This requires extensive experiments utilising mechanical loading at elevated temperatures.
4. Accurate prediction of the thermal response of polymer composites is highly dependent on the accurate knowledge of thermo physical properties and their variations with temperature, pore pressure and moisture. For GRP, the different molecular structure of the resin constituent before, during and after processing may affect these properties considerably. It is therefore important to obtain more information on polymer properties. For example, surface emissivity, permeability, porosity and surface chemistry are not currently available for polyester-based GRP.

BIBLIOGRAPHY

Agarwal, B. D.; Broutman, L. J. (1990): *Analysis and Performance of Fibre Composites.* 2nd ed., John Wiley & Sons, New York.

Anderson, D. A.; Tannehill, J. C.; Pletcher, R. H. (1984): *Computational Fluid Mechanics and Heat Transfer.* Hemisphere, Washington DC.

API RP 2A-LRFD (1993): Recommended Practice for Planning, Designing and Constructing Fixed Offshore Platforms. 1st ed., American Petroleum Institute.

Applegarth, I. (1990): A Non-Symmetric Profile Matrix Solver Using the Active Column Method. University of Newcastle-upon-Tyne, Newcastle-upon-Tyne, UK.

Bamford, C. H.; Crank, J.; Malan, D. H. (1946): The Combustion of Wood: Part I. *Cambridge Phil. Soc. Proc.*, **42**, 166-182.

Bejan, A. (1993): *Heat Transfer.* 1st ed., John Wiley & Sons, New York.

Bergland, J.; Willners, L. (1988): A Concept Study of a Deckhouse Made in FRP-Sandwich for Offshore Platforms. GVA Project 747-008, CTH, Goteborg, Sweden (in Swedish).

Bettess, P.; Bettess, J. A. (1986): A Finite Element Program for Stress Analysis. University of Newcastle-upon-Tyne, Newcastle-upon-Tyne, UK.

Boothby, P.; Vu, D. (1995): Personal Communication.

Bradley, H. B. (1992): *Petroleum Engineering Handbook.* 3rd ed., Society of petroleum Engineers, Richardson, TX.

Brennan, W. P.; Miller, B.; Whitwell, J. C. (1969): An Improved Method of Analyzing Curves in Differential Scanning Calorimetry. I&EC Fundamentals, **8**, 314-318.

BS476 (1987): Fire Tests on Building Materials and Structures: Part 7 - Method for Classification of the Surface Spread of Flame of Products; Part 20 - Method for Determination of the Fire Resistance of Elements of Construction (General Principles); Part 21 - Method for Determination of the Fire Resistance of Loadbearing Elements of Construction; Part 22 - Methods for Determination of the Fire Resistance of Non-Loadbearing Elements of Construction. British Standards Institution, London.

Churchill, S. W.; Chu, H. H. S. (1975): Correlating Equations for Laminar and Turbulent Free Convection from a Vertical Plate. *Int. J. Heat Mass Transfer*, **18**, 1323-1329.

Churchill, S. W.; Ozoe, H. (1973): Correlation for Laminar Forced Convection with Uniform Heating in Flow Over a Plate and in Developing and Fully Developed Flow in a Tube. *J. Heat Transfer*, **95**, 78-84.

Ciraldi, S.; Alkire, J. D.; Huntoon, G. (1991): Fibre Glass Fire Water System for Offshore Platforms. Paper OTC 6926, Proceedings of 23rd Annual *Offshore Technology Conference*, Houston, TX, 477-484.

Clausing, A. M. (1966): Heat Transfer at the Interface of Dissimilar Metals-The Influence of Thermal Strain. *Int. J. Heat Mass Transfer*, **9**, 791-801.

Clifton, J. V.; Chapman, A. J. (1969): Natural Convection on a Finite-Size Horizontal Plate. Int. J. Heat Mass Transfer, **12**, 1573.

Collatz, L. (1966): *The Numerical Treatment of Differential Equations*. 3rd ed., Springer-Verlag, Berlin, Germany.

Cullen, W. D. (1990): The Public Inquiry into the Piper Alpha Disaster. HMSO, London.

Datoo, M. H. (1991): *Mechanics of Fibrous Composites*. Elsevier Applied Science, New York.

Davies, J. M.; Dewhurst, D.; Wang, H-B. (1998): The Performance of Wet and Dry GRE Pipes under Hydrocarbon Fire Conditions. Proceedings of the 7th International Conference on *Fibre Reinforced Composites*, University of Newcastle-upon-Tyne, Newcastle-upon-Tyne, UK, 366-376.

Davies, J. M.; McNicholas, J. B.; Hakmi, R.; Wang, H-B. (1994a): Fire Resistant Sandwich Panels for Offshore Structures. Report CP205, Marinetech North West Programme on *Cost-Effective Use of Fibre Reinforced Composites Offshore*, Phase II, Marinetech Research, Manchester, UK.

Davies, J. M.; McNicholas, J. B.; Hakmi, R.; Wang, H-B. (1994b): Composites Pipework with Improved Fire Resistance. Report CP222, Marinetech North West Programme on *Cost-Effective Use of Glass Reinforce Composites Offshore*, Marinetech Research, Manchester, UK.

Davies, J. M.; Wang, H-B. (1998): Glass Reinforced Laminates Subject to Hydrocarbon Fire Tests. Proceedings of the 7th International Conference on *Fibre Reinforced Composites*, University of Newcastle-upon-Tyne, Newcastle-upon-Tyne, UK, 377-385.

Dodds, N.; Gibson, A. G. (1997): Personal Communication.

Dodds, N.; Incecik, A.; Gibson, A. G. (1998): Modelling the Response of Composite Materials to Severe Fires. Proceedings of the 7th International Conference on *Fibre Reinforced Composites*, University of Newcastle-upon-Tyne, Newcastle-upon-Tyne, UK, 357-365.

Drysdale, D. (1985): *An Introduction to Fire Dynamics*. John Wiley & Sons, Chichester, UK.

Finlayson, B. A.; Scriven, L. E. (1966): The Method of Weighted Residuals-A Review. *Appl. Mech. Rev.*, **19** (9), 735-748.

Fletcher, L. S. (1988): Recent Development in Contact Conductance Heat Transfer. *J. Heat Transfer*, **110**, 1059-1070.

Florio, J.; Henderson, J. B.; Test, F. L.; Ramamurthy, H. (1991): A Study of the Effect of the Assumption of Local-Thermal Equilibrium on the Overall Thermally-Induced Response of a Decomposing, Glass-Filled Polymer Composite. *Int. J. Heat Mass Transfer* **34** (1), 135-147.

Fourier, J. B. J. (1822): *Theorie Analytique De La Chaleur*. Didot, Paris.

Fredlund, B (1988): A Model for Heat and Mass Transfer in Timber Structures During Fire-A Theoretical, Numerical and Experimental Study. Report LUTVDG/(TVBB-1003), Lund University, Lund, Sweden.

Fredlund, B. (1993): Modelling of Heat and Mass Transfer in Wood Structures During Fire. *Fire safety J.*, **20**, 39-69.

Friedman, H. L. (1965): Kinetics of Thermal Degradation of Char-Forming Plastics from Thermogravimetry, Application to a Phenolic Plastic. *J. Polymer Sci.*, **6**, 183-195.

Fujii, T.; Imura, H. (1972): Natural Convection Heat Transfer from a Plate with Arbitrary Inclination. *Int. J. Heat Mass Transfer*, **15**, p. 755.

Gibson, A. G. (1997): Composites in Hydrocarbon Fires. Proceedings of Annual Conference on *Materials and Design Against Fire*, IMechE, London.

Gibson, A. G. (1993): Composites in Offshore Structures. Chap. 11. *Composite Materials in Maritime Structures-Practical Considerations*. Eds: Shenoi, R. N.; Wellicome, J. F., 1st ed., Vol. 2, Cambridge University Press, Cambridge.

Gibson, A. G.; Davies, J. M.; Dodds, N.; Dewhurst, D.; Wang, H-B. (1996): Models for the Fire Behaviour of Fibre Reinforced Composite Components. Reports CP301/302, Marinetech North West Programme on *Cost-Effective Use of Fibre Reinforced Composites Offshore*, Phase III, Marinetech Research, Manchester.

Gibson, A. G.; Spagni, D. A., Turner, M. J. (1992): The Cost-Effective Use of Fibre Reinforced Composites Offshore. Multi-Sponsor Research Programme, Final Report, Phase I, Marinetech North West, Manchester.

Gibson, A. G.; Wu, Y-S.; Chandler, H. W.; Wilcox, J. A. D.; Bettess, P. (1995): A Model for the Thermal Performance of Thick Composite Laminates in Hydrocarbon Fires. *Revue De L'Institut Francais Du Petrole*, **50** (1), 69-74.

Gnielinski, V. (1976): New Equations for Heat and Mass Transfer in Turbulent Pipe and Channel Flow. *Int. Chem. Eng.*, **16**, 359-368.

Grim, G. C. (1987): Shipboard Experience with Glass Reinforced Plastic (GRP) Pipes in Shell Fleet Vessels. Proceedings of the International Conference on *Polymers in a Marine Environment*, IMarE, London.

Grim, G. C. (1991): The Use of GRP Piping in the Oil and Ballast Water Systems of the Draugen Gravity Base Structure. Proceedings of the International Conference on *Polymers in a Marine Environment*, IMarE, London.

Grim, G. C.; Twilt, L. (1991): Fire Endurance of Glass Fibre Reinforced Plastic Pipes Onboard Ships. Proceedings of the International Conference on *Polymers in a Marine Environment*, IMarE, London.

Grove, S. M. (1985): *Anisotropy of Heat Conduction in Fibre Reinforced Composites.* Ph.D. Dissertation, Plymouth Polytechnic, Plymouth, UK.

Guiton, J. (1987): An All-GRP Piping, Support and Walkway System for Tanker Weather Deck Applications. Proceedings of the International Conference on *Polymers in a Marine Environment*, IMarE, London.

Hale, D. K. (1976): The Physical Properties of Composite Materials-A Review. *J. Mater. Sci.*, **11**, 2015-2141.

Hall, K. R.; Yarborough, L. (1971): A New Equation of State for z-Factor Calculations. *Oil Gas J.*, **71**, 82-91.

Harmathy, T. Z. (1965): Effect of Moisture on the Fire Endurance of Building Elements. 67th Annual Meeting Papers, ASTM Special Publication No. 385, 74-95.

Hashin, Z. (1983): Analysis of Composite Materials-A Survey. *J. Appl. Mech.*, **50**, 481-505.

Hatfield, D. W.; Edwards, D. K. (1981): Edge and Aspect Ratio Effects on Natural Convection from the Horizontal Heated Plate Facing Downwards. *Int. J. Heat Mass Transfer*, **24**, p. 1019.

Havens, J. A. (1969): *Thermal Decomposition of Wood.* Ph.D. Dissertation, University of Oklahoma, Normah, Oklahoma.

Henderson, J. B. (1980): *An Analytical and Experimental Study of the Pyrolysis of Composite Ablative Materials.* Ph.D. Dissertation, Oklahoma State University, Oklahoma.

Henderson, J. B.; Wiebelt, J. A.; Tant, M. R. (1985): A Model for the Thermal Response of Polymer Composite Materials with Experimental Verification. *J. of Comp. Mater.*, **19**, 579-595.

Hendeson, J. B.; Wiecek, T. E. (1987): A Mathematical Model to Predict the Thermal Response of Decomposing, Expanding Polymer Composites. *J. of Comp. Mater.*, **21**, 373-393.

Hill, P. (1996): Personal Communication.

Hollaway, L. (1978): *Glass Reinforced Plastics in Construction*. Surrey University Press, Surrey, UK.

Holman, J. P. (1997): *Heat Transfer*. 8th ed., McGraw-Hill, New York.

Huebner, K. H.; Thornton, E. A.; Byrom, T. G. (1995): *The Finite Element Method for Engineers*. 3rd ed., John Wiley & Sons, New York.

Hull, D. (1981): *An Introduction to Composite Materials*. Cambridge University Press, Cambridge.

Hume, J.; Kumar, S.; Patel, H.; Petlett, K.; Trew, R.; Williams, D. (1991): Assessment of Fire Performance of Fibre Reinforced Composites for Use Offshore. Report CP10, Marinetech North West Programme on *Cost-Effective Use of Fibre Reinforced Composites Offshore*, Marinetech Research, Manchester.

ISO 5660 (1989): Reaction to Fire Rate of Heat Release from Building Products. International Organisation for Standardisation.

ISO 834 (1975): Fire Resistance Test. 1st ed., International Organisation for Standardisation.

Jakob, M. (1949): *Heat Transfer*. Vol. 1., Chapman and Hall, London.

Johnston Pipes Limited (1997): Lightweight Centrifugally Spun Glass Reinforced Pipes (Aramflo). Product Data and Installation Procedure Catalogues, Surrey, UK.

Kansa, E. J.; Perlee, H. E.; Chaiken, R. F. (1977): Mathematical Model of Wood Pyrolysis Including Internal Forced Convection. *Combustion and Flame*, **29**, 311-324.

Kung, H-C. (1972): A Mathematical Model of Wood Pyrolysis. *Combustion and Flame*, **18**, 185-195.

Lee, G. C. (1968): Offshore Structures: Past, Present, Future and Design Considerations. *Offshore*, **28** (6), 45-55.

Lewis; R. W.; Morgan; K.; Thomas; H. R.; Seetharamu, K. N. (1996): *The Finite Element Method in Heat Transfer Analysis*. John Wiley & Sons, Chichester, UK.

Lide, D. R.; Kehiaian, H. V. (1994): *CRC Handbook of Thermophysical and Thermochemical Data*. CRC Press, Boca Raton.

Llyod, J. R.; Moran, W. R. (1974): Natural Convection Adjacent to Horizontal Surface of Various Platforms. ASME Paper 74-Wa/HT-66.

Looyeh, M. R. E. (1994): *Finite Element Simulation of One-Dimensional Heat Flow in Composite Fire Walls for Offshore Structures.* MSc Thesis, University of Newcastle-upon-Tyne, Newcastle-upon-Tyne, UK.

Looyeh, M. R. E.; Bettess, P. (1996): An Axi-Symmetric Finite Element Model for the Fire Performance of GRP Pipes Used for Natural Gas Transmission. Proceedings of the 2nd International Conference on *Mechanical Engineering*, ISME, Shiraz, Iran.

Looyeh, M. R. E.; Bettess, P. (1998a): A Finite Element Model for the Fire Performance of GRP Panels Including Variable Thermal Properties. *J. Finite Elements Analysis Design*, **30**, 313-324.

Looyeh, M. R. E.; Bettess, P. (1998b): The Effect of Surface Phenomena on the Thermal Response of Glass Reinforced Plastics During Fire. 3rd International Conference of *Mechanical Engineering*, ISME, Tehran, Iran.

Looyeh, M. R. E.; Bettess, P.; Gibson, A. G. (1997): A One-Dimensional Finite Element Simulation for the Fire Performance of GRP Panels for Offshore Structures. *Int. J. Num. Meth. Heat Fluid Flow*, **7** (6), 609-625.

Looyeh, M. R. E.; Bettess, P.; Gibson, A. G.; Dodds, N. (1998c): A Two-Dimensional Finite Element Model for the Thermal Response of GRP Panels under Fire. Proceedings of the 7th International Conference on *Fibre Reinforced Composites*, University of Newcastle-upon-Tyne, Newcastle-upon-Tyne, 386-393.

Marks, P. J. (1987): The Fire Endurance of Glass Reinforced Epoxy Pipes. Proceedings of the International Conference on *Polymers in a Marine Environment*, IMarE, London.

McClelland, B. *et al.* (1986): *Planning and Design of Fixed Offshore Platforms.* Van Nostrand Reinhold, New York.

Mehaffey, J. R. (1994): A Model for Predicting Heat Transfer Through Gypsum-Board/Wood-Stud Walls Exposed to Fire. *Fire Mater.*, **19**, 297-305.

Munson, T. R.; Spindler, R. J. (1961): Transient Thermal Behaviour of Decomposing Materials-Part I: General Theory and Application to Convective Heating. AVCO Corporation RAD-TR-61-10.

Murthy, K. A. (1969): *An Evaluation of the Physico-Chemical Factors Influencing the Burning Rate of Cellulosic Fuels and a Comprehensive Model for Solid Fuel Pyrolysis and Combustion.* Ph.D. Dissertation, University of Minnesota, Minneapolis, Minnesota.

Murty, K. A.; Blackshear, P. L. (1967): Pyrolysis Effects in the Transfer of Heat and Mass in Thermally Decomposing Organic Solids. 11th Symposium (international) on *Combustion*, The Combustion Institute, Pittsburgh, PA.

Ozisik, M. N. (1993): *Heat Conduction*. John Wiley & Sons, New York.

Panton, R. L.; Rittmann, J. G. (1969): Analytical Study of Pyrolysis Including Effects of Mass Loss and Completing Reactions. Paper Presented at Fall Meeting of the Western States Section of the Combustion Institute, La Joila, CA.

Parrott, J. E.; Audrey, D. S. (1975): *Thermal Conductivity of Solids*. Pion Limited.

Perry, R. H.; Green, D. W.; Maloney, J. O. (1984): *Perry's Chemical Engineers' Handbook*. 6th ed., McGraw-Hill, New York.

Pittman, C. M.; Brewer, W. D. (1966): Analytical Determination of the Effect of Thermal Property Variations on the Performance of a Charring Ablator. NASA TN D-3486.

Rohsenow, W. M.; Hartnett, J. P.; Ganic, E. N. (1985): *Handbook of Heat Transfer Fundamentals*. 2nd ed., McGraw-Hill, New York.

Saith, B.; Probert, S. D.; O'Callaghan, P. W. (1986): Thermal Resistance of Pressed Contacts. *J. Appl. Energy*, **22**, 31-84.

Sarpkaya, T.; Isaacson, M. (1981): *Mechanics of Wave Forces on Offshore Structures*. Van Nostrand Reinhold, New York.

Sheffield, J. W.; Veziroglu, T. N.; Williams, A. (1980): Thermal Contact Conductance of Multi-Layered Sheets. AIAA Paper No. 80-1468.

Sheldon, R. P. (1982): *Composite Polymeric Materials*. Applied Science, New York, pp. 98-101.

Shenoi, R. N.; Wellicome, J. F. (1993a): *Composite Materials in Maritime Structures: Fundamental Aspects*. 1st ed., Vol. 1., Cambridge University Press, Cambridge.

Shenoi, R. N.; Wellicome, J. F. (1993b): *Composite Materials in Maritime Structures: Practical Considerations*. 1st ed., Vol. 2., Cambridge University Press, Cambridge.

Smith, C. S. (1990): *Design of Marine Structures in Composite Materials*. Elsevier Applied Science, New York.

Spagni, D. A.; Gibson, A. G. (1994): General Principles and Guidelines for the Application of Glass Reinforced Composites Offshore. Report CP275, Marinetech North West Programme on *Cost-Effective Use of Fibre Reinforced Composites Offshore*, Phase II, Marinetech Research, Manchester, UK.

Sullivan, R. M. (1993): A Coupled Solution Method for Predicting the Thermostructural Response of Decomposing, Expanding Polymeric Composites. *J. of Comp. Mater.*, **27** (4), 408-434.

Sullivan, R. M.; Salamon, N. J. (1992b): A Finite Element Method for the Thermochemical Decomposition of Polymeric Materials-II.Carbon Phenolic Composites. *Int. J. Engng Sci.*, **30** (7), 939-951.

Sullivan, R. M.; Salamon, N. J. (1992a): A Finite Element Method for the Thermochemical Decomposition of Polymeric Materials-I.Theory. *Int. J. Engng Sci.*, **30** (4), 431-441.

Sykes, G. F. (1967): Decomposition Characteristics of a Char-Forming Phenolic Polymer Used for Ablative Composites. NASA Technical Note No. TN D-3810.

Taya, M.; Arsenault, R. J. (1989): *Metal Matrix Composites: Thermomechanical Behaviour*. Pergamon, New York.

Ulfvarson, A. Y. J. (1989): Superstructures of Large Ships and Floating Offshore Platforms Built in FRP-Sandwich: A feasibility Study. Proceedings of the First International Conference on *Sandwich Constructions*, Stockholm, Sweden.

Vinson, J. R.; Sierakowski, R. L. (1986): *The Behaviour of Structures Composed of Composite Materials*. Martinus Nijhoff, Boston.

Wang, H-B. (1995): *Heat Transfer Analysis of Components of Construction Exposed to Fire-A Theoretical, Numerical and Experimental Approach*. PhD Dissertation, University of Salford, Salford, UK.

Wu, Y-S.; Gibson, A. G. (1995): Personal Communication.

Wu, Y-S.; Gibson, A. G. (1996): Personal Communication.

Wu, Y-S.; Wilcox, J. A. D.; Gibson, A. G.; Bettess, P. (1994): Design of Composite Panels for Mechanical and Fire performance. Report CP244, Marinetech North West Programme on *Cost-Effective Use of Fibre Reinforced Composites Offshore*, Phase II, Marinetech Research, Manchester, UK.

Yovanovich, M. M. (1986): Recent Development in Thermal Contact, Gap and Joint Conductance Theories and Experiments. Proceedings of the 8th *International Heat Transfer Conference*, San Francisco, CA, 35-45.

Zienkiewicz, O. C. (1995): Personal Communication.

Zienkiewicz, O. C.; Taylor, R. L. (1991): *The Finite Element Method-Solid and Fluid Mechanics, Dynamics and Non-Linearity*. 4th ed., Vol. 2, McGraw-Hill, Berkshire, UK.

Zienkiewicz, O. C.; Taylor, R. L. (1994*): The Finite Element Method-Basic Formulation and Linear Problems*. 4th ed., Vol. 1, McGraw-Hill, Berkshire, UK.

Zienkiewicz, O. C.; Bettess, P.; Kelly, D. W. (1978): The Finite Element Method for Determining Fluid Loadings on Rigid Structures: Two- and Three-Dimensional Formulations, Chap. 4. *Numerical Methods in Offshore Engineering*. Eds: Zienkiewicz, O. C.; Lewis, R. W.; Stagg, K. G., John Wiley & Sons, Chichester, UK.

APPENDIX A

COMPOSITE MATERIALS

A useful classification of composite materials is: (i) Natural (e.g. wood); (ii) Micro-structural (e.g. steel) and (iii) Macro-structural (e.g. glass reinforced plastics). Among these, the macro-structural level is of current interest for large scale applications and can be further classified into [1,2]:

1. Fibre: Composed of continuous or chopped fibres.
2. Particulate: Composed of particles.
3. Laminar: Composed of layers or lamina constituents.
4. Flake: Composed of flat flakes.
5. Filled / Skeletal: Continuous skeletal matrix filled by second material.

Within the framework of this classification, the most important composite materials are the filamentary type which consists of selected fibre macro-constituents. These composites are defined as combinations of materials which differ in composition or form on a macroscopic level.

For the case of reinforced plastics the combination of matrix and fibrous elements depends on the constituents used (Figure A.1).

Figure A.1 Composite materials composed of matrices and reinforcements [2].

A general approach [2] to characterising material behaviour for composites can be described at the macroscopic level: (a) Homogeneous and isotropic; (b) Homogeneous and anisotropic; (c) Non-homogeneous and isotropic and (d) Non-homogeneous and anisotropic.

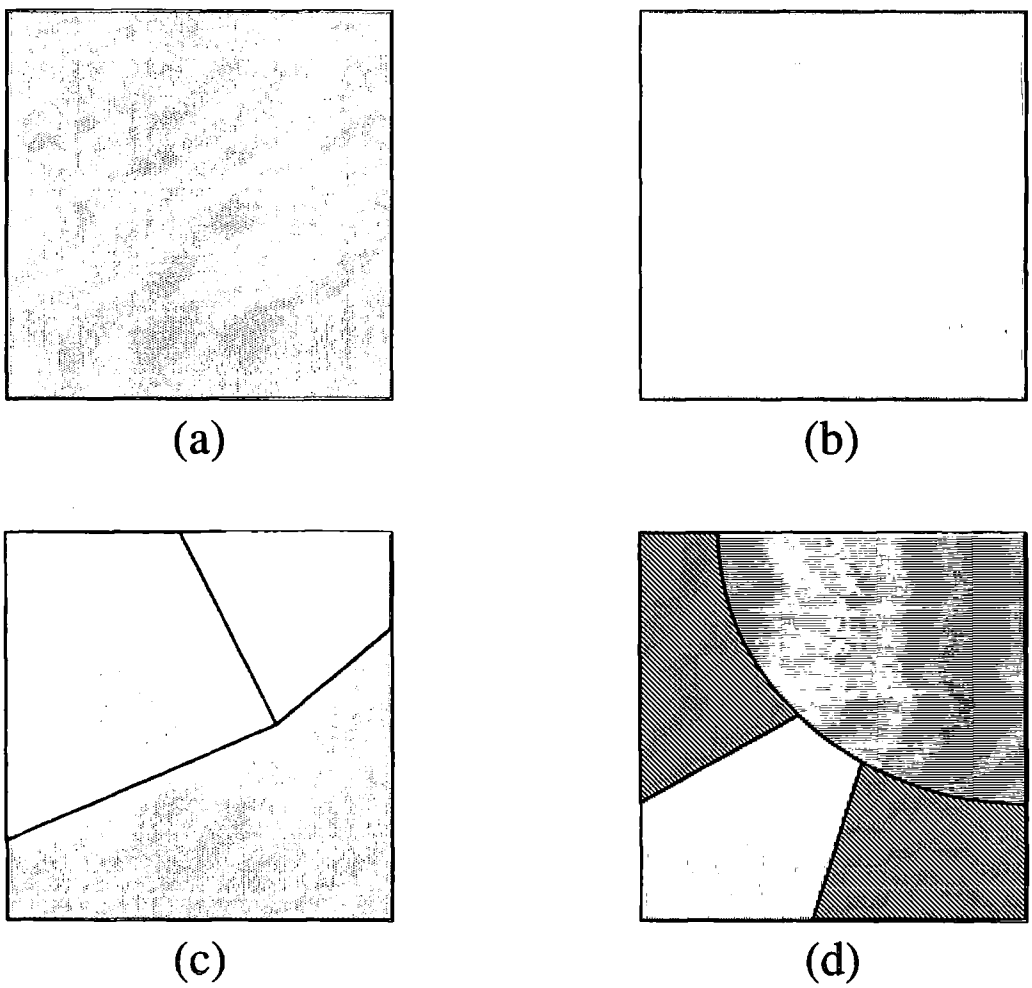

Figure A.2 Macroscopic classification of composite materials in terms of their homogeneity and isotropy. (a) homogeneous and isotropic; (b) homogeneous and anisotropic; (c) non-homogeneous and isotropic and (d) non-homogeneous and anisotropic [3].

A homogeneous body is one in which uniform properties exist throughout the body and for which the properties are not functionally dependent upon position. An isotropic body is one which has the same material properties in any direction at any point within the material. The possible macroscopic categories of composite materials are illustrated in Figure A.2. Most of the common composites are homogenous and anisotropic (Figure A.2b). For such materials most of the mechanical and thermal properties such

as Young's modulus and thermal conductivity are dependent upon the orientation of the material. Such dependence on orientations may be a serious limitation for some applications but in others may be an advantage since it allows the possibility of introducing stiffness and strength into a product where it is required.

Polymer composites are polymer-based compounds containing gaseous, particulate or fibrous matter. The range of such materials which have found applications across the spectrum of engineering is vast, ranging from foamed plastics in building and packaging to high-performance carbon fibre-reinforced resins in aerospace industry [Grim, 1987]. Potentially, any polymer can be used as a matrix, but in practice, only a limited number of materials are used due to factors such as ease of fabrication, compatibility with fibres, desired end properties and cost. The most common type of polymer composites are fibre reinforced plastics (FRP).

Polymers are simply divided into two: thermoplastics and thermosets [Hull, 1981]. A thermoplastic is produced based on the end-to-end joining of basic molecules which results in a long, chain-like linear polymer. The most common examples are polyethylene (PE), polypropylene (PP), polyvinylchloride (PVC) and polystyrene (PS). Thermoplastic matrices are normally used with short fibre reinforcement for applications in products made by injection moulding. In thermosetting polymers, the liquid resins are converted into hard brittle solids by chemical cross-linking which leads to the formation of a tightly bound three-dimensional network of polymer chains. Thermosetting resins are usually isotropic. Their most characteristic property is in response to heat since, unlike thermoplastics, they do not melt on heating. Among the thermoset plastics are polyester, phenolic and epoxy resins.

REFERENCES

1. Hull, D. (1981): *An Introduction to Composite Materials*, Cambridge University Press, New York.
2. Vinson, J. R. & Sierakowski, R. L. (1986): *The Behaviour of Structures Composed of Composite Materials*, Martinus Nijhoff, Boston.
3. Bejan, A. (1993): *Heat Transfer*, 1st ed., John Wiley & Sons, New York.

APPENDIX B

BASIC EQUATIONS FROM HEAT CONDUCTION

B.1 STEADY-STATE HEAT CONDUCTION

Heat conduction is the transfer of thermal energy through a solid due to a temperature gradient, i.e. thermal energy is transferred from a region of high temperature to a region of lower temperature at the molecular and atomic levels with no transfer of mass. The rate equation describing heat conduction is known as Fourier's Law [1] given by:

$$q_n = -k\frac{\partial T}{\partial n} \tag{B.1}$$

where q_n is heat flux (rate of heat flow per unit area) in n direction (Wm^{-2}); k is thermal conductivity ($Wm^{-1}K^{-1}$) and T is temperature (^{o}C). The minus sign appears because positive thermal energy transfer occurs from a warmer to a colder region which means the temperature gradient $\partial T/\partial n$ is negative in the direction of positive heat flow.

For a two-dimensional anisotropic medium, Equation B.1, in Cartesian co-ordinates, becomes [2,3]:

$$q_x = -\left(k_{11}\frac{\partial T}{\partial x} + k_{12}\frac{\partial T}{\partial y}\right) \quad , \quad q_y = -\left(k_{21}\frac{\partial T}{\partial x} + k_{22}\frac{\partial T}{\partial y}\right) \tag{B.2}$$

where q_x is heat flux in x direction (Wm^{-2}); q_y is heat flux in y direction (Wm^{-2}) and k_{ij} is element of conductivity matrix ($Wm^{-1}K^{-1}$). The principles of irreversible thermodynamics show that the thermal conductivity matrix is symmetric, i.e. $k_{12} = k_{21}$.

Polymer composites such as woven roving glass reinforced plastics (WR-GRP) are orthotropic, i.e. they have different thermal conductivities in two mutually perpendicular directions. When the co-ordinate axes are chosen to coincide with these directions, Equations B.2a and B.2b can be simplified to:

$$q_x = -k_x\frac{\partial T}{\partial x} \quad , \quad q_y = -k_y\frac{\partial T}{\partial y} \tag{B.3}$$

where k_x is thermal conductivity in x direction ($Wm^{-1}K^{-1}$) and k_y is thermal conductivity in y direction ($Wm^{-1}K^{-1}$).

For the case of an isotropic medium, the Equations B.3a and B.3b can be further simplified to:

$$q_x = -k\frac{\partial T}{\partial x} \quad , \quad q_y = -k\frac{\partial T}{\partial y} \tag{B.4}$$

B.2 TRANSIENT HEAT CONDUCTION

The differential equation describing the transient heat conduction in a solid including internal heat generation is derived by considering the energy balance on an elemental volume within the solid. Conservation of energy requires [2,3]:

$$\rho c_p \frac{\partial T}{\partial t} = -\frac{\partial q_n}{\partial n} + \dot{q} \tag{B.5}$$

where ρ is density (kgm^{-3}); c_p is specific heat at constant pressure ($Jkg^{-1}K^{-1}$) and $\dot{q}$ is internally generated heat per unit volume (Wm^{-3}). Equation B.5 becomes non-linear if any of thermal conductivity, specific heat or other thermal properties are temperature dependent. For constant thermal properties and an isotropic material, the heat conduction equation takes the form:

$$\frac{1}{\alpha}\frac{\partial T}{\partial t} = \frac{\partial^2 T}{\partial n^2} + \frac{\dot{q}}{k} \tag{B.6}$$

where α is thermal diffusivity defined by $\alpha = k/\rho c_p$ (m^2s^{-1}).

For a two-dimensional medium, Equation B.6 is given, in Cartesian co-ordinates (x,y) and polar co-ordinates (r,θ), by [2]:

$$\frac{1}{\alpha}\frac{\partial T}{\partial t} = \frac{\partial^2 T}{\partial x^2} + \frac{\partial^2 T}{\partial y^2} + \frac{\dot{q}}{k} \tag{B.7a}$$

$$\frac{1}{\alpha}\frac{\partial T}{\partial t} = \frac{1}{r}\frac{\partial}{\partial r}\left(r\frac{\partial T}{\partial r}\right) + \frac{1}{r^2}\frac{\partial^2 T}{\partial \theta^2} + \frac{\dot{q}}{k} \tag{B.7b}$$

B.3 INITIAL AND BOUNDARY CONDITIONS

The transient heat conduction equation, Equation B.5, must be solved subject to initial conditions and appropriate boundary conditions [2,3]. The initial conditions consist of specifying the temperature and thermal properties throughout the solid at an initial time. The boundary conditions take several forms and must be specified on all boundaries of the solid. Prescribed temperature, prescribed heat flow, convection and radiation are the typical boundary conditions which may be experienced by a solid.

Prescribed temperature

The surface temperature of a boundary is specified to be constant or a function of time or boundary position, known as *Dirichlet* condition. This is given by:

$$T_s = T(x, y, t) \tag{B.8}$$

where T_s is surface temperature (°C).

Prescribed heat flux

The heat flux across a boundary is specified to be constant or a function of time or boundary position. Using Fourier's law [1], this boundary condition may be given by:

$$q_x n_x + q_y n_y = q_s \tag{B.9}$$

, known as *Cauchy* condition, where n_x is normal vector in x direction; n_y is normal vector in y direction and q_s is surface heat flux (Wm^{-2}). When the heat flux across a boundary is zero, the boundary condition is simplified into:

$$q_x n_x + q_y n_y = 0 \tag{B.10}$$

which is known as *Neumann* condition or the adiabatic boundary condition.

Convective boundary condition

When the rate of heat flow across a boundary is proportional to the difference between the surface temperature T_s and a convective exchange temperature T_∞ of an adjacent fluid, the convective boundary condition takes the form:

$$q_x n_x + q_y n_y = h_c (T_s - T_\infty) \tag{B.11}$$

where h_c is the convective heat transfer coefficient ($W\ m^{-2}K^{-1}$).

The convective boundary condition can be either linear or non-linear. This is because the convection coefficient may be temperature or time dependent.

Radiative boundary condition

In this case the rate of heat flow across a boundary is specified in terms of the emitted energy from the surface and the incident radiant thermal energy absorbed by the surface from other elements. This boundary condition is given using Stefan's law [3]:

$$q_x n_x + q_y n_y = \sigma \varepsilon_s T_s^4 - \alpha_s q_r \tag{B.12}$$

where σ is Stefan-Boltzmann constant ($5.669 \times 10^{-8}\ Wm^{-2}K^{-4}$); ε_s is surface emissivity; α_s is surface absorptivity and q_r is incident radiant thermal energy (Wm^{-2}).

The first term on the right hand side is the emitted energy from the surface and the second term is the absorbed incident radiant energy by the surface. The surface emissivity and absorptivity are normally functions of surface temperature.

B.4 DIMENSIONLESS GROUPS

Several dimensionless groups are used to characterise the convective heat transfer. These are [2,3]:

1. Prandtl number is the ratio of viscous diffusion to thermal diffusion given by:

$$\mathrm{Pr} = \frac{\upsilon}{\alpha} = \frac{\mu c_p}{k} \tag{B.13a}$$

2. Reynolds number is the ratio of inertia force to viscous force given by:

$$\mathrm{Re} = \frac{\rho V L}{\mu} \tag{B.13b}$$

3. Peclet number characterises forced convection and is given by:

$$\mathrm{Pe} = \mathrm{Re}\,\mathrm{Pr} \tag{B.13c}$$

4. Grashof number is the ratio of buoyancy force to viscous force given by:

$$\mathrm{Gr} = \frac{g\beta(T_s - T_\infty)L^3\rho^2}{\mu^2} \tag{B.13d}$$

5. Nusselt number is a dimensionless convective coefficient given by:

$$\mathrm{Nu} = \frac{h_c L}{k} \tag{B.13e}$$

6. Rayleigh number represents free convection and is given by:

$$\mathrm{Ra} = \mathrm{Gr}\,\mathrm{Pr} \tag{B.13f}$$

where L is characteristic dimension which is replaced by the height or width of a plate or the diameter of a pipe (m); μ is dynamic viscosity ($\mathrm{Nsm^{-1}}$); g is gravitational acceleration ($\mathrm{ms^{-2}}$) and β is coefficient of volumetric thermal expansion, $\beta = 1/T$ ($\mathrm{K^{-1}}$).

REFERENCE

1. Fourier, J. B. J. (1822): *Theorie Analytique De La Chaleur*, Didot, Paris.
2. Huebner, K. H., Thornton, E. A. & Byrom, T. G. (1995): *The Finite Element Method for Engineers*, 3rd ed., John Wiley & Sons, New York.
3. Bejan, A. (1993): *Heat Transfer*, 1st ed., John Wiley & Sons, New York.

APPENDIX C

SOME BASICS OF THE FINITE ELEMENT METHOD

C.1 SHAPE FUNCTIONS

Shape functions are chosen based on certain continuity requirements which must be met to ensure the convergence criteria are satisfied [1]. These requirements, in one- and two dimensions, are:

$$N_i = \begin{cases} 1 & \text{at node } i \\ 0 & \text{at every other node} \end{cases} \tag{C.1a}$$

$$\sum_{i=1}^{r} N_i = 1 \qquad r = \text{number of nodes} \tag{C.1b}$$

$$\sum_{i=1}^{r} x_i N_i = x \quad , \quad \sum_{i=1}^{r} y_i N_i = y \tag{C.1c}$$

One-dimensional linear element

Choosing a linear polynomial, a field variable can be approximated by (Figure C.1a):

$$T(x,t) = \mathbf{N}(x)\mathbf{T}(t) = \sum_{i=1}^{2} N_i(x) T_i(t) \tag{C.2}$$

where

$$N_1(x) = \frac{x_2 - x}{x_2 - x_1} \quad , \quad N_2(x) = \frac{x - x_1}{x_2 - x_1} \tag{C.3}$$

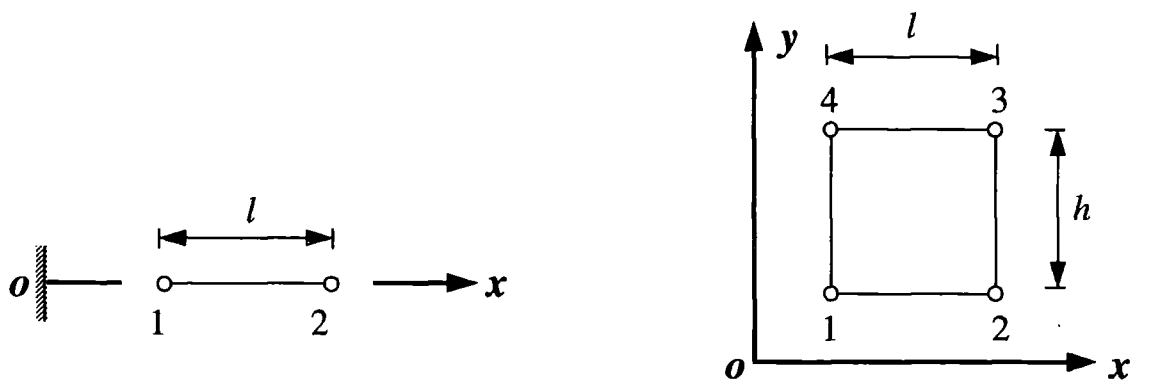

(a) (b)

Figure C.1 (a) One-dimensional two-node element, (b) Two-dimensional rectangular element.

When $x_1 = 0$ and $x_2 = l$, the linear shape functions become:

$$N_1(x) = \frac{l-x}{l} \quad , \quad N_2(x) = \frac{x}{l} \tag{C.4}$$

The shape functions can be expressed in the local co-ordinate ξ, with co-ordinate transformation $\xi = (2x\text{-}l)/l$, by:

$$N_1(\xi) = \frac{1}{2}(1-\xi) \quad , \quad N_2(\xi) = \frac{1}{2}(1+\xi) \tag{C.5}$$

where $-1 \leq \xi \leq 1$.

Two-dimensional rectangular element

A field variable can be approximated by (Figure C.1b):

$$T(x,y,t) = \mathbf{N}(x,y)\mathbf{T}(t) = \sum_{i=1}^{4} N_i(x,y)T_i(t) \tag{C.6}$$

When $x_1=0$ and $y_1=0$ the shape functions are given by [2]:

$$\begin{aligned} N_1(x,y) &= 1 - \frac{x}{l} - \frac{y}{h} + \frac{xy}{hl} \quad , \quad N_2(x,y) = \frac{x}{l} - \frac{xy}{lh} \\ N_3(x,y) &= \frac{xy}{hl} \quad , \quad N_4(x,y) = \frac{y}{h} - \frac{xy}{hl} \end{aligned} \tag{C.7}$$

These are also given in the local co-ordinates (ξ,η), with co-ordinates transformation $\xi=(2x\text{-}l)/l$ and $\eta=(2y\text{-}h)/h$, by [2]:

$$\begin{aligned} N_1(\xi,\eta) &= \frac{1}{4}(1-\xi)(1-\eta) \quad , \quad N_2(\xi,\eta) = \frac{1}{4}(1+\xi)(1-\eta) \\ N_3(\xi,\eta) &= \frac{1}{4}(1+\xi)(1+\eta) \quad , \quad N_4(\xi,\eta) = \frac{1}{4}(1-\xi)(1+\eta) \end{aligned} \tag{C.8}$$

where $-1 \leq \xi \leq 1$ and $-1 \leq \eta \leq 1$.

C.2 INTEGRATION BY PARTS

One-dimensional domain $a \leq x \leq b$ [2,3]:

$$\int_a^b u\,dv = uv\Big|_a^b - \int_a^b v\,du \tag{C.9a}$$

Two- or three-dimensional domain Ω bounded by Γ [2,3]:

$$\int_\Omega u\,(\nabla.\mathbf{v})\,d\Omega = \int_\Gamma u\,(\mathbf{v}.\mathbf{n})\,d\Gamma - \int_\Omega \mathbf{v}.\nabla u\,d\Omega \tag{C.9b}$$

where

$$\nabla = \frac{\partial}{\partial x}\hat{i} + \frac{\partial}{\partial y}\hat{j} + \frac{\partial}{\partial z}\hat{k} \tag{C.9c}$$

$$\mathbf{n} = n_x\hat{i} + n_y\hat{j} + n_z\hat{k} \tag{C.9d}$$

The integration by parts in two dimension is known as Green's theorem and in three dimension as Gauss's theorem [2].

C.3 NUMERICAL INTEGRATION

Gaussian or Gauss-Legendre quadrature [1,3] is used for the numerical evaluation of the finite element integrals. An integral of the form:

$$\mathrm{I} = \int_a^b f(x)dx \tag{C.10}$$

in the global co-ordinate x is transformed to the local co-ordinate ξ and then evaluated by:

$$\mathrm{I} = \int_{-1}^{1} f(\xi)d\xi = \sum_{i=1}^{n} w_i f(\xi_i) \tag{C.11}$$

where w_i and ξ_i represent tabulated values of the weights and abscissae associated with n (Gaussian) points in the interval (-1,1).

For the case of two dimension, an integral of the form:

$$\mathrm{I} = \int_{\Omega} f(x,y)dxdy \tag{C.12}$$

is transformed to local co-ordinates (ξ,η) and then numerically integrated by:

$$\mathrm{I} = \int_{-1}^{1}\int_{-1}^{1} f(\xi,\eta)d\xi d\eta = \sum_{i=1}^{n}\sum_{j=1}^{n} w_i w_j f(\xi_i,\eta_j) \tag{C.13}$$

Values of w_i, w_j, ξ_i and η_j for n=1,2,3,4 are shown in Table C.1.

Table C.1 Abscissae and weight coefficients of the Gaussian quadrature

No. of Gauss points, n	Values of ξ_i and η_j	Values of w_i and w_j
1	0	2.000000
2	±0.577350	1.000000
3	±0.774597	0.555556
	0	0.888889
4	±0.861136	0.347855
	±0.339981	0.652145

C.4 INTRODUCING DIRICHLET BOUNDARY CONDITION

To include Dirichlet boundary conditions or prescribed nodal variables into the matrix equation $\mathbf{A}_{n\times n}\mathbf{X}_{n\times 1}=\mathbf{B}_{n\times 1}$, two methods may be used [2]:

1. If i is the subscript of a prescribed nodal variable, the ith row and ith column of **A** are set equal to zero and a_{ii} is set equal to unity. The term b_i of the right hand side vector **B** is replaced by known value of x_i. Each of the n-1 remaining terms of **B** is modified by subtracting from it the value of the prescribed nodal variable multiplied by the appropriate column term from the original **A** matrix. This procedure is repeated for each prescribed x_i until all of them have been included.
2. The diagonal term of **A** associated with a specified nodal variable is multiplied by a large number, e.g. 1×10^{15}, while the corresponding term in **B** is replaced by the specified nodal variable multiplied by the same large factor times the corresponding diagonal term. This procedure is repeated until all prescribed nodal variables have been treated. Effectively, this procedure makes the unmodified terms of **A** very small compared to the modified terms.

C.5 MATRIX DIAGONALISATION

The element mass matrix **C** in the finite element formulation always contains off-diagonal terms, meaning that the heat capacity is distributed among nodes rather than being concentrated at nodes. To implement an explicit finite element solution and to simplify the inversion of the mass matrix, diagonalisation is used. This method is defined by [4]:

$$\begin{aligned} c_{ij} &= \sum_{m=1}^{n} c_{im} \qquad \text{if} \qquad i = j \\ c_{ij} &= 0 \qquad\qquad\ \ \text{if} \qquad i \neq j \end{aligned} \tag{C.14}$$

For simple elements, diagonalisation does not appear to significantly reduce solution accuracy [4,5].

REFERENCES

1. Lewis, P. E. & Ward, J. P. (1991): *The Finite Element Method-Principles and Applications*, Addison-Wesley, Reading, UK.
2. Huebner, K. H., Thornton, E. A. & Byrom, T. G. (1995): *The Finite Element Method for Engineers*, 3rd ed., John Wiley & Sons, New York.
3. Zienkiewicz, O. C. & Taylor, R. L. (1994): *The Finite Element Method-Basic Formulation and Linear Problems*, 4th ed., Vol. 1, McGraw-Hill, Berkshire, UK.
4. Rohsenow, W. M., Hartnett, J. P. & Ganic, E. N. (1985): *Handbook of Heat Transfer Fundamentals*, McGraw-Hill, New York.
5. Gerald, C. F. & Wheatly, P. O. (1989): *Applied Numerical Analysis*, Addison-Wesley, Reading, UK.